

NASA Contractor Report 187092

Advanced Development Receiver Thermal Vacuum Tests With Cold Wall

Final Report

Leigh M. Sedgwick
*The Boeing
Company
Seattle, WA*

June 1991

Prepared for
Lewis Research Center
Under Contract
NAS3-25716



(NASA-CR-187092) ADVANCED DEVELOPMENT
RECEIVER THERMAL VACUUM TESTS WITH COLD WALL
Final Report (Boeing Co.) 282 p CSCL 22B

N91-24227

Unclass
23/19 0015259

Report Documentation Page

1. Report No. NASA CR-187092		2. Government Accession No.		3. Recipient's Catalog No.	
4. Title and Subtitle Advanced Development Receiver Thermal Vacuum Test With Cold Wall Final Report				5. Report Date May 1991	
				6. Performing Organization Code	
7. Author(s) Leigh M. Sedgwick				8. Performing Organization Report No. D180-32816-1	
				10. Work Unit No. 474-52-10	
9. Performing Organization Name and Address Boeing Defense and Space Group P.O. Box 3999 Seattle, WA 98124-2499				11. Contract or Grant No. NAS3-25716	
				13. Type of Report and Period Covered Contractor Report Final	
12. Sponsoring Agency Name and Address National Aeronautics and Space Administration Lewis Research Center Cleveland, Ohio 44135-3191				14. Sponsoring Agency Code	
15. Supplementary Notes Project Managers, Kerry L. McLallin and Thomas W. Kerslake, Systems Engineering and Integration Division, NASA Lewis Research Center					
16. Abstract The first ever testing of a full-size, 102 kW _t , solar dynamic heat receiver utilizing high-temperature thermal energy storage has been completed. The heat receiver was designed to meet the requirements for operation on the Space Station Freedom. The purpose of the test program was to quantify the receiver thermodynamic performance, its operating temperatures, and thermal response to changes in environmental and power module interface boundary conditions. The heat receiver was tested in a vacuum chamber with liquid nitrogen cold shrouds and an aperture cold plate to partially simulate a low-Earth-orbit environment. The cavity of the receiver was heated by an infrared quartz lamp heater with 30 independently controllable zones to produce flux distributions typical of candidate concentrators. A closed-Brayton-cycle engine simulator conditioned a helium-xenon gas mixture to specific interface conditions to simulate various operational modes of the solar dynamic power module. Inlet gas temperature, pressure, and flow rate were independently varied. A total of 58 simulated orbital cycles (94 minutes each) were completed during the test conduct period. This document describes the test hardware, execution of testing, test data, and post-test inspections.					
17. Key Words (Suggested by Author(s)) Closed Brayton cycle Heat receiver Solar dynamic power Space power Thermal energy storage			18. Distribution Statement Unclassified - Unlimited Subject Category 18		
19. Security Classif. (of this report) Unclassified		20. Security Classif. (of this page) Unclassified		21. No. of pages 280	
				22. Price	

ABSTRACT

The first ever testing of a full-size, 102 kW_e, solar dynamic heat receiver utilizing high-temperature thermal energy storage has been completed. The heat receiver was designed to meet the requirements for operation on the Space Station Freedom. The purpose of the test program was to quantify the receiver thermodynamic performance, its operating temperatures, and thermal response to changes in environmental and power module interface boundary conditions. The heat receiver was tested in a vacuum chamber with liquid nitrogen cold shrouds and an aperture cold plate to partially simulate a low-Earth-orbit environment. The cavity of the receiver was heated by an infrared quartz lamp heater with 30 independently controllable zones to produce flux distributions typical of candidate concentrators. A closed-Brayton-cycle engine simulator conditioned a helium-xenon gas mixture to specific interface conditions to simulate various operational modes of the solar dynamic power module. Inlet gas temperature, pressure, and flow rate were independently varied. A total of 58 simulated orbital cycles (94 minutes each) were completed during the test conduct period. This document describes the test hardware, execution of testing, test data, and post-test inspections.

KEY WORDS

Calcium Fluoride
Closed Brayton Cycle
Electrical Power Generation
Energy Storage
Heat Receiver
Helium-Xenon
High-Temperature
Lithium Fluoride
Low Earth Orbit
Phase Change
Quartz Lamp
Solar Dynamic Heat Receiver
Solar Dynamic Power Generation
Space
Space Station Freedom
Test Plan
Test Procedures
Thermal Energy Storage
Vacuum

ACKNOWLEDGEMENTS

The constructive program guidance afforded by the following personnel of the NASA Lewis Research Center is gratefully acknowledged:

Mr. Kerry McLallin	ADRT Project Manager
Mr. Thomas Kerslake	Assistant Project Manager
Mr. Ken Mellott	Solar Dynamic Testing

The assistance of the following personnel at Rocketdyne, the prime contractor to NASA on the Space Station Freedom electrical power system, is gratefully acknowledged.

Mr. Chuck Kudija	CBC Project Engineer
Mr. Johnny Paterson	CBC Test Engineer

The following subcontractor personnel also provided significant input to the ADRT program and are gratefully acknowledged.

Mr. Michael Iles	Lukas Machine - Seattle, WA
Mr. Patrick Heller	Manville Insulation - Elkhart, IN
Mr. George Robinson	Rembar - Dobbs Ferry, NY

Sincere appreciation is expressed to the following Boeing personnel for their assistance and participation on the ADRT program.

Dr. Ted Kramer	AST Manager
Dr. Frank Marshall	AST Manager
Mr. Harold Nordwall	ADRT Program Manager
Mr. Leigh Sedgwick	ADRT Test Director
Mr. Ernie Valley	ADRT Contracts
Mr. Kenneth Kaufmann	ADRT Design and Deputy Test Director
Mr. Richard Saadeh	ADRT Design Engineering
Mr. Tom Huber	ETL Test Conductor
Mr. Joe McCartney	ETL Test Conductor
Mr. Bill Hadley	ETL Instrumentation
Mr. Scott Ulen	ETL - Test Planning
Mr. Al Kwant	ETL Technician
Mr. Ted Andrews	ETL Technician
Mrs. Rose Hall	Secretarial/Everything

TABLE OF CONTENTS

Section	Description	Page
	ABSTRACT and KEY WORDS	2
	ACKNOWLEDGMENTS	3
	TABLE OF CONTENTS	4
	LIST OF FIGURES	6
	NOMENCLATURE	13
1.0	SUMMARY	14
2.0	TEST PROGRAM OVERVIEW	17
2.1	Scope	17
2.2	Test Program Objectives	17
2.3	Test Program Requirements	17
2.4	ADRT Test Description	18
2.4.1	Verification Tests	18
2.4.2	Flux Variation Tests	19
2.4.3	Receiver Shutdown and Cold Soak Start Up Tests	20
3.0	TEST HARDWARE, FACILITIES, AND INSTRUMENTATION	21
3.1	AD Heat Receiver and Support Cart	21
3.2	CBC Engine Simulator	24
3.3	Quartz Lamp Heater	27
3.4	LN2 Cold Shrouds and Aperture Cold Plate	27
3.5	Optical Borescope	27
3.6	Facilities	28
3.7	Instrumentation and Data Acquisition	30
3.7.1	Receiver Instrumentation	30
3.7.2	Instrumentation to Characterize Receiver Performance	44
3.7.3	Test Support Equipment and Facility Measurements	44
3.7.4	Helium-Xenon Gas Composition	52
3.7.5	Data Acquisition and Control System (DACS)	52
4.0	TEST ASSEMBLY	53
4.1	Facilities	53
4.2	Receiver Installation	53
4.3	CBC Simulator Installation	62
4.4	Quartz Lamp Heater Assembly and Installation	62

TABLE OF CONTENTS

Section	Description	Page
5.0	TEST CONDUCT	81
5.1	Test Readiness Review Meeting	81
5.2	Initial Attempts To Begin Testing	81
5.3	Steady-State Heat Balance Test, VT.1	82
5.4	Steady-State Heat Balance Test, VT.2	85
5.5	Initial Baseline Orbit, VT.3	92
5.6	Gas Flow Rate Variation Test, VT.5	99
5.7	Orbital Variation Test, VT.6	104
5.8	Maximum Insolation Orbit Test, VT.8	109
5.9	Peaking Orbit Simulation, VT.12	118
5.10	Axial Flux Variation, SS.1	121
5.11	Circumferential Flux Variation, SS.4	127
5.12	Modified Baseline Orbit, VT.3B	140
5.13	Return to Baseline Orbit, VT.3A	140
5.14	Shutdown to Cold Soak, CS.1	149
5.15	Cold Start Up Tests, CS.3	149
5.16	Shutdown to Ambient and Test Termination	157
6.0	DISCUSSION OF RESULTS	160
6.1	Data Modifications	160
6.2	Receiver Thermodynamic Performance	160
6.3	Quartz Lamp Heater Power	164
6.4	Receiver Operating Temperatures and Gradients	169
6.5	Felt Metal Performance	177
6.6	Helium-Xenon Gas Composition	177
6.7	Steady-State Heat Loss Adjustments	180
7.0	POST-TEST HARDWARE INSPECTION	184
8.0	CONCLUSIONS AND RECOMMENDATIONS	199
	REFERENCES	202
	APPENDIX A - Test Summaries	203
	APPENDIX B - ADRT Data File Description	235
	APPENDIX C - Selected Test Data Plots	239

LIST OF FIGURES

No.	Description	Page
2-1	Summary of the ADRT Test Program Parametric Requirements.	18
2-2	The Prioritized ADRT Test Matrix.	19
3-1	SDHRT Heat Receiver Design Configuration.	22
3-2	SDHRT Heat Receiver Mounted in Support Cart During Preparation for Testing.	23
3-3	CBC Engine Simulator Functional Schematic.	25
3-4	CBC Engine Simulator Pictured At the Tulalip Test Site.	26
3-5	Typical Wiring Schematic for Quartz Lamp Zones.	29
3-6	ADRT Instrumentation List.	31
3-7	Location of Instrumented Heat Storage Tubes Inside the Receiver Cavity.	40
3-8	Internal Thermocouples at the Exit End of Heat Storage Tube #19.	41
3-9	Thermocouple Alignment With Respect to Flux, Cavity Wall, and Gravity for Heat Storage Tube #19.	42
3-10	Thermocouple Attachment to the Convolution Peaks at the Middle of Heat Storage Tube #19.	43
3-11	Thermocouple Alignment With Respect to Flux, Cavity Wall, and Gravity for Heat Storage Tube #12.	45
3-12	Instrumented Heat Storage Tube #4.	46
3-13	Close Up Showing the Thermocouple Attachment to the Convolution Peaks and Valleys at the Inlet End of Heat Storage Tube #4.	47
3-14	Thermocouple Alignment With Respect to Flux, Cavity Wall, and Gravity for Heat Storage Tube #4.	48
3-15	Structural Temperature Measurement Locations Associated With Heat Storage Tube #4.	49
3-16	Method of Attachment of Sheathed Thermocouples to Cavity Wall Insulation.	50
3-17	Method of Shielding Thermocouples Attached to the Cavity Insulation.	51
4-1	Completion Dates of Significant Test Set Up Activities.	54
4-2	Vertical Lift of Receiver With Crane During Receiver Tilting Operations.	55
4-3	Lifting Front End of the Receiver With Forklift During Receiver Tilting Operations.	56
4-4	Lowering Receiver to the Ground in a Horizontal Orientation.	57
4-5	Receiver Setting on Support Blocks While Switching the Lifting Fixture From the Vertical to the Horizontal Lift Configuration.	58

LIST OF FIGURES

No.	Description	Page
4-6	Lifting the Receiver in a Horizontal Orientation With Forklift.	59
4-7	Proper Support Cart Cable Attachment Prior to Setting Receiver Inside the Support Cart.	60
4-8	Setting Receiver Inside Support Cart.	61
4-9	Inlet and Exit Gas Piping Runs Between CBC Engine Simulator and Vacuum Chamber.	63
4-10	Vacuum Chamber High-Temperature Feed-Through for Helium-Xenon Gas Piping.	64
4-11	Welded Attachments of the Inlet and Exit Gas Lines to the Heat Receiver.	65
4-12	Expansion Bellows Configuration on the Cold (Inlet) Gas Line Between the Receiver and the Vacuum Chamber.	66
4-13	Cantilever Stand Supporting Columbium Box Beam and Receiver Aperture Plug During Final Assembly Operations of the Quartz Lamp Heater.	67
4-14	Installation of the Top Zone A On To the Box Beam During Final Assembly Operations of the Quartz Lamp Heater.	68
4-15	Installation of the Zones B and F On To the Box Beam During Final Assembly Operations of the Quartz Lamp Heater.	69
4-16	Installation of Zones E On To the Box Beam During Final Assembly Operations of the Quartz Lamp Heater.	70
4-17	Installation of the Bottom Zone D On To the Box Beam During Final Assembly Operations of the Quartz Lamp Heater.	71
4-18	Completed Quartz Lamp Array Prior To Installation Into the Receiver Cavity.	72
4-19	Rolling the Heat Receiver Over the Lamp Array During the Installation Operations of the Lamp Array Into the Receiver Cavity.	74
4-20	Rear Lamp Support Molybdenum Rod Attachment To the Receiver Support Cart.	75
4-21	View of Quartz Lamp Zones F, A, and B (Left to Right) Inside the Receiver Cavity.	76
4-22	View of Quartz Lamp Zones E, D, and C (Left to Right) Inside the Receiver Cavity.	77
4-23	Final Configuration of the Heat Receiver Just Prior to the Installation of the Aperture Cold Plate.	78
4-24	Attachment of #4 Electrical Cables to the Quartz Lamp Bus Rods.	79
4-25	Support of Electrical Cables and Chamber-Side Attachments to Vacuum Chamber Electrical Feed-Throughs.	80

LIST OF FIGURES

No.	Description	Page
5-1	Cavity Side-Wall Surface Temperatures at the Front (Aperture End), Middle, and Back of the Receiver Cavity During VT.1.	83
5-2	(a) Total Quartz Lamp Heater Power During VT.1; and (b) Chamber Vacuum Level During VT.1.	84
5-3	(a) Exterior Side-Wall Surface Temperatures Parallel to Heat Storage Tube #4 During VT.1; and (b) Exterior Side-Wall Surface Temperatures Parallel to Heat Storage Tube #12 During VT.1.	86
5-4	Cavity Side-Wall Surface Temperatures Located At 60° at the Front, Middle, and Back End of the Receiver Cavity During VT.2.	87
5-5	(a) Total Quartz Lamp Heater Power During VT.2; and (b) Chamber Vacuum Level During VT.2.	88
5-6	Borescope Photograph of the Receiver Cavity Just Prior to Thermal Arrest During VT.2	90
5-7	Blurred Image Through Borescope After Loss of Site Electrical Power.	91
5-8	Initial Power Up of the Quartz Lamp Heater Zones During VT.3 As Viewed Through the Borescope.	94
5-9	Full Power Operation of the Quartz Lamp Heater During Orbit #1 of VT.3.	95
5-10	Lens Contamination Image Obtained By Focusing on the Front Lens of Borescope.	96
5-11	Flux-Facing Surface Temperature Located in the Convolution Valley at the Inlet End of Heat Storage Tube #4 During VT.3.	97
5-12	(a) Total Quartz Lamp Heater Power During VT.3; and (b) Chamber Vacuum Level During VT.3.	98
5-13	Borescope Image Showing the Loss of Quartz Lamp Heater Zones E and F at the End of Orbit #1.	100
5-14	(a) Receiver Inlet Static Pressure During VT.3; and (b) Receiver Flow Rate During VT.3.	101
5-15	VT.3 Internal Salt Temperatures Closest to the Heat Exchanger Tube Located at the Inlet and Exit Ends of (a) the Flux-Facing Sides of Tube #12; and (b) the Top Sides of Tube #19.	102
5-16	Inlet and Exiting Gas Temperatures During VT.3.	103
5-17	Flux-Facing Surface Temperature Located in the Convolution Valley at the Inlet End of Heat Storage Tube #4 During VT.5.	105
5-18	(a) Total Quartz Lamp Heater Power During VT.5; and (b) Chamber Vacuum Level During VT.5.	106
5-19	VT.5 Internal Salt Temperatures Closest to the Heat Exchanger Tube Located at the Inlet and Exit Ends of (a) the Flux-Facing Sides of Tube #12; and (b) the Top Sides of Tube #19.	107
5-20	Inlet and Exiting Gas Temperatures During VT.5.	108

LIST OF FIGURES

No.	Description	Page
5-21	Flux-Facing Surface Temperature Located in the Convolution Valley at the Inlet End of Heat Storage Tube #4 During VT.6.	110
5-22	(a) Total Quartz Lamp Heater Power During VT.6; and (b) Chamber Vacuum Level During VT.6.	111
5-23	Cavity Borescope Image Near the End of the Sunlit Period of Orbit #17.	112
5-24	Cavity Borescope Image Near the Beginning of the Eclipse Period of Orbit #17.	113
5-25	VT.6 Internal Salt Temperatures Closest to the Heat Exchanger Tube Located at the Inlet and Exit Ends of (a) the Flux-Facing Sides of Tube #12; and (b) the Top Sides of Tube #19.	114
5-26	Inlet and Exiting Gas Temperatures During VT.6.	115
5-27	Flux-Facing Surface Temperature Located in the Convolution Valley at the Inlet End of Heat Storage Tube #4 During VT.8.	116
5-28	(a) Total Quartz Lamp Heater Power During VT.8; and (b) Chamber Vacuum Level During VT.8.	117
5-29	VT.8 Internal Salt Temperatures Closest to the Heat Exchanger Tube Located at the Inlet and Exit Ends of (a) the Flux-Facing Sides of Tube #12; and (b) the Top Sides of Tube #19.	119
5-30	Inlet and Exiting Gas Temperatures During VT.8.	120
5-31	Flux-Facing Surface Temperature Located in the Convolution Valley at the Inlet End of Heat Storage Tube #4 During VT.12.	122
5-32	(a) Total Quartz Lamp Heater Power During VT.12; and (b) Chamber Vacuum Level During VT.12.	123
5-33	Helium-Xenon Gas Flow Rate During VT.12.	124
5-34	VT.12 Internal Salt Temperatures Closest to the Heat Exchanger Tube Located at the Inlet and Exit Ends of (a) the Flux-Facing Sides of Tube #12; and (b) the Top Sides of Tube #19.	125
5-35	Inlet and Exiting Gas Temperatures During VT.12.	126
5-36	Flux-Facing Surface Temperature Located in the Convolution Valley at the Inlet End of Heat Storage Tube #4 During SS.1.	128
5-37	(a) Total Quartz Lamp Heater Power During SS.1; and (b) Chamber Vacuum Level During SS.1.	129
5-38	Beginning of Borescope Image Improvement As Solid Contamination Flakes Off Front Lens; Sunlit Period of Orbit #27.	130
5-39	Continued Improvement in Borescope Image; Sunlit Period of Orbit #29.	131
5-40	Return of Good Cavity Field of View Through the Borescope; Sunlit Period of Orbit #31.	132

LIST OF FIGURES

No.	Description	Page
5-41	Continued New Deposition of Solid Contamination of the Front Lens of Borescope; Orbit #34.	133
5-42	SS.1 Internal Salt Temperatures Closest to the Heat Exchanger Tube Located at the Inlet and Exit Ends of (a) the Flux-Facing Sides of Tube #12; and (b) the Top Sides of Tube #19.	134
5-43	Inlet and Exiting Gas Temperatures During SS.1.	135
5-44	Flux-Facing Surface Temperature Located in the Convolution Valley at the Inlet End of Heat Storage Tube #4 During SS.4.	136
5-45	(a) Total Quartz Lamp Heater Power During SS.4; and (b) Chamber Vacuum Level During SS.4.	137
5-46	SS.4 Internal Salt Temperatures Closest to the Heat Exchanger Tube Located at the Inlet and Exit Ends of (a) the Flux-Facing Sides of Tube #12; and (b) the Top Sides of Tube #19.	138
5-47	Inlet and Exiting Gas Temperatures During SS.4.	139
5-48	Flux-Facing Surface Temperature Located in the Convolution Valley at the Inlet End of Heat Storage Tube #4 During VT.3B.	141
5-49	(a) Total Quartz Lamp Heater Power During VT.3B; and (b) Chamber Vacuum Level During VT.3B.	142
5-50	VT.3B Internal Salt Temperatures Closest to the Heat Exchanger Tube Located at the Inlet and Exit Ends of (a) the Flux-Facing Sides of Tube #12; and (b) the Top Sides of Tube #19.	143
5-51	Inlet and Exiting Gas Temperatures During VT.3B.	144
5-52	Flux-Facing Surface Temperature Located in the Convolution Valley at the Inlet End of Heat Storage Tube #4 During VT.3A.	145
5-53	(a) Total Quartz Lamp Heater Power During VT.3A; and (b) Chamber Vacuum Level During VT.3A.	146
5-54	VT.3A Internal Salt Temperatures Closest to the Heat Exchanger Tube Located at the Inlet and Exit Ends of (a) the Flux-Facing Sides of Tube #12; and (b) the Top Sides of Tube #19.	147
5-55	Inlet and Exiting Gas Temperatures During VT.3A.	148
5-56	Helium-Xenon Gas Flow Rate During CS.1.	150
5-57	Flux-Facing Surface Temperature Located in the Convolution Valley at the Inlet End of Heat Storage Tube #4 During CS.1.	151
5-58	(a) Exiting Helium-Xenon Gas Temperature During CS.1; and (b) Temperature Difference of Gas Between Inlet and Exit During CS.1.	152
5-59	CS.1 Internal Salt Temperatures Closest to the Heat Exchanger Tube Located at the Inlet and Exit Ends of (a) the Flux-Facing Sides of Tube #12; and (b) the Top Sides of Tube #19.	153

LIST OF FIGURES

No.	Description	Page
5-60	Flux-Facing Surface Temperature Located in the Convolution Valley at the Inlet End of Heat Storage Tube #4 During CS.3.	154
5-61	(a) Helium-Xenon Gas Flow Rate During CS.3; and (b) Static Pressure at the Receiver Inlet During CS.3.	155
5-62	(a) Total Quartz Lamp Heater Power During CS.3; and (b) Chamber Vacuum Level During CS.3.	156
5-63	CS.3 Internal Salt Temperatures Closest to the Heat Exchanger Tube Located at the Inlet and Exit Ends of (a) the Flux-Facing Sides of Tube #12; and (b) the Top Sides of Tube #19.	158
5-64	Inlet and Exiting Gas Temperatures During CS.3.	159
6-1	Stabilized Orbits or Periods Used to Compare Significant ADRT Test Data.	161
6-2	Manual and DACS Helium-Xenon Flow Rate Measurements and Calculated Correction Factor.	162
6-3	Summary of the AD Receiver Thermodynamic Performance by Test Mode.	163
6-4	Summary of the Quartz Lamp Zone Electrical Power Distributions by Test Mode.	165
6-5	Maximum and Minimum Gas and Heat Storage Tube Temperatures by Test Mode.	170
6-6	Maximum and Minimum Cavity Insulation Temperatures and Temperature Gradients by Test Mode.	171
6-7	Comparison of Exiting Gas Temperatures Over the Most Stabilized Orbits of Testing	173
6-8	Maximum Heat Storage Tube Temperature Gradients by Test Mode.	174
6-9	Internal Salt Temperatures of Heat Storage Tube #19 (a) At the Inlet End and (b) At the Exit End.	178
6-10	Internal Salt Temperatures of Heat Storage Tube #12 (a) At the Inlet End and (b) At the Exit End.	179
6-11	Post-Test Comparison of Compositions of Gas Samples Taken From the Supply Bottle and CBC Piping Loop.	180
6-12	Thermal Conductivity of Mansville Q-Fiber Insulation in Vacuum.	181
6-13	Comparison of Thermal Conductivities of Mansville Q-Fiber and Cerablanket Insulations in Air.	183
7-1	Contamination Collected on Cold Plate Surface During Testing.	185
7-2	Contamination Collected on Borescope Lens During Testing.	186
7-3	Quartz Lamp Array During Removal From the Receiver Cavity.	187
7-4	Results of the Electrical Testing of All 30 Lamp Zones After Its Removal From the Receiver Cavity.	188

LIST OF FIGURES

No.	Description	Page
7-5	Results of Post-Test Inspection of the Receiver Cavity and Vacuum Chamber.	189
7-6	Crack At the Peak of the First Convolution at the Inlet End of Heat Storage Tube #3.	195
7-7	Buckled Felt Metal Kink Near the Inlet End of Heat Storage Tube #1.	197

NOMENCLATURE

AD	Advanced Development
ADRT	Advanced Development Receiver Thermal Vacuum Tests With Cold Wall
BA&E	Boeing Aerospace & Electronics
BOL	Beginning of Life
CaF ₂	Calcium Difluoride
CBC	Closed Brayton Cycle
DACS	Data Acquisition and Control System
EOL	End of Life
GFP	Government Furnished Property
LEO	Low Earth Orbit
LeRC	Lewis Research Center
LiF	Lithium Fluoride
LN ₂	Liquid Nitrogen
NASA	National Aeronautics and Space Administration
PCM	Phase Change Material
PCU	Power Conversion Unit
SD	Solar Dynamic
SDHRT	Solar Dynamic Heat Receiver Technology
TES	Thermal Energy Storage

1.0 SUMMARY

The first ever testing of a full-size, 102 kW_e solar dynamic (SD) heat receiver utilizing high-temperature thermal energy storage (TES) has been completed. The test program is entitled the Advanced Development Receiver Thermal Vacuum Tests With Cold Wall (ADRT) program and was conducted for the NASA Lewis Research Center (NASA-LeRC) under NASA contract NAS3-25716. The SD heat receiver was tested in a vacuum chamber with liquid nitrogen (LN₂) cold shrouds and cold plate to partially simulate a low-Earth-orbit (LEO) environment. The purpose of the tests was to quantify the receiver thermodynamic performance and its thermal response to changes in environmental and SD module interface boundary conditions. The testing was conducted by Boeing Aerospace & Electronics (BA&E) during the period 9 October 1990 through 3 November 1990 at the Tulalip hazardous test site, located in Marysville, WA. A total of 58 simulated orbital cycles, each 94 minutes in duration, were completed during the test conduct period. The receiver was designed and fabricated by BA&E during conduct of the Solar Dynamic Heat Receiver Technology (SDHRT) program, NASA contract NAS3-24669. The SDHRT and ADRT contracts are both NASA Advanced Development (AD) programs supporting the electrical power system design for the Space Station Freedom.

The SDHRT AD heat receiver was designed to meet the performance requirements specified for SD operation on the Space Station Freedom. The function of the receiver in the SD module is to transfer the Sun energy delivered by a concentrator to a mixture of helium and xenon gas to power a heat engine in a closed-Brayton cycle (CBC). The SD module is sized to provide 25 kW of electrical power and requires a nominal 102 kW thermal input to the CBC heat engine. The module operates continuously throughout the 94 minute orbit, including when the space craft is eclipsed for up to 36 minutes from the sun. The receiver employs an integral TES system that utilizes the latent heat available through phase change of a eutectic salt mixture of lithium fluoride and calcium difluoride (LiF-CaF₂). The salt mixture has a melt temperature of about 771°C (1420°F). The salt is contained within a nickel felt matrix that enhances heat transfer and controls the locations of voids that form during the solidification of the salt during the phase change process.

Special test support hardware were also designed and fabricated during the conduct of the SDHRT program including: (1) a quartz lamp heater array that mounts inside the receiver cavity to produce required flux distributions; (2) a CBC engine simulator that circulates the cooling gas through the receiver, removes heat, and conditions the gas to provide the required inlet temperature and pressure to simulate various power cycle operating modes; and (3) a support cart that interfaces the heat receiver with the facility vacuum chamber. Test support equipment that were designed and fabricated during the ADRT program included an LN₂ cold shroud and aperture cold plate to cold soak the receiver and an optical borescope to photograph the receiver cavity during testing.

The receiver was tested inside of a vacuum chamber to preclude convection effects and installed in a horizontal orientation to minimize the influence of gravity on the salt void distribution in the felt metal material. Temperature, pressure, power, and gas flow rate data were recorded during the test conduct. The cavity of the receiver was heated by the infrared quartz lamp array. The heater has 5 axial and 6 circumferential independently controllable zones. The electrical power distribution to the quartz lamp zones was set to produce an absorbed power profile inside the receiver cavity that matches that predicted for an on-axis, parabolic Newtonian reflector. The characteristics of this type of a concentrator were used to design the SDHRT receiver. The lamp array zone power distribution was also varied to quantify the effect of nonuniform incident flux distributions like the distribution produced by the Space Station

Freedom off-axis concentrator design. The CBC engine simulator circulated and conditioned the helium-xenon gas mixture through the receiver and allowed different operational modes to be simulated. Inlet gas temperature, pressure, and gas flow rate were independently varied.

Test modes conducted during receiver testing included:

- (1) The initial heat up of the receiver to achieve a steady-state cavity temperature of 538°C (1000°F) with no gas flow through the receiver.
- (2) Continued heat up of the receiver cavity through the melt temperature of the salt to achieve a steady-state cavity temperature of 871°C (1600°F) with no gas flow through the receiver.
- (3) Simulation of the nominal baseline design orbit cycling through 58 minute sun and 36 minute eclipse periods with 198 kW thermal input to the quartz lamp heater.
- (4) Continued operation of the heat receiver with baseline parameters except for an increase in the gas flow rate.
- (5) Continued operation of the receiver with an increased gas flow rate and a change in the heater duty cycle to simulate orbits with 66-minute sun and 28-minute eclipse periods.
- (6) Simulation of receiver operation during a maximum insolation, solar perihelion orbit with a total heat input to the cavity of 225 kW.
- (7) Simulation of the SD module peaking orbits.
- (8) Operation with baseline parameters but with a modified axial cavity flux distribution.
- (9) Operation with baseline parameters but with a modified axial and circumferential cavity flux distribution.
- (10) Shut down of the receiver to ambient conditions.
- (11) Simulation of the rapid start up of the receiver to full power operation (at baseline conditions) within 2 orbits from ambient conditions.

The receiver, test support equipment, and facilities operated well together although several anomalies and facility problems were encountered during the test period. The anomalies concerned 3 major vacuum off-gassing events that occurred at random times and significantly slowed the progress through the test matrix. Facility power problems contributed to the off-gassing events because LN₂ flow to the cold shrouds and cold plate was lost several times for brief periods. The most serious equipment problem encountered was corona inside the receiver cavity that forced shut down of the test conduct with all but 1 of the planned test modes completed.

Data collection was very successful during the test conduct. The only data lost during testing were (1) the measurement of gas composition because of a failure of the mass spectrometer and (2) 2 thermocouples both located on the LN₂ cold plate. In addition, the test data showed the receiver thermodynamic performance and its operating temperatures to remain within pre-test predictions. Useful data were obtained from all thermocouples but especially those installed inside the TES salt annulus and on the cavity side-walls because they were shielded from the high-flux output of the quartz lamps. Heat storage tube surface temperature measurements were less accurate because of significant radiation errors induced by high lamp heat flux and a lack of contact area between the sheathed thermocouples and the surface of the tubes. During baseline receiver operation (modified for the slightly higher thermal losses

measured through the insulation), the exiting gas temperature varied between 742°C (1368°F) and 696°C (1285°F) with a near constant inlet gas temperature of 488°C (910°F). The integrated receiver thermal efficiency over a single orbit at the modified baseline conditions was approximately 84%. The receiver manifold and pressure piping system performed better than pre-test prediction with a measured gas pressure drop of about 1% at an inlet static pressure of about 658 kPa (95.4 psia). The simulation of the maximum insolation orbit test mode showed that increasing gas flow rate through the receiver results in receiver performance and operating temperatures that are comparable to those measured during the baseline orbit. Little significant change in either the receiver operating temperatures and/or temperature gradients were seen during operation with the modified lamp power distributions suggesting that the receiver may be forgiving to non-symmetric cavity incident fluxes. Receiver response during a cold start up from ambient temperature showed that measured temperature gradients are large but are also lower than pre-test predictions and confirmed that sufficient thermal storage capacity is attained to start the CBC engine during the 2nd orbit.

Post-test inspections of the receiver showed 10 of the 24 receiver heat storage tubes had ruptured and leaked small amounts of salt into the receiver cavity. This no doubt caused the corona electrical problems which ended the test conduct. The most significant ruptures all occurred at the inlet end of the corrugated TES containment tubes on the peak of the 1st convolution. In addition, all of the cracks center on the low, gravity side of the tube implying that the failure is probably a result of localized expansion of salt that collects inside the bottom convolutions in this stiff region of the bellows. It is believed that most or all of these ruptures occurred during the cold soak start up test mode because during normal cycling, the salt in this region of the tube remains frozen. It should be noted that no stress analyses were performed on the receiver for this highly transient condition because no cold start up requirement existed when the SDHRT heat receiver was designed. Funding limitations prevented post-test data and failure mode analyses from being performed under the ADRT contract. Although this issue remains unresolved as of this writing, NASA-LeRC will perform metallographic inspections of a convolution crack to determine a plausible failure mode explanation. NASA-LeRC will also remove several heat storage tubes and inspect the condition of the felt metal and the distribution of the salt using computed tomography and mechanical sectioning of the salt annulus.

Despite not meeting the combined SDHRT and ADRT program objective of no hardware failures during testing, the success of these 2 AD programs cannot be disputed. Most other program objectives were met and the testing provided the majority of the data required to support a future flight design program. The thermal performance of the SDHRT heat receiver was close to pretest predictions and its overall design is believed to have potential for space flight operation. The rupture of the TES containment bellows can be corrected with a partial redesign of the heat storage tube augmented with more detailed thermal and mechanical analyses. Minimal analyses and no optimizations were performed to fully understand the mechanical performance of this component because of time and budget constraints during the SDHRT program. All other design aspects of the receiver appear to be solid and the thermal performance meets all of the specified Space Station Freedom requirements. Furthermore, it has been demonstrated that this receiver design can be fabricated at a reasonable cost, especially now that problems associated with molten salt filling have been solved. Certainly, some of the key design aspects of this receiver should be considered in any receiver that is eventually built for space flight operation on Freedom or other future space missions.

2.0 TEST PROGRAM OVERVIEW

The purpose of the ADRT program was to operate the NASA AD heat receiver in a partially simulated LEO environment and quantify its performance envelope. The test data is intended to aid NASA and their prime contractors in the design of the SD hardware for the Space Station Freedom. The AD heat receiver was delivered to NASA from the SDHRT program in June 1990 and provided to the ADRT program as Government Furnished Property (GFP). The receiver was to be initially tested during conduct of the SDHRT program but cost over-runs associated with problems encountered during receiver fabrication and the resulting schedule delays caused NASA to delete all of the verification testing from the SDHRT program. The SDHRT verification testing was combined with the additional testing planned by NASA in the follow-on test program which was more cost effective because all of the duplication in effort between the two programs was eliminated. NASA had originally planned to conduct the follow-on receiver testing at their facilities in Ohio but these facilities could not be made available in time to support the Space Station Freedom schedule. Therefore, the ADRT program was competitively bid and eventually awarded to Boeing Aerospace & Electronics by NASA-LeRC in November 1989.

2.1 Scope

Documentation of the ADRT program is contained in 4 separate documents: (1) The ADRT Work Plan, reference 1; (2) the ADRT Test Plan Document, reference 2; (3) the ADRT Detailed Test Procedures Document, reference 3; and (4) the ADRT Final Test Report. The Final Test Report Document describes the ADRT program, test hardware and instrumentation, test assembly operations, test conduct period, test results, post-test hardware inspections, and conclusions and recommendations. A set of Appendices provide (1) the log of test conduct activities and significant events, (2) the ADRT computer data files and data storage format, and (3) comparisons of selected data during the most stabilized test mode orbital simulations.

2.2 Test Program Objectives

The primary objective of the ADRT thermal vacuum testing was to demonstrate the operation of the NASA AD heat receiver and quantify its thermal performance envelope for the required range of SD power module interface and environmental boundary conditions. A second program objective was to correlate selected test data with predicted temperature and performance data obtained using the AD receiver thermal math model, SDTEST (reference 2). The ADRT program success criteria were as follows: (1) the successful operation of the heat receiver and test support hardware with no hardware failures; (2) the collection and storage of all test instrumentation data; (3) measuring a baseline receiver thermal performance that compares with that predicted by the thermal model; and (4) measured receiver temperatures remaining below maximum rated values.

2.3 Test Program Requirements

The ADRT test program parametric requirements are summarized in Figure 2-1 and are described in detail in the Test Plan Document, reference 2.

BOEING

Parameter	Minimum Insolation	Maximum Insolation
Sunlit Period	58 min	66 min
Eclipse Period	36 min	28 min
Absorbed Power	170.5 kWt	191.5 kWt
Inlet Gas Temperature	482°C (900°F)	491°C (915°F)
Outlet Gas Temperature	705°C (1300°F)	760°C (1400°F)
Gas Flow Rate	53 kg/min (117 lbm/min)	75 kg/min (165 lbm/min)
Sink Temperature	ambient	ambient
Inlet Gas Pressure	634 kPa (92 psia)	634 kPa (92 psia)
Vacuum	$< 1.0 \times 10^{-5}$ torr	$< 1.0 \times 10^{-5}$ torr
Minimum Cold Soak	-88°C (-126°F)	N/A
Gas % Helium	72%±5%	72%±5%

Figure 2-1: Summary of the ADRT Test Program Parametric Requirements.

2.4 Test Description

Three types of testing were conducted: verification tests, flux variation tests, and shutdown and cold soak start up tests. Contract cost overruns, caused primarily by delays in correcting facility problems prior to the start of the actual test conduct, forced NASA and Boeing to prioritize the test modes given in the original ADRT test matrix, reference 2. Only 14 of the 26 original test modes could be attempted within the contract resources remaining at the time the test modes were initiated. The prioritized test modes planned at the beginning of test conduct are shown in Figure 2-2. All but 1 of these test modes were executed during the test conduct. A detailed description of the individual test modes as they were conducted (or attempted) is given in Section 5.0 of this document.

2.4.1 Verification Tests

Verification tests were conducted to establish the receiver performance envelope with changes in its environmental and operational boundary conditions including: (1) the seasonal solar intensity; (2) concentrator optical properties; and (3) the CBC engine interface parameters of gas temperature and flow rate. The objective of the verification tests was to measure the receiver thermodynamic performance and its operating temperatures over the expected range of environmental and module operational PCU interfaces. The recorded database will be useful for determining the practical limits for various thermal control and system design options during the detailed design phase for the SD flight hardware on the Space Station Freedom.

Test Mode	Test Mode Description
VT.1	Steady-State Heat Balance 1
VT.2	Steady-State Heat Balance 2
VT.3	SDHRT Baseline Orbit
VT.5	Gas Flow Variation 2
VT.6	Orbital Parameter Variation
VT.8	Maximum Insolation Orbit 2
VT.12	Peaking Orbits
SS.1	Axisymmetric Flux Variation
SS.4	Circumferential Flux Variation 3
VT.3	SDHRT Baseline Orbit
CS.1	Shut Down to Cold Soak 1 (near ambient)
CS.3	Cold Soak Start Up to Nominal 2
CS.6	Coolant Loss Shut Down to Ambient

Figure 2-2: The Prioritized ADRT Test Matrix.

2.4.2 Flux Variation Tests

The SDHRT heat receiver was designed using the flux distribution from an on-axis, parabolic concentrator with no circumferential flux variation. The verification testing, described in 2.4.1, used a heater zone power distribution determined by matching the predicted rates that energy is absorbed by the heat storage tubes when the incident flux is delivered from both an on-axis, parabolic concentrator and the quartz lamp heater array. With the absorbed energy profile duplicated, differences in wavelength, internal cavity reflections, and radiative exchange between the 2 heat sources are eliminated.

Analyses of the off-axis concentrator has been limited to characterizing the incident flux on cylindrical cavity side and back walls. These data provide insight into the apparent distribution of cavity energy but do not include the real effects of reflection and reradiation in an operational cavity containing heat storage tubes. The objective of the flux variation tests was to quantify the changes in receiver thermodynamic performance and its operating temperatures with changes in the axial and circumferential flux distribution inside the cavity. The quartz lamp input power distributions specified for these test modes were obtained by extrapolation of incident flux data for the off-axis concentrator inside the SDHRT receiver cavity.

2.4.3 Receiver Shutdown and Cold Soak Start Up Tests

Start up of the solar dynamic power module from a cold soak condition may be the most severe receiver operating mode. The rate of temperature rise of receiver components from a cold soak condition is rapid due to the large amount of energy delivered into the cavity upon acquisition of sun. The resulting thermal stresses will substantially exceed normal orbital values. Fortunately, the structural design parameters allowed for receiver alloys are higher at lower operating temperatures and, therefore, during part or all of the heat up cycle the components should be capable of withstanding the higher loading. However, after prolonged operating at high temperature, receiver alloys may become more brittle and a rapid increase in stress level could cause cracking and failure of critical structure.

The receiver is first cooled to ambient temperature (or cooler if time permits) by continuing operation of the CBC with no heater power input to the cavity until temperatures drop to near ambient. Gas flow is terminated and the LN₂ cold shrouds and cold plate then cool the receiver to the desired cold soak temperature.

When the desired temperature is achieved, the quartz lamp heater is then operated at full power in a normal 58 minute sun and 36 minutes eclipse duty cycle. The CBC engine simulator is not operated until the second sunlit period after a substantial melt of the salt inside the heat storage tubes has been achieved. CBC gas flow is then initiated and the receiver continues to cycle until stabilized conditions are obtained. The baseline interface boundary parameters, heater power, and power distribution are used during the cold start up test modes.

A stress analysis of the SDHRT heat receiver operating during a cold start up was not performed during the SDHRT program. Therefore, the cold soak shutdown and subsequent start up test modes were conducted last after all other test modes were completed because of the unknown (i.e., unanalyzed) risk of damage. Prior to executing these test modes, an inspection of the receiver was desired to ensure that any damage seen at the completion of testing could be attributed to the proper cause. It was originally planned to shutdown the receiver to ambient and open the chamber for a physical inspection inside the receiver cavity. However, opening the chamber to air would require another long-term off-gassing bake out to ensure good vacuum conditions at operating temperatures. Therefore, an optical borescope was installed into the aperture end of the receiver to be used to continuously observe and photograph the cavity during operation of all of the test modes. It was hoped that the images of the heat storage tubes and cavity side walls obtained using the borescope would be adequate to observe any significant cavity damage prior to the cold start up test modes.

3.0 TEST HARDWARE, FACILITIES, AND INSTRUMENTATION

3.1 AD Heat Receiver and Support Cart

The AD heat receiver is described in Figure 3-1 and is pictured in Figure 3-2 mounted in its support cart during preparation for testing. The receiver is shown in both figures without the aperture assembly or LN₂ cold shrouds in place. The receiver was designed and built for NASA-LeRC by Boeing Aerospace & Electronics during the SDHRT program and was supplied to the ADRT program as GFP. Detailed descriptions of the AD heat receiver design evolution and its fabrication history are given in references 4 and 5 respectively.

The receiver has a cylindrical cavity 1778 mm (70 in) in diameter and 2032 mm (80 in) in length. The outer diameter (OD) is 2184 mm (86 in) and the total length is 2794 mm (110 in). The test receiver weighs approximately 2178 kg (4,797 lbs). The receiver heat exchange system is comprised of 24 parallel heat exchanger tubes, each surrounded by an annulus containing a salt/felt metal composite. The salt is a near eutectic mixture of LiF-CaF₂ and is capable of storing about 72 kw-hrs of energy during its change of phase from solid to liquid at a temperature of 771°C (1420°F). The felt metal is used to improve the heat conduction across the salt annulus and to prevent the gravity force from controlling the locations of voids that form in the salt while it solidifies during discharge of the TES.

The salt is contained around the heat exchanger tubes by an exterior bellows. The convolutions distribute the net thermal expansion of the TES containment tube and maintain peak stress at an acceptable level (reference 4). The operating life in space is predicted to exceed the 20 year Space Station requirement. The 24 heat storage tubes are cantilevered from the front end of the receiver to minimize the constraint of the axial growth caused by thermal expansion from the initial cold temperature of the receiver. A flow annulus, formed by inserting a tube (called the "spud") inside the heat exchanger, allows the internal convective heat transfer coefficient to be adjusted by changing the spud diameter. This feature allows the heat exchange to be tailored to specific interfaces without a complete re-design of the heat exchanger/TES tube assemblies. It also allows a larger diameter tube to provide the structural support required in the cantilevered design of the tubes inside the receiver cavity. Gas flow is split between the 24 heat exchanger tubes by an inlet domed plenum and collected for return to the engine by an exit domed plenum. The plenum design minimizes the pressure drop, fabrication costs, and the physical constraint of the gas loop piping system.

The receiver is suspended in the vacuum chamber by the receiver support cart pictured in Figure 3-2. This structure also supports the back end of the quartz lamp array and the aperture cold plate. It is designed to roll out of the vacuum chamber onto a portable platform that mates up to the front of the chamber. This platform can also be seen in Figure 3-2. The cart/platform interface allows the quartz lamp heater array to be assembled and mated with the receiver while outside the vacuum chamber. The entire assembly is then rolled into the vacuum chamber on rail tracks installed inside the vacuum chamber. The rolling capability of the support cart inside the chamber also allows the receiver to roll forward as the inlet and exit pipes connecting the receiver to the CBC engine simulator grow in length during their initial heat up to operational temperatures. Redundancy in growth accommodation is also provided by the cable support of the receiver inside the support cart itself.

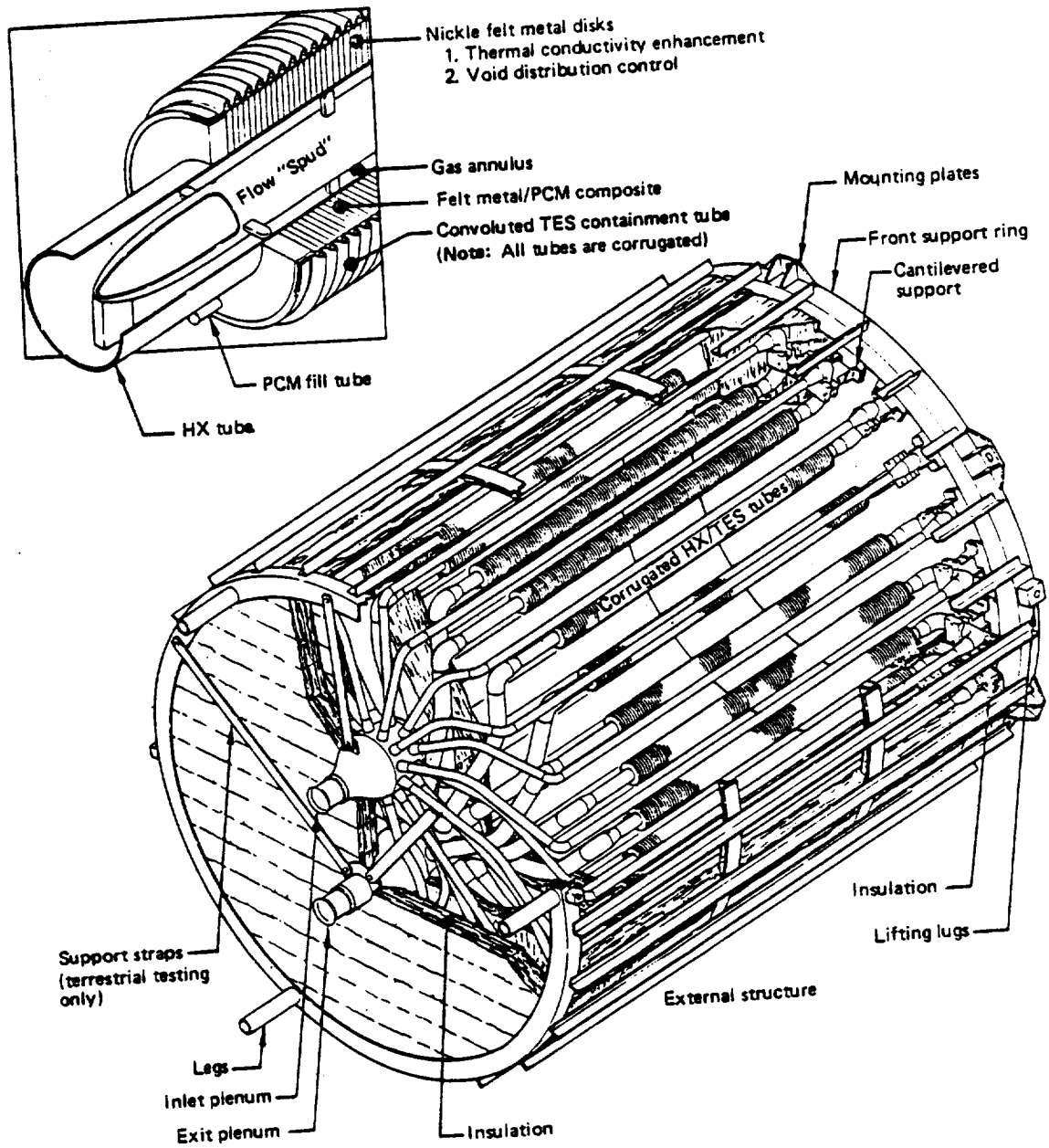


Figure 3-1: SDHRT Heat Receiver Design Configuration.

BOEING

ORIGINAL PAGE
BLACK AND WHITE PHOTOGRAPH

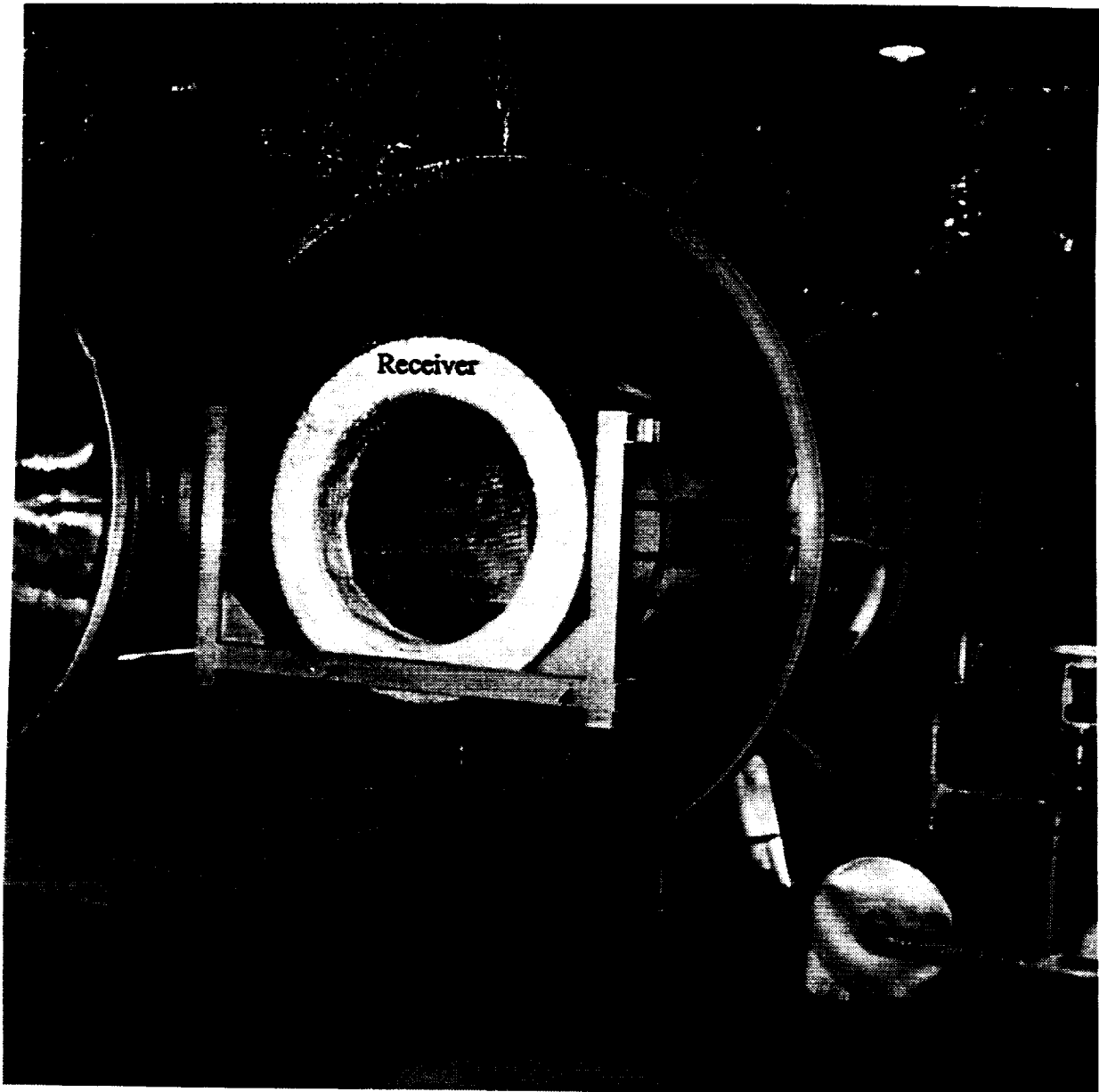


Figure 3-2: SDHRT Heat Receiver Mounted in Support Cart During Preparation for Testing.

3.2 CBC Engine Simulator

The CBC engine simulator, supplied as GFP from the SDHRT program, is used to properly condition the receiver working fluid to the desired test mode conditions. Figure 3-3 shows a functional schematic of the CBC engine simulator which is pictured in Figure 3-4.

The CBC engine simulator flows a gas mixture of 72% helium and 28% xenon (molecular) through the receiver at required test flow rates, pressures, and temperatures during all defined test modes. A single-stage rotary lobe blower pressurizes and moves the working fluid through the piping network. A pulse damper is located between the blower outlet and a vortex shedding flow meter to smooth the pulsations inherent in the blower. The flow rate through the receiver is controlled manually using the blower by-pass valve. Hot helium-xenon gas returning from the receiver is cooled to an acceptable blower inlet temperature by first passing through a regenerative gas-to-gas heat exchanger and then through a water cooled heat exchanger. The water cooled heat exchanger drops the gas temperature to about 52°C (125°F) prior to entering the blower. The hot water exiting the heat exchanger is cooled by spraying it through a series of "mistifiers" prior to its discharge into the environment. The gas is repressurized and slightly heated by the blower and heated to the desired receiver inlet temperature when it passes through the regenerative heat exchanger.

The temperature control of the gas at the receiver inlet is achieved using a regenerative heat exchanger by-pass system consisting of 2 flow control valves in parallel. A large, coarse control valve is set manually to produce gas at the exit of the regenerator that is slightly higher in temperature than the desired inlet value. A smaller, fine metering control valve with temperature feedback then modulates the bypass flow of cool gas to achieve a mixed gas temperature at the desired inlet conditions. The temperature of the gas is measured just upstream of the inlet plenum on the heat receiver and controls temperature to within $\pm 6^{\circ}\text{C}$ ($\pm 10^{\circ}\text{F}$) of the desired set point. The temperature controlled feed-back system was provided by Boeing as facility hardware. The fine control valve is designed to fail full open (fail-safe) to prevent over-heating of the receiver if an air pressure failure occurs.

Temperatures and pressures are monitored throughout the CBC engine simulator to provide required receiver operating parameters. If the leak-tight lines in the CBC gas loop need to be opened for an unplanned shutdown of the system, a gas reclamation system is used to recover most of the expensive helium-xenon gas from the CBC test loop. A two-stage metal bellows pump is used to reclaim the gas mixture and is capable of producing 791 kPa (100 psig) outlet pressure with a 48 kPa (7 psia) inlet pressure.

The gas reclamation system is also used to control the inlet pressure of the receiver. Initially, the CBC gas loop is filled from a premixed, high pressure bottle of helium-xenon to a predetermined static pressure of about 343 kPa (35 psig). The CBC blower is then activated and the gas is allowed to rise in temperature until quasi-steady conditions are achieved. If the receiver inlet pressure is too low, more helium-xenon gas is introduced into the loop from the high-pressure bottle. If the receiver inlet pressure is too high, gas in the loop is pumped into the gas reclamation storage tank. A helium-xenon sampling port is included to allow the gas mixture composition to be monitored. A mass spectrometer, supplied by Boeing as facility property, is used to determine the helium-xenon mixture ratio. If the gas is deficient in helium, which is the most likely case, pure helium is added to the loop until the required gas mixture is obtained.

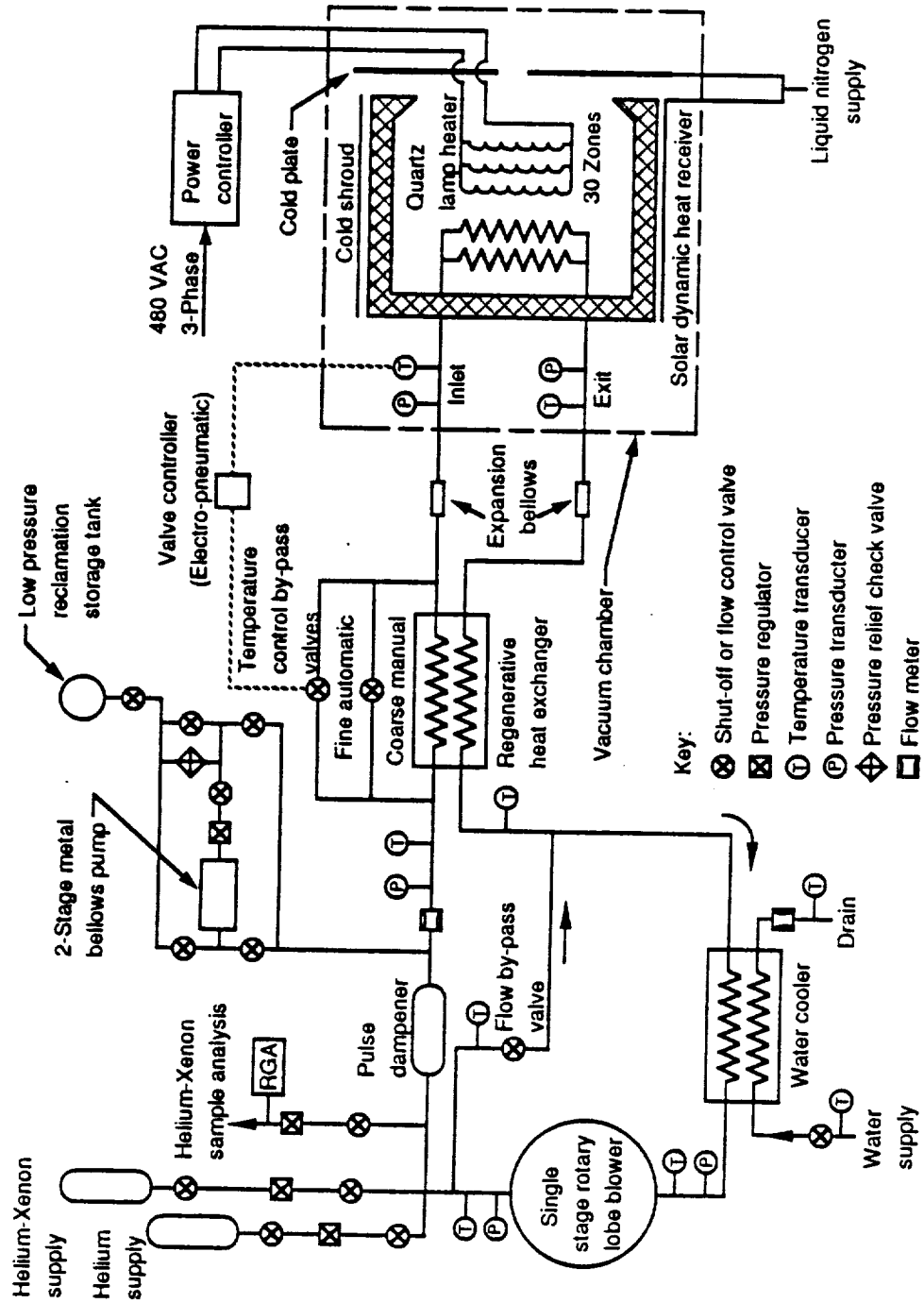


Figure 3-3: CBC Engine Simulator Functional Schematic.



Figure 3-4: CBC Engine Simulator Pictured At the Tulalip Test Site.

ORIGINAL PAGE
BLACK AND WHITE PHOTOGRAPH

3.3 Quartz Lamp Heater

The cavity of the receiver is heated with the infrared quartz lamp array supplied as GFP from the SDHRT program. Heat is produced by 456 quartz lamps (General Electric part number QH1000T3/CL/HT). The lamps are rated at 1000 watts but are operated at about half power during testing to increase lamp life (lamp life is exponential with operating voltage). The lamp array is configured into 5 axial and 6 circumferential independently controllable zones.

The support structure for the lamp array consists of a single box beam. The beam is supported by a cable at the front (aperture) end and by a molybdenum rod at the back end of the receiver. The rear end attachment is made to the receiver support cart and the front end is hung from the large structural ring on the receiver. Six bus plates form a hexagonal structure when hung from the box beam at eight axial locations. The bus plates support and supply electrical power to the individual quartz lamps. The plates are electrically isolated from each other and from the box beam by ceramic insulators. Cylindrical bus rods extend from the front end of the receiver and attach to the individual bus plates. Electrical connections are made to the ends of these rods outside the heated area of the receiver cavity. The 30 lamp zones are powered by 6 power controllers provided by Boeing as facility hardware. The beam, bus plates, and bus rods are all fabricated from columbium and columbium alloys and should only be elevated to high temperature in a vacuum. The configuration of the lamp array can be seen in Figures 4-18 through 4-22 in Section 4.4.

3.4 LN₂ Cold Shrouds and Aperture Cold Plate

An LN₂ cooled cold plate is used to absorb the heat lost through the receiver aperture and to collect off-gassing products liberated from within the receiver cavity during high-temperature operation. The cold plate is supplied as GFP from the SDHRT program. An LN₂ cold shroud surrounds the outer cylindrical area of the receiver and was intended to cold soak the receiver to a temperature of -88°C (-126°F) (as measured on the surfaces of the heat storage tubes).

The cold shrouds and cold plate are made from aluminum sheet with aluminum D-tubing welded to their surfaces. LN₂ cooling flow through the 4 shroud panels and the cold plate are controlled by throttling valves. The pre-test estimated maximum rate of LN₂ consumption (boil-off in the sub-cooler) was about 371 liters/hour (98 gallons per hour).

The LN₂ cold shroud is comprised of four nearly identical sections that are installed directly onto the cylindrical cage of the receiver before the cart/receiver is rolled into the vacuum chamber. The four shroud panels are connected to each other with turnbuckles and hang onto the support angles on the receiver cage. The panels are plumbed to produce two parallel flow loops; each consisting of two panels flowing in series. The upper cold shroud panels are visible in Figure 4-20 provided in Section 4.4.

The cold plate is a single piece of aluminum sheet with welded D-tubing LN₂ flow channels. It is suspended by turnbuckles from the receiver support cart, and is installed immediately before closing the chamber door. It has a third, separate LN₂ flow loop.

3.5 Optical Borescope

Viewing of the inside of the receiver cavity during thermal vacuum testing was made possible by using a high temperature borescope. The borescope has a 120° field of view. The borescope is mounted in a flange in the chamber door on axis with the receiver center line. It has a camera mount outside of the chamber with an integral focusing ring. The final image size is 25 mm (1-in) in diameter and provides full frame coverage on a 35 mm negative.

The borescope is constructed of a 57 mm (2.25 inch) diameter stainless steel tube with an external quartz window and internal glass lenses. It is actively cooled with GN₂ permitting continuous operation at temperatures in excess of 927°C (1700°F). The seal between the cooling gas and the vacuum environment is made with an O-ring surrounding the quartz front view window. The window is held securely in place by a mounting cap so that in the unlikely event of loss of coolant, the resulting overheating and failure of the O-ring would cause a leak of nitrogen into the chamber, but the window would retain its integrity and would remain in place. The use of GN₂ instead of air as the cooling gas eliminates the risk of introducing oxygen into the chamber which cannot be tolerated because of the use of columbium materials in the quartz lamp heater structure.

3.6 Facilities

The thermal vacuum testing of the AD receiver was conducted in a large vacuum chamber located in Area 5 at the Boeing Tulalip hazardous test site in Marysville, WA. The vacuum chamber sits on a large concrete slab under a covered shelter but is otherwise exposed to the outside environment. Therefore, no special environmental control systems are needed to reject energy lost from the vacuum facility. The concrete slab is ideal for supporting the weight of the CBC engine simulator which weighs approximately 4,536 kg (10,000 lbs).

The vacuum test chamber inside dimensions are approximately 4.3 meters (14 feet) in diameter and 5.5 meters (18 feet) long. A 813-mm (32-inch) diffusion pumping system is used to achieve vacuum in the 1×10^{-6} torr range (no LN₂ cold shroud operation in the chamber). The vacuum chamber has many vacuum feed-through ports available for instrumentation, electrical power, liquid nitrogen, and receiver gas lines.

The site has approximately 400 kW of electrical power available to operate the vacuum systems, quartz lamp array heater, CBC engine simulator, data acquisition, and miscellaneous demands. A special water dispersion system is installed to allow the cooling water from the gas/water heat exchanger on the CBC simulator to be discharged to the environment in a safe manner. A large capacity (37,854 liter) LN₂ storage and piping system exist at the site for interfacing with the LN₂ cold plate and cold wall. At the pre-test predicted rate of LN₂ consumption of 371 liters/hr, filling of the storage tank was planned for about every 3 days (actual LN₂ consumption rates required filling of the tank once a day).

The quartz lamp heater array was powered by 6 phase angle firing, silicon controlled rectifier (SCR) power controllers specially designed for corona environments. These SCR power supplies were loaned to the ADRT program by the Boeing Environmental Test Laboratories and are not supplied to NASA-LeRC with the quartz lamp array. A total of 36 controllable channels or zones are available (6 spares) and each channel is capable of controlling from 0 to 26.6 KW in the range of 166 volts at 160 amps to 240 V at 111 amps. Each channel is independently controlled, single phase, and incorporates an instantaneous current trip circuit which will sense an over-current condition, such as a corona discharge, and break the channel circuit. The power controllers automatically attempt to repower the affected heater zone 3 times before terminating operation. Each power controller provides electrical power to the 5 axial zones of each circumferential bank of zones. The wiring for 2 racks is shown in Figure 3-5. The SCR power controllers have built-in capability to provide a calibrated signal to the data acquisition and control system (DACS) for recording lamp zone power.

The power supplies were located next to the vacuum chamber but were remotely controlled from inside the instrumentation trailer. A "kill" breaker was provided to allow test personnel to remove power from all 30 zones of the lamp array with a single command.

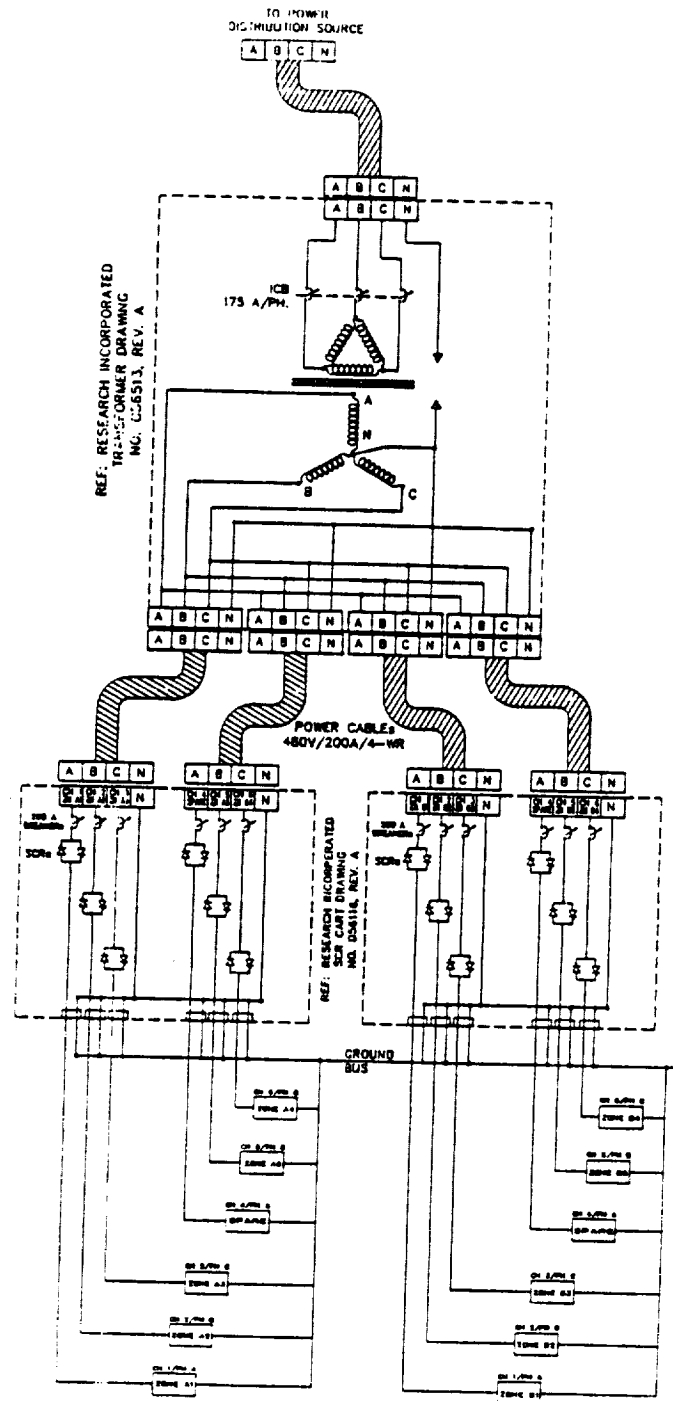


Figure 3-5: Typical Wiring Schematic for Quartz Lamp Zones.

Electrical power vacuum chamber pass-throughs were also supplied by Boeing as part of the vacuum chamber equipment and were not supplied to NASA-LeRC with the quartz lamp heater after the completion of testing. Adaptor plates for all other instrumentation pass-throughs were built by the ADRT program but remained with the vacuum facility because the existing chamber flanges were modified to reduce program costs.

3.7 Instrumentation and Data Acquisition

Test measurements included: (1) temperature measurements to determine the temperature distributions within the receiver and support equipment; (2) temperature measurements to determine thermal energy storage subsystem performance; (3) temperature, pressure, and gas flow rate measurements to determine overall receiver thermodynamic performance; (4) heater power measurements for each of the 30 heater zones; (5) vacuum chamber pressure; (6) ambient pressure and temperature; and (7) the molecular percentages of helium and xenon in the gas mixture. Figure 3-6 lists the ADRT test measurements, required ranges, transducer type, and transducer output. There were a total of 114 temperature measurements distributed as follows: 88 on the receiver, 10 on miscellaneous structure, the cold plate, and cold shroud panels, 9 in fluid lines associated with the CBC engine simulator, 3 on heater structure and components, 3 on the vacuum chamber facility, and 1 for ambient.

3.7.1 Receiver Instrumentation

Three of the 24 receiver heat storage tubes were instrumented. The locations of all 24 heat storage tubes by serial number (S/N) and cavity location are shown in Figure 3-7 and the 3 instrumented tubes are identified. All references to the instrumented heat storage tubes in this document is by cavity location, i.e., either position #4, #12, or #19 as viewed from the aperture end, beginning at the top, and incrementing in the clockwise direction. Care must be exercised when looking back to the Test Plan Document (reference 2) and the Detailed Test Procedures (reference 3) because these documents referenced tubes by serial number. Two of the instrumented heat storage tubes have thermocouples installed internal to the TES annulus at both the inlet and exit ends of the tubes to characterize TES performance. The thermocouples extend into the TES annulus to a 305 mm (12 in) depth and are sealed at the end-caps by a high-temperature braze. The internal thermocouples on the exit end of tube #19 are shown in Figure 3-8.

Heat storage tube #19 was installed normally inside the receiver cavity with the weld seam of the TES containment bellows oriented towards the cavity side wall. In this orientation, the inlet end salt fill tube is closest to the cavity side wall and the internal thermocouples are aligned approximately 7.5° off the vertical gravity vector as shown in Figure 3-9. The internal thermocouples are aligned $\pm 90^\circ$ from the highest and lowest flux regions on the heat storage tube. Therefore, the heat flux should be nearly the same at both thermocouple locations and measured temperature differences, if they exist, should result primarily from gravity effects on the formation of salt voids. Surface temperature measurements were made on the peaks of the convolutions, 305 mm (12 in) from each end-cap and in the middle of the tube. Nichrome wire was used to attach the thermocouples to the peaks of the convolutions as pictured in Figure 3-10. The tips of the thermocouples were preloaded against the surface of the tube. This method of thermocouple attachment was used during subscale canister tests and produced reasonable results. An alternative method of attaching the thermocouples using a ceramic adhesive was not used because it caused excessive oxidation and damage to the Inconel 617 containment bellows during the subscale canister tests (reference 4). The thermocouples were attached every 90° around the tube, with 0° always referenced from the location of the inlet

Measurement Description	Trans. Type	CH. #	Maximum Range	Accuracy	Units	Transducer Output
Tube #4 - Peak/Inlet @ 0°	"K" Sh	0	-15/1650	±0.75%	°F	-6 to 40mV
Tube #4 - Valley/Inlet @ 0°	"K" Sh	1	-15/1650	±0.75%	°F	-6 to 40mV
Tube #4 - Peak/Inlet @ 90°	"K" Sh	2	-15/1650	±0.75%	°F	-6 to 40mV
Tube #4 - Valley/Inlet @ 90°	"K" Sh	3	-15/1650	±0.75%	°F	-6 to 40mV
Tube #4 - Peak/Inlet @ 180°	"K" Sh	4	-15/1650	±0.75%	°F	-6 to 40mV
Tube #4 - Valley/Inlet @ 180°	"K" Sh	5	-15/1650	±0.75%	°F	-6 to 40mV
Tube #4 - Peak/Inlet @ 270°	"K" Sh	6	-15/1650	±0.75%	°F	-6 to 40mV
Tube #4 - Valley/Inlet @ 270°	"K" Sh	7	-15/1650	±0.75%	°F	-6 to 40mV
Tube #4 - Peak/Mid @ 0°	"K" Sh	8	-15/1650	±0.75%	°F	-6 to 40mV
Tube #4 - Peak/Mid @ 90°	"K" Sh	9	-15/1650	±0.75%	°F	-6 to 40mV
Tube #4 - Peak/Mid @ 180°	"K" Sh	10	-15/1650	±0.75%	°F	-6 to 40mV
Tube #4 - Peak/Mid @ 270°	"K" Sh	11	-15/1650	±0.75%	°F	-6 to 40mV
Tube #4 - Peak/Exit @ 0°	"K" Sh	12	-15/1650	±0.75%	°F	-6 to 40mV
Tube #4 - Peak/Exit @ 90°	"K" Sh	13	-15/1650	±0.75%	°F	-6 to 40mV
Tube #4 - Peak/Exit @ 180°	"K" Sh	14	-15/1650	±0.75%	°F	-6 to 40mV
Tube #4 - Peak/Exit @ 270°	"K" Sh	15	-15/1650	±0.75%	°F	-6 to 40mV
Tube #4 - Inlet PCM Fill Tube	"K" Sh	16	-15/1650	±0.75%	°F	-6 to 40mV
Tube #4 - Exit PCM Fill Tube	"K" Sh	17	-15/1650	±0.75%	°F	-6 to 40mV
Tube #4 - Saddle Bracket	"K" Wr	18	-50/1000	±0.75%	°F	-6 to 40mV
Reference Junction	"K"	19	70		°F	
Tube #4 - Support Plate - Front	"K" Wr	20	-50/1000	±0.75%	°F	-6 to 40mV

Figure 3-6: ADRT Instrumentation List.

Measurement Description	Trans. Type	Ch. #	Maximum Range	Accuracy	Units	Transducer Output
Tube #4 - Support Plate - Rear	"K" Wr	21	-100/800	±0.75%	°F	-6 to 40mV
Tube #4 - Gusset - Mid	"K" Wr	22	-100/800	±0.75%	°F	-6 to 40mV
Tube #4 - Ring Exterior - Side	"K" Wr	23	-300/400	±0.75%	°F	-6 to 40mV
Tube #4 - Ring Exterior - Front	"K" Wr	24	-300/400	±0.75%	°F	-6 to 40mV
Tube #12 - Peak/Inlet @ 0°	"K" Sh	25	-15/1650	±0.75%	°F	-6 to 40mV
Tube #12 - Peak/Inlet @ 90°	"K" Sh	26	-15/1650	±0.75%	°F	-6 to 40mV
Tube #12 - Peak/Inlet @ 180°	"K" Sh	27	-15/1650	±0.75%	°F	-6 to 40mV
Tube #12 - Peak/Inlet @ 270°	"K" Sh	28	-15/1650	±0.75%	°F	-6 to 40mV
Tube #12 - Peak/Mid @ 0°	"K" Sh	29	-15/1650	±0.75%	°F	-6 to 40mV
Tube #12 - Peak/Mid @ 90°	"K" Sh	30	-15/1650	±0.75%	°F	-6 to 40mV
Tube #12 - Peak/Mid @ 180°	"K" Sh	31	-15/1650	±0.75%	°F	-6 to 40mV
Tube #12 - Peak/Mid @ 270°	"K" Sh	32	-15/1650	±0.75%	°F	-6 to 40mV
Tube #12 - Peak/Exit @ 0°	"K" Sh	33	-15/1650	±0.75%	°F	-6 to 40mV
Tube #12 - Peak/Exit @ 90°	"K" Sh	34	-15/1650	±0.75%	°F	-6 to 40mV
Tube #12 - Peak/Exit @ 180°	"K" Sh	35	-15/1650	±0.75%	°F	-6 to 40mV
Tube #12 - Peak/Exit @ 270°	"K" Sh	36	-15/1650	±0.75%	°F	-6 to 40mV
Chamber - Inside @ Hot F/T Weld	"K" Wr	37	50/300	±4°F	°F	-6 to 40mV
Tube #12 - TES/Inner/Inlet @ 90°	"K" Sh	38	-15/1650	±0.75%	°F	-6 to 40mV
Reference Junction		39	70		°F	
Tube #12 - TES/Inner/Exit @ 270°	"K" Sh	40	-15/1650	±0.75%	°F	-6 to 40mV

Figure 3-6 (con't): ADRT Instrumentation List.

Measurement Description	Trans. Type	CH. #	Maximum Range	Accuracy	Units	Transducer Output
Tube #12 - TES/Inner/Inlet @ 270°	"K" Sh	41	-15/1650	±0.75%	°F	-6 to 40mV
Tube #12 - TES/Outer/Inlet @ 270°	"K" Sh	42	-15/1650	±0.75%	°F	-6 to 40mV
Tube #12 - TES/Outer/Exit @ 90°	"K" Sh	43	-15/1650	±0.75%	°F	-6 to 40mV
Tube #12 - TES/Inner/Exit @ 90°	"K" Sh	44	-15/1650	±0.75%	°F	-6 to 40mV
Tube #12 - TES/Outer/Exit @ 270°	"K" Sh	45	-15/1650	±0.75%	°F	-6 to 40mV
Tube #19 - Peak/Inlet @ 0°	"K" Sh	46	-15/1650	±0.75%	°F	-6 to 40mV
Tube #19 - Peak/Inlet @ 90°	"K" Sh	47	-15/1650	±0.75%	°F	-6 to 40mV
Tube #19 - Peak/Inlet @ 180°	"K" Sh	48	-15/1650	±0.75%	°F	-6 to 40mV
Tube #19 - Peak/Inlet @ 270°	"K" Sh	49	-15/1650	±0.75%	°F	-6 to 40mV
Tube #19 - Peak/Mid @ 0°	"K" Sh	50	-15/1650	±0.75%	°F	-6 to 40mV
Tube #19 - Peak/Mid @ 90°	"K" Sh	51	-15/1650	±0.75%	°F	-6 to 40mV
Tube #19 - Peak/Mid @ 180°	"K" Sh	52	-15/1650	±0.75%	°F	-6 to 40mV
Tube #19 - Peak/Mid @ 270°	"K" Sh	53	-15/1650	±0.75%	°F	-6 to 40mV
Tube #19 - Peak/Exit @ 0°	"K" Sh	54	-15/1650	±0.75%	°F	-6 to 40mV
Tube #19 - Peak/Exit @ 90°	"K" Sh	55	-15/1650	±0.75%	°F	-6 to 40mV
Tube #19 - Peak/Exit @ 180°	"K" Sh	56	-15/1650	±0.75%	°F	-6 to 40mV
Tube #19 - Peak/Exit @ 270°	"K" Sh	57	-15/1650	±0.75%	°F	-6 to 40mV
Zone 2D Power Cable	"K" Sh	58	-300/500	±4°F	°F	-6 to 40mV
Reference Junction	"K"	59	70		°F	
Tube #19 - TES/Inner/Inlet @ 90°	"K" Sh	60	-15/1650	±0.75%	°F	-6 to 40mV

Figure 3-6 (con't): ADRT Instrumentation List.

Measurement Description	Trans. Type	CH. #	Maximum Range	Accuracy	Units	Transducer Output
Tube #19 - TES/Inner/Inlet @ 270°	"K" Sh	61	-15/1650	±0.75%	°F	-6 to 40mV
Tube #19 - TES/Outer/Inlet @ 270°	"K" Sh	62	-15/1650	±0.75%	°F	-6 to 40mV
Tube #19 - TES/Outer/Exit @ 90°	"K" Sh	63	-15/1650	±0.75%	°F	-6 to 40mV
Tube #19 - TES/Inner/Exit @ 90°	"K" Sh	64	-15/1650	±0.75%	°F	-6 to 40mV
Tube #19 - TES/Inner/Exit @ 270°	"K" Sh	65	-15/1650	±0.75%	°F	-6 to 40mV
Tube #19 - TES/Outer/Exit @ 270°	"K" Sh	66	-15/1650	±0.75%	°F	-6 to 40mV
Cavity - Back Wall @R=17"/60°	"K" Sh	67	-25/1800	±0.75%	°F	-6 to 40mV
Cavity - Back Wall @R=17"/180°	"K" Sh	68	-25/1800	±0.75%	°F	-6 to 40mV
Cavity - Back Wall @R=17"/277.5°	"K" Sh	69	-25/1800	±0.75%	°F	-6 to 40mV
Cavity - Front Side Wall @60°	"K" Sh	70	-25/1800	±0.75%	°F	-6 to 40mV
Cavity - Front Side Wall @180°	"K" Sh	71	-25/1800	±0.75%	°F	-6 to 40mV
Cavity - Front Side Wall @277.5°	"K" Sh	72	-25/1800	±0.75%	°F	-6 to 40mV
Cavity - Mid Side Wall @60°	"K" Sh	73	-25/1800	±0.75%	°F	-6 to 40mV
Cavity - Mid Side Wall @180°	"K" Sh	74	-25/1800	±0.75%	°F	-6 to 40mV
Cavity - Mid Side Wall @277.5°	"K" Sh	75	-25/1800	±0.75%	°F	-6 to 40mV
Cavity - Rear Side Wall @60°	"K" Sh	76	-25/1800	±0.75%	°F	-6 to 40mV
Cavity - Rear Side Wall @180°	"K" Sh	77	-25/1800	±0.75%	°F	-6 to 40mV
Cavity - Rear Side Wall @277.5°	"K" Sh	78	-25/1800	±0.75%	°F	-6 to 40mV
Reference Junction	"K"	79	70			
Cavity - Inner Aperture @60°	"K" Sh	80	-100/1300	±0.75%	°F	-6 to 40mV

Figure 3-6 (con't): ADRT Instrumentation List.

Measurement Description	Trans. Type	CH. #	Maximum Range	Accuracy	Units	Transducer Output
Cavity - Inner Aperture @180°	"K" Sh	81	-100/1300	±0.75%	°F	-6 to 40mV
Cavity - Inner Aperture @277.5°	"K" Sh	82	-100/1300	±0.75%	°F	-6 to 40mV
Lamp Array - Zone 2 Box Beam	"K" Sh	83	-25/1800	±0.75%	°F	-6 to 40mV
Lamp Array - Front Beam Support	"K" Sh	84	-250/1000	±0.75%	°F	-6 to 40mV
Inlet Plenum - Gas @ Inlet	"K" Pr	85	-100/1100	±0.75%	°F	-6 to 40mV
Inlet Plenum - Dome	"K" Wr	86	-100/1200	±0.75%	°F	-6 to 40mV
Exit Plenum - Gas @ Exit	"K" Pr	87	-100/1400	±0.75%	°F	-6 to 40mV
Exit Plenum - Dome	"K" Wr	88	-100/1500	±0.75%	°F	-6 to 40mV
Borescope - Tip	"K" Sh	89	-200/800	±0.75%	°F	-6 to 40mV
Exterior - Front Side Wall @60°	"K" Wr	90	-300/300	±4°F	°F	-6 to 40mV
Exterior - Front Side Wall @180°	"K" Wr	91	-300/300	±4°F	°F	-6 to 40mV
Exterior - Front Side Wall @277.5°	"K" Wr	92	-300/300	±4°F	°F	-6 to 40mV
Exterior - Rear Side Wall @60°	"K" Wr	93	-300/300	±4°F	°F	-6 to 40mV
Exterior - Rear Side Wall @180°	"K" Wr	94	-300/300	±4°F	°F	-6 to 40mV
Exterior - Rear Side Wall @277.5°	"K" Wr	95	-300/300	±4°F	°F	-6 to 40mV
Exterior - Aft Wall @60°	"K" Wr	96	-300/300	±4°F	°F	-6 to 40mV
Exterior - Aft Wall @180°	"K" Wr	97	-300/300	±4°F	°F	-6 to 40mV
Exterior - Aft Wall @277.5°	"K" Wr	98	-300/300	±4°F	°F	-6 to 40mV
Reference Junction	"K"	99	70			
LN ₂ Line - Exiting Cold Plate	"K" Wr	100	-330/100	±4°F	°F	-6 to 40mV

Figure 3-6 (con't): ADRT Instrumentation List.

Measurement Description	Trans. Type	CH. #	Maximum Range	Accuracy	Units	Transducer Output
LN ₂ Line - Exiting Upper Shroud 1	"K" Wr	101	-330/100	±4°F	°F	-6 to 40mV
LN ₂ Line - Exiting Upper Shroud 2	"K" Wr	102	-330/100	±4°F	°F	-6 to 40mV
LN ₂ Inlet - Cold Plate	"K" Wr	103	-330/100	±4°F	°F	-6 to 40mV
Cold Plate - Center	"K" Wr	104	-330/300	±4°F	°F	-6 to 40mV
Cold Plate - Edge	"K" Wr	105	-330/300	±4°F	°F	-6 to 40mV
Cold Shroud Panel - Upper Center	"K" Wr	106	-330/300	±4°F	°F	-6 to 40mV
Cold Shroud Panel - Lower Center	"K" Wr	107	-330/300	±4°F	°F	-6 to 40mV
Borescope - Tip (redundant)	"K" Wr	108	-100/300	±4°F	°F	-6 to 40mV
Chamber Wall - Mid Side	"K" Wr	109	50/150	±4°F	°F	-6 to 40mV
Chamber Wall - Center Front Door	"K" Wr	110	50/150	±4°F	°F	-6 to 40mV
CBC - Exit Water	"K" Wr	111	60/190	±4°F	°F	-6 to 40mV
Ambient	"K" Wr	112	40/100	±4°F	°F	-6 to 40mV
CBC - Blower Inlet	"K" Pr	113	75/125	±4°F	°F	-6 to 40mV
CBC - Blower Exit	"K" Pr	114	150/205	±4°F	°F	-6 to 40mV
CBC - Recuperator Hot-leg Exit	"K" Pr	115	400/700	±0.75%	°F	-6 to 40mV
CBC - Flow Meter Exit	RTD Pr	116	150/205	±4°F	°F	0-5V
CBC - Flow Bypass Leg	"K" Pr	117	150/205	±4°F	°F	-6 to 40mV
CBC - Inlet Water	"K" Wr	118	45/75	±4°F	°F	-6 to 40mV
Reference Junction	"K"	119	70			
Chamber Pressure - Mantessa	ion	120	0-10	±10%	-	0-10V

Figure 3-6 (con't): ADRT Instrumentation List.

Measurement Description	Trans. Type	CH. #	Maximum Range	Accuracy	Units	Transducer Output
Ambient Pressure	baro.	121	12.5-14.8	±0.01%	psia	0-10V
Chamber Pressure - Exponent	ion	122	10 ⁻³ -10 ⁻⁹	±10%	torr	0-10V
Spare - channel not used		123				
Static Pressure - RCVR Inlet		124	80/100	±0.25%	psia	0-30mV
Static Pressure - Blower Inlet		125	80/100	±0.25%	psia	0-30mV
Static Pressure - Blower Exit		126	80/100	±0.25%	psia	0-30mV
Static Pressure - Flow Meter Exit		127	80/100		psia	0-5V
Differential Pressure - RCVR		128	0/7	±0.025%	psid	0-30mV
Helium-Xenon Gas Flow Rate	Vortex	129	90-180		lbm/min	0-5V
Spare - channel not used		130				
Cold Water Flow Rate	Turbine	131	5-50	±0.05%	GPM	0-5V
Fine Metering Valve Position		132	0-100		% closed	0-5V
Power - Zone 1A		133	12500	±1%	watts	0-5V
Power - Zone 2A		134	12167	±1%	watts	0-5V
Power - Zone 3A		135	5727	±1%	watts	0-5V
Power - Zone 4A		136	3958	±1%	watts	0-5V
Power - Zone 5A		137	3207	±1%	watts	0-5V
Power - Zone 1B		138	12500	±1%	watts	0-5V
Power - Zone 2B		139	12167	±1%	watts	0-5V
Power - Zone 3B		140	5727	±1%	watts	0-5V

Figure 3-6 (con't): ADRT Instrumentation List.

Measurement Description	Trans. Type	CH. #	Maximum Range	Accuracy	Units	Transducer Output
Power - Zone 4B		141	3958	±1%	watts	0-5V
Power - Zone 5B		142	3207	±1%	watts	0-5V
Power - Zone 1C		143	12500	±1%	watts	0-5V
Power - Zone 2C		144	12167	±1%	watts	0-5V
Power - Zone 3C		145	5727	±1%	watts	0-5V
Power - Zone 4C		146	3958	±1%	watts	0-5V
Power - Zone 5C		147	3207	±1%	watts	0-5V
Power - Zone 1D		148	12500	±1%	watts	0-5V
Power - Zone 2D		149	12167	±1%	watts	0-5V
Power - Zone 3D		150	5727	±1%	watts	0-5V
Power - Zone 4D		151	3958	±1%	watts	0-5V
Power - Zone 5D		152	3207	±1%	watts	0-5V
Power - Zone 1E		153	12500	±1%	watts	0-5V
Power - Zone 2E		154	12167	±1%	watts	0-5V
Power - Zone 3E		155	5727	±1%	watts	0-5V
Power - Zone 4E		156	3958	±1%	watts	0-5V
Power - Zone 5E		157	3207	±1%	watts	0-5V
Power - Zone 1F		158	12500	±1%	watts	0-5V
Power - Zone 2F		159	12167	±1%	watts	0-5V
Power - Zone 3F		160	5727	±1%	watts	0-5V

Figure 3-6 (con't): ADRT Instrumentation List.

Measurement Description	Trans. Type	CH. #	Maximum Range	Accuracy	Units	Transducer Output
Power - Zone 4F		161	3958	±1%	watts	0-5V
Power - Zone 5F		162	3207	±1%	watts	0-5V

Notes:

- Sh - refers to sheathed thermocouples
- Wr - refers to thermocouple wire
- Pr - refers to thermocouple probe in thermowell

Figure 3-6 (concluded): ADRT Instrumentation List.

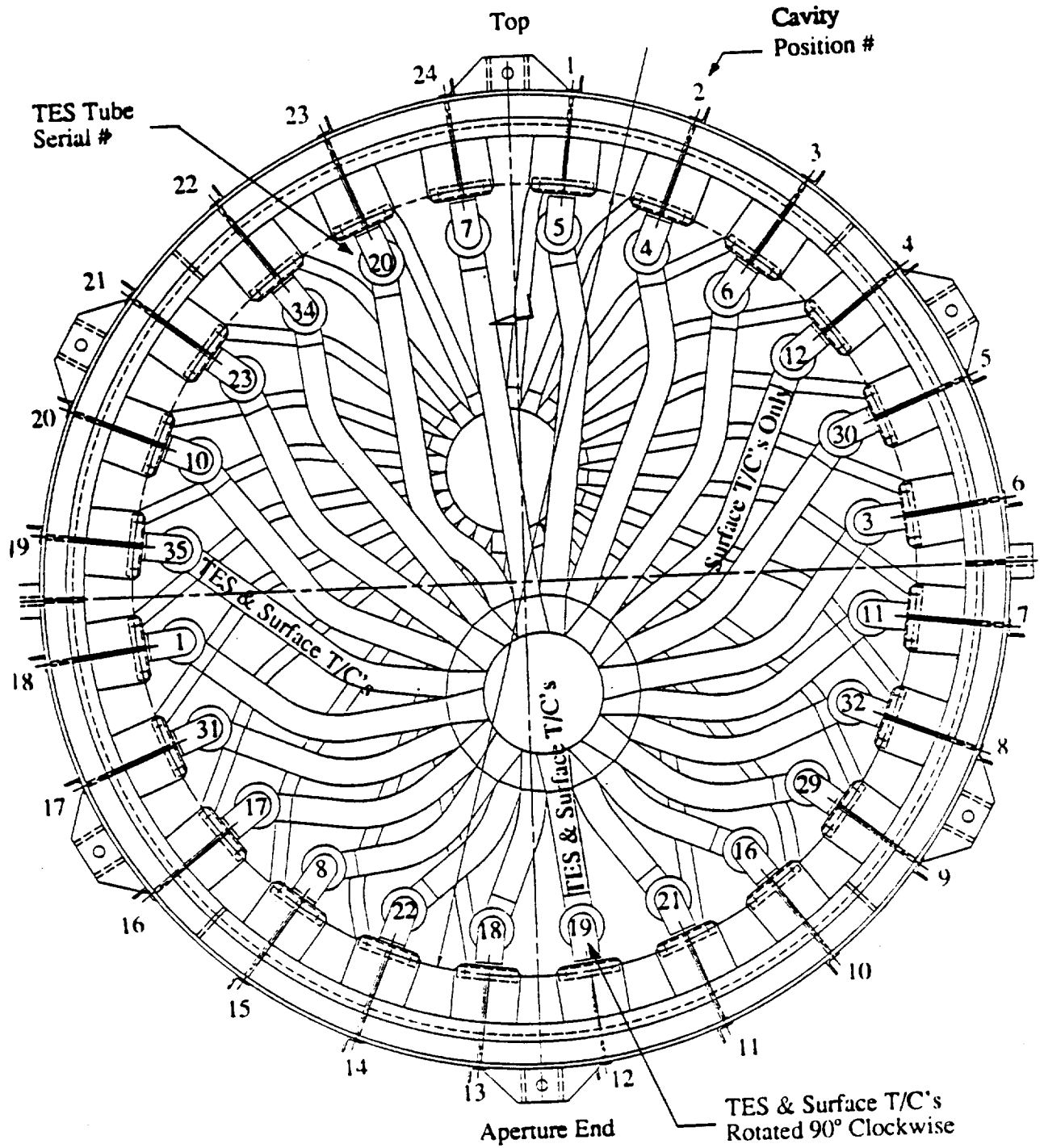


Figure 3-7: Location of Instrumented Heat Storage Tubes Inside the Receiver Cavity.

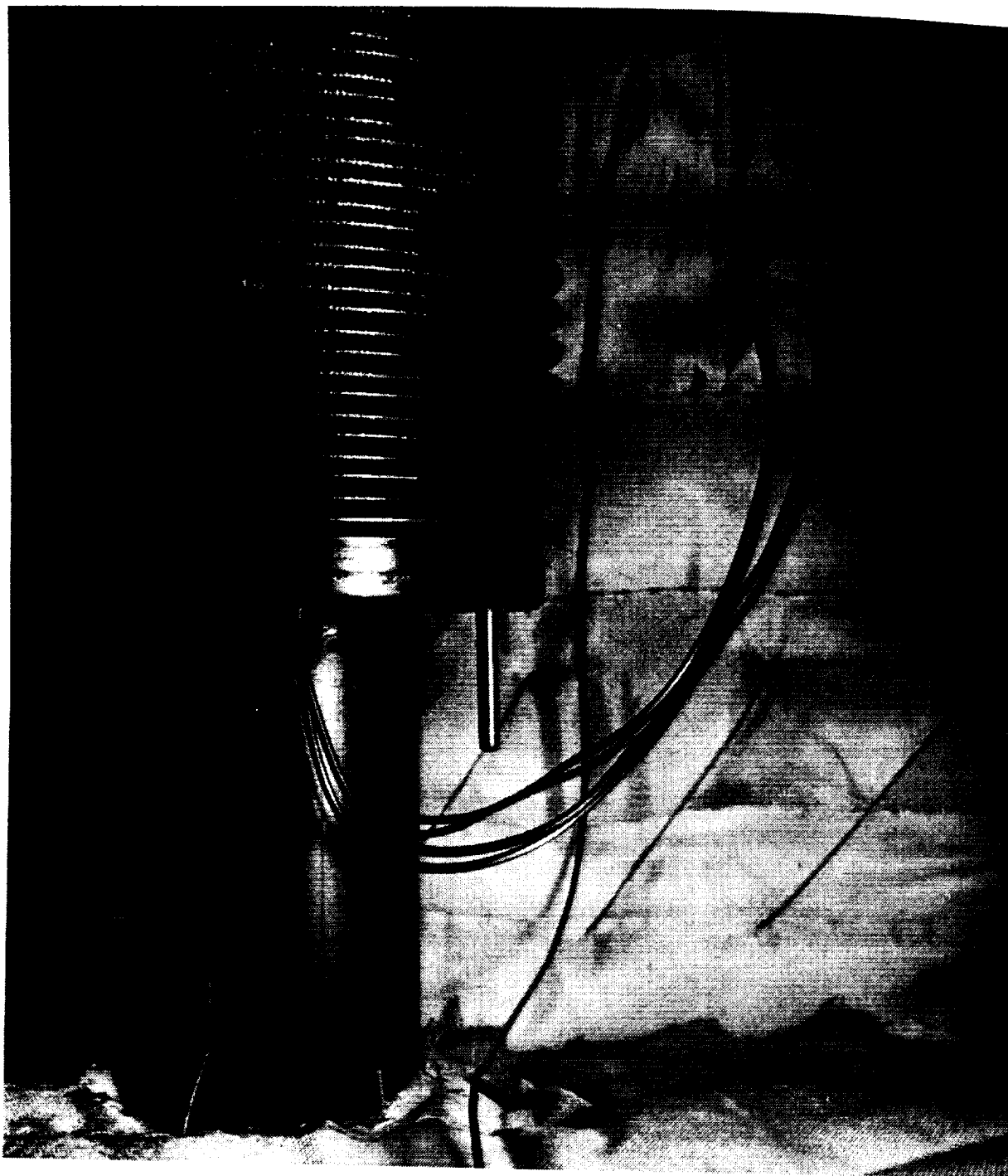


Figure 3-8: Internal Thermocouples at the Exit End of Heat Storage Tube #19.

ORIGINAL PAGE
BLACK AND WHITE PHOTOGRAPH

D180-32816-1

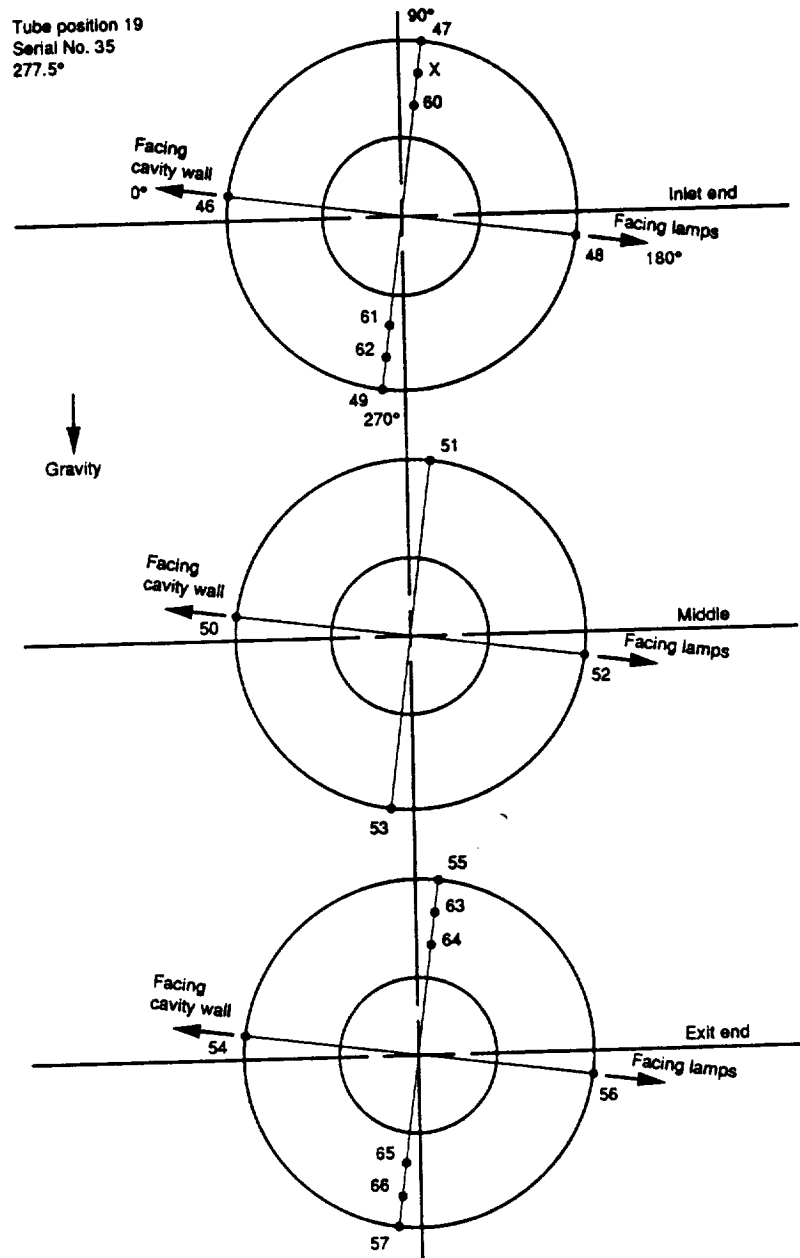


Figure 3-9: Thermocouple Alignment With Respect to Flux, Cavity Wall, and Gravity for Heat Storage Tube #19.

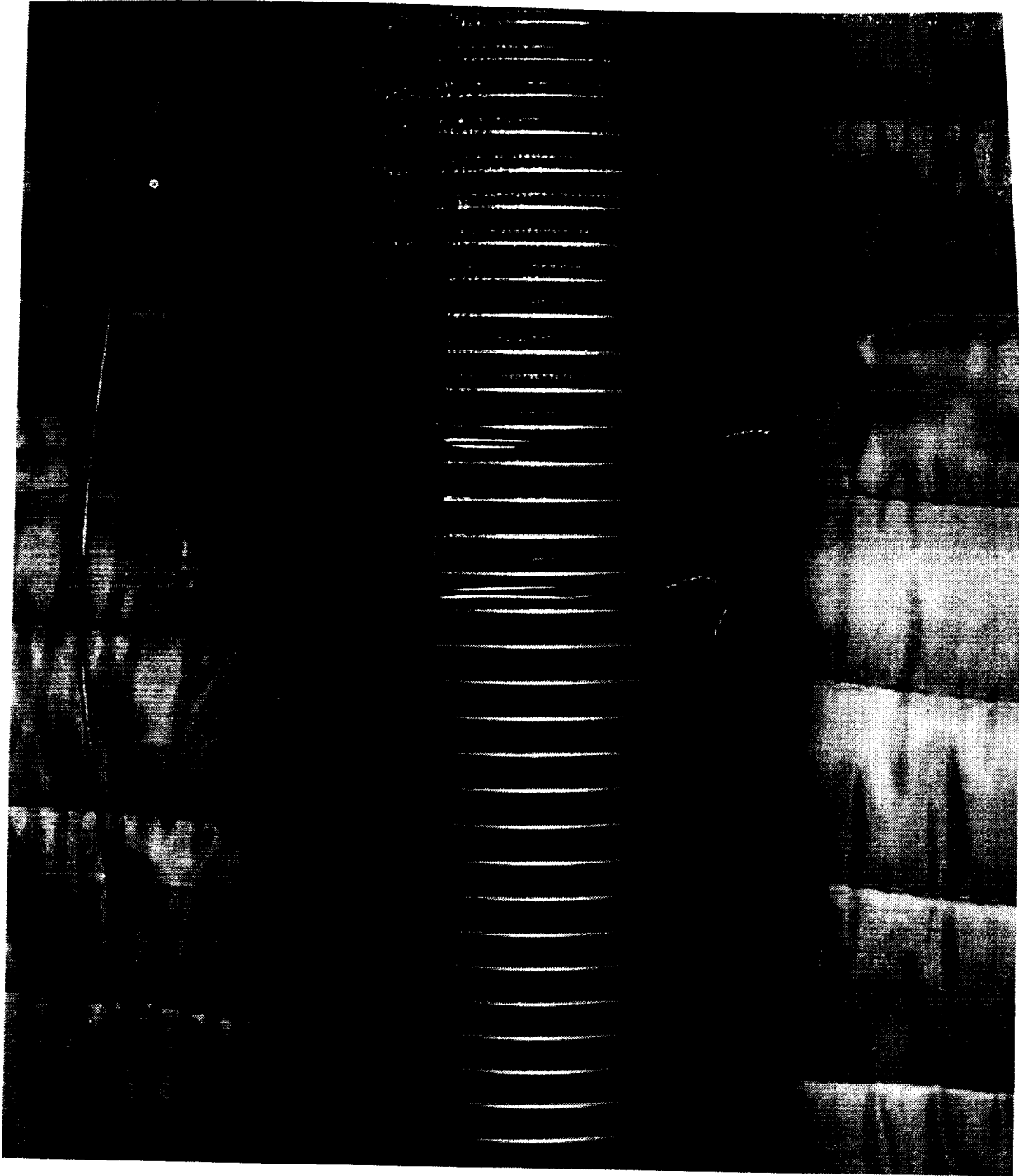


Figure 3-10: Thermocouple Attachment to the Convolution Peaks at the Middle of Heat Storage Tube #19.

ORIGINAL PAGE
BLACK AND WHITE PHOTOGRAPH

end salt fill tube. Therefore, 0° on heat storage tube #19 faces the cavity side wall as shown in Figure 3-9. Sheathed, grounded end, type K thermocouples were used throughout the receiver cavity.

Heat storage tube #12 was rotated 90°, locating the weld seam towards the neighboring tube in position #13. Rotating the tube aligned the internal thermocouples towards the maximum and minimum heat flux regions of the tube, approximately 7.5° off the vertical gravity vector as shown in Figure 3-11. A comparison of data from the internal thermocouples of heat storage tube #'s 12 and 19 will help to characterize the effect of heat flux on the distribution of the salt inside the TES annulus. Sheathed thermocouples were also attached 305 mm (12-in) from the end-caps and at the middle of the bellows section of the heat storage tube.

Heat storage tube #4, pictured in Figure 3-12, has no internal thermocouples but included thermocouples attached in the convolution valleys at the inlet end of the tube as pictured in Figure 3-13. The location of this tube oriented the thermocouples as shown in Figure 3-14. Thermocouples were also wired onto the inlet and exit end salt fill tubes. Several thermocouples were attached to the cantilevered structure associated with heat storage tube #4 for quantifying structural temperatures and the amount of heat loss through this significant heat conduction path. Their locations are identified in Figure 3-15. Thermocouples were also attached to the domed sections of both the inlet and exit plenums.

Cavity wall temperatures were measured at 3 axial locations in the high-flux (inlet end), middle, and low-flux (exit end) of the cavity. Each axial location had 3 circumferential thermocouples, located at 60° (half way between tube #'s 4 and 5), 180° (half way between tube #'s 12 and 13), and 270° (half way between tube #'s 18 and 19). Three thermocouples were attached to the back wall and on the aperture wall and are aligned with the cavity wall thermocouples at 60°, 180°, and 270°. The sheathed thermocouples were attached to the cavity surfaces by stitching as pictured in Figure 3-16. They were then covered from a direct view of the quartz lamp array by a quartz cloth patch as shown in Figure 3-17.

The exterior insulation on the cylindrical surface had 3 thermocouples attached at two axial locations, aligned with the internal cavity wall measurements in the high-flux (inlet end) and exit ends of the cavity. Three thermocouples each aligned with the 60°, 180°, and 270° locations were attached to the exterior front aperture face and aft-end of the receiver.

3.7.2 Instrumentation to Characterize Receiver Performance

Temperature, pressure, and gas flow rate measurements associated with the CBC engine simulator were identified in Figure 3-3. Measurements of the gas temperature at the inlet and outlet of the receiver and the gas flow rate were made to allow the thermodynamic performance to be calculated. The inlet and exit gas temperature thermowells were installed within 305 mm (12 in) of the plenums at the back end of the receiver. The gas flow rate was measured on the CBC engine simulator using a vortex shedding flow meter. The static and differential pressure taps were installed approximately 610 mm (24 inches) from the receiver plenums.

3.7.3 Test Support Equipment and Facility Measurements

Several measurements were made to ensure safe temperatures are maintained on test support equipment and to characterize the exterior environment of the test area. A sheathed thermocouple was installed inside at the mid-point of the quartz lamp array box beam to ensure the design temperature of 1038°C (1900°F) was not exceeded. A thermocouple was also attached to the support cable on the front end of the box beam. Two thermocouples were attached near the tip of the optical borescope to ensure sufficient cooling was maintained to prevent a failure of the o-ring seal. Temperatures of the LN₂ lines exiting the cold shroud and aperture cold

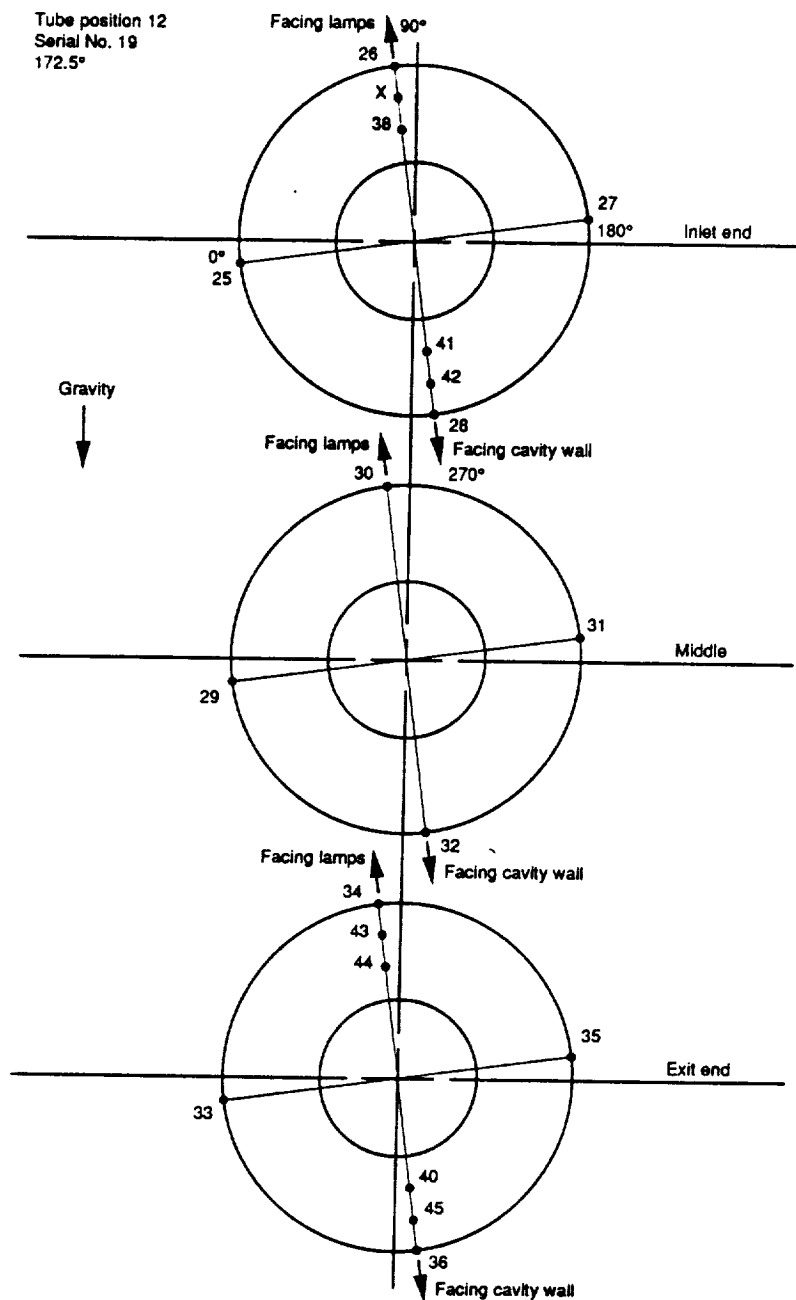


Figure 3-11: Thermocouple Alignment With Respect to Flux, Cavity Wall, and Gravity for Heat Storage Tube #12.

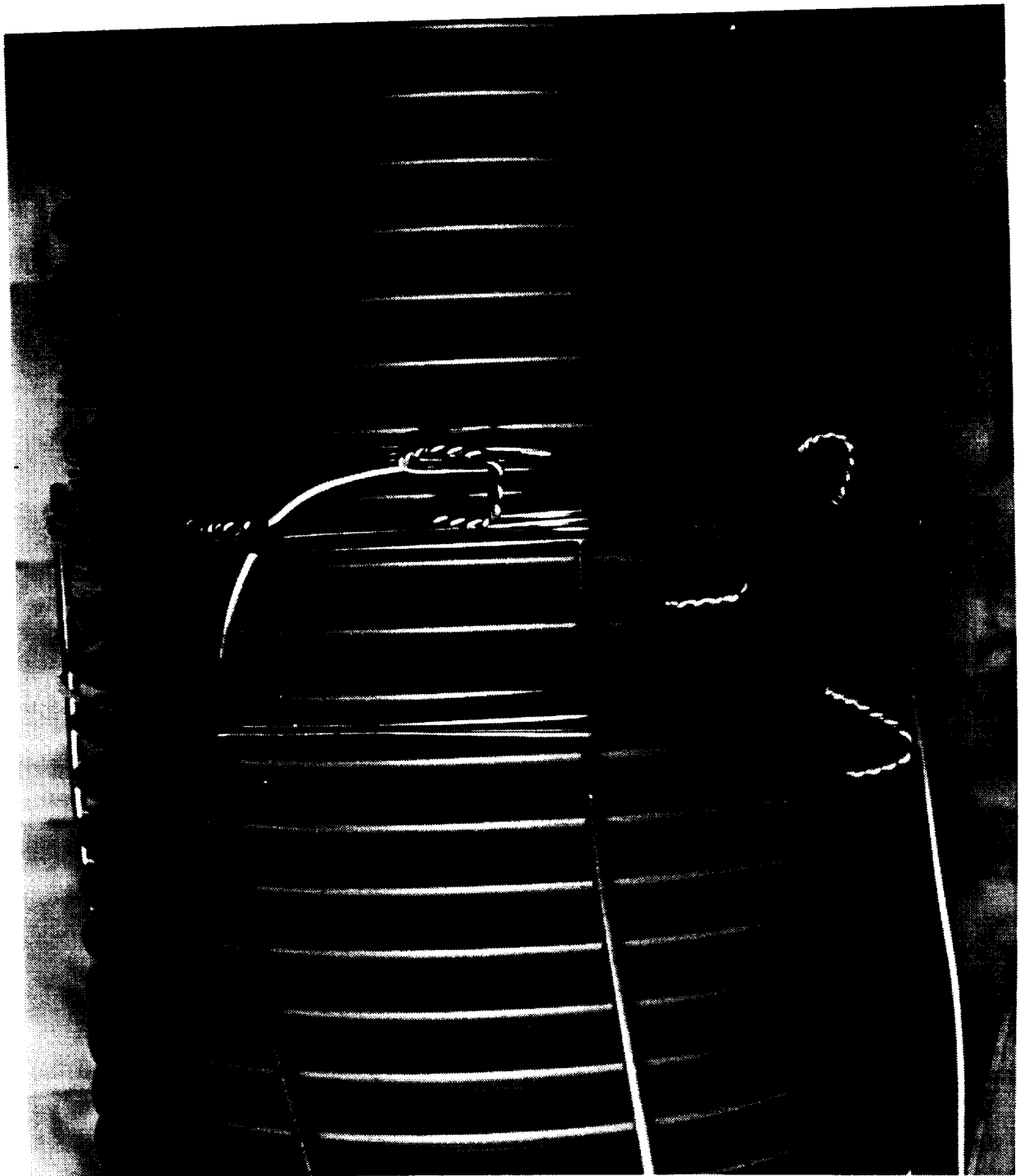


Figure 3-13: Close Up Showing the Thermocouple Attachment to the Convolution Peaks and Valleys at the Inlet End of Heat Storage Tube #4.

BLACK AND WHITE PHOTOGRAPH

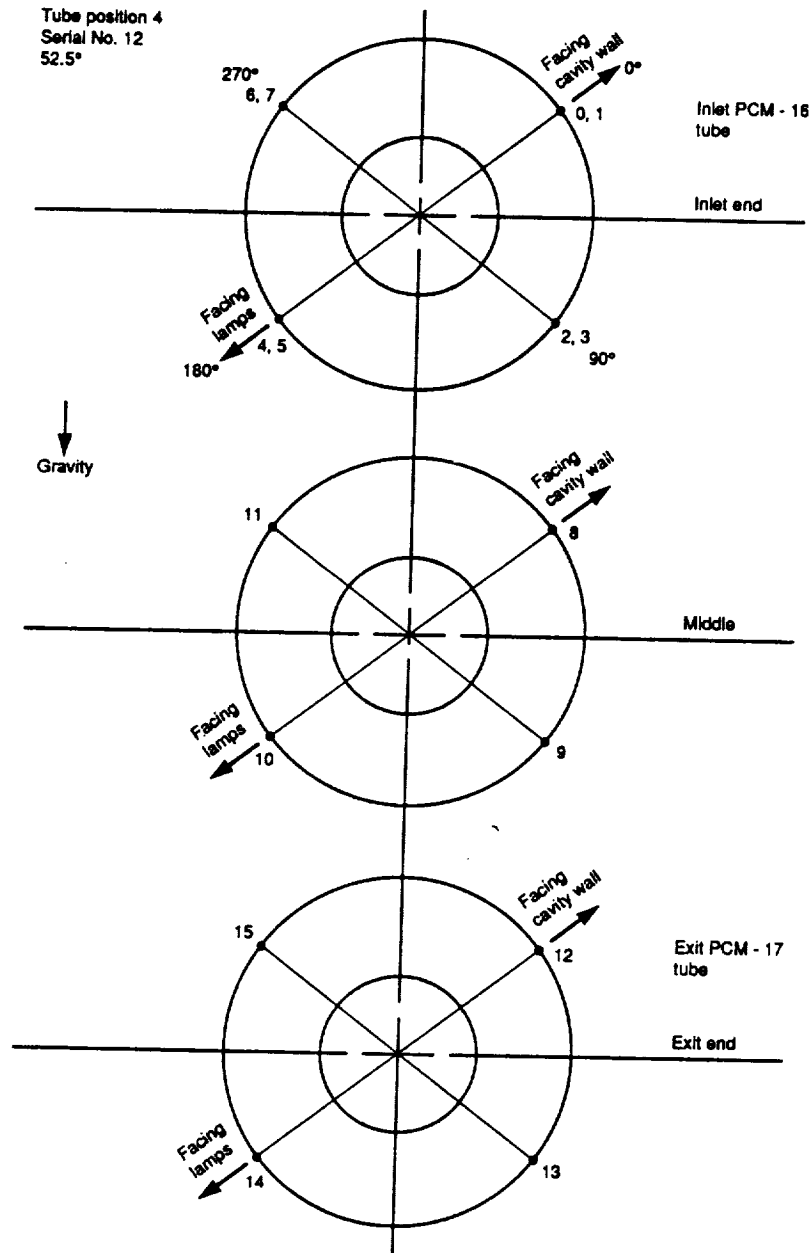


Figure 3-14: Thermocouple Alignment With Respect to Flux, Cavity Wall, and Gravity for Heat Storage Tube #4.

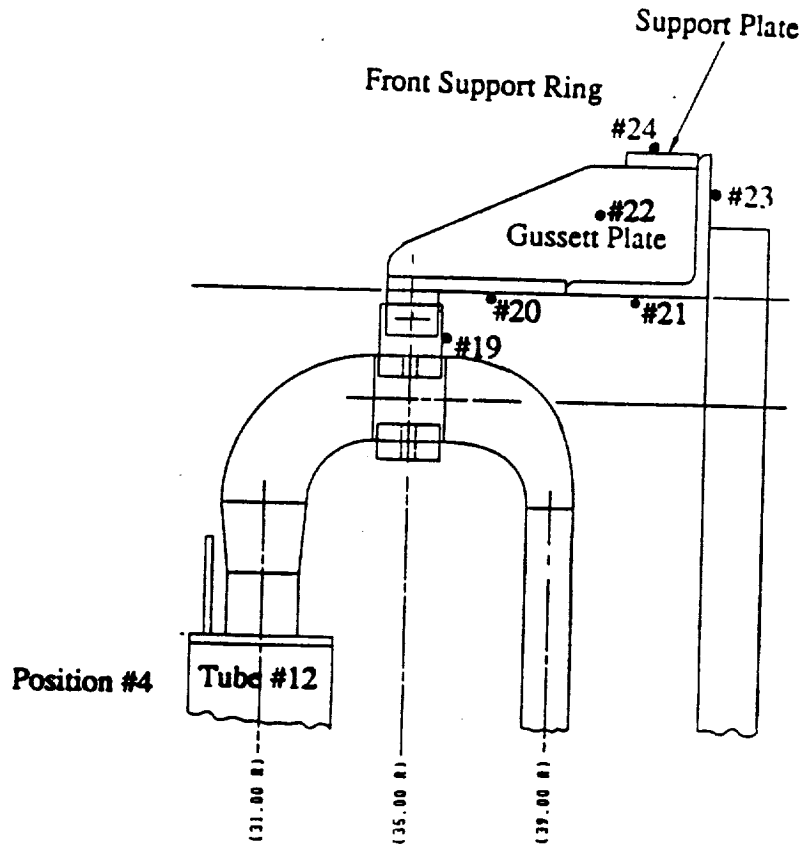
BOEING



Figure 3-12: Instrumented Heat Storage Tube #4.

ORIGINAL PAGE
BLACK AND WHITE PHOTOGRAPH

D180-32816-1



(Measurements in inches)

Figure 3-15: Structural Temperature Measurement Locations Associated With Heat Storage Tube #4.



Figure 3-16: Method of Attachment of Sheathed Thermocouples to Cavity Wall Insulation.

ORIGINAL PAGE
BLACK AND WHITE PHOTOGRAPH

D180-32816-1

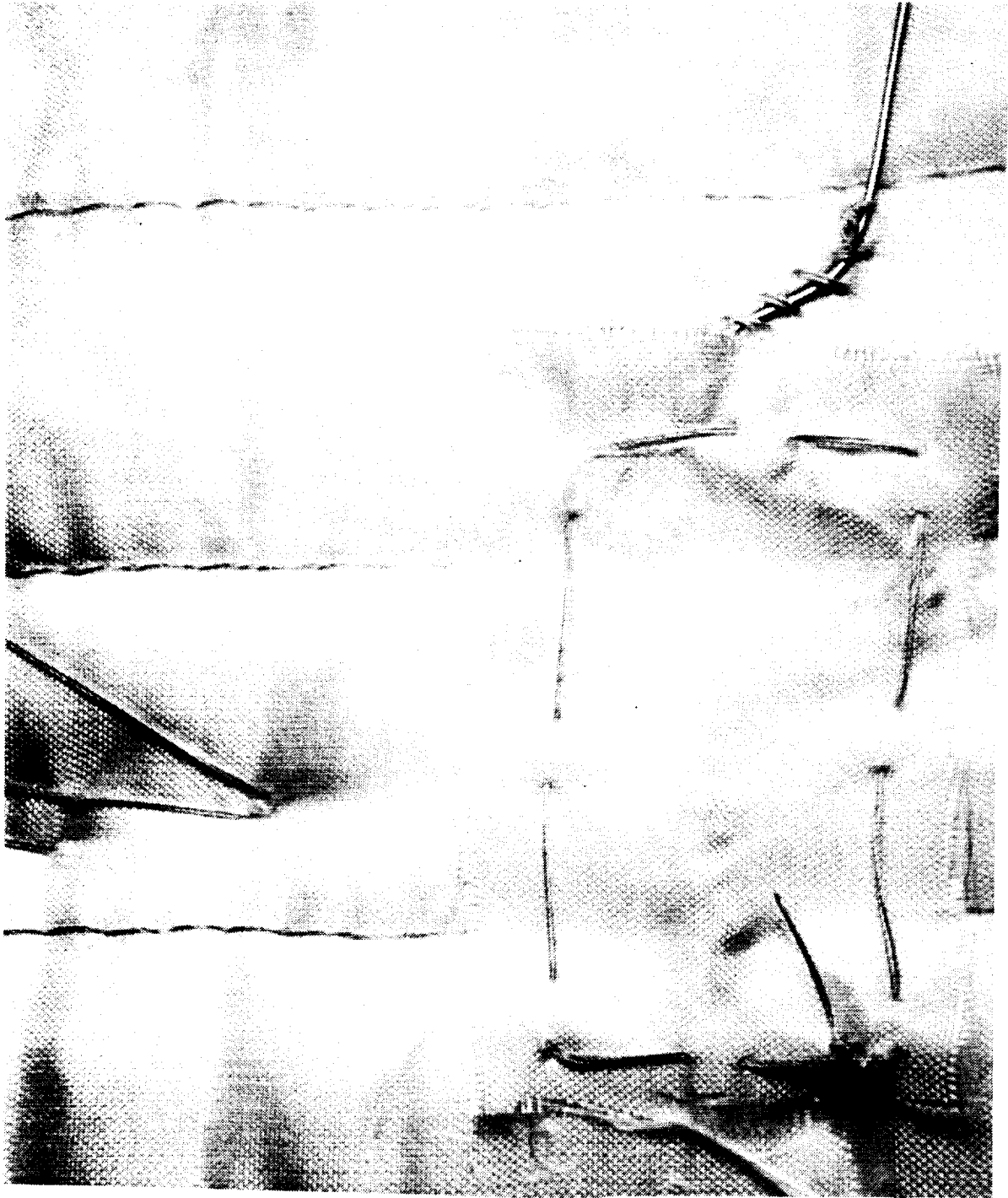


Figure 3-17: Method of Shielding Thermocouples Attached to the Cavity Insulation.

plate were measured to ensure sufficient LN_2 flow is being supplied to these units. Thermocouples were also attached to the cold shroud and cold plate to characterize their performance. Three thermocouples were attached to the vacuum chamber. One of these, located near the weld of the vacuum pass-through of the exiting gas pipe (see Figure 4-10 in Section 4.3), ensured temperature limits were not exceeded at this location (260°C). A portable fan was used to provide additional cooling to the feed-through at the chamber wall. Ambient temperature and pressure were recorded to characterize the environment and its effect on receiver temperatures and absolute pressures.

3.7.4 Helium-Xenon Gas Composition

A Residual Gas Analyzer (RGA) was installed for use during ADRT testing to determine the mole fraction of helium in the helium-xenon gas mixture. The RGA system consists of a quadrupole mass spectrometer, a high vacuum pumping system, and a differentially-pumped capillary sampling system. The capillary allows sampling gases from atmospheric pressure. The mass spectrometer distinguishes gas species in the sample on the basis of mass to charge ratio (m/z). There is no special difficulty in determining the percent levels of helium ($m/z = 4$) and xenon ($m/z = 132$).

The output from the RGA is displayed on a cathode ray tube (CRT) in a variety of forms that would allow a near real-time assessment of the gas composition. Therefore, in theory, the gas composition could be monitored as helium was added to the loop. However, the rate at which molecules from the CBC loop are introduced into the RGA for analysis is too slow for a real time assessment and the adjustments must be made over a period of an hour or more. The RGA failed prior to the beginning of testing and was not used.

3.7.5 Data Acquisition and Control System (DACS)

All measured test data including temperatures, pressures, flow rates, and electrical lamp power were recorded onto permanent storage by computer. Data sampling rates were variable and set by the test conductor based upon the rate of change in test conditions. A single Hewlett Packard 3852S data acquisition computer was used to scan, display, record, and process data. Software was customized to display key parameters in real time on various plot pages, including a page of heater power settings and another showing a complete schematic of the gas loop, receiver cavity, key structure, LN_2 loops, and environmental measurements with data points for all key interfaces displayed and updated at each scan. The CRT screen data or any other data could be printed or plotted during the test on demand from the operator. A total of 163 channels were used for the test and a complete backup computer system was on hand for total redundancy in the event of a hardware failure. The data was permanently recorded on an internal hard drive and transferred to off-line storage after testing was completed.

4.0 TEST ASSEMBLY

The completion dates of significant test set up activities are listed in Figure 4-1 and are described in the sections to follow.

4.1 Facilities

The facility modifications to the Tulalip Area 5 test site began in 1989 to support the verification testing planned during the SDHRT program. These modifications included (1) increasing electrical power capacity to 400 kW; (2) installation of a rail system inside the vacuum chamber to interface with the receiver support cart; (3) cleaning the vacuum chamber; and (4) operational checkout of the vacuum and LN₂ systems. Successful demonstrations of both the vacuum and LN₂ systems were required prior to installing ADRT test hardware to prevent any risk of damage to the test components. However, these systems had not been used in over 3 years and had only been operated briefly in 1986. A number of the seals on the vacuum chamber had deteriorated and the chamber diffusion pump required a complete rebuild. The pump on the LN₂ subcooler also had to be rebuilt because of shaft damage that occurred when it was activated for the first time. These problems delayed initiation of ADRT test hardware installation until mid-September. Problems with the vacuum chamber were corrected and a successful pump down was demonstrated on 14 September 1990.

4.2 Receiver Installation

The receiver was shipped to the test site in a vertical orientation (reference 5). This required the receiver to be tilted to a horizontal orientation before it could be mounted inside the receiver support structure. Detailed procedures were provided in the Detailed Test Procedures Document, reference 3. In summary, the procedures were executed as follows:

The receiver was lifted vertically with a crane using the receiver lifting fixture as shown in Figure 4-2. An steel I-beam was bolted to the front support ring as shown.

A cable was attached to the end of the channel and to the forks on a fork lift vehicle. The crane slowly lowered the receiver while the fork lift truck slowly raised its forks to tilt the receiver as shown in Figure 4-3.

Carefully, the crane and the fork lift lowered the receiver down onto the wood fixtures as shown in Figures 4-4 and 4-5.

The aluminum channel was removed from the front end of the receiver and the receiver lifting fixture was installed onto the receiver for lifting into the horizontal orientation, shown in Figure 4-6. Figure 4-7 shows how the cables used to secure the receiver into its support cart were installed so that they do not interfere with those on the lifting fixture.

The receiver was then lifted into a horizontal orientation and placed inside the support structure as shown in Figure 4-8.

The receiver was installed in the support structure on 9 July 1990 and was stored inside the vacuum chamber during periods of inactivity.

DATE	EVENT
03-21-90	CBC engine simulator delivered to Tulalip Test Site, Area 5.
06-28-90	SDHRT heat receiver delivered to Tulalip Test Site, Area 5.
07-09-90	SDHRT heat receiver tilted from vertical to horizontal orientation and installed in the receiver support structure.
07-13-90	Gas piping and vacuum chamber feed-through components installed between the CBC engine simulator and vacuum chamber. Jumper installed inside vacuum chamber to allow checkout of the CBC.
08-10-90	CBC engine simulator argon checkout 1.
08-10-90	LN ₂ cold shrouds and cold plate delivered to Tulalip Test Site, Area 5.
08-15-90	LN ₂ cold shrouds installed on heat receiver.
09-14-90	Area 5 vacuum chamber demonstrated pump down to a vacuum level of 1.2×10^{-6} torr.
09-19-90	Quartz lamp array assembled and installed inside heat receiver.
09-21-90	Jumper removed from gas lines inside vacuum chamber and helium-xenon gas piping installed between the vacuum chamber gas feed-throughs and the inlet and outlet plenums on the heat receiver.
10-03-90	CBC engine simulator argon checkout 2.
10-09-90	Test Readiness Review meeting conducted. Borescope installed and vacuum chamber closed and ready for test.

Figure 4-1: Completion Dates of Significant Test Set Up Activities.

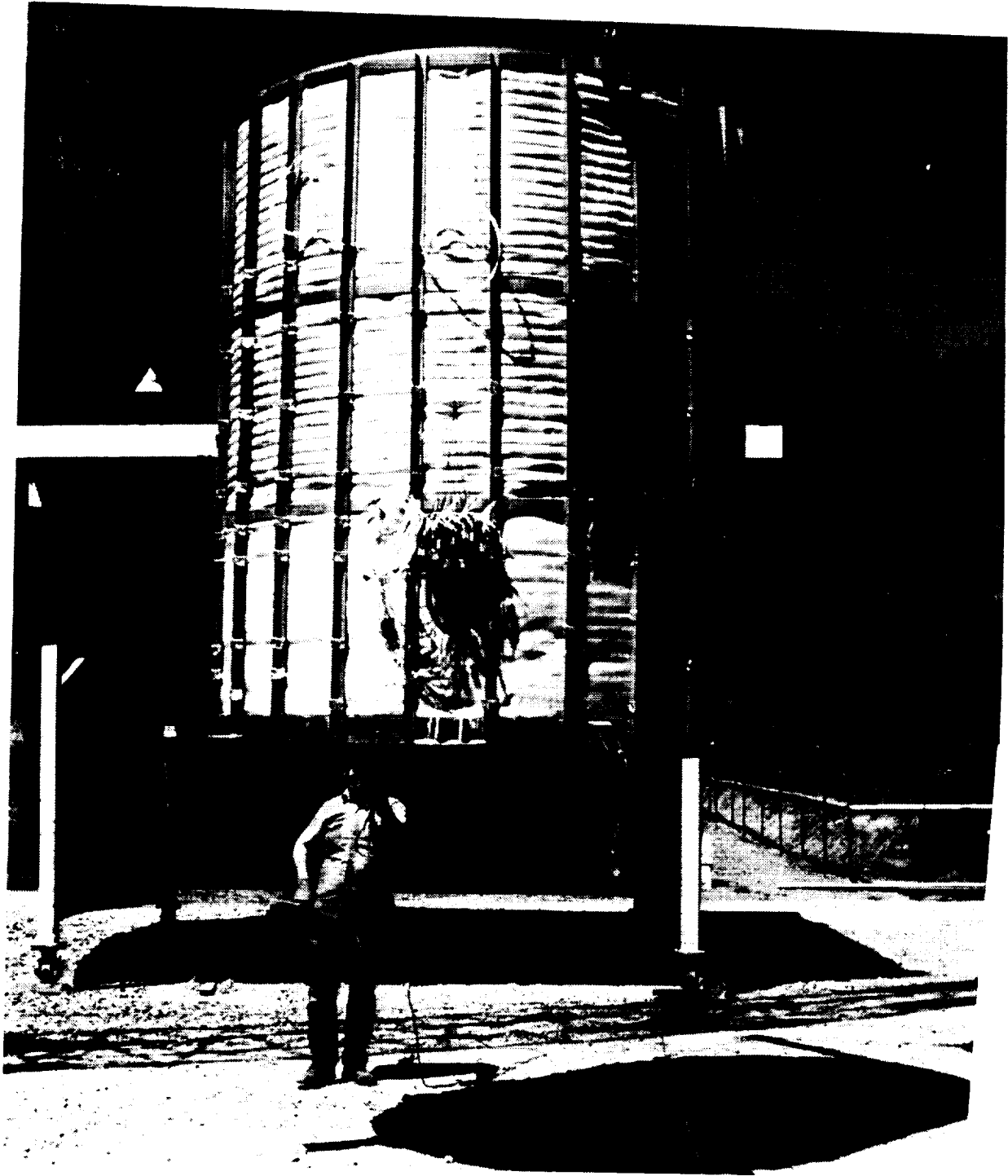


Figure 4-2: Vertical Lift of Receiver With Crane During Receiver Tilting Operations.

D180-32816-1

55

ORIGINAL PAGE
BLACK AND WHITE PHOTOGRAPH



Figure 4-3: Lifting Front End of the Receiver With Forklift During Receiver Tilting Operations.



Figure 4-4: Lowering Receiver to the Ground in a Horizontal Orientation.

ORIGINAL PAGE
BLACK AND WHITE PHOTOGRAPH

D180-32816-1

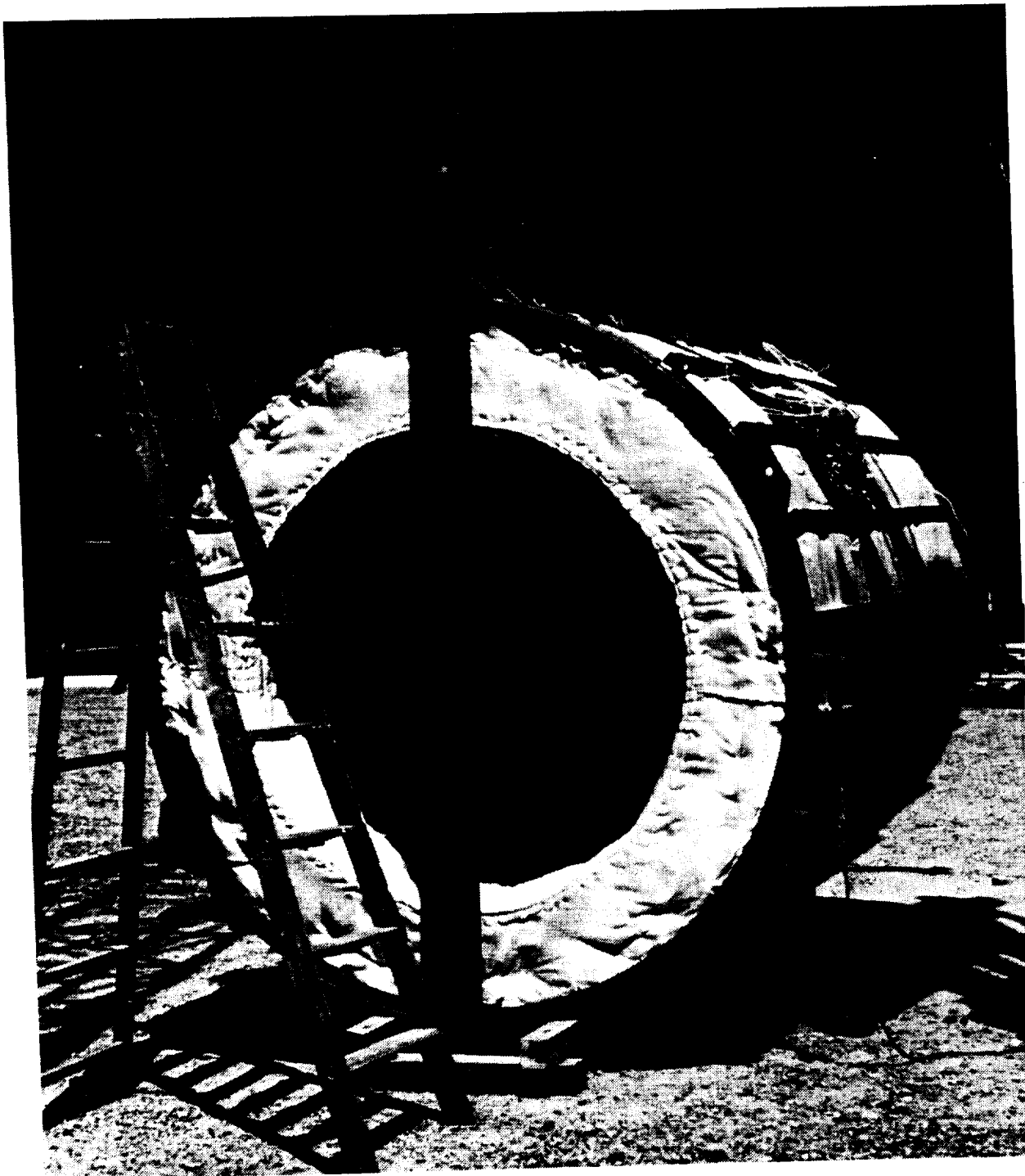


Figure 4-5: Receiver Setting on Support Blocks While Switching the Lifting Fixture From the Vertical to the Horizontal Lift Configuration.

ORIGINAL PAGE
BLACK AND WHITE PHOTOGRAPH

D180-32816-1

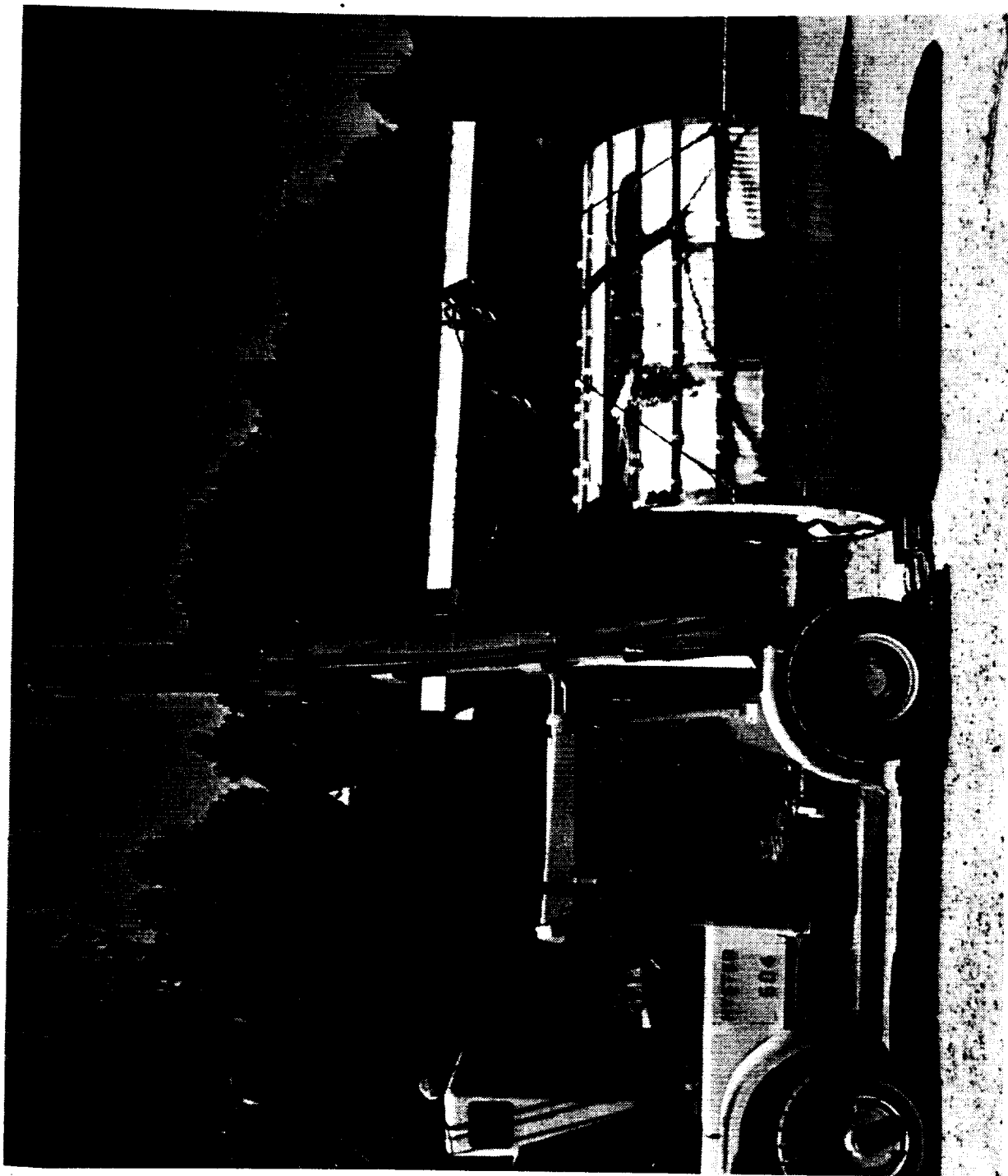


Figure 4-6: Lifting the Receiver in a Horizontal Orientation With Forklift.

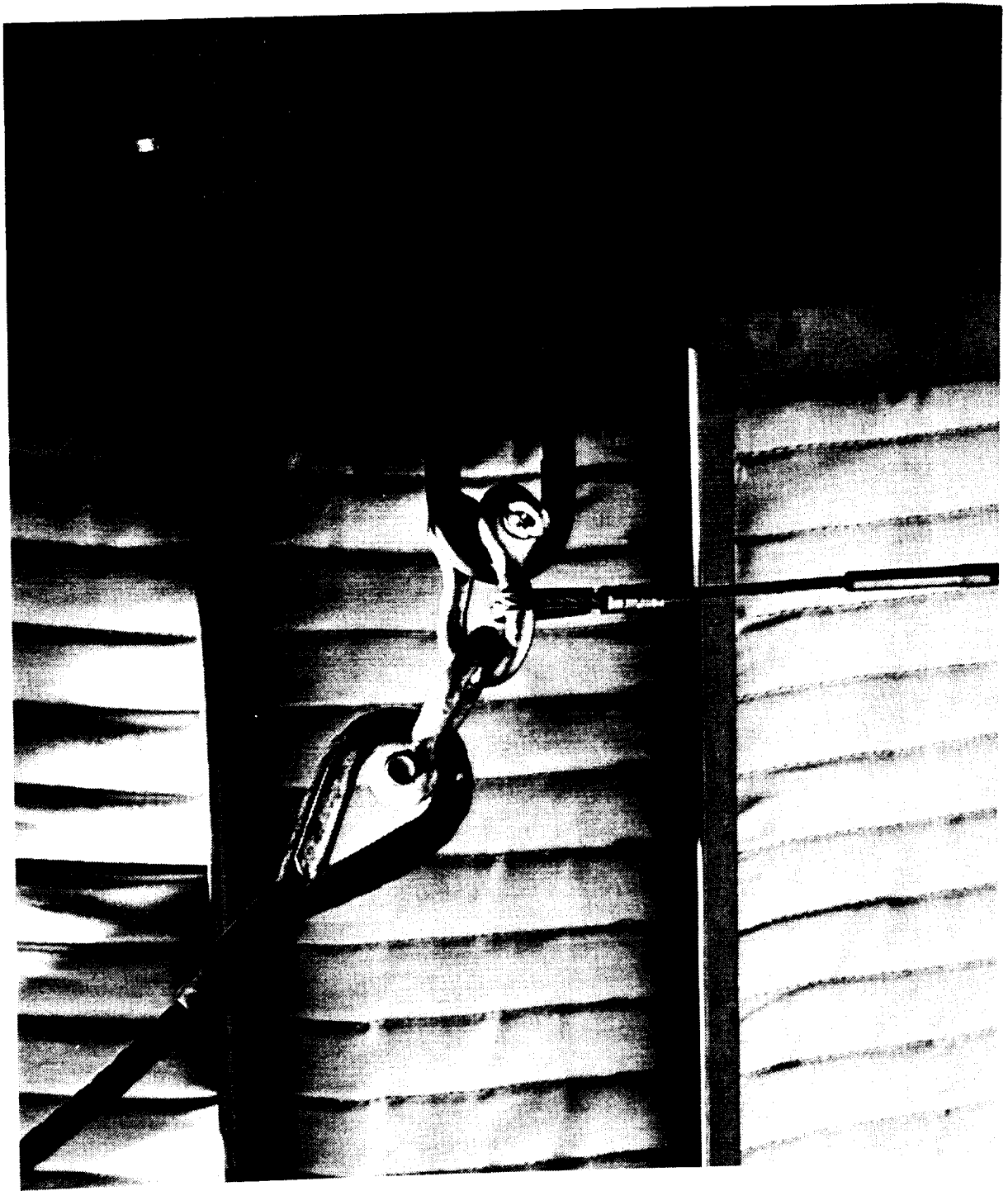


Figure 4-7: Proper Support Cart Cable Attachment Prior to Setting Receiver Inside the Support Cart.

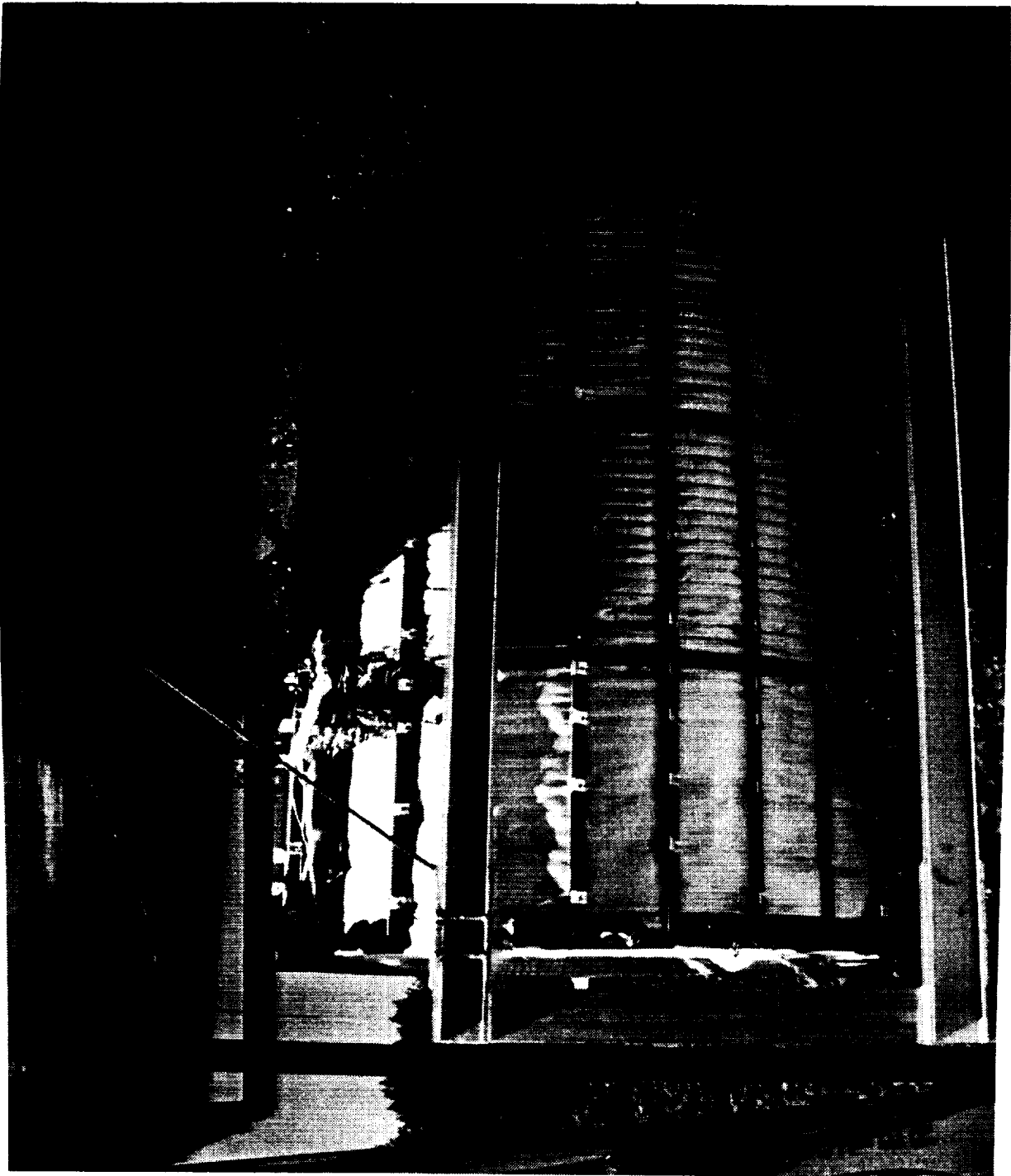


Figure 4-8: Setting Receiver Inside Support Cart.

4.3 CBC Simulator Installation

The CBC engine simulator was placed beside the vacuum chamber and interconnecting piping was installed on 13 July 1990. Figure 4-9 shows the expansion bellows and piping runs between the vacuum chamber and CBC simulator pallet prior to insulating these lines. The piping runs were made from 102 mm (4-in) diameter schedule 40 stainless steel (316) pipe. Special high-temperature thermal feed-throughs were designed, fabricated, and installed in the chamber wall to keep vacuum chamber wall temperatures below 149°C (300°F). Figure 4-10 shows a close-up of the feed-through for the exiting gas line viewed from inside the vacuum chamber. A jumper was temporarily installed inside the chamber connecting the inlet and exit lines to allow operational checkout of the CBC prior to welding these connections to the receiver. The jumper was removed after the checkout was completed.

The inlet and exit gas lines were welded to the receiver as shown in Figure 4-11 after the installation of the quartz lamp heater array was completed. The exit (hot) gas line was a straight pipe run from the chamber to the receiver. The receiver was allowed to roll on the rails with expansion of the hot gas pipe run. Displacements could also be accommodated by movement of the receiver on its support cables in the support cart. The cold gas line used expansion bellows to take up the difference in expansion between the hot exit and the cold inlet gas lines. The gas lines are pictured in Figure 4-12 along with the stainless steel bands used to provide vertical support from the back tee section of the receiver support cart. The CBC pipe runs including the expansion bellows on both sides of the vacuum chamber were insulated with 51 mm (2 in) of Cerablanket, the same insulation as that used inside the receiver (reference 5).

4.4 Quartz Lamp Heater Assembly and Installation

The quartz lamp array components were assembled in 2 stages. First, each of the 6 circumferential zones were assembled, packaged, and shipped to the test site. Reference 5 describes this portion of the assembly process. The second stage assembled the 6 circumferential zones to complete the 30 zone lamp array. This portion of the assembly was performed on the portable platform in front of the vacuum chamber. Detailed procedures for assembling the lamp array are given in reference 3 and a brief pictorial summary follows:

The cantilever stand shown in Figure 4-13 was used to support the quartz lamp heater structure during the assembly process. Figure 4-13 shows the front aperture assembly supported by the lamp array box beam prior to the installation of the six circumferential quartz lamp zones. The top lamp zone (Zone A) was assembled onto the box beam first as shown in Figure 4-14. Simple wood supports were used at each end of the heater to secure the aluminum rails that provided temporary support of the lamp zones. The wood supports were disassembled after the lamp zones were secured to each other by their ceramic insulated attachments. Figures 4-15 through 4-17 illustrate the assembly process at various stages in the operation. The zones were assembled in the following order: zone A, zones B and F, zones C and E, and zone D (zone A is the top zone and the zone letters increment clockwise around the circumference as viewed from the front, aperture end of the array). All parts were white-gloved handled during this assembly operation. Figure 4-17 shows the lamp array after all of the lamp zones were in place but prior to installing the ceramic insulators attaching zone D to zones C and E. After these were in place, the wood support structure was disassembled leaving the completed lamp array supported by the cantilever stand as shown in Figure 4-18.

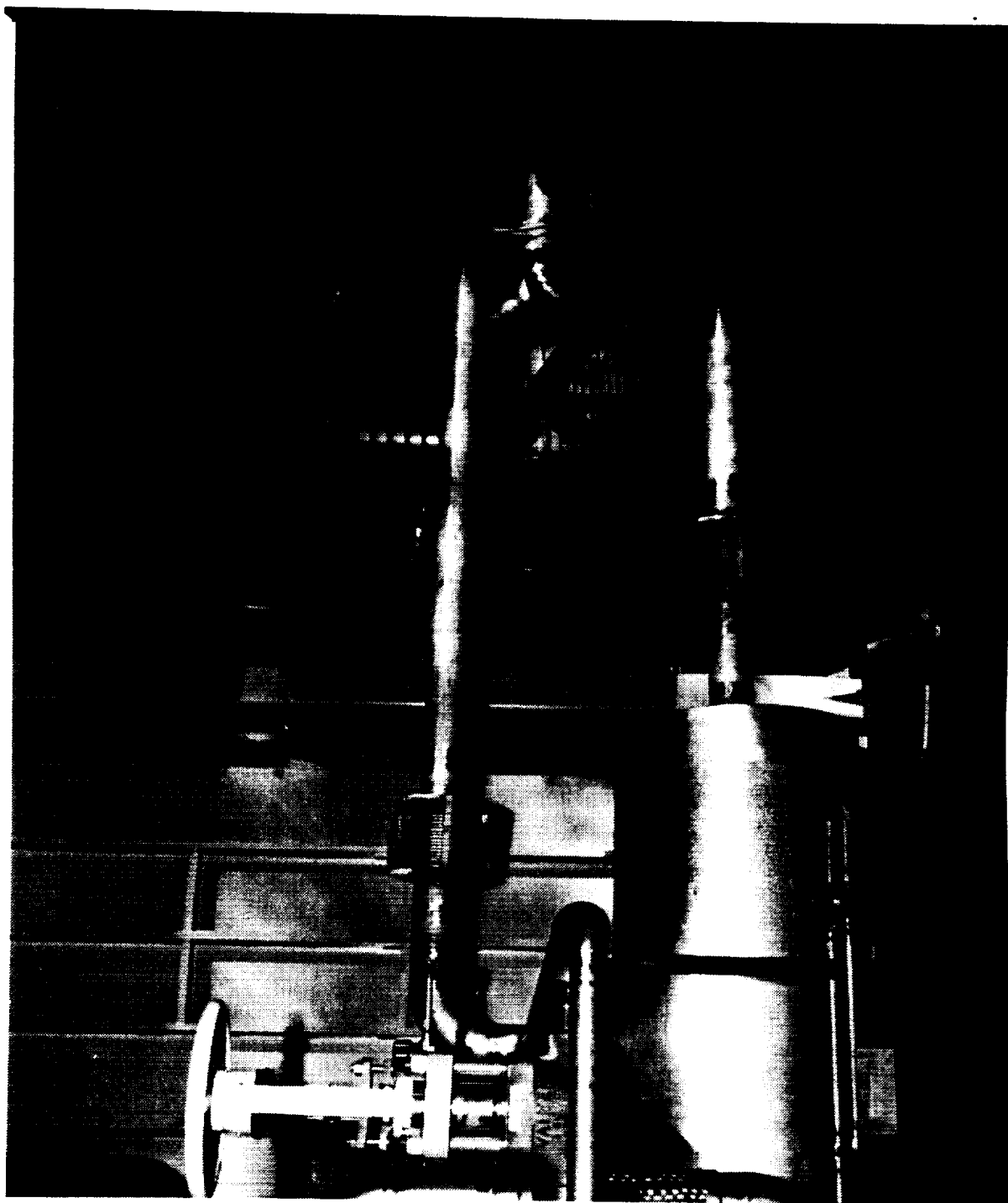


Figure 4-9: Inlet and Exit Gas Piping Runs Between CBC Engine Simulator and Vacuum Chamber.

D180-32816-1

63

ORIGINAL PAGE
BLACK AND WHITE PHOTOGRAPH



Figure 4-10: Vacuum Chamber High-Temperature Feed-Through for Helium-Xenon Gas Piping.

D180-32816-1

64

ORIGINAL PAGE
BLACK AND WHITE PHOTOGRAPH

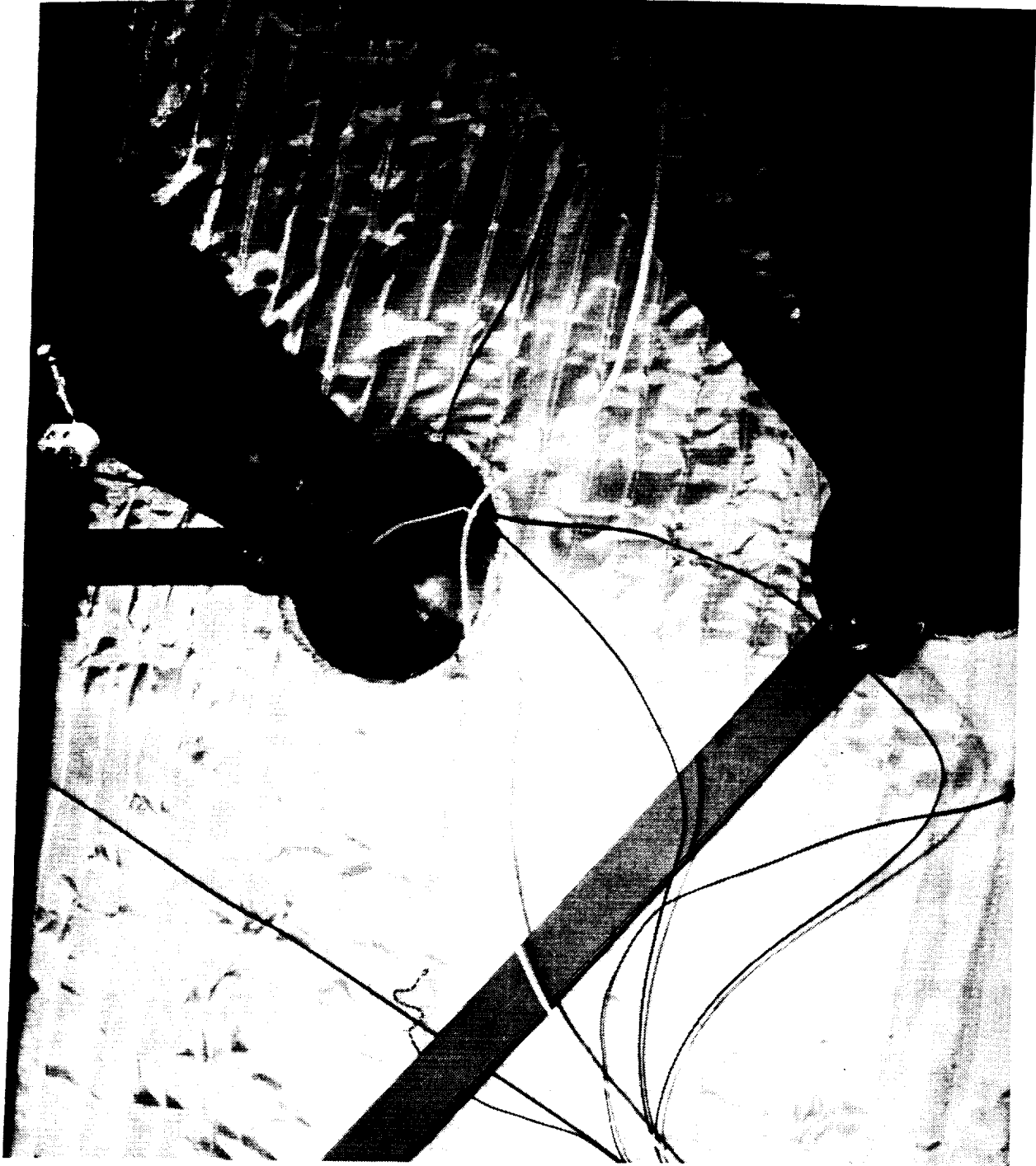


Figure 4-11: Welded Attachments of the Inlet and Exit Gas Lines to the Heat Receiver.

BOEING

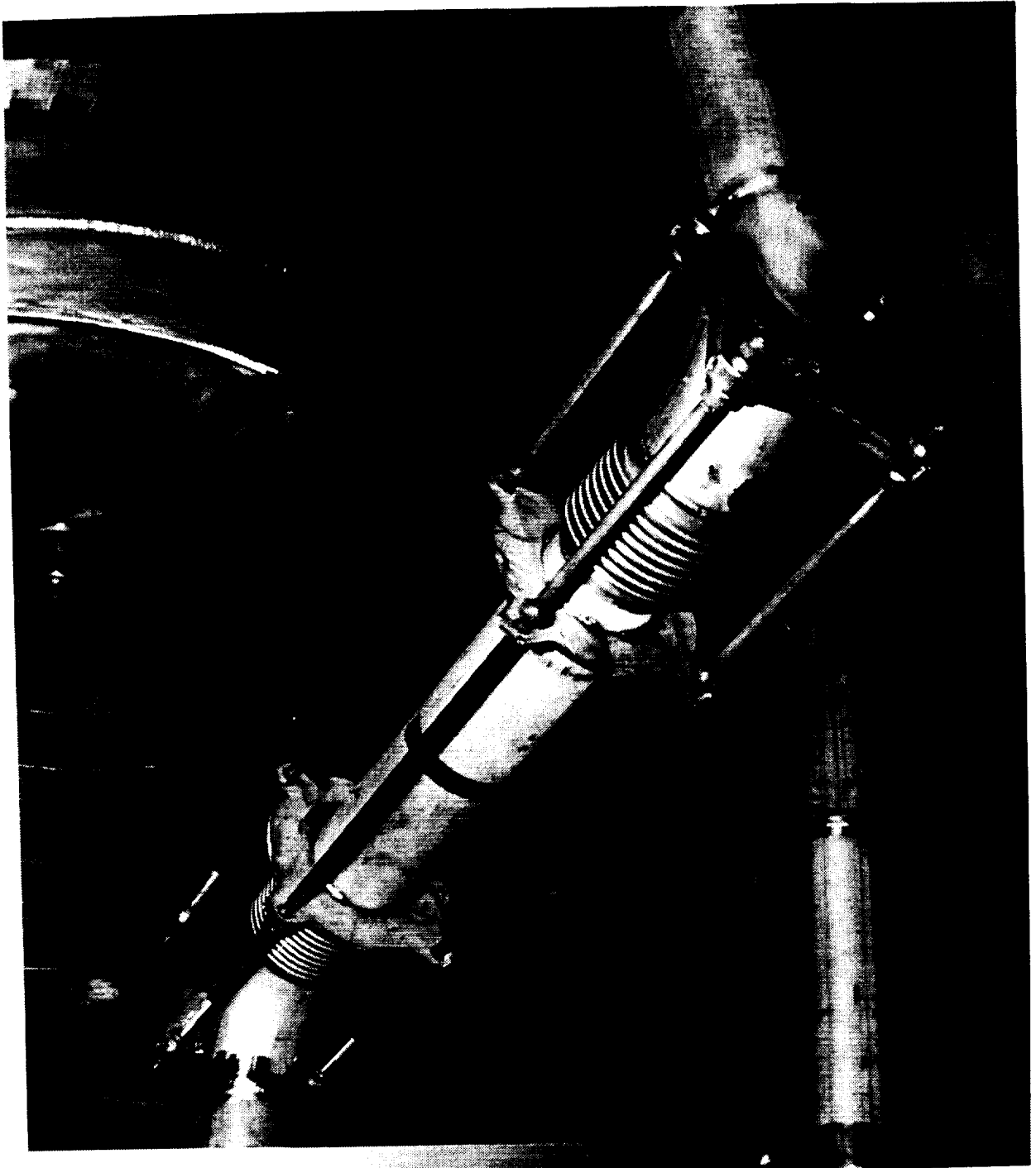


Figure 4-12: Expansion Bellows Configuration on the Cold (Inlet) Gas Line Between the Receiver and the Vacuum Chamber.

D180-32816-1

66

ORIGINAL PAGE -
BLACK AND WHITE PHOTOGRAPH

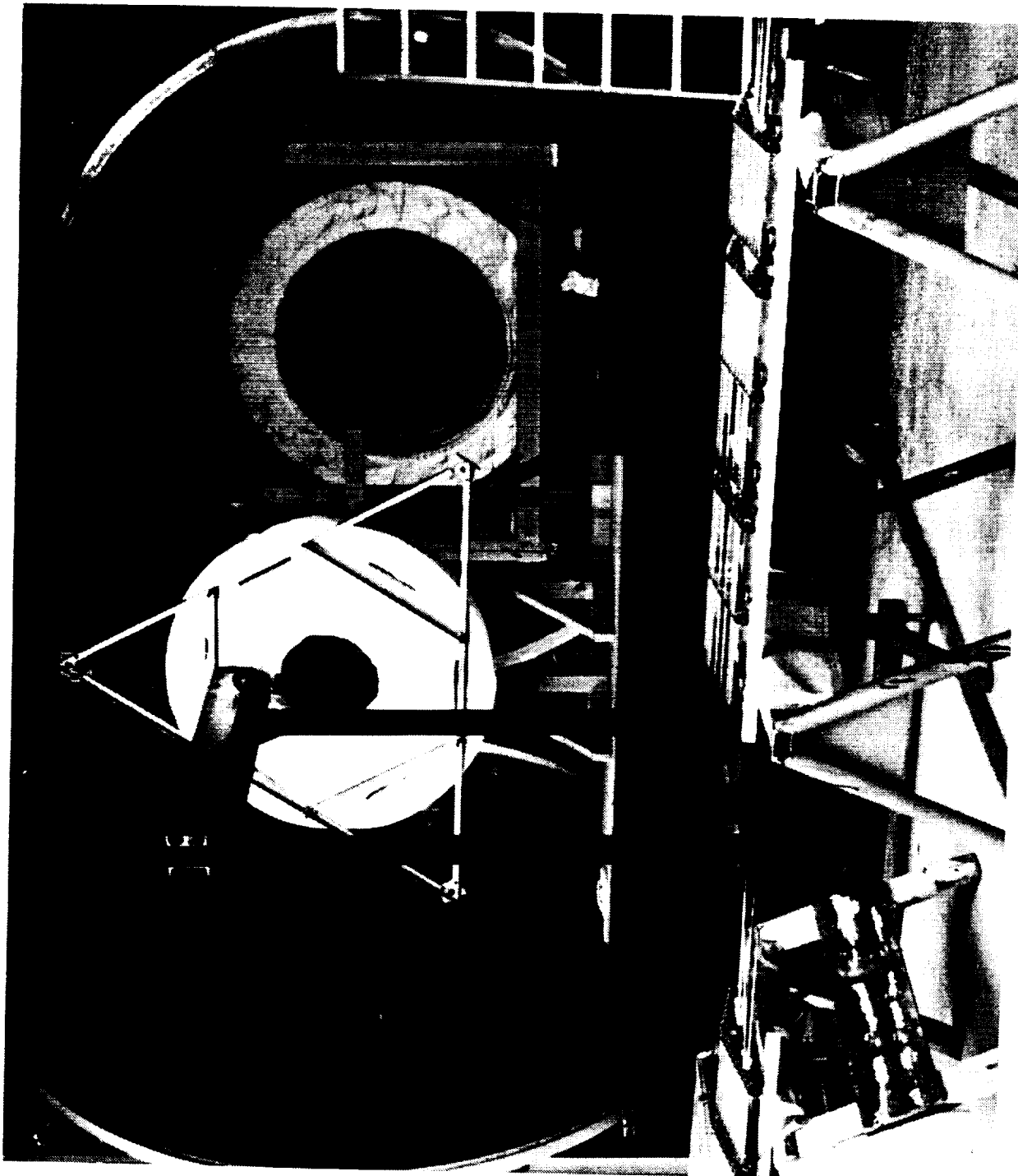


Figure 4-13: Cantilever Stand Supporting Columbium Box Beam and Receiver Aperture Plug During Final Assembly Operations of the Quartz Lamp Heater.

D180-32816-1

67

ORIGINAL PAGE
BLACK AND WHITE PHOTOGRAPH



Figure 4-14: Installation of the Top Zone A On To the Box Beam During Final Assembly Operations of the Quartz Lamp Heater.

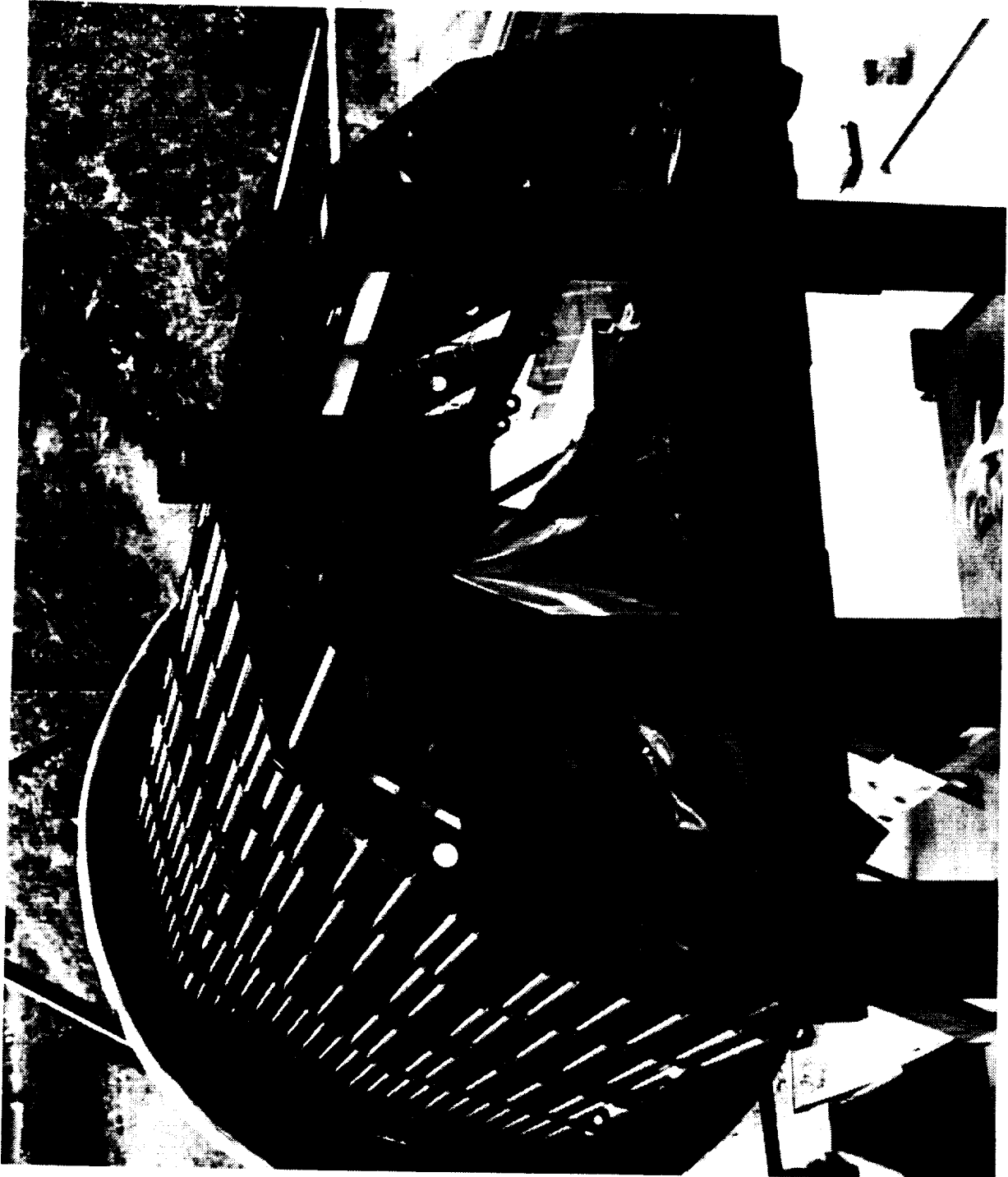


Figure 4-15: Installation of the Zones B and F On To the Box Beam During Final Assembly Operations of the Quartz Lamp Heater.

D180-32816-1

69

ORIGINAL PAGE
BLACK AND WHITE PHOTOGRAPH

BOEING

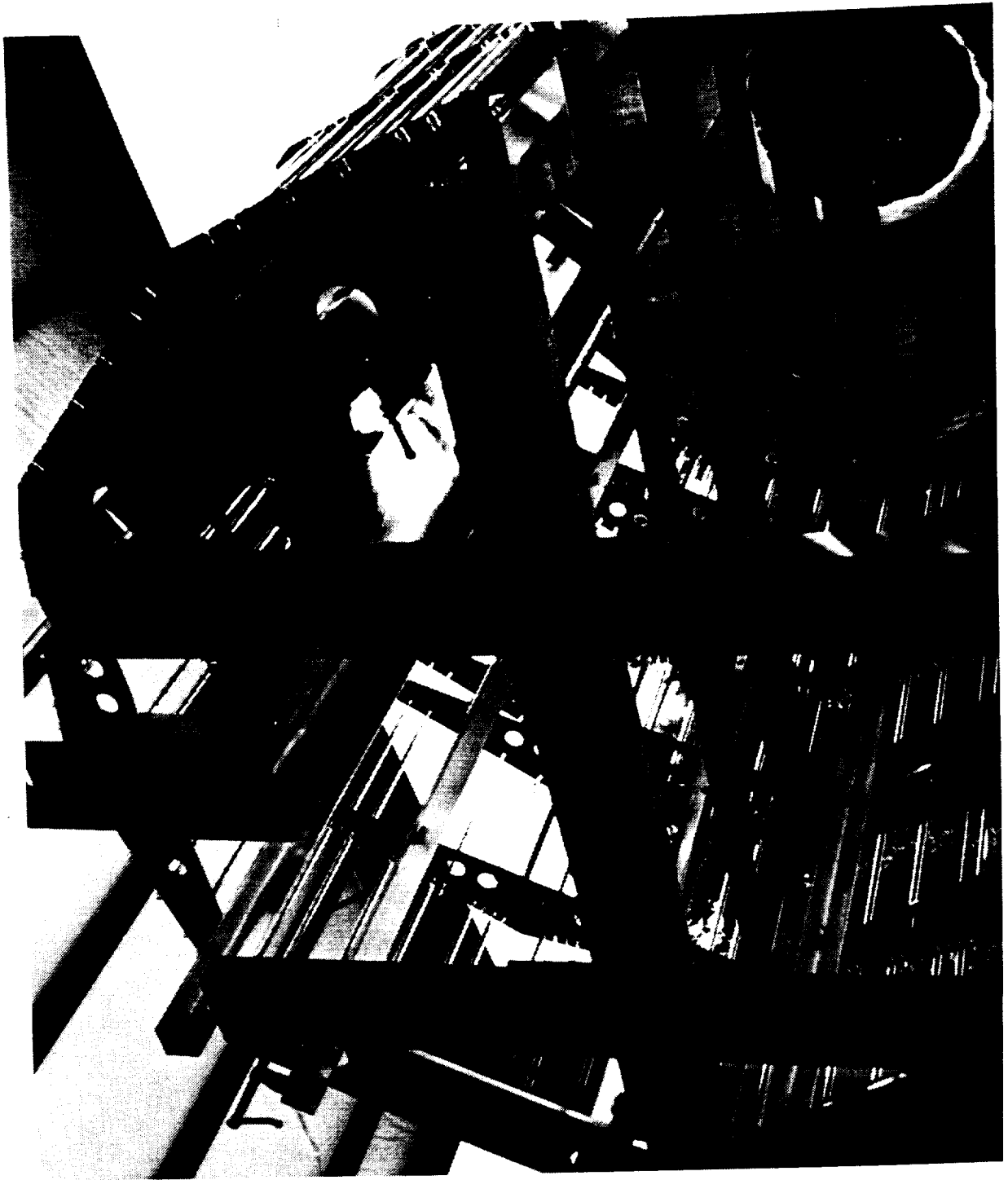


Figure 4-16: Installation of Zones E On To the Box Beam During Final Assembly Operations of the Quartz Lamp Heater.

D180-32816-1

70

PHOTOGRAPH
BLACK AND WHITE PHOTOGRAPH



Figure 4-17: Installation of the Bottom Zone D On To the Box Beam During Final Assembly Operations of the Quartz Lamp Heater.

D180-32816-1

71

ORIGINAL PAGE
BLACK AND WHITE PHOTOGRAPH

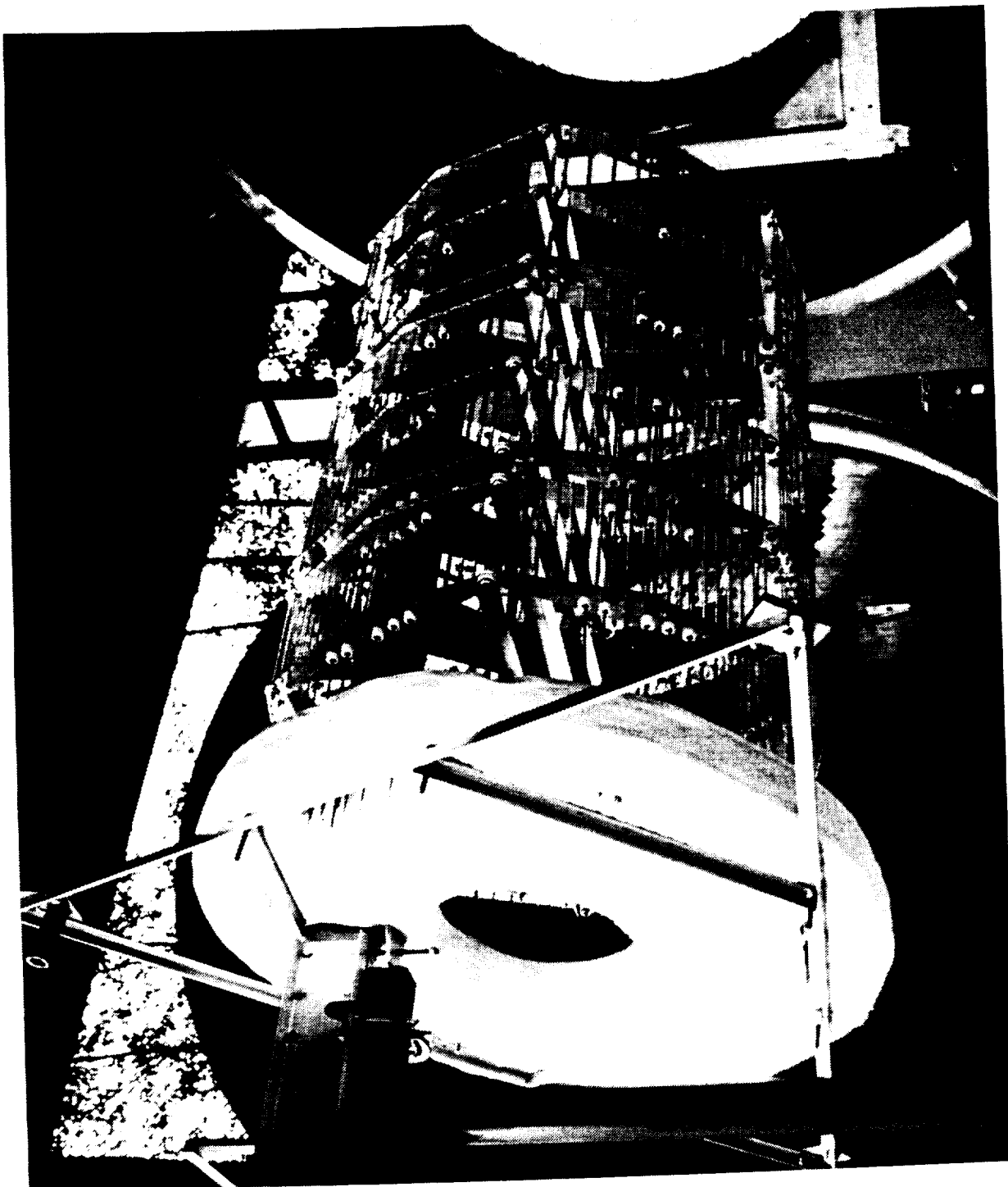


Figure 4-18: Completed Quartz Lamp Array Prior To Installation Into the Receiver Cavity.

Prior to installing the lamp array into the receiver cavity, a check was made of all 30 heater zones to ensure no shorts existed and that all quartz lamps were operational. A large variac was used to supply just enough voltage to each of the heater zones to dimly illuminate the lamps (about 30 volts). The lamps were all wiped down with alcohol just prior to the illumination tests. No shorts were detected but about 7 lamps had cracked quartz envelopes and burned out upon power up (elements oxidized and broke). The burned out lamps showed no particular pattern in the lamp array. After replacement of all of the burned out lamps, a 2nd low power checkout confirmed that all quartz lamps were operational.

Installation of the lamp array into the receiver cavity was accomplished by leaving the lamp array supported over the chamber extension cart and rolling the receiver out of the vacuum chamber over the lamp array as shown in Figure 4-19. A molybdenum rod was then inserted through the insulation at the rear of the cavity and secured to the back of the box beam per the detailed procedures. The rod was secured to the tee section of the receiver support cart as shown in Figure 4-20. The front aperture plug structure was then secured to the receiver frame allowing the cantilever stand to be removed from the box beam. The lamp array was now fully supported inside the receiver cavity. The front support cable and the rear support molybdenum rod were adjusted to give proper alignment of the lamp array inside the receiver cavity. The receiver was then rolled back into the vacuum chamber for the last time. Figures 4-21 and 4-22 picture the top and bottom (respectively) of the receiver cavity with the lamp array installed. The lamps were on an average radius of about 589 mm (23 in), approximately 127 mm (5 in) from the front faces of the heat storage tubes.

The receiver was now ready for final assembly which included welding the CBC inlet and exit gas lines, attachment of the LN₂ lines to the cold shrouds, attachment of the electrical cables to the lamp array bus rods, installation of miscellaneous thermocouples to the front of the receiver and to structure, installation of the aperture cold plate, and installation of the optical borescope. Detailed procedures for all of these operations are given in reference 3. The receiver is shown just prior to the installation of the aperture cold plate in Figure 4-23. Ceramic plates mounted to the aperture assembly structure were used to insulate and provide structural support of the lamp array electrical bus rods and cabling. A close-up of the cable attachments to the bus rods is pictured in Figure 4-24. Cable trays were used to guide and support the heavy gauge (# 4) electrical cables to the electrical feed-throughs in the vacuum chamber as pictured in Figure 4-25. Checkouts were made of all of the test hardware per the procedures given in reference 3 prior to initiating test.

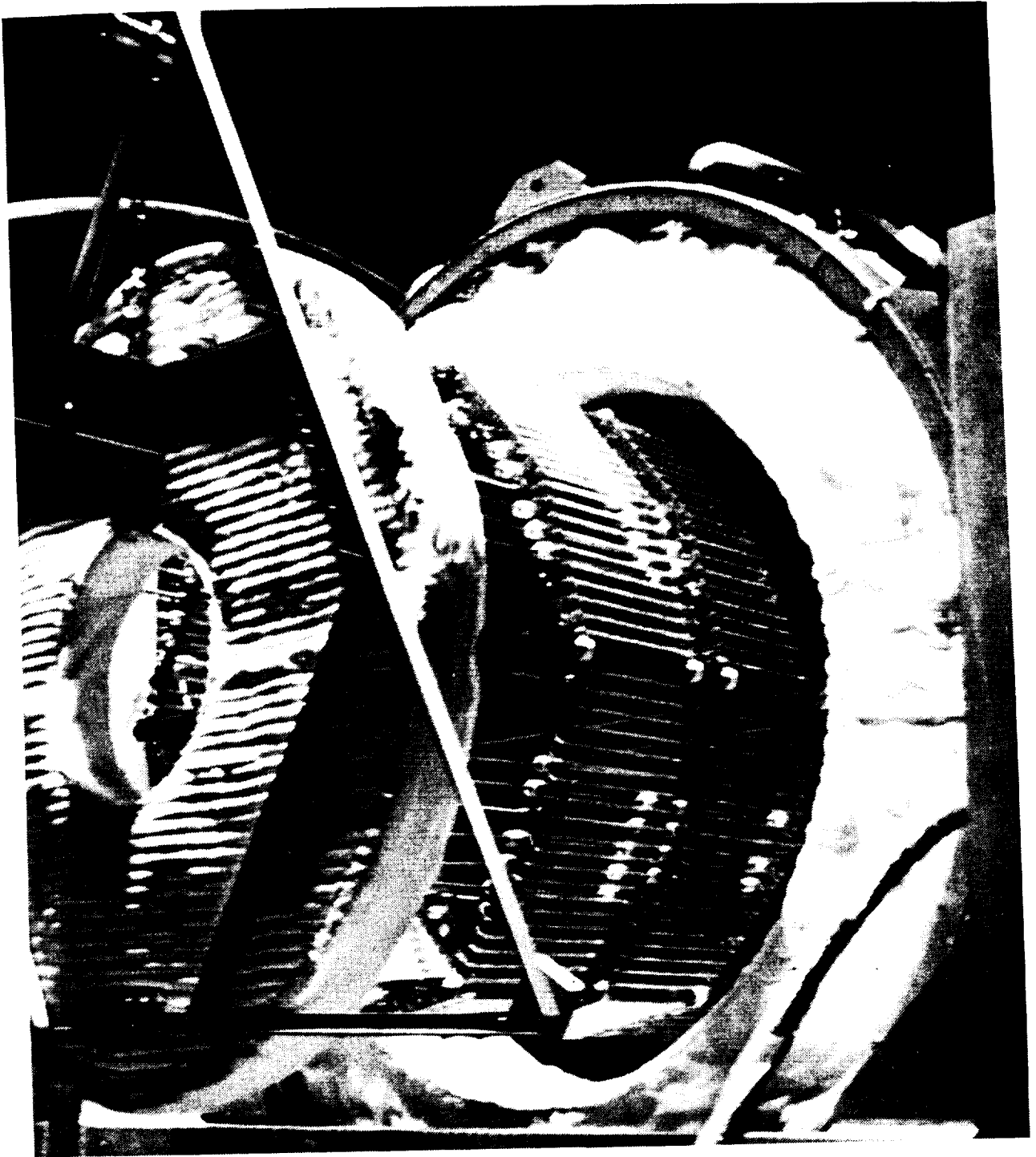


Figure 4-19: Rolling the Heat Receiver Over the Lamp Array During the Installation Operations of the Lamp Array Into the Receiver Cavity.

D180-32816-1

74

ORIGINAL PAGE
BLACK AND WHITE PHOTOGRAPH



Figure 4-20: Rear Lamp Support Molybdenum Rod Attachment To the Receiver Support
Cart.

D180-32816-1

75

ORIGINAL PAGE
BLACK AND WHITE PHOTOGRAPH

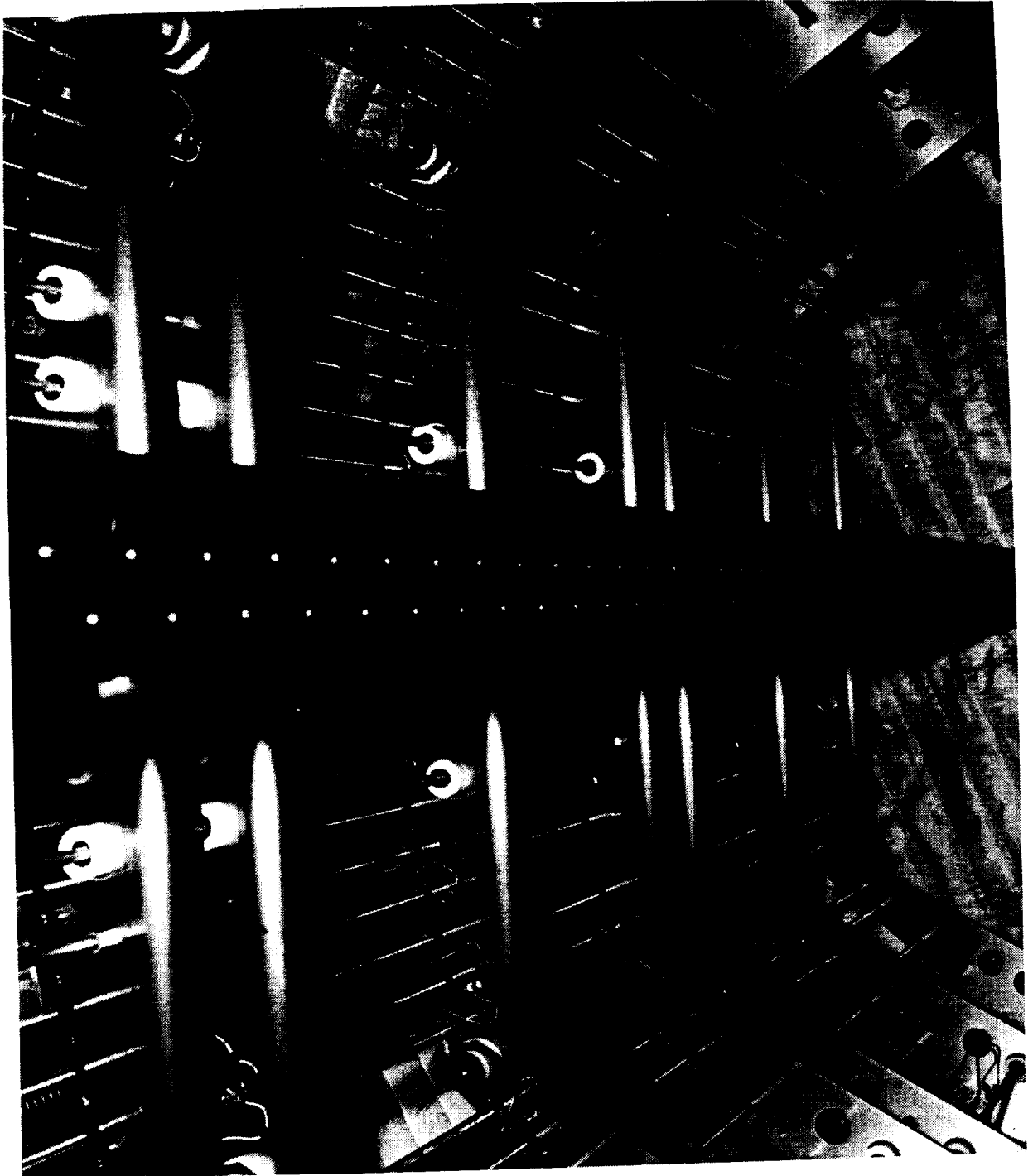


Figure 4-21: View of Quartz Lamp Zones F, A, and B (Left to Right) Inside the Receiver Cavity.

D180-32816-1

76

ORIGINAL PAGE
BLACK AND WHITE PHOTOGRAPH

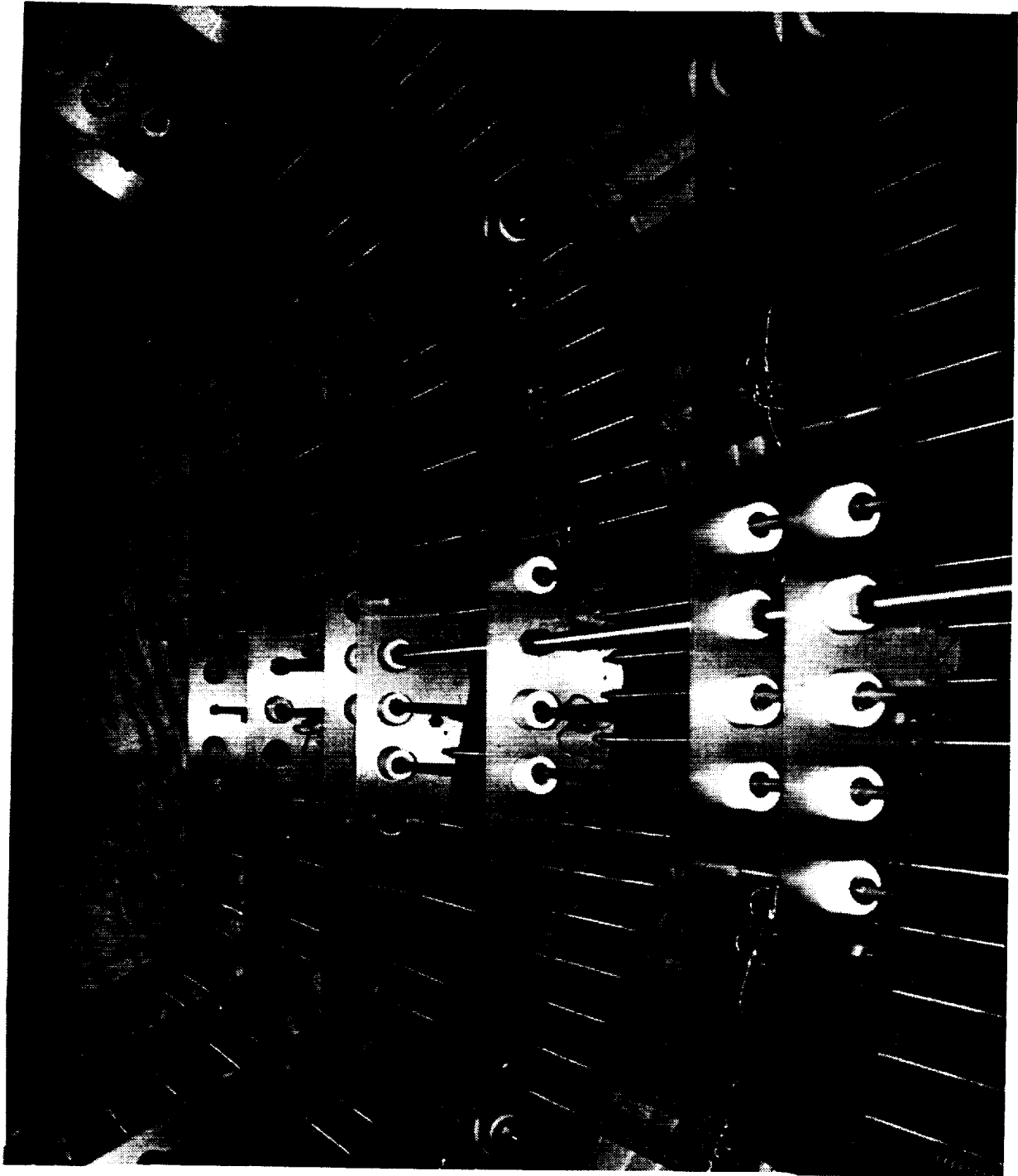


Figure 4-22: View of Quartz Lamp Zones E, D, and C (Left to Right) Inside the Receiver Cavity.

D180-32816-1

77

ORIGINAL PAGE
BLACK AND WHITE PHOTOGRAPH

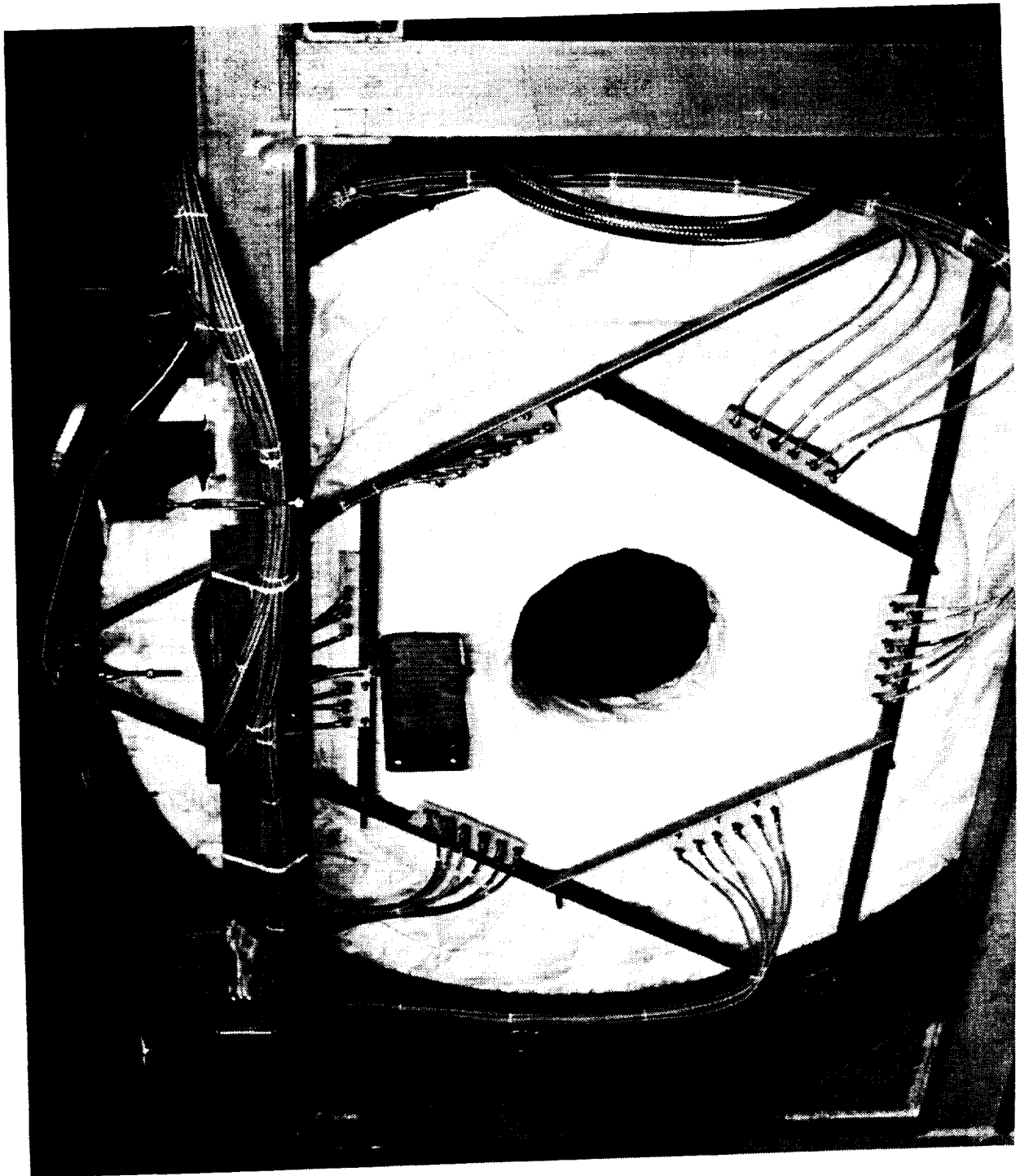


Figure 4-23: Final Configuration of the Heat Receiver Just Prior to the Installation of the Aperture Cold Plate.

D180-32816-1

RECEIVED FROM
BLACK AND WHITE PHOTOGRAPH



Figure 4-24: Attachment of #4 Electrical Cables to the Quartz Lamp Bus Rods.



Figure 4-25: Support of Electrical Cables and Chamber-Side Attachments to Vacuum Chamber Electrical Feed-Throughs.

5.0 TEST CONDUCT

ADRT testing was conducted continuously beginning on 24 October 1991 and lasting until 3 November. A total of 58 orbital cycles were conducted while completing the ADRT test matrix. A test notebook was kept at the test site for recording all test events. Significant events recorded in the test notebook have been compiled in a test log given in Appendix A of this report. The ADRT test log lists the date and times of all test anomalies, changes in test modes, and events that occurred during the test conduct period. The more significant events are described in the sections to follow along with data which show important trends and support the description of events. Other compilations of test information are also provided in Appendix A including summaries of: (1) all of the vacuum events that occurred during testing; (2) the dates, times, and events associated with the borescope pictures taken of the receiver cavity; and (3) the LN₂ consumption history during the test conduct period. Appendix B contains a description of the ADRT computer files by name, date, time, and significant events. Space limitations in this document do not allow hard copy plots to be supplied for all the test data but Appendix C contains selected test data plotted for the most stabilized test mode orbits.

Figure 3-7, given in Section 3.7.1, should be used to reference the location of the heat storage tubes that are described in the sections to follow. All tube numbers refer to cavity position, incrementing clockwise, and beginning with tube #1 located 7.5° from the top, center of the cavity as viewed from the aperture end of the receiver. Specific measurement numbers correspond the instrumentation list given in Section 3.7.

5.1 Test Readiness Review Meeting

The Test Readiness Review (TRR) meeting was conducted on 9 October 1990. The purpose of the TRR was to have a final review of the test procedures and inspection of the test facilities and hardware. The meeting was attended by Boeing representatives from the Engineering Test Laboratories (ETL), Safety, Facilities and Logistics, Fire and Security, and the ADRT Project. All remaining actions were closed at the meeting and the test procedures were approved.

5.2 Initial Attempts To Begin Testing

The first attempt to begin testing was initiated after completion of the TRR on 9 October 1990. However, during the initial pump down of the vacuum chamber, routine instrumentation and power checks showed an electrical short of several hundred ohms across several of the lamp zones to chamber ground. A vacuum leak was also discovered through the optical borescope. Test mode VT.1 was terminated to correct the problems.

The electrical shorts were traced to dielectric leakage through the o-rings sealing the electrical feed-throughs. The problem was probably due to some type of contamination on the o-ring surface and was corrected by replacing all of the o-rings. A high-voltage source was used to ensure that the electrical isolation capabilities of the o-rings would not break down during full-power operation.

The leak through the optical borescope was repaired by replacing a grafoil gasket with a Viton o-ring at the seal of the quartz lens on the front of the borescope. Viton o-rings are only rated to 149°C (about 56°C less than the grafoil seal) so the decision was made to reposition the end of the borescope just outside of the receiver cavity. This turned out to be a wise decision as temperatures measured at the end of the borescope exceeded 149°C (300°F) during full power operation and would have likely been higher if the borescope had extended fully into the receiver cavity.

A second attempt to begin test mode VT.1 was made on 12 October 1990. The vacuum chamber was evacuated to 1.6×10^{-6} torr and LN_2 flow was initiated through the cold plate. Initially the chamber vacuum dropped down to about 7×10^{-7} torr but the vacuum began to rapidly degrade to the point where the chamber diffusion pump had to be shut off. A helium leak check showed the leak to be at the seal of the LN_2 line feed-throughs to the vacuum chamber. Test mode VT.1 was again terminated to repair the leaks.

The leaks were repaired by replacing all of the fittings in the LN_2 lines with welded connections inside the vacuum chamber and by replacing an o-ring with a copper metal gasket seal at the LN_2 feed-through flange on the chamber wall. The repairs were completed and pump down of the vacuum chamber was begun on 22 October 1990. A brief check of the LN_2 system while the chamber was being evacuated showed the new LN_2 feed-through seals to function properly.

5.3 Steady-State Heat Balance Test, VT.1

The steady-state heat balance test, VT.1, provided (1) a slow and controlled heat up to allow insulation and other materials to off-gas while rising in temperature during the initial heat up of the receiver; (2) a condition for maintaining reasonably high receiver temperatures (below the melt temperature of the salt) without operation of the CBC engine simulator or the LN_2 cold shroud during periods of test inactivity; and (3) data for correlating measured receiver thermal losses with those predicted by the receiver thermal model (reference 2). This test mode was conducted under high-vacuum, with the aperture LN_2 cold plate operating but with no gas flow through the receiver and no LN_2 flow through the receiver cold shrouds. The quartz lamps were operated at very low voltage to reduce the risk of corona during high off-gassing periods. Test mode VT.1 was to be completed when the receiver cavity was maintained at a near isothermal temperature of $538^\circ\text{C} \pm 28^\circ\text{C}$ ($1000^\circ\text{F} \pm 50^\circ\text{F}$) with a chamber pressure of less than 5×10^{-5} torr and a maximum rate of change in any receiver temperatures of less than $3^\circ\text{C}/\text{hour}$.

Figure 5-1 shows cavity side-wall surface temperatures at the front (aperture end), middle, and back of the receiver cavity throughout test mode VT.1. This set of measurements were located 60° clockwise from the top of the receiver cavity as viewed from the aperture end and aligns between tube position #'s 4 and 5. Significant events for test mode VT.1 are described on the plot for reference. Figure 5-2 (a) shows the total quartz lamp heater power and (b) the chamber vacuum level during VT.1 for reference.

LN_2 flow to the aperture cold plate was initiated on 24 October with the vacuum chamber pressure at 6×10^{-6} torr. The chamber quickly dropped in pressure to about 6×10^{-7} torr. Lamp power was then slowly increased to about 4 kW to ensure chamber vacuum pressure remained below 5×10^{-4} as required by the test procedures (reference 3). Receiver temperatures began to slowly increase without much effect on chamber vacuum level allowing the heater power to be gradually increased to about 15 kW to reduce the time to achieve the required 538°C cavity temperature. Vacuum level rose only slightly.

The initial 25 hours of heater operation showed that the rate of LN_2 consumption required to operate the aperture cold plate was much higher rate than originally planned for and the supply tank was nearly empty. The high LN_2 consumption rate was caused by inefficiencies of the LN_2 subcooler hardware (the LN_2 subcooler is designed for operation with a much higher heat load). Attempts to arrange an early delivery of LN_2 from the supplier were unsuccessful so it was likely that the heaters would have to be shut down for 8 to 10 hours.

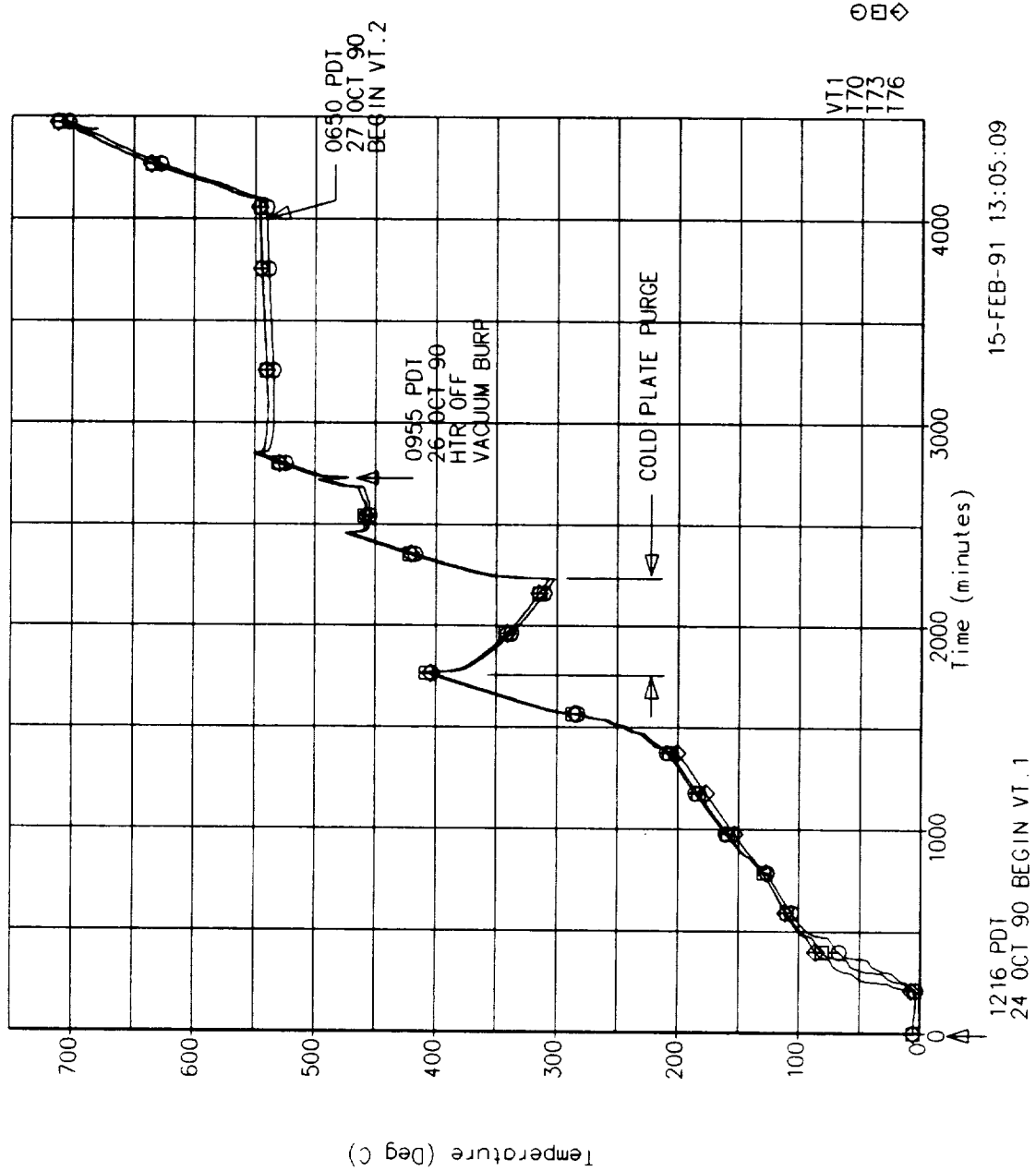


Figure 5-1: Cavity Side-Wall Surface Temperatures at the Front (Aperture End), Middle, and Back of the Receiver Cavity During VT.1.

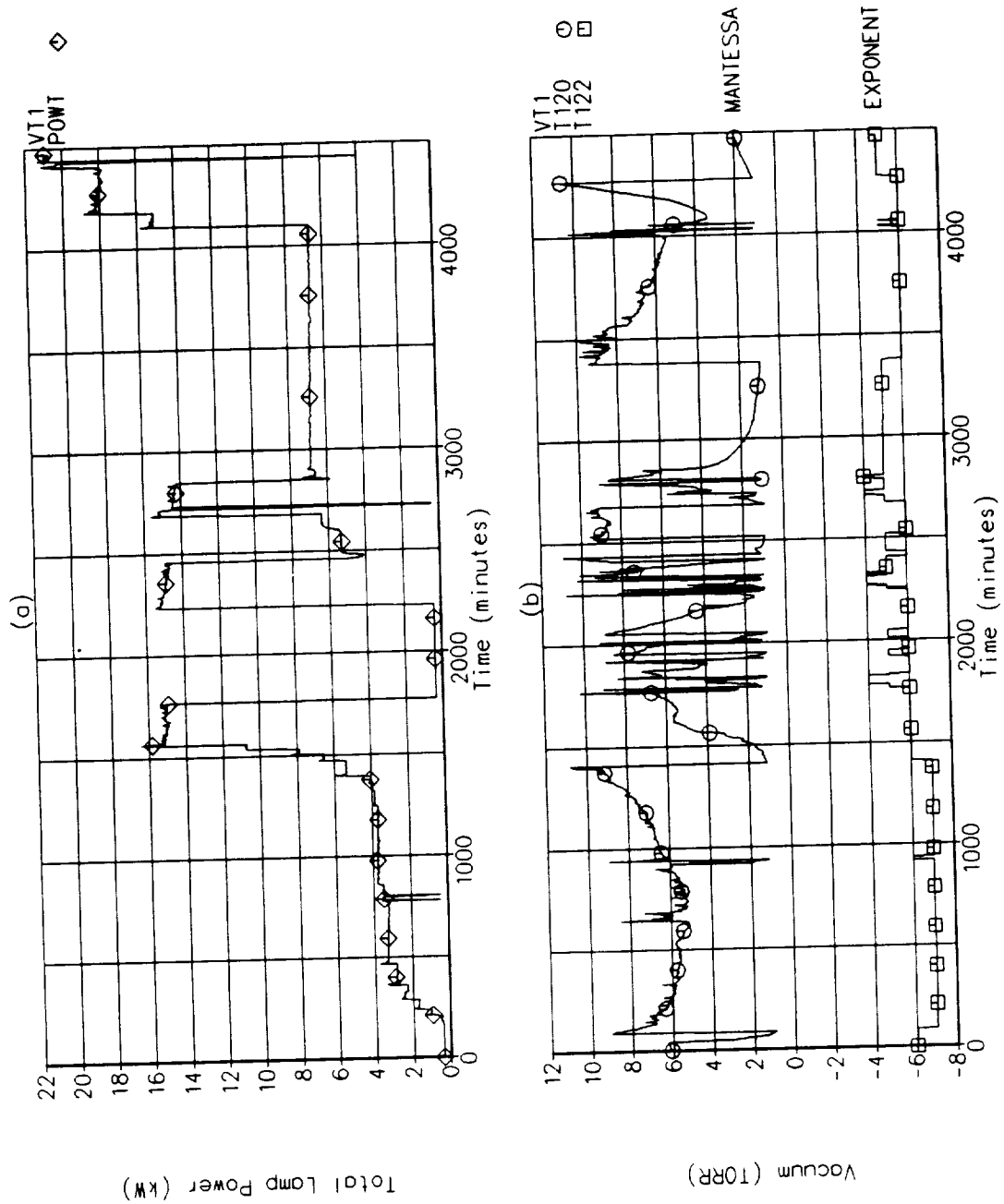


Figure 5-2: (a) Total Quartz Lamp Heater Power During VT.1; and (b) Chamber Vacuum Level During VT.1.

The cold plate purge operation, required by the ADRT test procedures (reference 3), was conducted to make the most efficient use the heater down-time and preserve the test matrix. During the cold plate purge operation, electrical power to the quartz lamp heater and LN₂ flow to the cold plate were shut off to allow the cold plate to heat up and drive off contaminants that had collected on its surface. The contaminants were then (theoretically) removed from the chamber by the vacuum pumps. When the LN₂ flow to the cold plate was shut off, its temperature quickly rose to about 94°C (200°F) and chamber vacuum rose to about 4×10^{-4} torr. LN₂ flow was quickly reestablished through the cold plate using a portable LN₂ tank brought to the site for this contingency. The LN₂ flow rate was much lower than that supplied by the subcooler and cold plate temperatures were not as low as during normal operation but were sufficient to prevent any further degradation in chamber vacuum. Cold plate temperatures quickly dropped back down to about -88°C (-120°F) and chamber vacuum was maintained at around 4×10^{-6} torr until the LN₂ delivery was made approximately 8 hours later. Full LN₂ cold plate flow was then reestablished through the subcooler and the lamps were repowered to continue the heat up to 538°C.

Several minor vacuum off-gassing events occurred during VT.1 where the chamber pressure would rapidly rise but would quickly drop back to original levels over a period of several minutes. No other significant events occurred during the conduct of VT.1. The total time to achieve a near 538°C isothermal condition after activating the heater zones was about 43 hours and approximately 6.8 kW of electrical power was required to maintain this temperature in the cavity.

Figure 5-3 (a) shows the exterior side-wall surface temperatures parallel to heat storage tube #4 and (b) parallel to heat storage tube #12, at the front and back ends of the receiver throughout test mode VT.1. It is apparent that true thermal equilibrium had not been achieved at the end of VT.1 because these temperatures had not yet stabilized and the rates of change of exterior temperatures were greater than the 3°C/hr termination requirement. The decision to terminate test mode VT.1 and continue on to test mode VT.2 was based upon the need to preserve test funding for the thermal cycling test modes. It is doubtful that a significant change in cavity temperatures would have occurred if the test mode was allowed to continue to complete thermal equilibrium because the rate of temperature change in the cavity was very small as seen in Figure 5-1.

Attempts to view the receiver cavity through the optical borescope during VT.1 were unsuccessful. The illumination of the lamps was not sufficient to produce an image and no photographs were recorded.

5.4 Steady-State Heat Balance Test, VT.2

The steady-state heat balance test mode, VT.2, continued the controlled heat up of the receiver cavity from 538°C (1000°F) to 871°C (1600°F) without operating the CBC engine simulator. At 871°C, all of the salt in the heat storage tubes is molten providing a known distribution of the salt prior to the initiation of thermal cycling. This was considered an important step considering that the exact distribution of the salt in the annulus after the salt fill operations was not known with certainty. The VT.2 test mode also provides another set of high-temperature data to correlate with the losses predicted by the receiver thermal model.

Test mode VT.2 was initiated on 27 October by establishing LN₂ flow through the receiver cold shrouds (the drop in the exterior surface temperatures of the receiver can be seen in Figure 5-3). Heater power was then increased to about 18 kW. Figure 5-4 shows cavity side-wall surface temperatures located at 60° and axially at the front, middle, and back end of the cavity. Test log events are noted on the plot for reference. The total quartz lamp heater power history

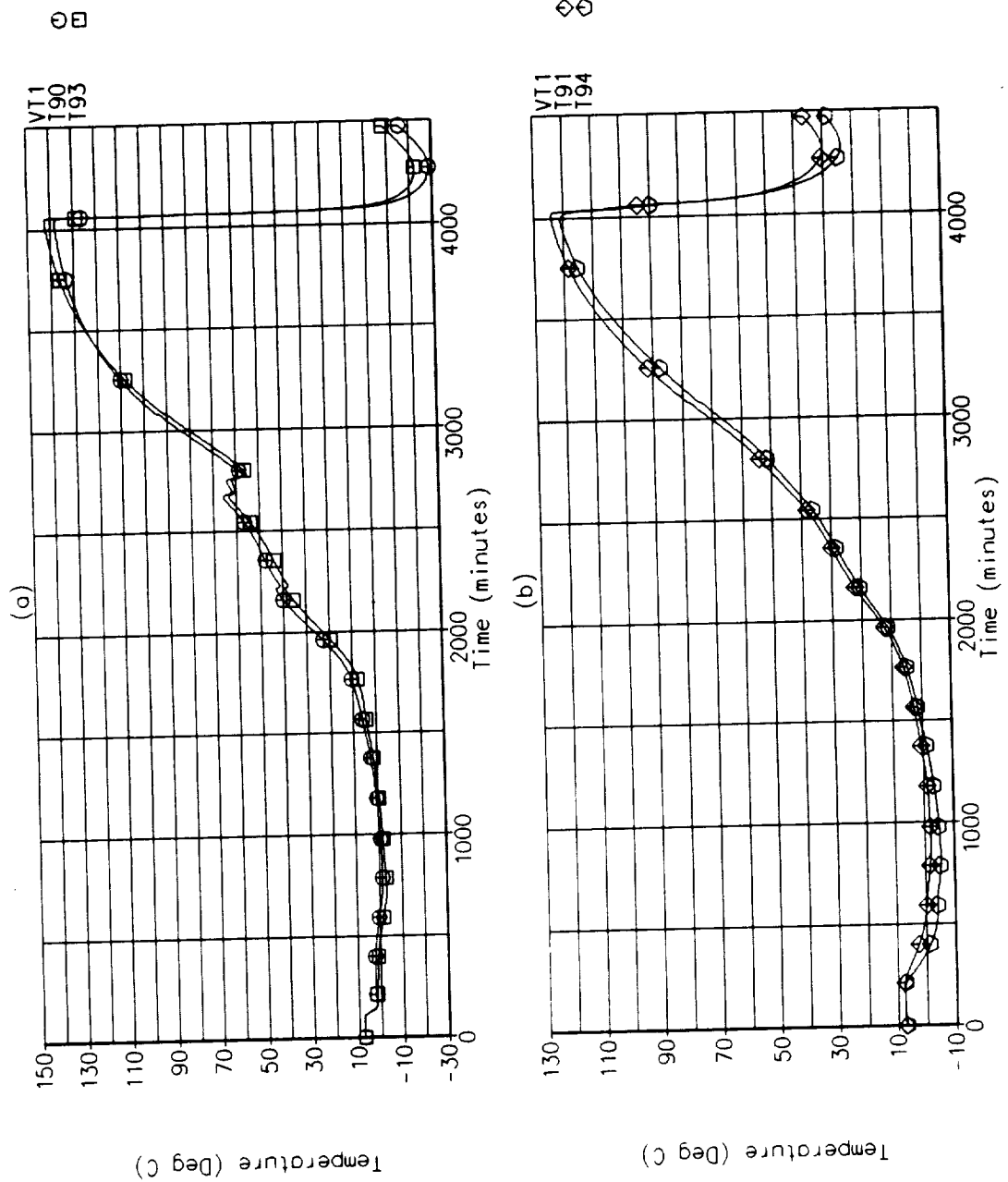
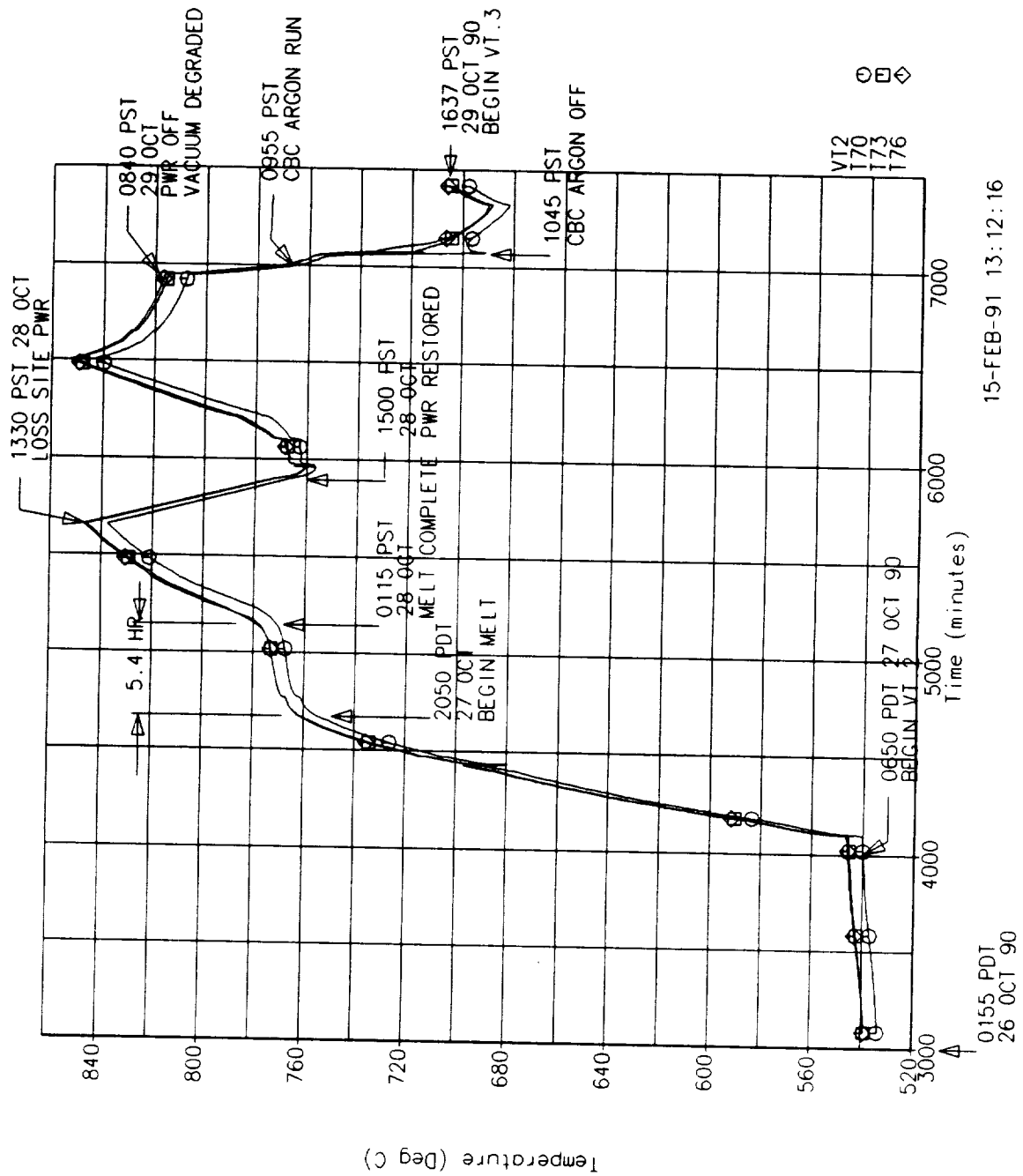


Figure 5-3: (a) Exterior Side-Wall Surface Temperatures Parallel to Heat Storage Tube #4 During VT.1; and (b) Exterior Side-Wall Surface Temperatures Parallel to Heat Storage Tube #12 During VT.1.



15-FEB-91 13:12:16

Figure 5-4: Cavity Side-Wall Surface Temperatures Located At 60° at the Front, Middle, and Back End of the Receiver Cavity During VT.2.

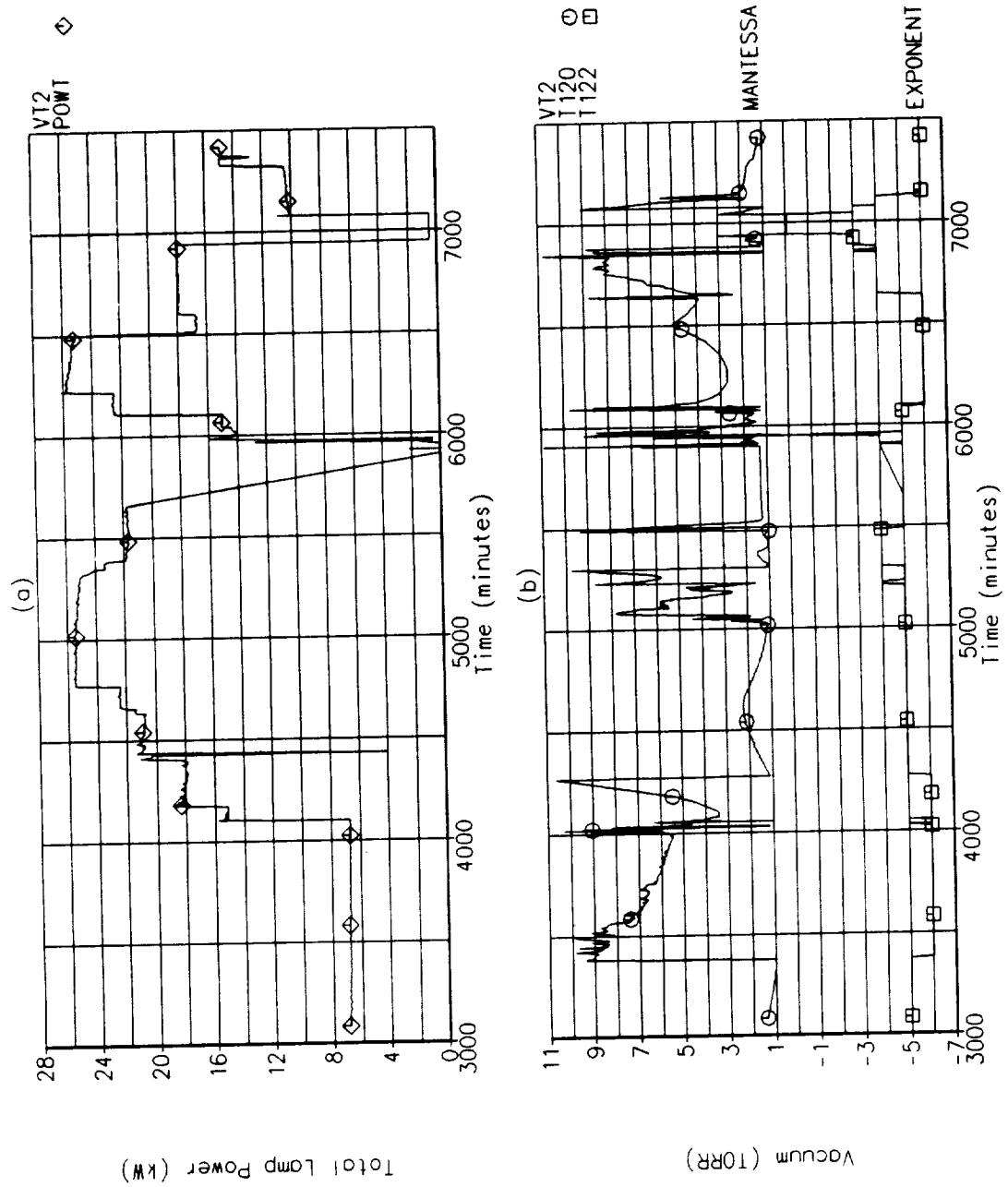


Figure 5-5: (a) Total Quartz Lamp Heater Power During VT.2; and (b) Chamber Vacuum Level During VT.2.

for test mode VT.2 is shown in Figure 5-5 (a). The initial heat up period to the salt melt temperature, through thermal arrest, and up to a cavity temperature of about 838°C (1540°F) occurred without any significant anomalies. During thermal arrest, the heater zones were powered at 25.8 kW to achieve a complete melt of the salt in about 6 hours. Figure 5-4 shows the actual thermal arrest period was about 5.4 hours, reasonably close to predictions considering an extrapolated heat loss was used in the calculations.

During the heating to the salt melt temperature, images could finally be seen through the optical borescope. At first, the image was slightly blurred by off-gassing materials that collected on its cooled surface. However, as the temperature in the cavity rose, the image began to clear. Figure 5-6 shows the first clear image recorded by photograph through the borescope. This photograph was taken just prior to beginning thermal arrest and is one of the clearest image viewed during the entire test period. Unfortunately, very little of the heat storage tubes can be seen in the field of view, primarily because of blockage by the heater bus plates. The blockage was much worse than originally planned because the end of the borescope was moved outside the cavity (see Section 5.2). However, the borescope still had significant value and was utilized throughout the test to confirm proper heater operation and to watch for catastrophic failures inside the receiver cavity. Furthermore, the changes in image clarity help to explain some of the anomalies which occurred throughout the test matrix.

Chamber vacuum is shown for the entire VT.2 test period in Figure 5-5 (b). Three long-term material out-gassing events occurred during the test conduct, the first of which began at about 17 hours into the VT.2 conduct period. This event lasted approximately 7 hours and the pressure rose to about 1.5×10^{-4} torr and stabilized at about 1.2×10^{-5} torr after the event had ended. Lamp power was maintained during the event because the chamber vacuum never rose above 5×10^{-4} torr (ADRT requirement). The source of the out-gassing is not known.

The first significant unplanned event occurred after reaching 844°C (1550°F) in the cavity. A power surge caused two fuses to open in one of the three main power distribution boxes. The cause of the power surge was never determined but is attributed to a large storm that was in progress during this period of time. Fortunately, the circuit that powered the vacuum chamber was not interrupted and all of the vacuum chamber pumps continued to operate (if these had failed, it probably would have terminated the testing). Electrical power was lost to the LN₂ subcooler, quartz lamp heaters, and the instrumentation trailer and DACS.

The loss of LN₂ flow to the cold shrouds and cold plate during the first few minutes of the power loss caused several problems. The most obvious was that the rapid increase in the cold plate surface temperature caused tape adhesive that held 2 thermocouples onto the cold plate surface to de-bond and fall off. In addition, materials that had collected onto the cold plate and cold shroud surfaces began to rapidly boil off causing chamber vacuum to degrade to the 10^{-3} torr range. Some of these off-gassing materials collected and baked onto the cooled borescope lens which caused optical distortions of viewed images throughout the remainder of the testing. After about 5 minutes, LN₂ was introduced into the lines directly from the supply tank at a low flow rate to prevent further vacuum degradation.

Repair of the electrical power distribution box required about 1.5 hours during which, an estimated 190 lbs or 26 percent of the salt contained in the heat storage tubes may have solidified because of the cavity heat losses. The heater zones were then powered to about 22 kW to slowly remelt the salt. The effect of the off-gassing event associated with the loss of LN₂ to the cold plate and shrouds is visible in the blurred and distorted borescope image shown in Figure 5-7 which was taken after repowering of the heater zones.

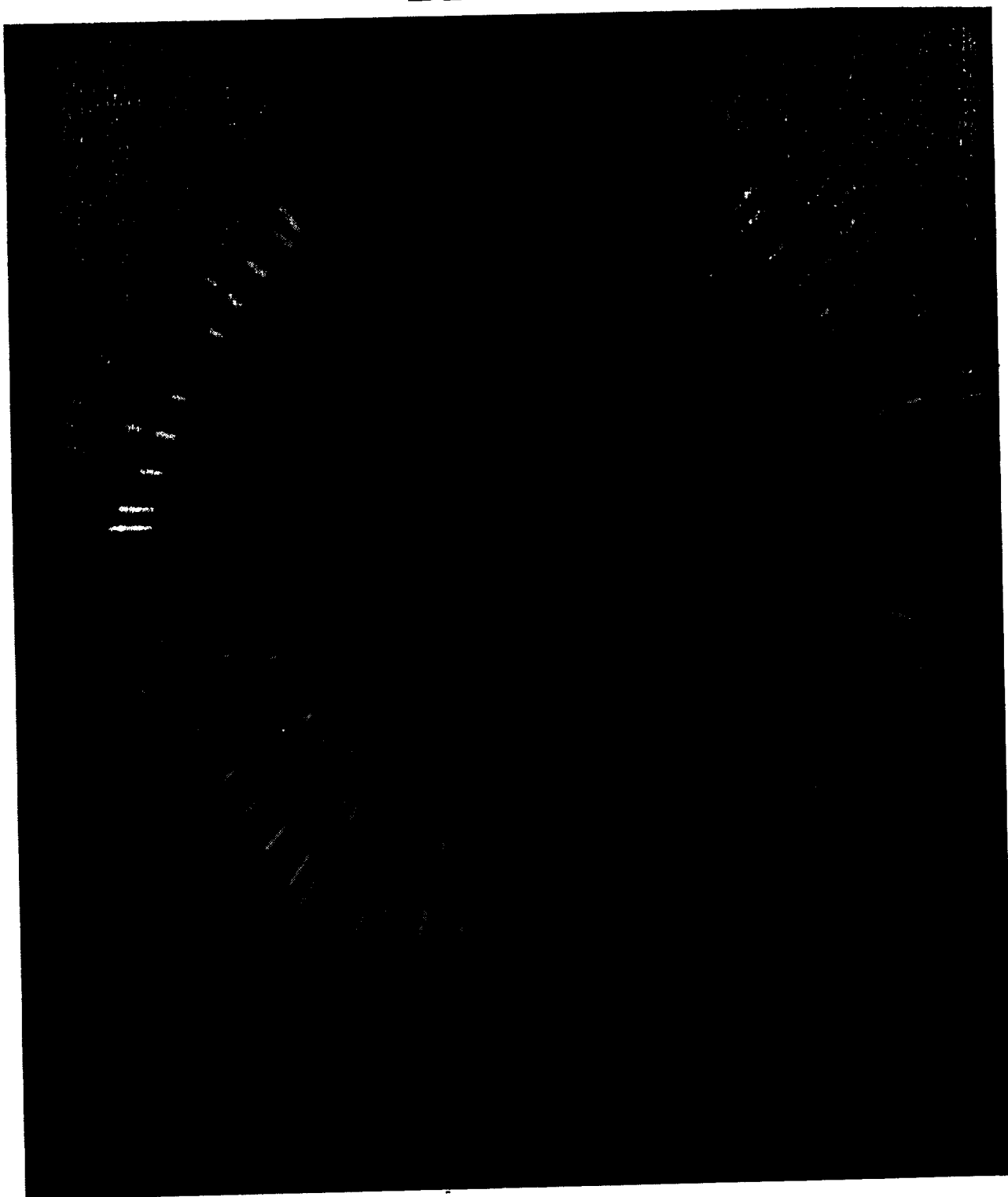


Figure 5-6: Boroscope Photograph of the Receiver Cavity Just Prior to Thermal Arrest During VT.2.

BOEING

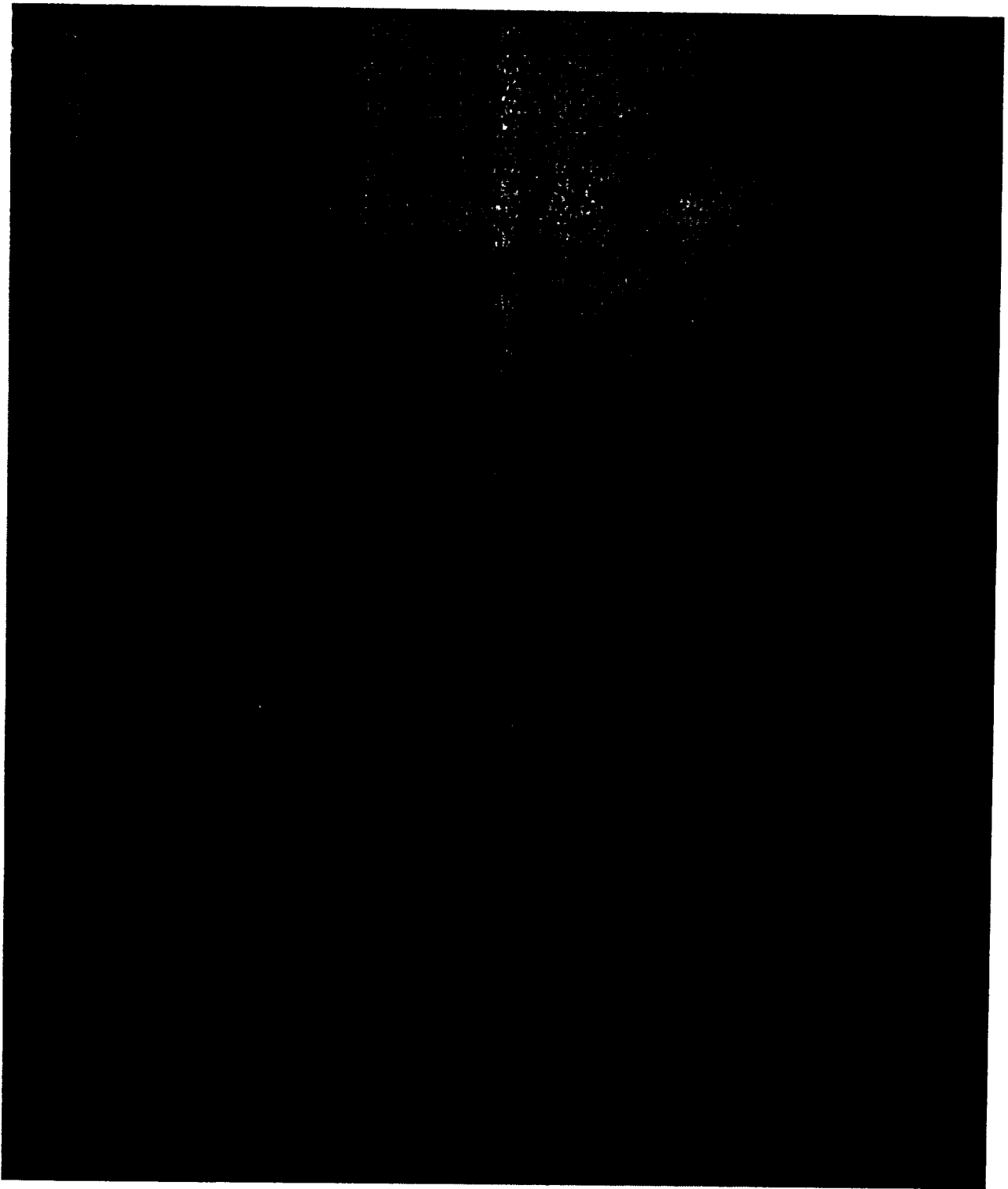


Figure 5-7: Blurred Image Through Borescope After Loss of Site Electrical Power.

D180-32816-1

91

ORIGINAL PAGE
BLACK AND WHITE PHOTOGRAPH

Heater power was increased to about 26 kw after thermal arrest was completed and maintained at this level to heat the receiver cavity up to the required 871°C (1600°F) temperature. However, a second major vacuum off-gassing event required a manual shutdown of the heaters. At the beginning of the event, chamber pressure was 4×10^{-6} torr. The event lasted for about 7 hours and chamber pressure rose to the 10^{-2} torr level. When this occurred, the decision was made to charge the CBC simulator with argon gas and discharge the TES tubes to prevent the salt from solidifying from their outside surfaces inward. The CBC simulator was operated for about 50 minutes until the tube temperatures had all dropped to about 677°C (1250°F). Heater power was then resumed at a low level to prevent any further decay of cavity temperatures. It is worth noting that during this event, decreasing cavity temperatures had little or no effect on the chamber vacuum level suggesting that the off-gassing was caused by material released from the outside of the receiver cavity. After about 7 hours, the chamber vacuum level began to drop rapidly ending the second major off-gassing event. Chamber vacuum stabilized at about 2×10^{-6} torr.

The delay caused by the excessive off-gassing event caused a reassessment of test priorities. If test mode VT.2 were continued to the required termination conditions, it would jeopardize the completion of the full-power thermal cycling test modes. To complicate matters further, a storm was forecast for the region with potential winds as high as 60 MPH. It was feared that the site electrical power could be completely lost shutting down the vacuum system and potentially damaging the test hardware in the chamber. However, if the testing was temporarily shutdown to ambient, insufficient funding was available to repeat test modes VT.1 and VT.2 and complete the remainder of the test matrix.

It was decided to preserve the ADRT test matrix by initiating the baseline orbit cycling with test mode VT.3 instead of either shutting down to ambient or continuing with test mode VT.2. This was made possible by the previous operation of the CBC to solidify the salt inside the heat storage tubes to a working distribution. Heater power was set at about 15 kW to slowly heat the cavity while preparations were made to begin full-power cyclic operation. Test mode VT.2 was declared completed at 16:37 PST on 29 October after a total of about 125 hours of elevated temperature exposure. The best estimate of receiver losses during VT.2 occurred during the period between 6,651 minutes to 6,942 minutes with cavity temperatures nearing a stabilized temperature of about 810°C (1490°F). The total heater power input during this period was 12.8 kW.

5.5 Initial Baseline Orbit, VT.3

The SDHRT heat receiver was designed to deliver 102 kW of continuous thermal power to a mixture of helium xenon gas (molecular weight of 40) with 198 kW of solar power input to the cavity for 58 minutes of a 94 minute orbit. The gas mixture enters the receiver at a temperature of $482^{\circ}\text{C} \pm 3^{\circ}\text{C}$ ($900^{\circ}\text{F} \pm 5^{\circ}\text{F}$), a pressure of 634 ± 14 kPa (92 ± 2 psia), and with a mass flow rate of 53 ± 0.9 kg/min (117 ± 2 lbm/min). Test mode VT.3 establishes the nominal design operating envelope of the receiver and was repeated several times during the test matrix to quantify changes in the receiver that might be attributed to material property changes and/or hardware failures.

The distribution of electrical power input to the 30 quartz lamp heater zones was determined from previous analyses that matched the predicted rates that energy was absorbed by each heat storage tube when (1) operating in space with an on-axis, parabolic concentrator (reference 4) and (2) when operating with the quartz lamp, infrared heater inside the cavity. Because the absorbed energy profiles are matched, differences between radiation wavelength, thermal radiative properties of the materials, and blockage by the heater structure inside the cavity are

minimized. The baseline distribution assumes circumferential symmetry. A digital controller was programmed to power the quartz lamp heater for a duty cycle of 58 minute on and 36 minute off. The electrical power supplied to the heater zones was ramped by the SCR controllers to full power over a period of about 9 seconds to improved lamp life.

It was originally planned to begin VT.3 at the end of VT.2 with the salt in the tubes fully melted at 871°C (1600°F). The tubes would then be discharged by initiating the operation of the CBC simulator in a 36 minute eclipse period. However, for the reasons described in Section 5.4, the cavity was at a temperature of about 705°C (1300°F) and the heat storage tubes were fully discharged requiring VT.3 to be initiated with full-power, sunlit operation.

Test mode VT.3 was begun on 29 October at 17:25 PST. The CBC engine simulator was initially charged with 343 kPa (35 psig) of premixed, bottled, helium-xenon gas and the blower was activated. The flow by-pass valve (see Figure 3-3) was fully opened and the regenerator by-pass valves were on manual control and opened up about 50 percent. The heater duty cycle control computer was activated and the electrical power to the 30 heater zones was ramped to full power, 1 zone at a time. The borescope photograph given in Figure 5-8 shows the heater zones being powered from the back of the cavity forward (lowest to highest power). Figure 5-9 shows the quartz lamp array after reaching full power. The aberrations in the straightness of the lamps is caused by the refraction of light through off-gassing materials that collected on the quartz lens (the lamps were found to be perfectly straight after testing was completed). The contamination materials can be seen in Figure 5-10, which focused on the front lens rather than on the inside of the cavity. The contamination pattern seen on the lens became visible after the loss of electrical power event described in Section 5.4 and it never disappeared throughout the remainder of the testing.

Figure 5-11 shows the flux-facing surface temperature located in the convolution valley at the inlet end of heat storage tube #4. Significant events and orbit numbers are noted on the figure for the entire VT.3 test period. This measurement is used throughout this section to describe test mode events because (1) it is believed to be more accurate than surface temperature measurements made on the convolution peaks (more contact area with the tube) and (2) it is in the highest flux, highest-temperature region of the heat storage tube. The data for this thermocouple show a rapid rise in tube wall temperature at the beginning of the sunlit periods followed by a rapid drop to a lower temperature level. This type of behavior was seen during subscale canister tests (reference 4) is believed to be caused by a lack of salt in contact with the tube wall at the initiation of sun that requires a high surface temperature to transfer the energy by radiation to the salt and felt metal. This is then quickly followed by a drop in wall temperature as the salt melts, expands, and comes in contact with the tube wall. This trend is observed in almost all of the remaining test modes. Figure 5-12 (a) shows the total quartz lamp heater power and (b) the chamber vacuum level during the VT.3 test mode sequence. The total power to the quartz lamp heater was lowered from the required 198 kW to about 193 kW because tube surface temperatures appeared to be too high. However, experience showed later that the surface temperatures facing the heater were not effectively coupled to the heat storage tube and had significant error induced by the high-flux environment. The total power in later test modes was increased to the required 198 kW.

A number of site electrical problems occurred during the initial orbit of VT.3. After about 20 minutes into the first sunlit period, fuses in one of the site electrical power distribution panels opened and power was lost to the LN₂ subcooler, CBC engine simulator, and instrumentation trailer including the DACS. The site was fully manned at the initiation of full power operation so that lamp power was quickly shut off manually and LN₂ flow was reestablished through the supply lines while the fuses were replaced. Repairs only required a couple of minutes so start

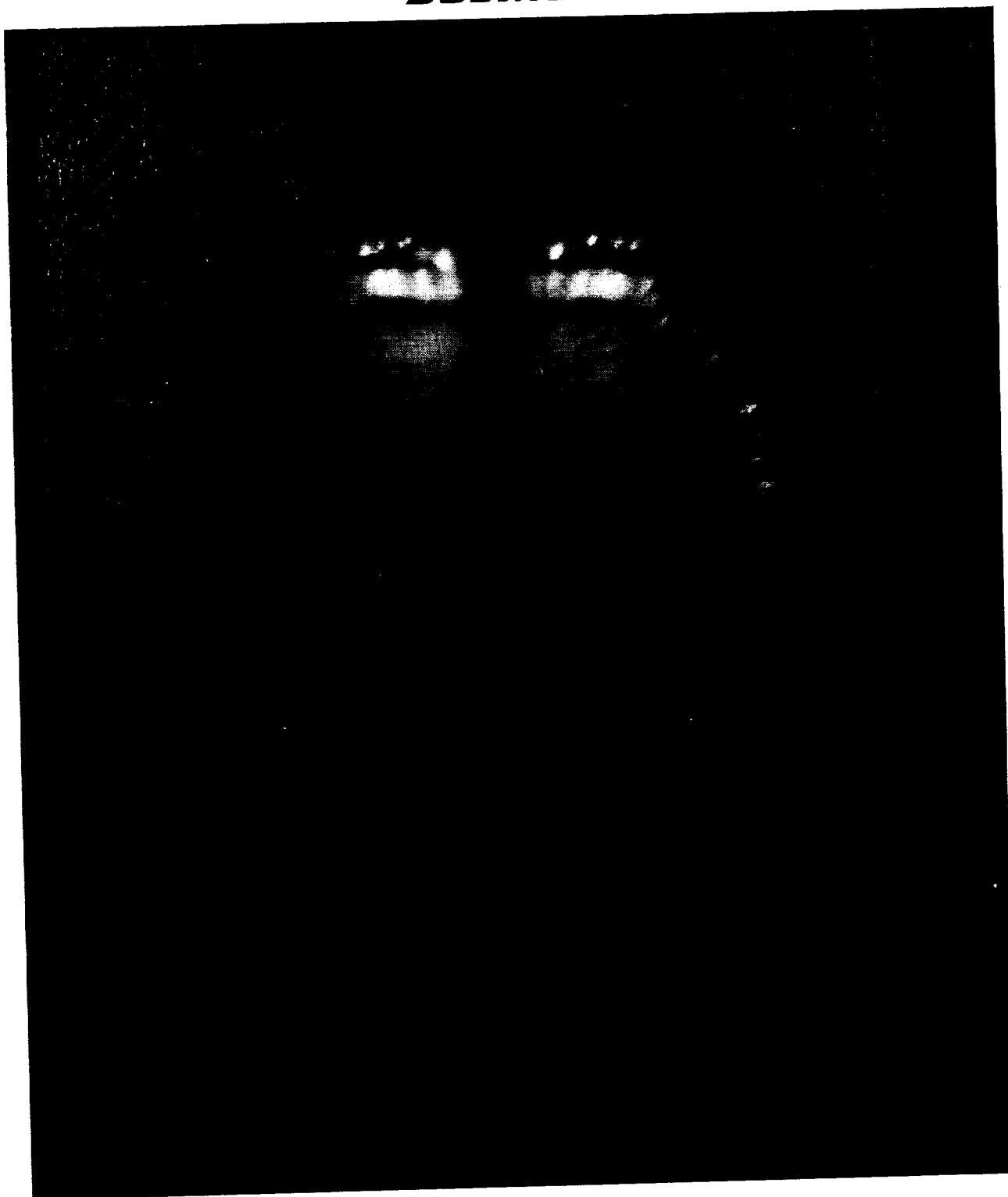


Figure 5-8: Initial Power Up of the Quartz Lamp Heater Zones During VT.3 As Viewed Through the Borescope.

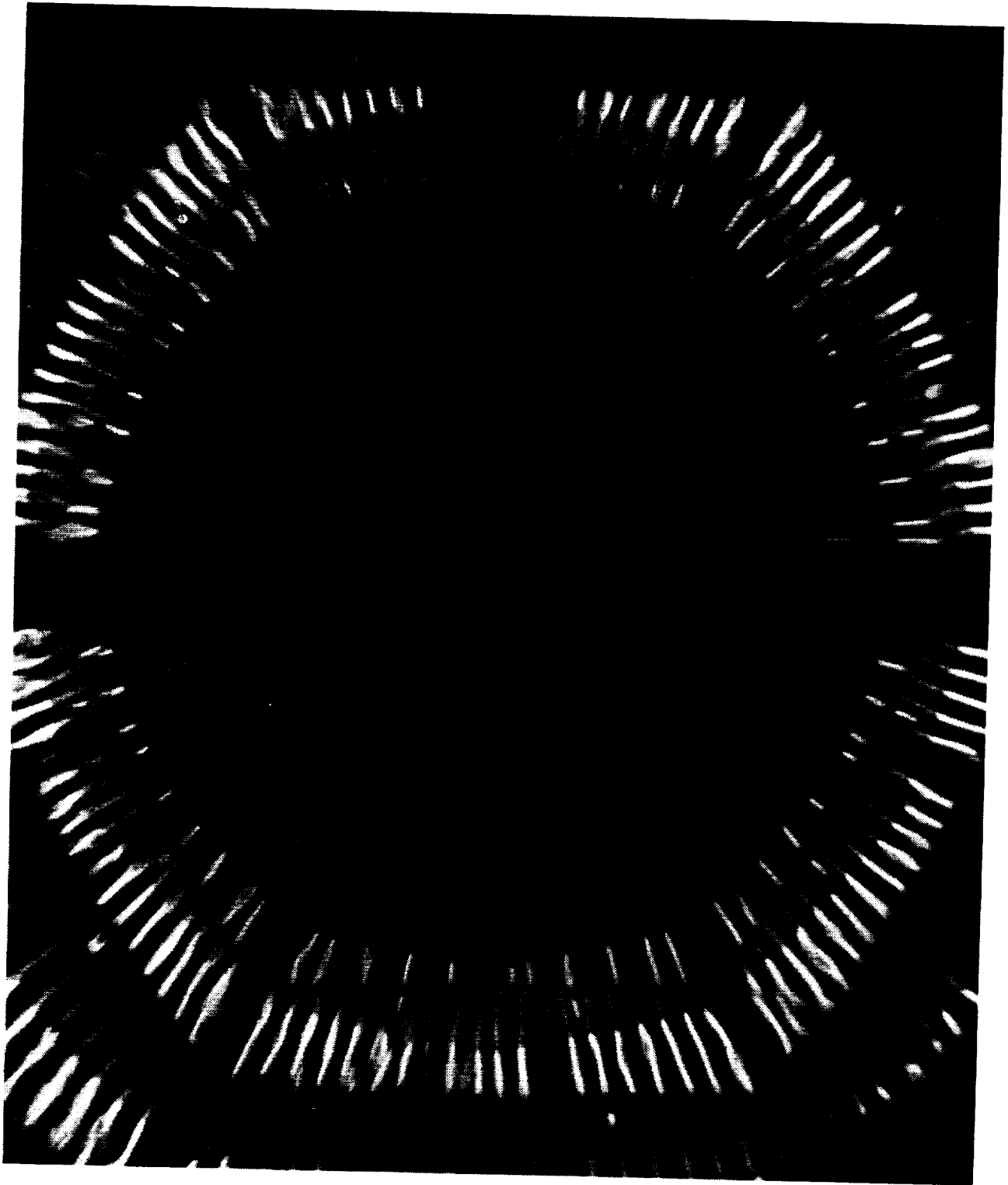


Figure 5-9: Full Power Operation of the Quartz Lamp Heater During Orbit #1 of VT.3.

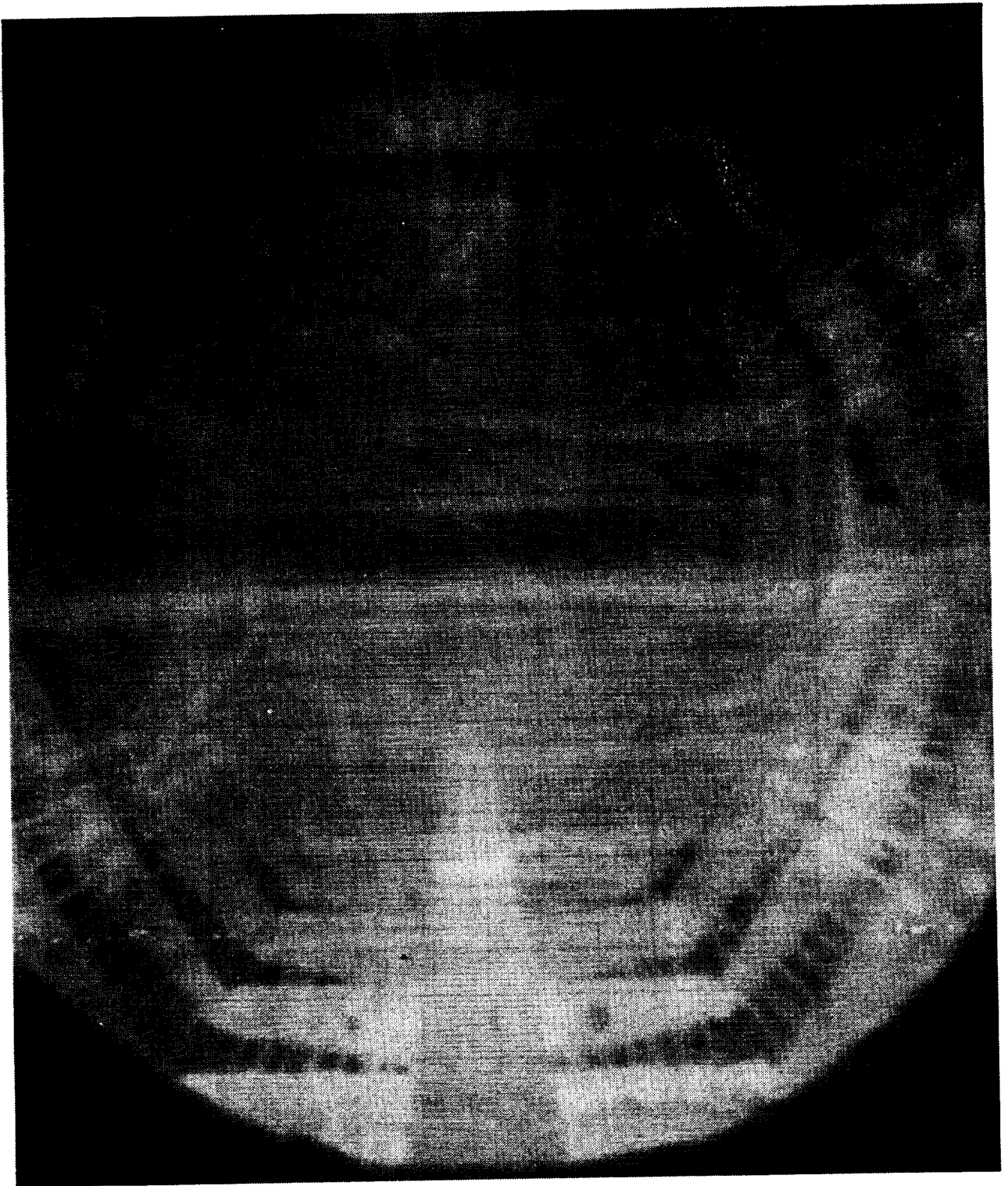


Figure 5-10: Lens Contamination Image Obtained By Focusing on the Front Lens of Bore-scope.

ORIGINAL PAGE
BLACK AND WHITE PHOTOGRAPH

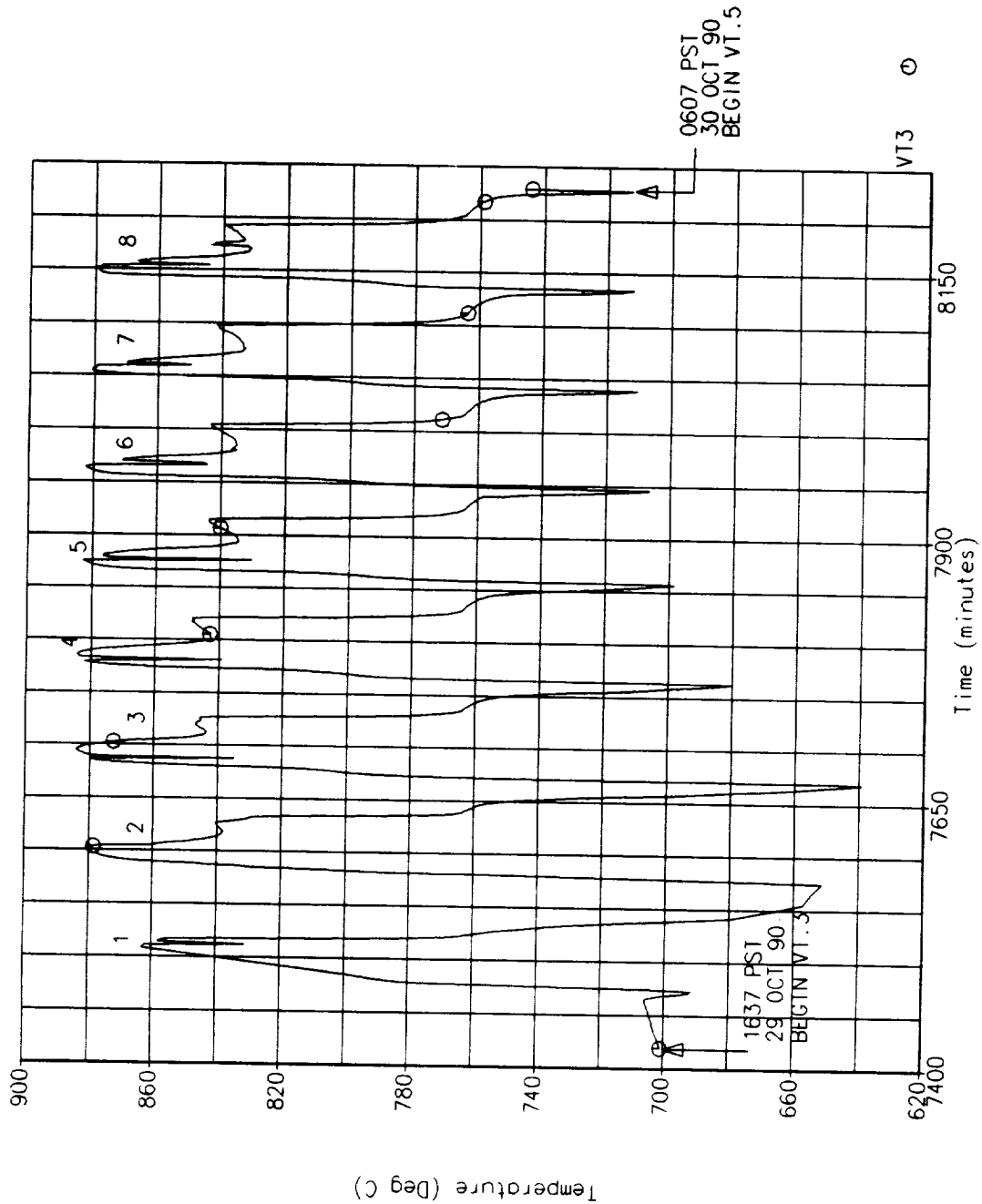


Figure 5-11: Flux-Facing Surface Temperature Located in the Convolution Valley at the Inlet End of Heat Storage Tube #4 During VT.3.

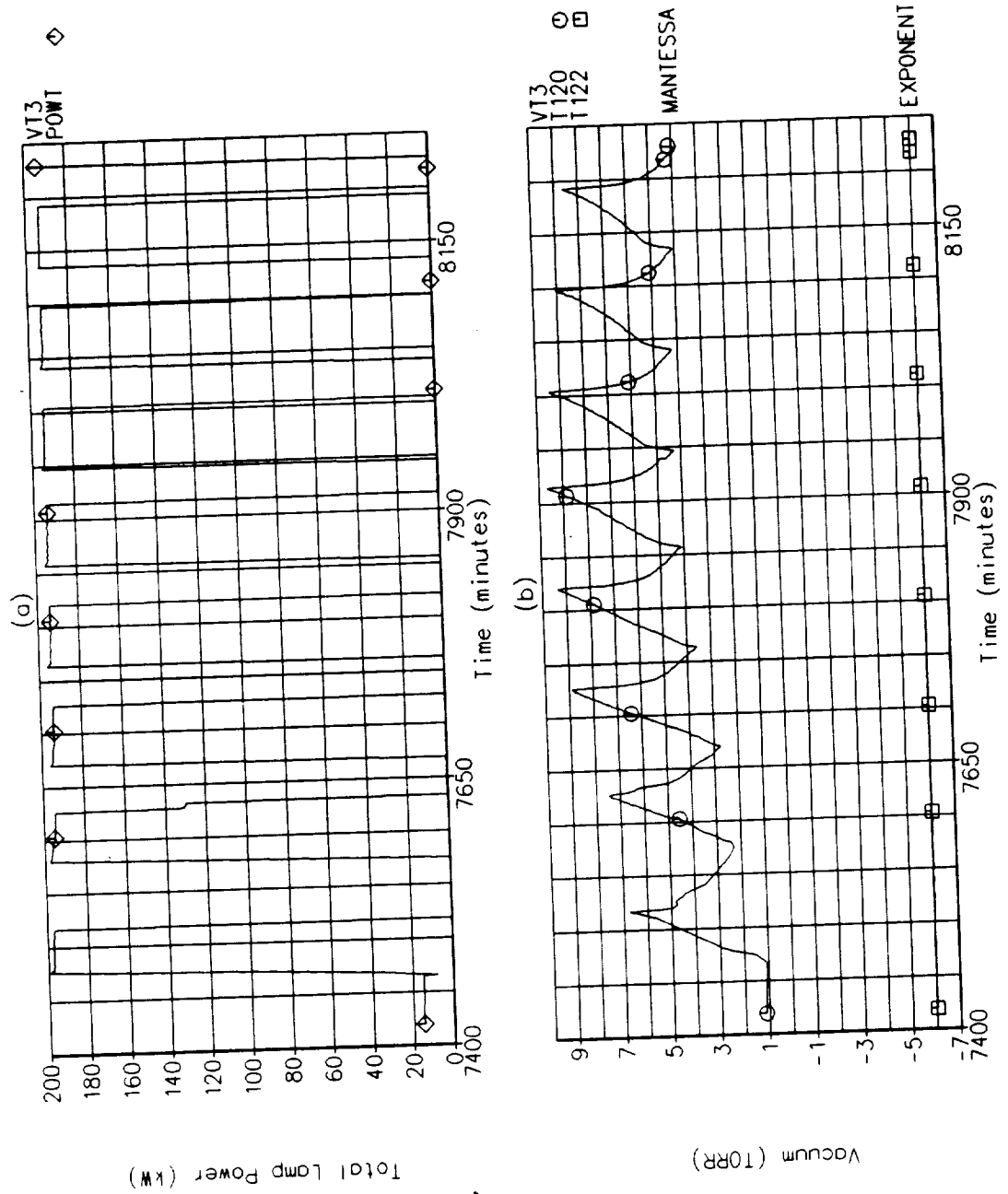


Figure 5-12: (a) Total Quartz Lamp Heater Power During VT.3; and (b) Chamber Vacuum Level During VT.3.

up of the LN_2 subcooler only required repowering the pump (if the lines heat up, a 20 minute procedure is required to establish LN_2 flow through the subcooler). The temporary loss of electrical power did not cause any significant problems but it was decided to move the CBC engine simulator power line to another circuit during the next eclipse period to more evenly distribute the site power consumption. The eclipse period of orbit #1 was begun 8 minutes early to facilitate the change. After 23 minutes of eclipse operation (to fully discharge the heat storage tubes), the CBC engine simulator was shut off to complete the maintenance which required about 30 minutes to complete. Power was then restored to all equipment and the sunlit period of orbit #2 was begun. Another momentary power loss occurred after 24 minutes of heater operation into the 2nd orbit which was caused by an unseated power plug. Power was only lost to the DACS and it was restored to operation within several minutes.

The electrical power to heater zones E and F was lost during the last few minutes of the 2nd orbit. The problem was caused by a temperature-sensitive circuit breaker on the large power transformer that supplied the SCR's for those zones. Figure 5-13 shows a photograph of the cavity while these 2 zones were off and illustrates the usefulness of the borescope to confirm proper heater operation.

Additional helium-xenon gas was introduced into the CBC piping at several times to slowly increase the inlet static pressure. Figure 5-14 (a) shows the receiver inlet static pressure and (b) the receiver flow rate during VT.3 and shows that required flow rate and static pressure were achieved by the 5th orbit.

The internal salt temperatures appear to be the most effective measurement for judging if temperature stabilization has been achieved although the exiting gas temperature was used in specifying the initial stabilization criterion (reference 3). Figure 5-15 shows the internal salt temperature closest to the heat exchanger tube (a) located at the flux-facing side of tube #12 at the inlet and exit end of the tube and (b) located on the top side of tube #19 at the inlet and exit ends of the tube. These data show internal salt temperatures are reasonably steady by the 8th orbit although another VT.3 orbit would have given a better comparison. The inlet and exiting gas temperatures are shown in Figure 5-16 and also show that reasonably steady conditions were achieved by the 8th orbit. The CBC simulator was very effective at controlling the inlet temperature to the required $482^\circ\text{C} \pm 3^\circ\text{C}$ ($900^\circ\text{F} \pm 5^\circ\text{F}$) requirement. Test mode VT.3 was completed at the end of the 8th orbit.

5.6 Gas Flow Rate Variation Test, VT.5

The solar dynamic power module will adjust for the seasonal and optical property induced variations in the solar power input to the heat receiver by varying the helium-xenon gas flow rate and receiver inlet gas temperature. The gas flow rate variation test was performed to quantify the effect of increasing gas flow rate on the thermal performance and operating temperatures of the heat receiver. Test mode VT.5 was also the first of 2 gradual transitions to begin the simulation of a maximum insolation, perihelion orbit by changing only one variable at a time.

All receiver interface parameters except for gas flow rate were the same as those used in VT.3. Test mode VT.5 was initiated at the beginning of orbit #9 on 30 October by increasing the gas flow rate from 53 kg/min to 75 ± 0.9 kg/min (165 ± 2 lbm/min). Figure 5-17 shows the flux-facing surface temperature located in the convection valley at the inlet end of heat storage tube #4. Significant events and orbit numbers are noted on the figure for the entire VT.5 test period. Notice that the surface temperature behavior is different from the previous (and all remaining) test modes in that there is no rapid change during the heating cycle. This is attributed to a significant decrease in the quantity of salt melt that occurs because of the increased heat

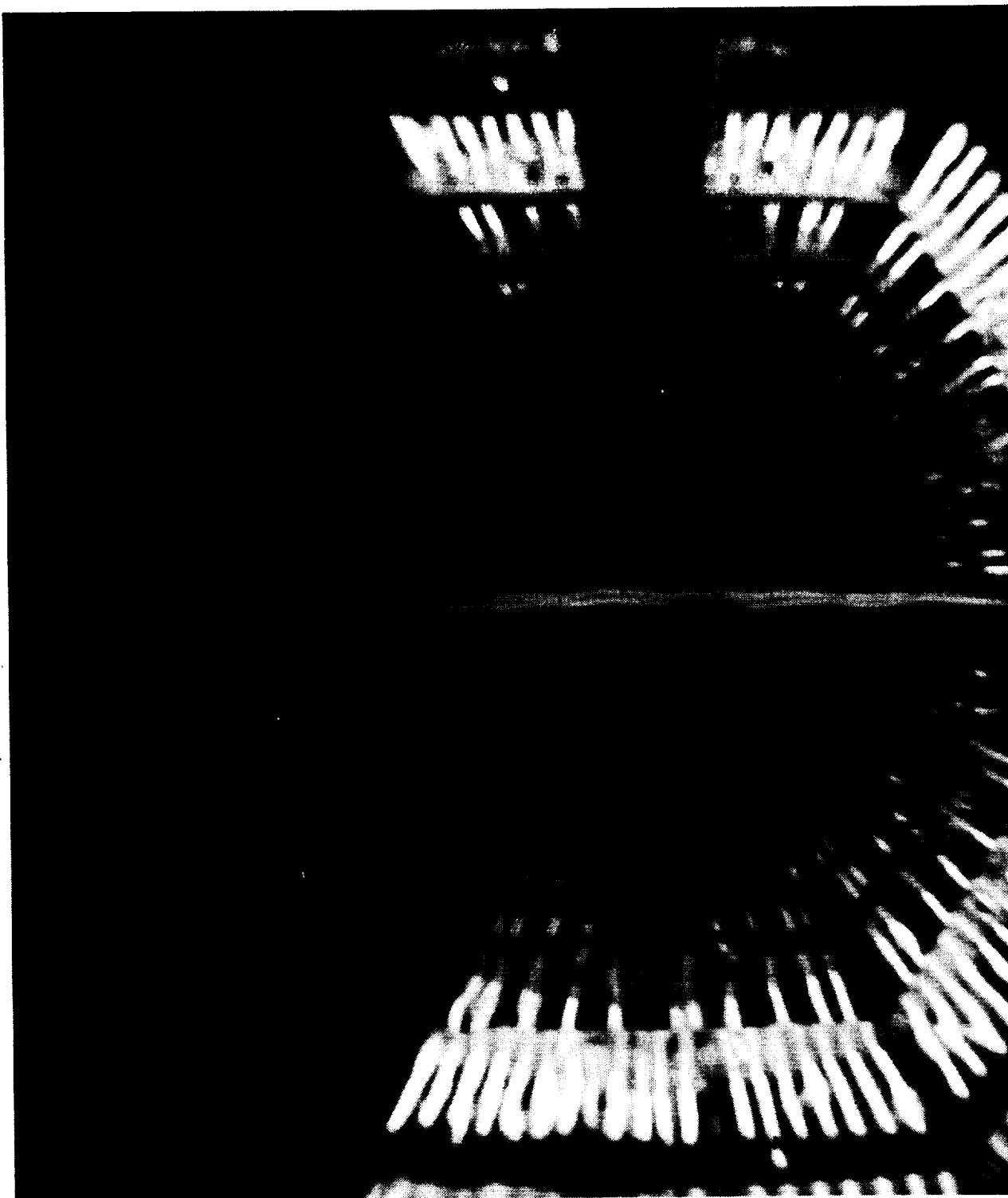


Figure 5-13: Borescope Image Showing the Loss of Quartz Lamp Heater Zones E and F at the End of Orbit #1.

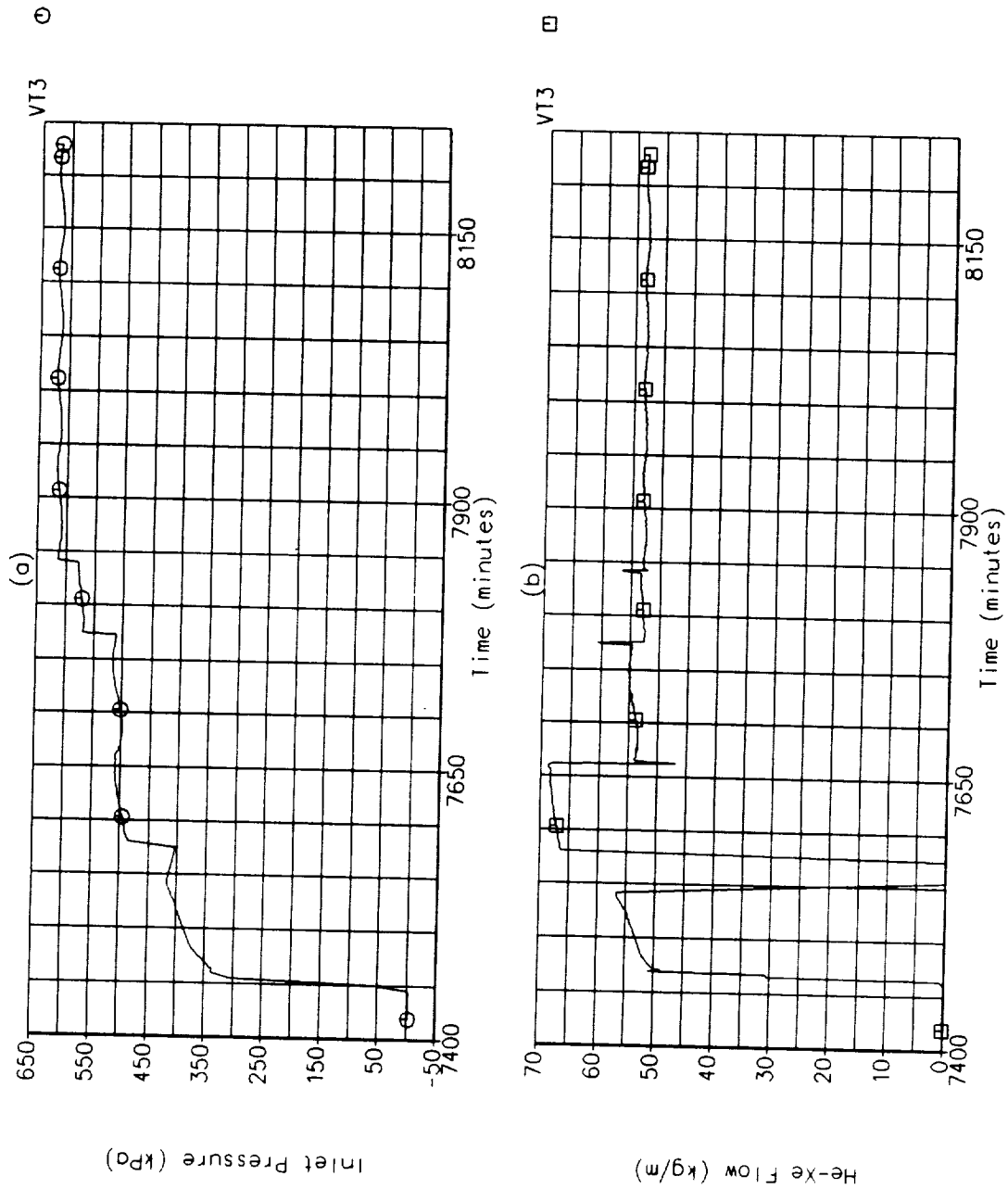


Figure 5-14: (a) Receiver Inlet Static Pressure During VT.3; and (b) Receiver Flow Rate During VT.3.

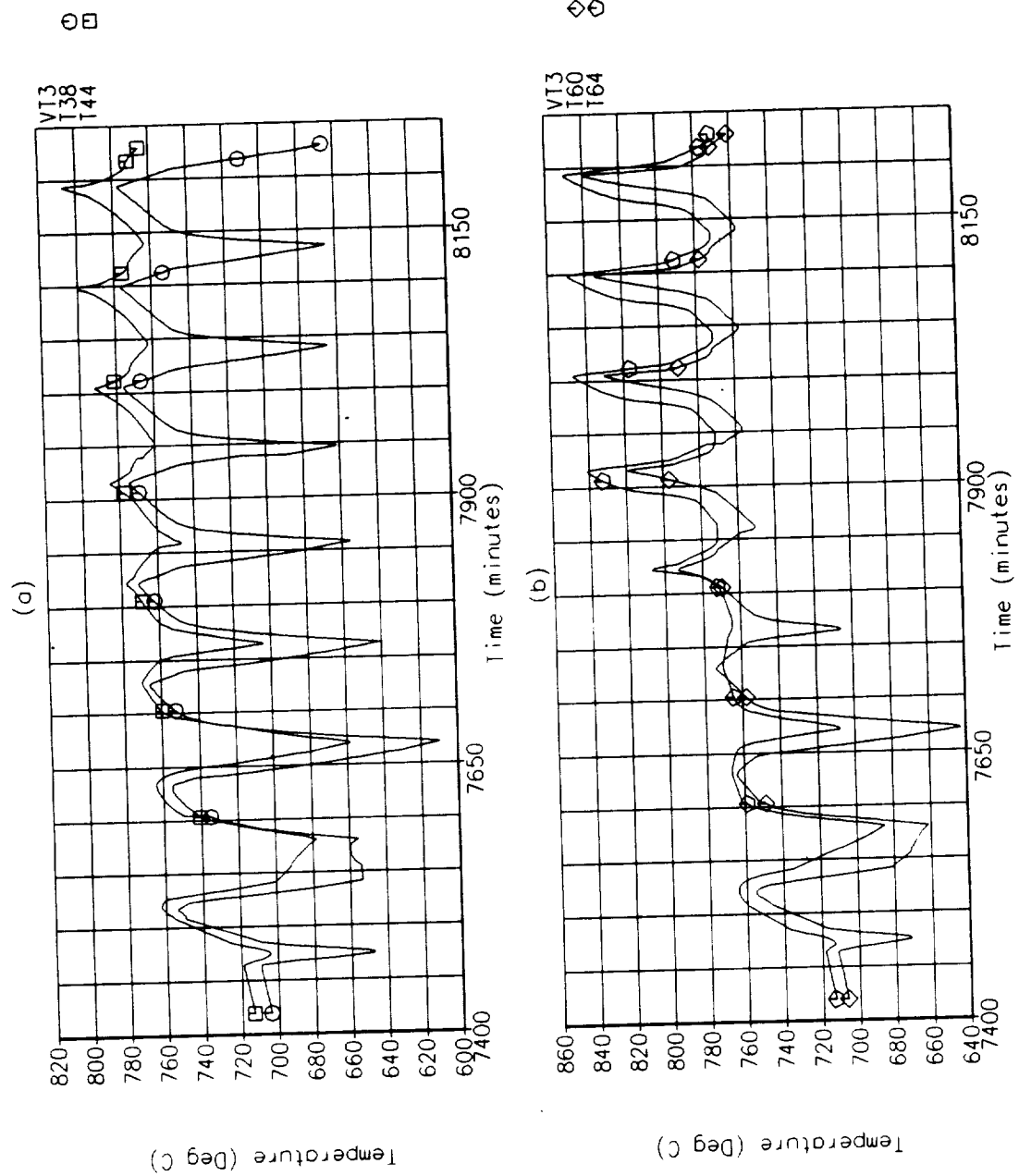


Figure 5-15: VT.3 Internal Salt Temperatures Closest to the Heat Exchanger Tube Located at the Inlet and Exit Ends of (a) the Flux-Facing Sides of Tube #12; and (b) the Top Sides of Tube #19.

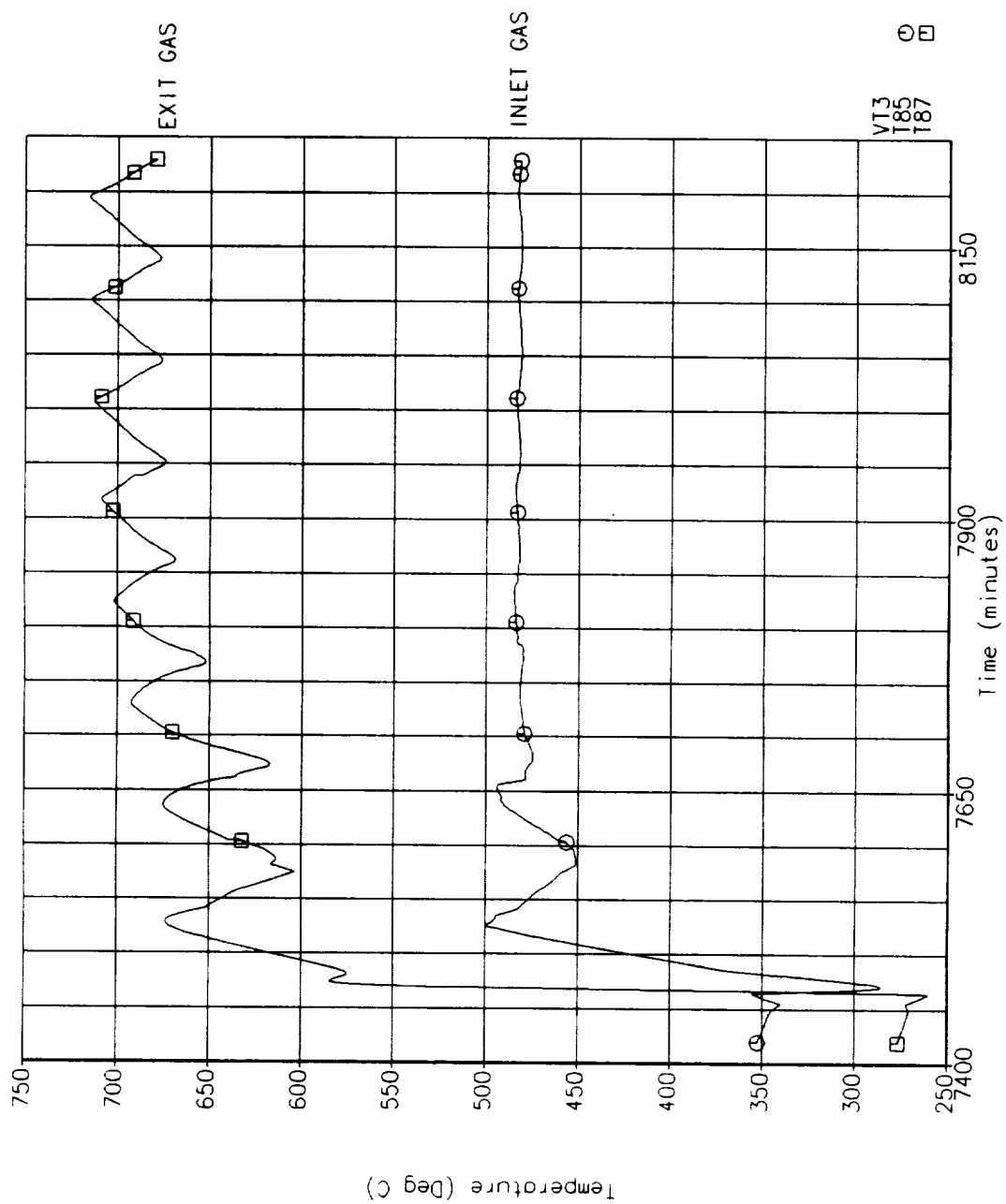


Figure 5-16: Inlet and Exiting Gas Temperatures During VT.3.

transferred to the gas. It is reasonable to assume that for these condition, no salt is melted 30 cm from the inlet of the heat storage tube. The total quartz lamp heater power and chamber vacuum level are shown in Figure 5-18 (a) and (b) respectively. Heater power was maintained at the lower power level of 193 kW because tube surface temperatures were still perceived to be too high.

An abrupt change in the chamber vacuum occurred during the 9th orbit that began the final and longest-term vacuum out-gassing event of the test conduct period. Previous to this event (see Figure 5-12), the vacuum level cycled within the 10^{-6} torr range with the orbital cycles. During the event, the vacuum no longer was driven by cavity temperatures and gradually increased up to the 10^{-4} torr range. Test mode VT.5 was continued despite the increase in chamber vacuum to preserve as much of the original test matrix as possible. The higher vacuum increased the risk of a corona arching between the lamp zones and/or to the heat storage tubes and, therefore, test mode VT.5 was terminated with somewhat marginal steady conditions at the end of orbital simulation #12.

Figure 5-19 shows the internal salt temperature closest to the heat exchanger tube (a) located at the flux-facing side of tube #12 at the inlet and exit end of the tube and (b) located on the top side of tube #19 at the inlet and exit ends of the tube. These data show that conditions were still changing inside the TES annulus but that the most significant changes were complete. Inlet and exiting gas temperatures, shown in Figure 5-20, also had not quite achieved true stabilized conditions but were reasonably close. The CBC engine simulator was shut off to preserve cavity temperatures for an eventual restart of the next test mode, VT.6. The heater zones were operated at about 18 kW to help preserve cavity temperatures to just below the melt temperature of the salt. It is interesting to note that the chamber pressure did not change when the CBC and lamp array operations were stopped. This again confirms that the source of the off-gassing materials was probably external to the receiver cavity. To date, the source of the off-gassing has not been identified.

The chamber vacuum level continued to fluctuate dramatically for about 13 hours before it began to stabilize in the low 10^{-4} torr range. It was obvious that the off-gassing source was not related to the heat storage tubes since all of the salt had been in the solid state for hours. Therefore, the decision was made to continue with test mode VT.6 to preserve as much of the test matrix as possible.

5.7 Orbital Variation Test, VT.6

The orbital variation test mode VT.6 continued the gradual change to the maximum insolation orbit while isolating the effects of changing the heater duty cycle on the receiver performance. Gas flow rate and inlet temperature were maintained at 75 kg/min and 482°C respectively. The electrical power supplied to the quartz lamp heater zones was maintained at the VT.3 baseline distribution, lowered slightly to 193 kW.

Test mode VT.6 was begun on 30 October during the long dormant vacuum event period that began near the beginning of test mode VT.5. The circuit breaker for the CBC engine simulator would not remain engaged during the initial attempts to power the blower. Power was shut down briefly to the DACS to swap the trailer and blower power circuits which put the CBC simulator on a 70-amp breaker. Current measurements made during blower operation showed the high current draw only occurred during blower start up and switching the blower motor to the 70 amp circuit cured the problem.

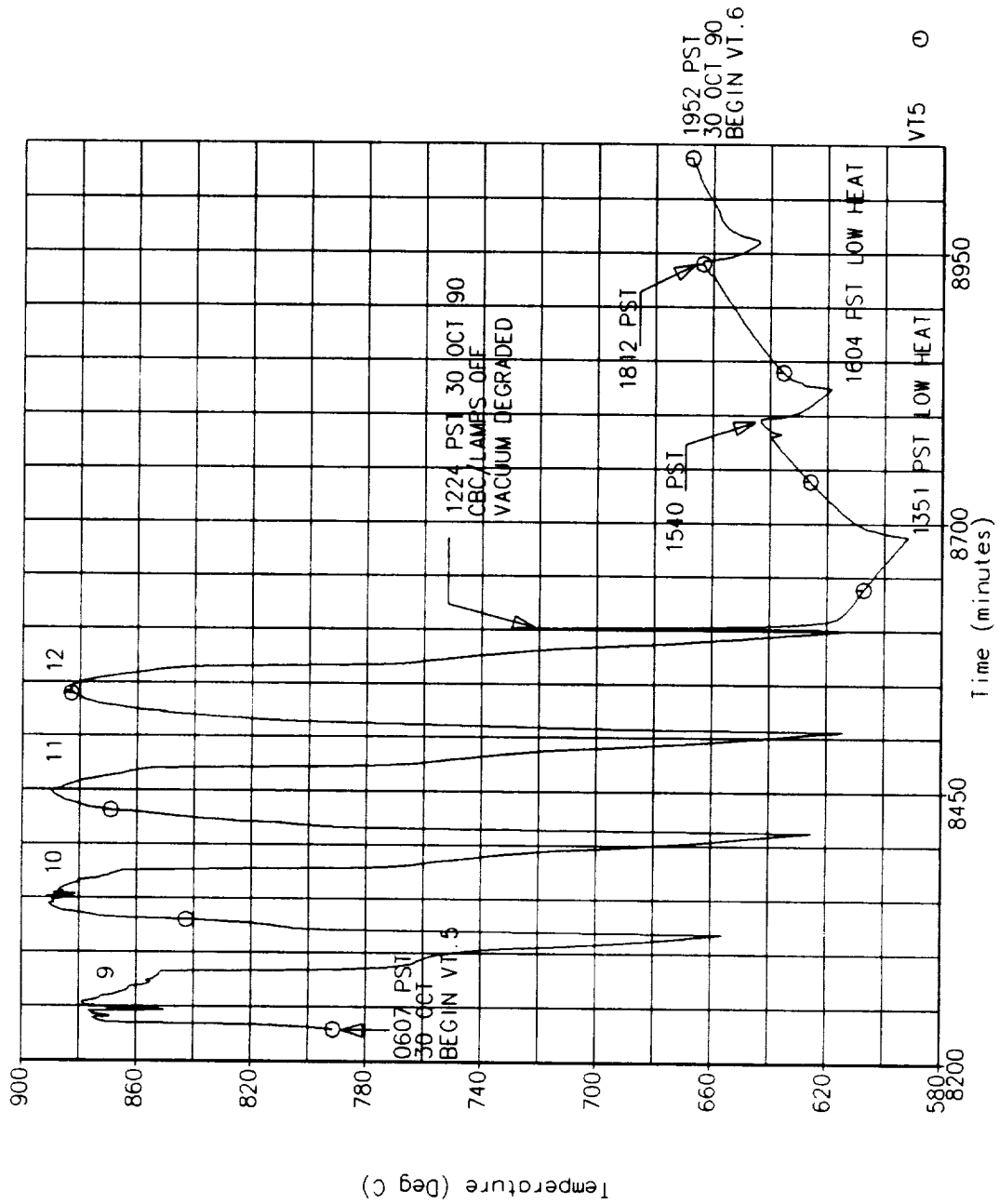


Figure 5-17: Flux-Facing Surface Temperature Located in the Convolution Valley at the Inlet End of Heat Storage Tube #4 During VT.5.

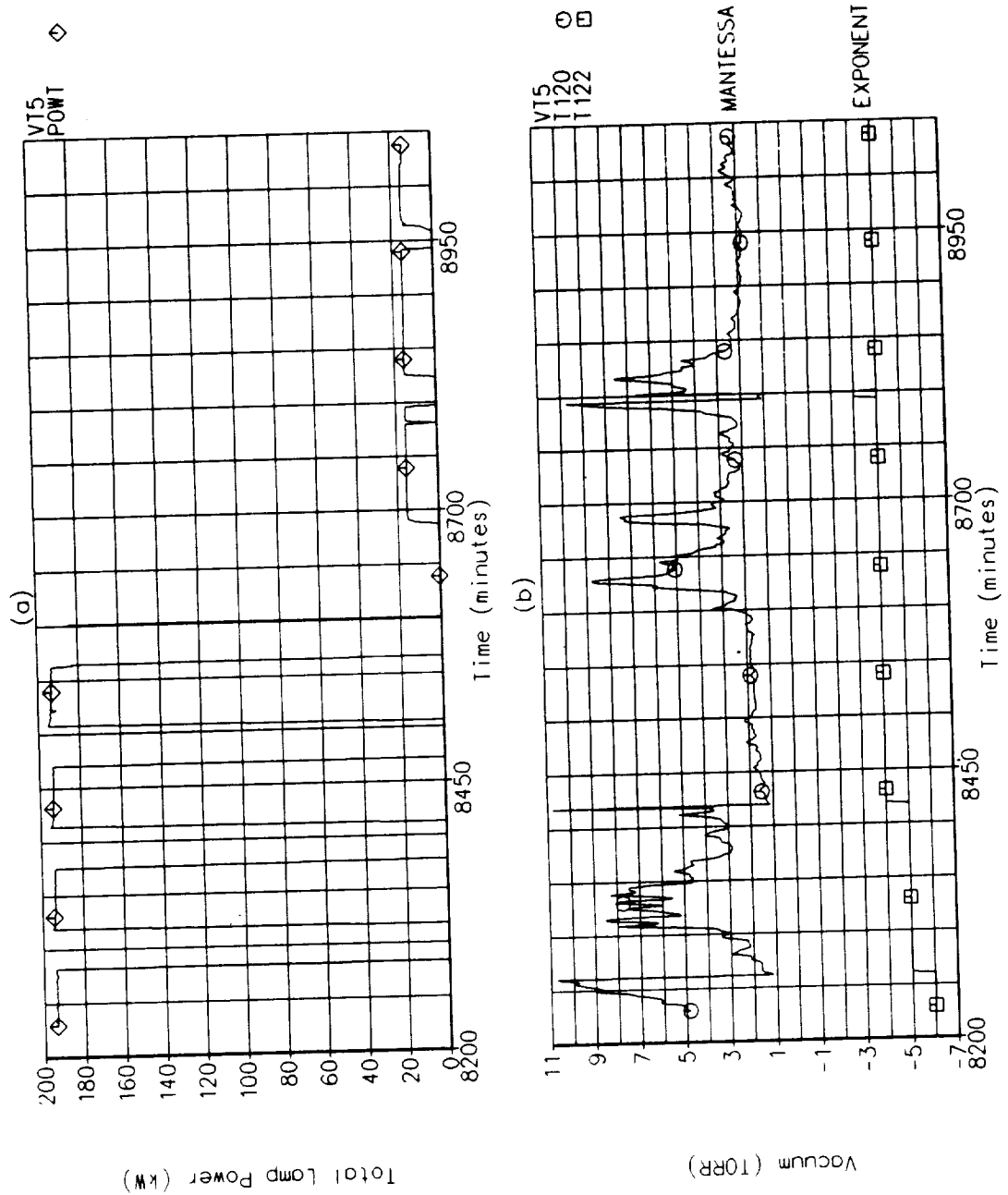


Figure 5-18: (a) Total Quartz Lamp Heater Power During VT.5; and (b) Chamber Vacuum Level During VT.5.

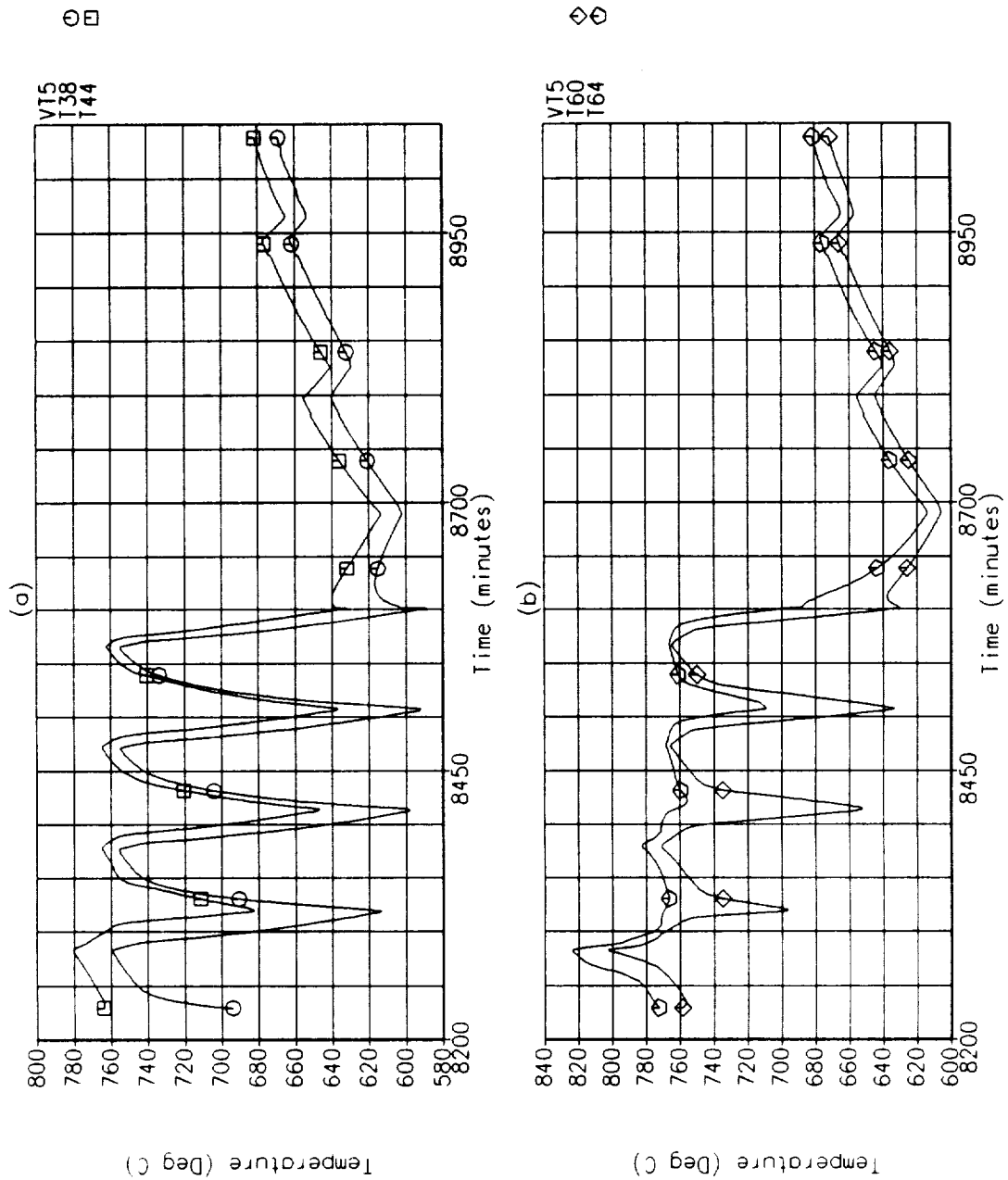


Figure 5-19: VT.5 Internal Salt Temperatures Closest to the Heat Exchanger Tube Located at the Inlet and Exit Ends of (a) the Flux-Facing Sides of Tube #12; and (b) the Top Sides of Tube #19.

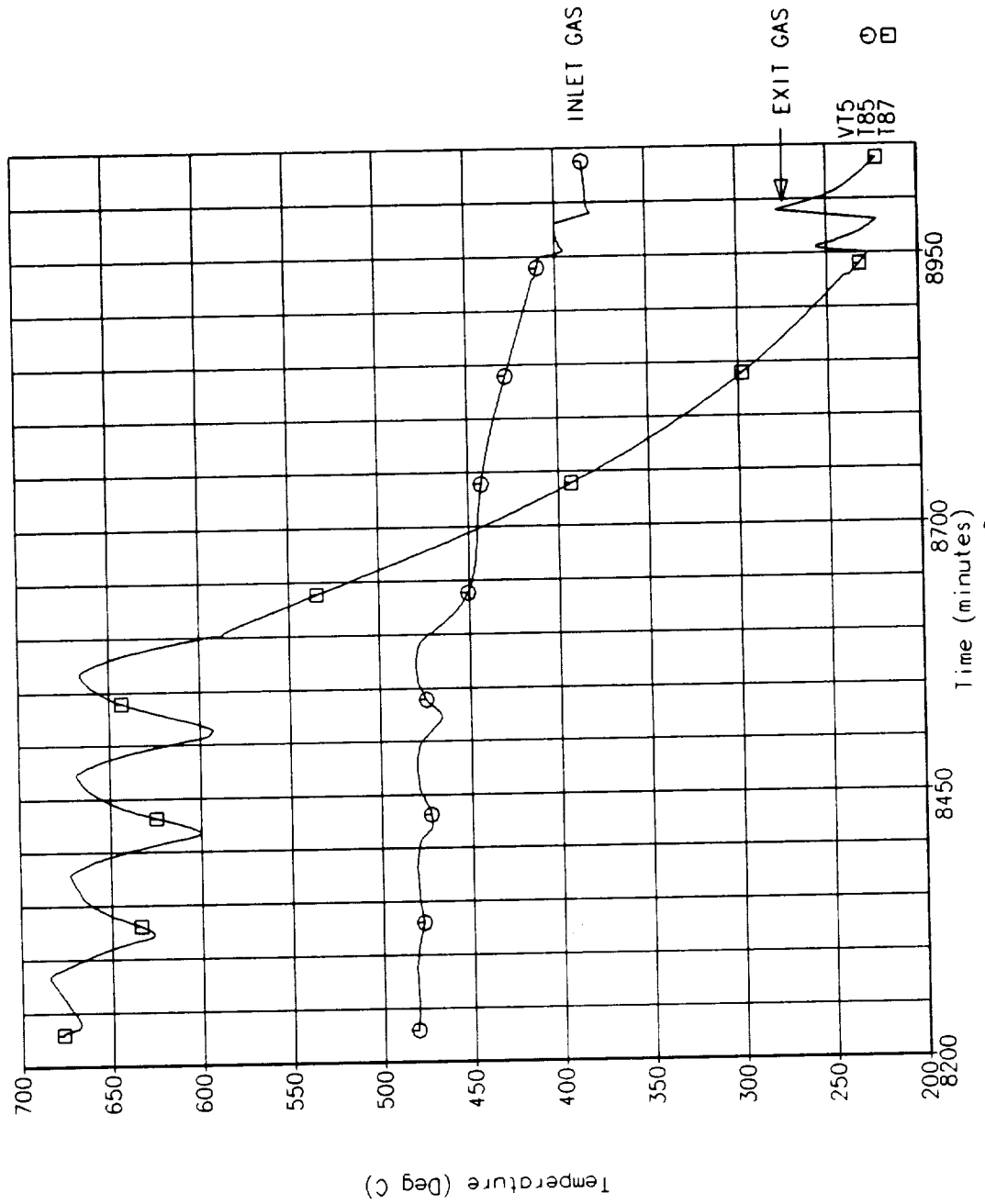


Figure 5-20: Inlet and Exiting Gas Temperatures During VT.5.

Figure 5-21 shows the flux-facing surface temperature located in the convolution valley at the inlet end of heat storage tube #4. Significant events and orbit numbers are noted on the figure for the entire VT.6 test period. Figure 5-22 (a) shows the total quartz lamp heater power and (b) the chamber vacuum level through the VT.6 test period. Note that the chamber vacuum did not improve during this test mode and high-temperature cycling inside the cavity had no effect the chamber pressure.

The total heater power was increased to 198 kW because tube surface temperatures facing the quartz lamp heater showed little change when the gas flow rate was increased during test mode VT.5. All other heat storage tube temperatures showed a substantial drop in temperature. This suggested that the very high temperatures measured on the flux-facing side of the heat storage tubes were not very accurate because of radiation-induced error caused by a lack of contact are between the thermocouple and the tube surface. All other cavity temperatures were close to or lower than pretest predictions.

No significant events occurred during the conduct of test mode VT.6. Pictures of the cavity taken through the borescope appeared to be changed very little (and maybe slightly improved) from those of earlier orbits. Figures 5-23 and 5-24 show views of the cavity taken at the end of the sunlit period and beginning of the eclipse period of orbit #17. While not too spectacular in black and white, these photographs show the degree of image clarity that could be seen through the borescope at this point in time with the lamps on and off in the cavity.

Test mode VT.6 was continued until near-steady conditions were achieved, 5 orbits after initiation of the test mode. Figure 5-25 shows the internal salt temperature closest to the heat exchanger tube (a) located at the flux-facing side of tube #12 at the inlet and exit end of the tube and (b) located on the top side of tube #19 at the inlet and exit ends of the tube and confirm that near steady conditions had been achieved. This is also confirmed by plots of the inlet and exit gas temperature shown in Figure 5-26.

5.8 Maximum Insolation Orbit Test, VT.8

Test mode VT.8 simulated receiver operation during a maximum insolation orbit. The total power to the quartz lamp heater was increased from 198 kW to 224 kW with the percentage of the total power distributed per zone the same as that used for the baseline VT.3 orbit. A comparison of power distributions between test modes is given in Section 6.0. Most other parameters were maintained at the VT.6 settings including a heater duty cycle of 66 minutes of heater power during the 94 minute orbit and a gas flow rate at a constant 75 kg/min. Receiver inlet gas temperature was increased slightly to $491^{\circ}\text{C} \pm 3^{\circ}\text{C}$ ($915 \pm 5^{\circ}\text{F}$). The purpose of this test mode was to demonstrate the capability of the SDHRT receiver to operate effectively with maximum heat input to the cavity by utilizing a thermal control option of modulating flow rate to the receiver.

Test mode VT.8 was initiated with the sunlit period of orbit #18 on 31 October. The flux-facing surface temperature located in the convolution valley at the inlet end of heat storage tube #4 is shown in Figure 5-27 with the significant VT.8 events and orbit numbers noted on the plot. Figure 5-28 (a) shows the total quartz lamp heater power and (b) the chamber vacuum level through the VT.6 test period. The chamber vacuum did show some slight improvement during conduct of this test mode but remained in the low 10^{-4} torr range. Again, temperature cycling inside the cavity did not effect the chamber vacuum level.

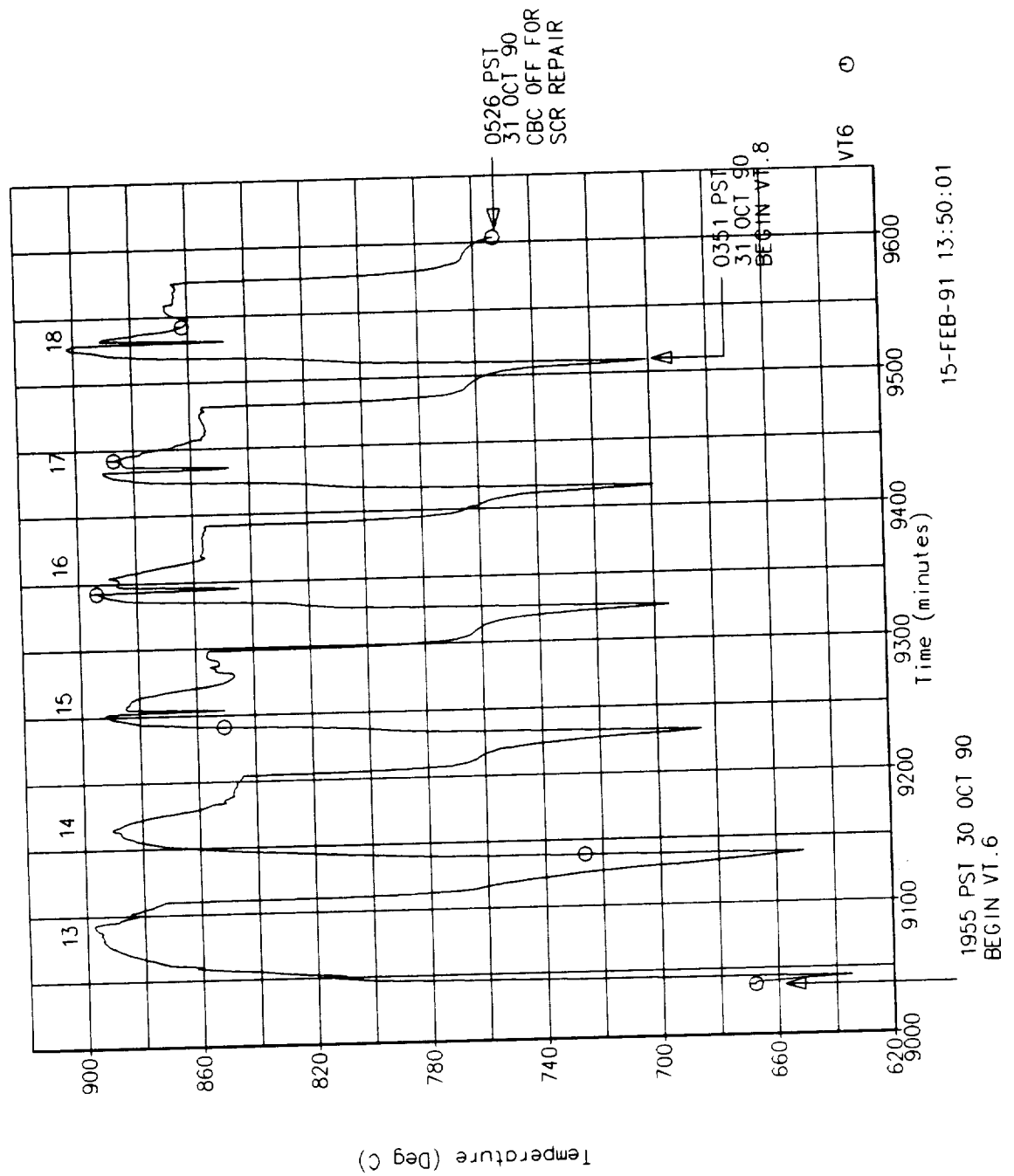


Figure 5-21: Flux-Facing Surface Temperature Located in the Convection Valley at the Inlet End of Heat Storage Tube #4 During VT.6.

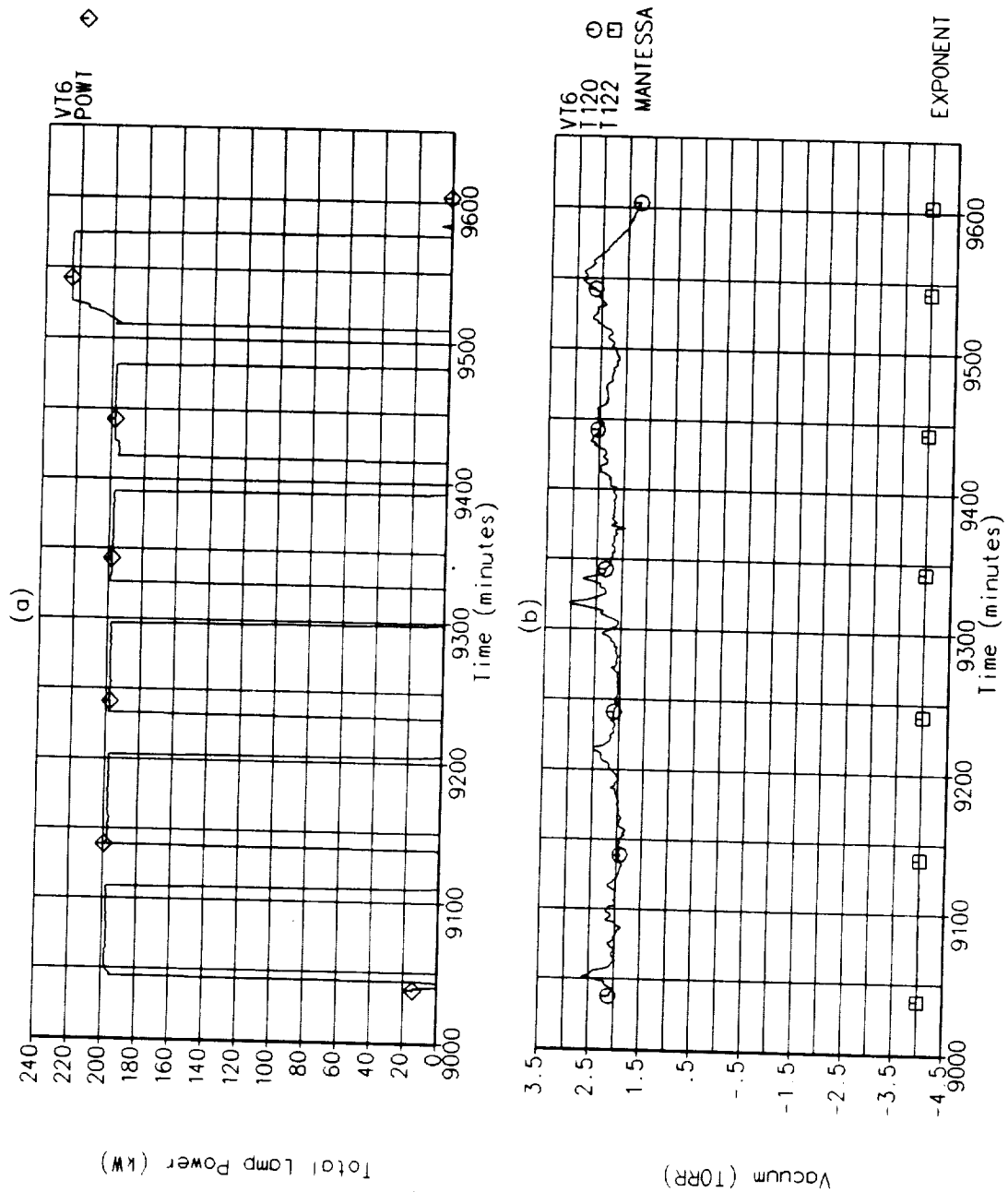


Figure 5-22: (a) Total Quartz Lamp Heater Power During VT.6; and (b) Chamber Vacuum Level During VT.6.

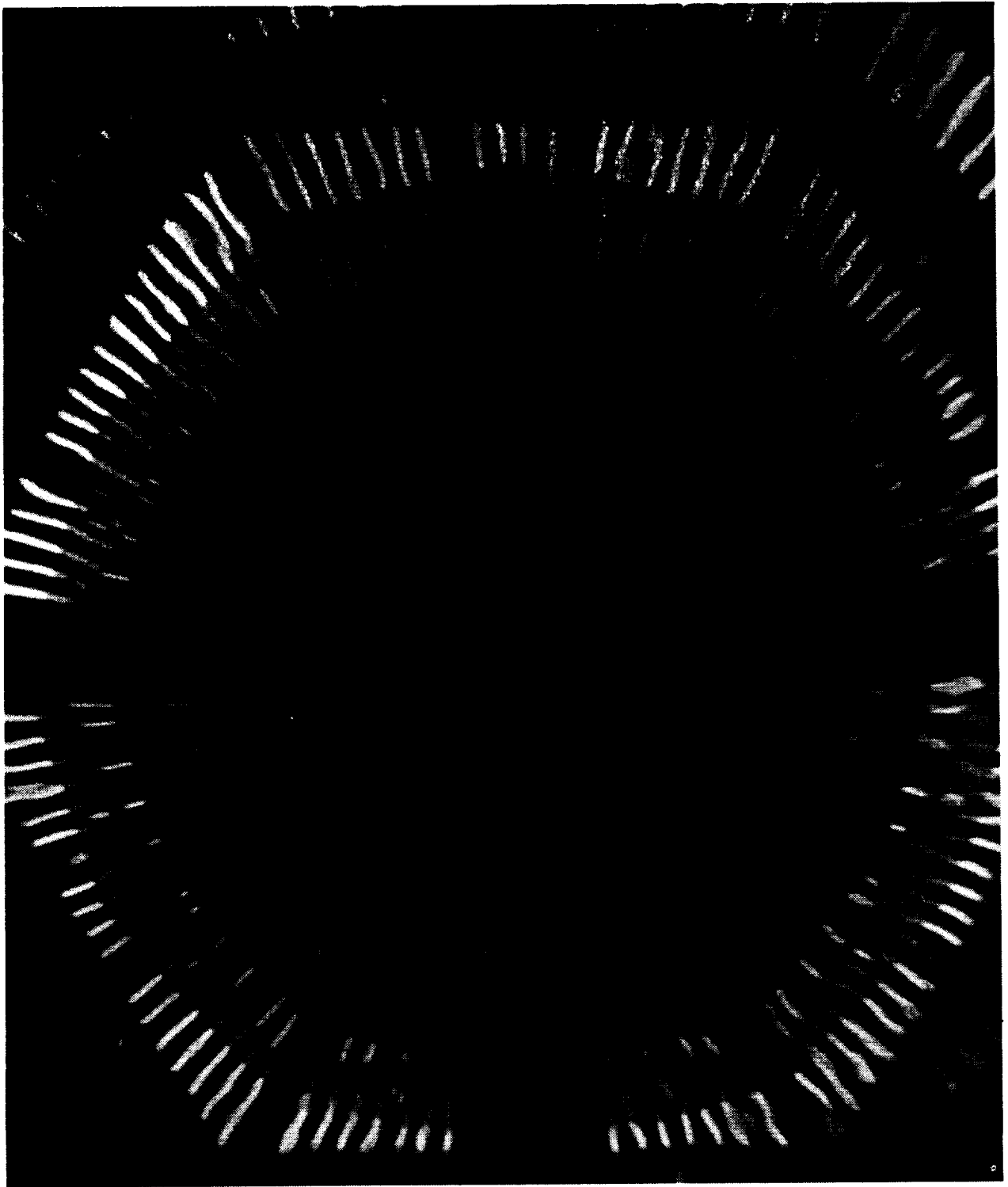


Figure 5-23: Cavity Borescope Image Near the End of the Sunlit Period of Orbit #17.

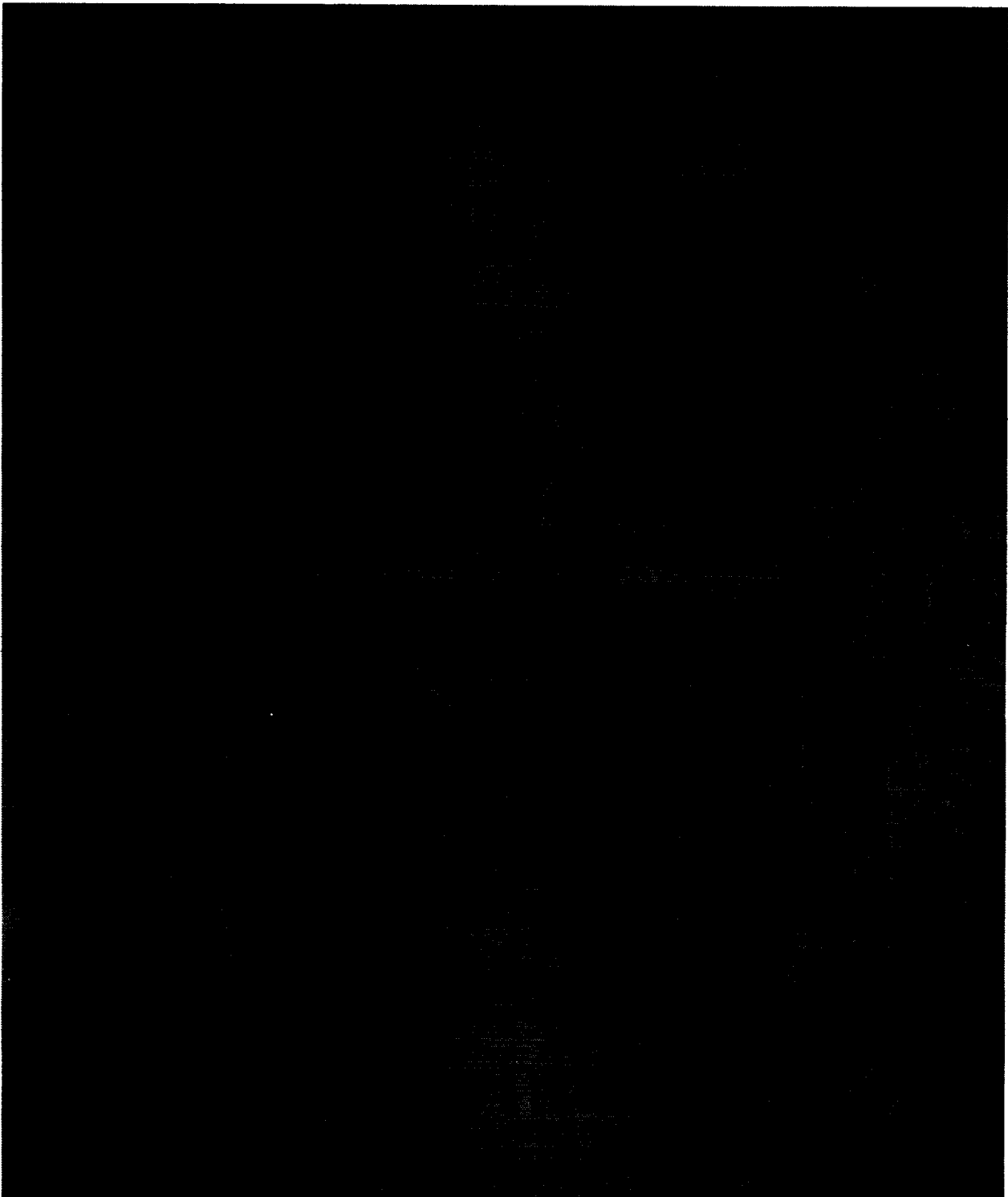


Figure 5-24: Cavity Borescope Image Near the Beginning of the Eclipse Period of Orbit #17.

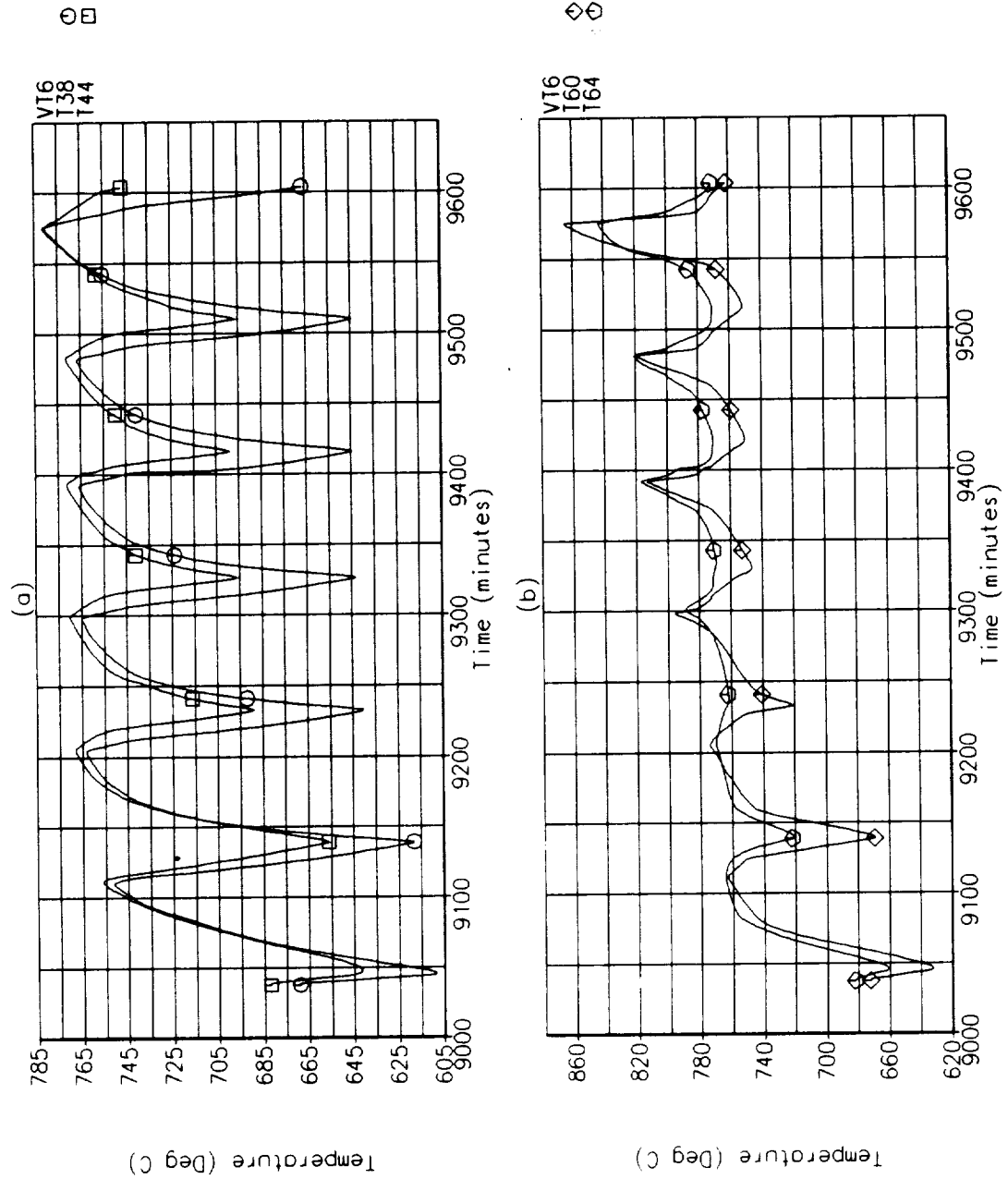


Figure 5-25: VT.6 Internal Salt Temperatures Closest to the Heat Exchanger Tube Located at the Inlet and Exit Ends of (a) the Flux-Facing Sides of Tube #12; and (b) the Top Sides of Tube #19.

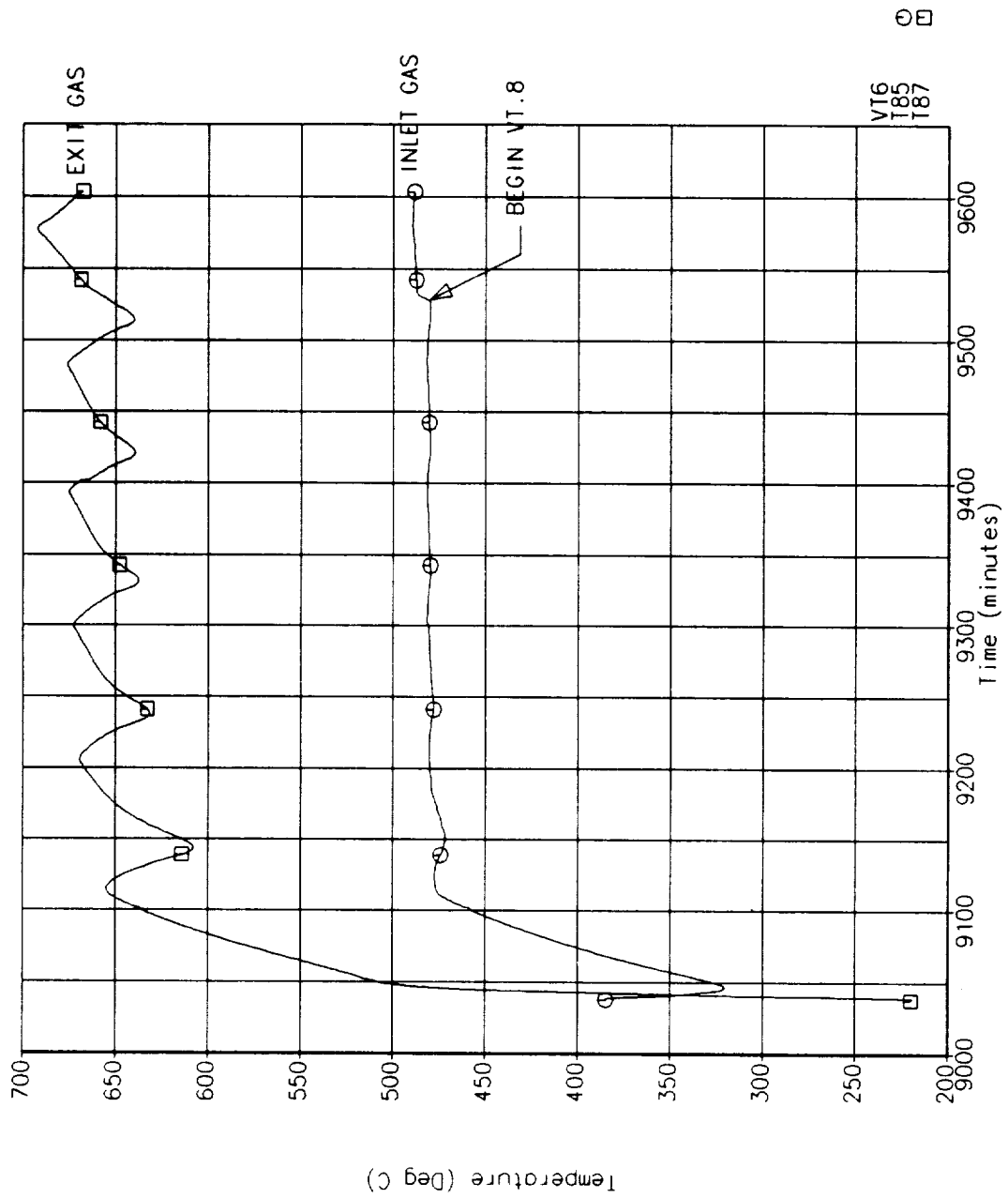


Figure 5-26: Inlet and Exiting Gas Temperatures During VT.6.

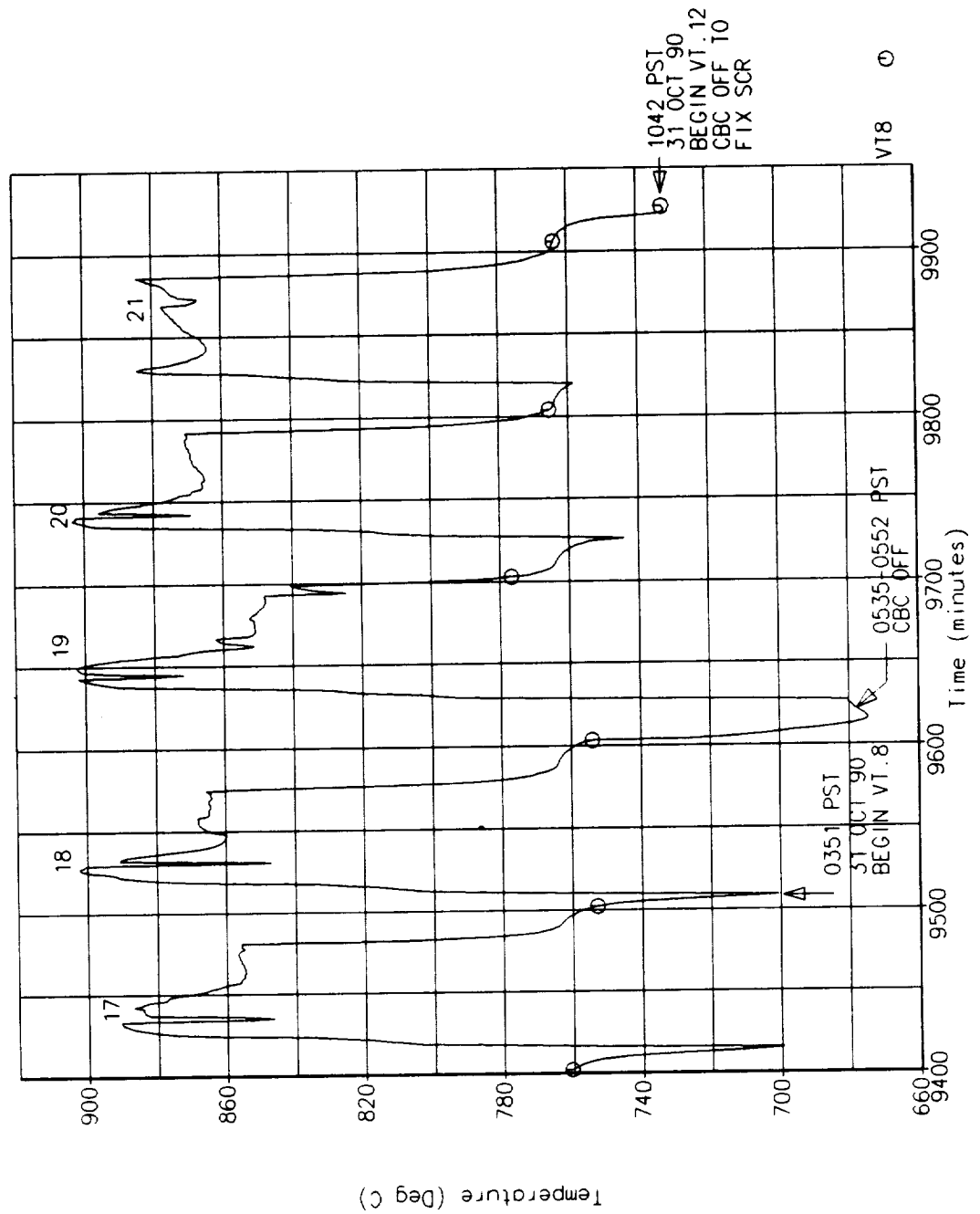


Figure 5-27: Flux-Facing Surface Temperature Located in the Convolution Valley at the Inlet End of Heat Storage Tube #4 During VT.8.

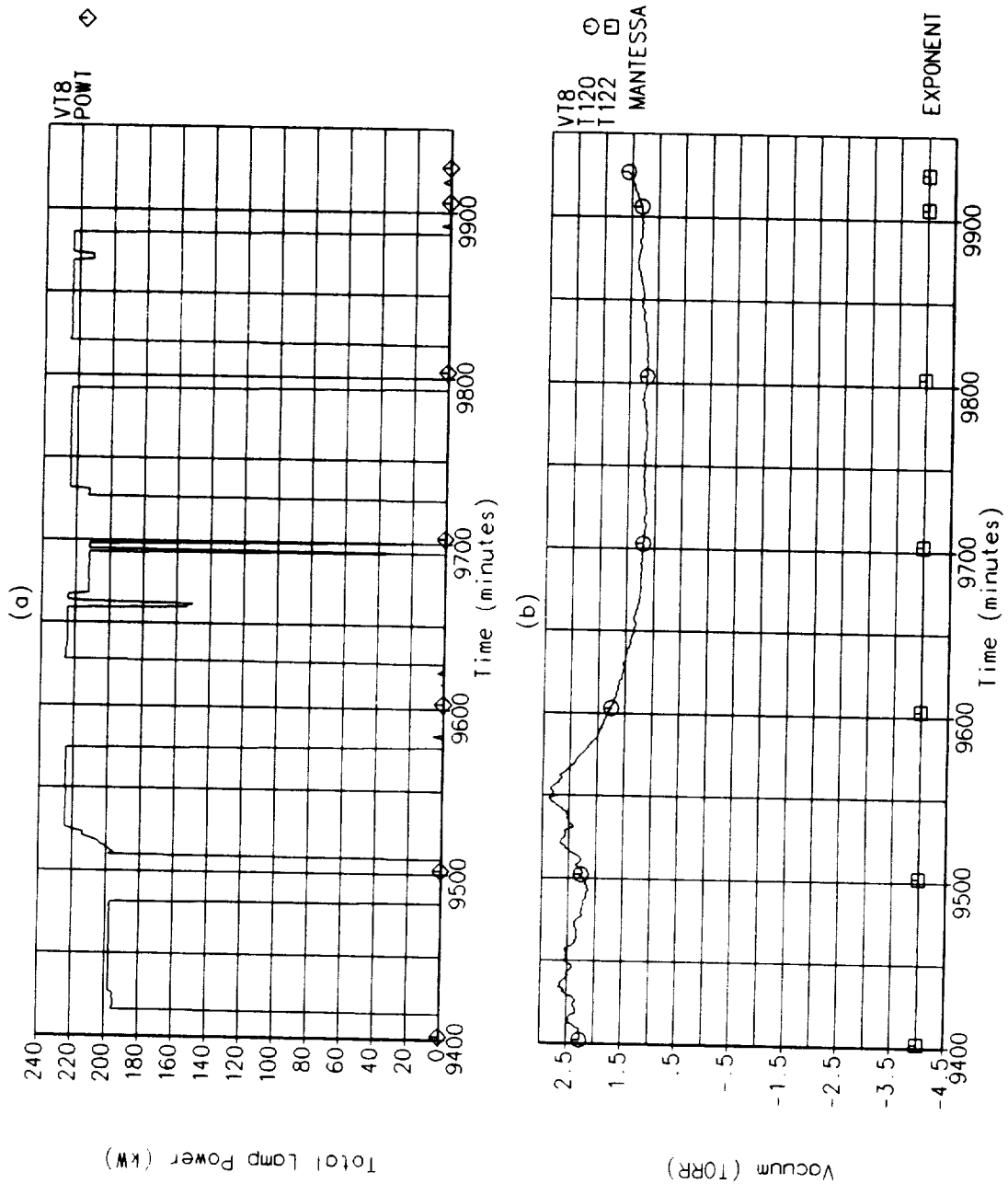


Figure 5-28: (a) Total Quartz Lamp Heater Power During VT.8; and (b) Chamber Vacuum Level During VT.8.

A number of heater problems were encountered during the conduct of this test mode. It is still not clear if they were related to problems in the SCR power controllers or whether they can be attributed to corona arcing inside the receiver cavity. The first heater problem occurred during power up for the sunlit period of orbit #19. Several small fuses blew inside the SCR power controllers and no power was supplied to the lamps. The cause of these fuse failures is not clear but the problem occurred at several different times throughout the test conduct period. The CBC simulator was shut off during the period of repair to preserve cavity temperatures. Power was quickly restored to the lamps and the sunlit period of orbit #19 continued for about 35 minutes until zones E and F were lost. The loss of zones E and F appeared to be related to the temperature-sensitivity of the power controller breaker (encountered earlier in the test) and power was quickly restored to the lamps. Several minutes later, power was lost to zone 2B which was not noticed until the power up for the next sunlit period. Power was lost again at the beginning of the sunlit period of orbit #22 because of blown fuses inside the SCR controllers.

Another anomaly that occurred during conduct of VT.8 was a complete loss of view into the cavity through the borescope. A small heating pad had been previously installed near the camera mount on the back-end of the borescope in an attempt to improve the image quality. It was thought that some of the borescope image distortion might be attributable to ice formation on the back lens near the GN_2 cooling gas inlet. The heating pad was installed during test mode VT.5. Little or no change was seen in the image quality so the heating pad was removed some time around orbit #19 (specific time was not noted in the test notebook). Within an hour after removing the pad, all view into the cavity was lost as the end lens of the borescope became coated with a foreign material. The source of the material is not known. No borescope pictures were taken during this period because the image was dark and nothing significant could be seen.

The continuation of poor chamber vacuum, problems encountered with the heater zones, and the blockage of view through the borescope caused concern on the part of the test conductor and the decision was made to terminate the high-power test mode VT.8 prior to achieving steady-state conditions. Test mode VT.8 was declared complete at the end of orbit #21. Figure 5-29 shows the internal salt temperature closest to the heat exchanger tube (a) located at the flux-facing side of tube #12 at the inlet and exit end of the tube and (b) located on the top side of tube #19 at the inlet and exit ends of the tube. It is obvious that it cannot be confirmed that steady conditions had been achieved but it is also apparent that the majority of the trend changes in these temperatures had occurred by orbit #22. Inlet and exit gas temperatures, shown in Figure 5-30, show a fairly large difference in magnitudes between orbits #21 and #22 but are likely nearing their steady-state values as well.

It should be noted that if corona occurs inside the receiver cavity, the SCR power controllers are designed to immediately shut off power to the effected zone and then attempt to repower the zone 3 times. Thus, cycling of the SCR power controllers is an indication of corona problems. No cycling of the SCR power controllers was observed during the period of conduct of VT.8.

5.9 Peaking Orbit Simulation, VT.12

The SDHRT heat receiver was not designed (and has not been analyzed) for orbital peaking because peaking requirements had not been developed when the receiver was being designed. However, the SDHRT receiver should be able to perform within the currently defined peaking requirements (reference 6,7). The purpose of test mode VT.12 was to quantify the SDHRT receiver performance through end-of-sun and end-of-eclipse peaking scenarios. The test mode

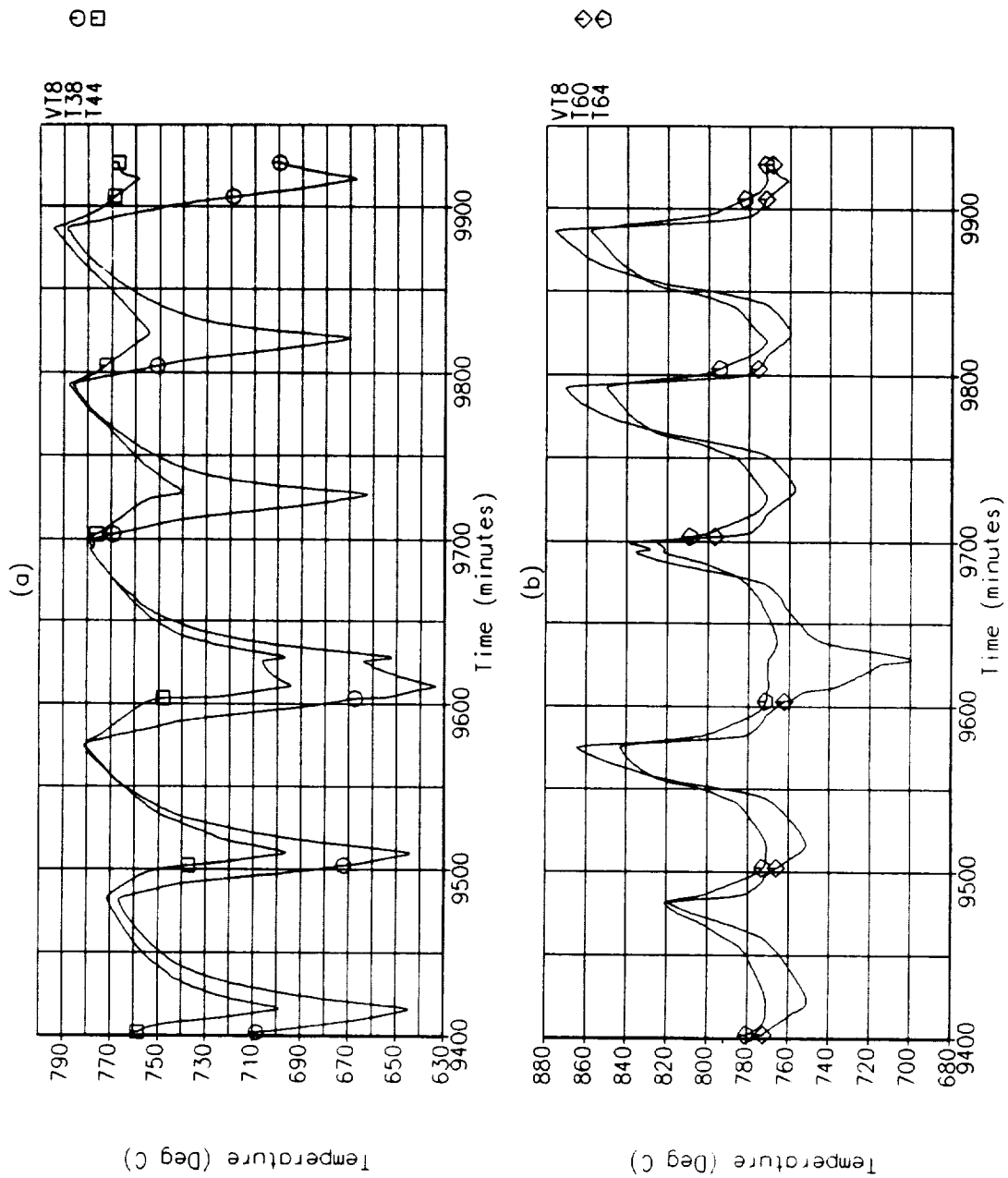


Figure 5-29: VT.8 Internal Salt Temperatures Closest to the Heat Exchanger Tube Located at the Inlet and Exit Ends of (a) the Flux-Facing Sides of Tube #12; and (b) the Top Sides of Tube #19.

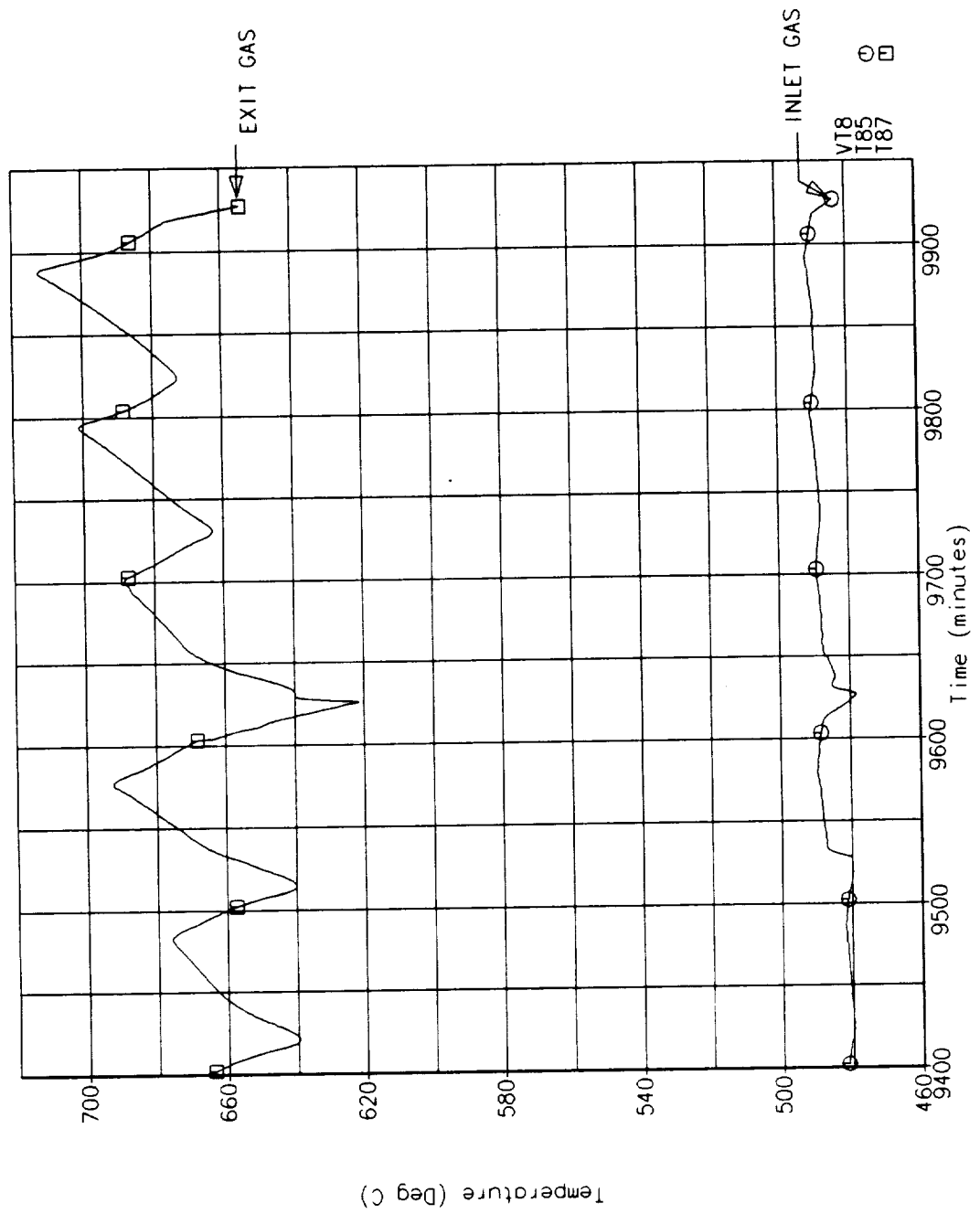


Figure 5-30: Inlet and Exiting Gas Temperatures During VT.8.

was initiated by establishing the baseline orbital conditions. Two complete peaking orbits were then planned beginning 7.5 minutes prior to eclipse and 7.5 minutes prior to sun. Changes in flow rate associated with the peaking orbits were defined in reference 3.

Test mode VT.12 was initiated with the sunlit period of orbit #22 on 31 October. The flux-facing surface temperature located in the convolution valley at the inlet end of heat storage tube #4 is shown in Figure 5-31 with the significant VT.12 events and orbit numbers noted on the plot. Figure 5-32 (a) shows the total quartz lamp heater power and (b) the chamber vacuum level through the VT.6 test period. The major vacuum off-gassing event that had begun almost 25 hours before the initiation of this test mode finally ended as chamber vacuum return to the 10^{-5} torr range and began to once again cycle with chamber temperatures.

Attempted flow rate adjustments for the peaking orbit are shown in Figure 5-33. The high flow rate requirement of 73 ± 0.9 kg/min (161 ± 2 lbm/min) was easily provided by the CBC engine simulator but the low flow rate of 48 ± 0.9 kg/min (106 ± 2 lbm/min) required during the recovery period could not be provided by the CBC engine simulator at these operating conditions. This was the only required parametric boundary condition that could not be met by the SDHRT and ADRT test support hardware. The minimum flow rate reached with full blower by-pass at these operating conditions was about 52 kg/min (115 lbm/min). The reason that the CBC engine simulator could not produce the lower flow rates was because the actual pressure drop through the receiver gas distribution plenums was lower than pretest predictions used to size the flow bypass valve. Therefore, the pressure drop through the bypass line across the blower was not appreciably lower than that through the regenerative heat exchanger and receiver loop except as flow rates were increased through the receiver.

Since the actual peaking orbital conditions could not be satisfied, the test parameters were returned to the baseline orbital conditions at the beginning of orbit #26 and allowed to stabilize before continuing with the flux variation test modes. Temperatures appeared to be reasonably stable at the end of the same orbit (the receiver had been operating at near baseline conditions for 5 orbits). Figure 5-34 shows the internal salt temperature closest to the heat exchanger tube (a) located at the flux-facing side of tube #12 at the inlet and exit end of the tube and (b) located on the top side of tube #19 at the inlet and exit ends of the tube. These data confirm that steady conditions were achieved at the end of orbit #26. Inlet and exit gas temperatures, shown in Figure 5-35, also confirm stabilization of temperatures. The data from orbit #26 better represent the baseline orbit than those obtained during orbit #8 (VT.3) because they are more stabilized and were obtained with the full 198 kW heater power.

5.10 Axial Flux Variation, SS.1

Matching the rate that solar energy is absorbed by the heat storage tubes after internal cavity reflections and infrared radiative exchange provides is a method of minimizing the differences between the operation of the receiver with a space-based concentrator versus operation with the quartz lamp heater array. However, these data have not been produced for the SDHRT or the Space Station Freedom baseline heat receivers operating with the off-axis concentrator. Therefore, an exact simulation of the SDHRT receiver with the off-axis concentrator flux distribution was not possible.

Test mode SS.1 examines the performance of the SDHRT heat receiver operating with an axisymmetric heater power distribution based upon averaged circumferential flux values obtained from off-axis concentrator data (reference 8). The peak flux has been moved forward because of the shorter heat storage tube length in the SDHRT heat receiver. The total electrical input power to the heater equals the nominal value of 198 kW and the power distributed to the 6 circumferential zones at each of the 5 axial zones, are equal. All other parameters are based

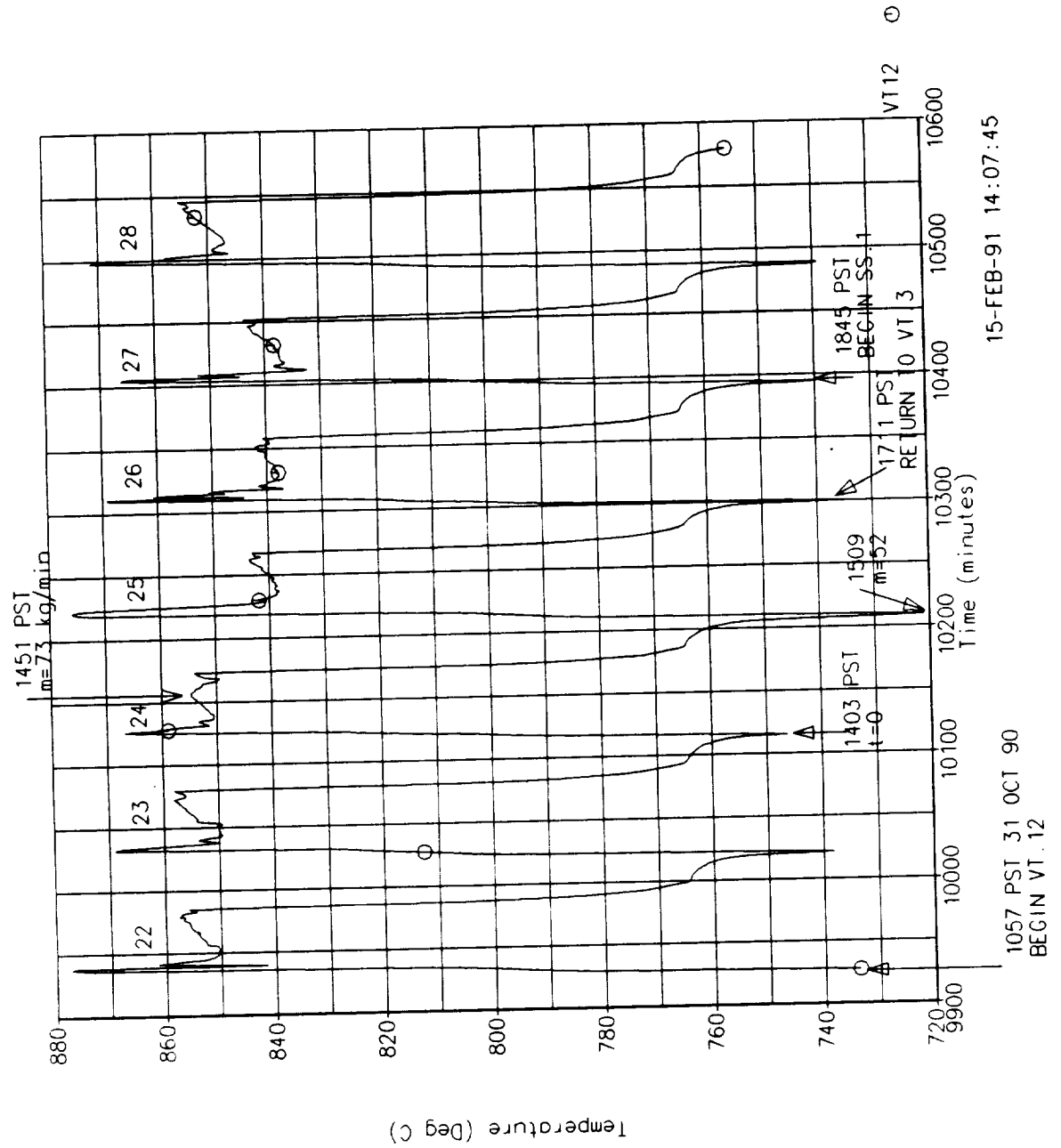


Figure 5-31: Flux-Facing Surface Temperature Located in the Convection Valley at the Inlet End of Heat Storage Tube #4 During VT.12.

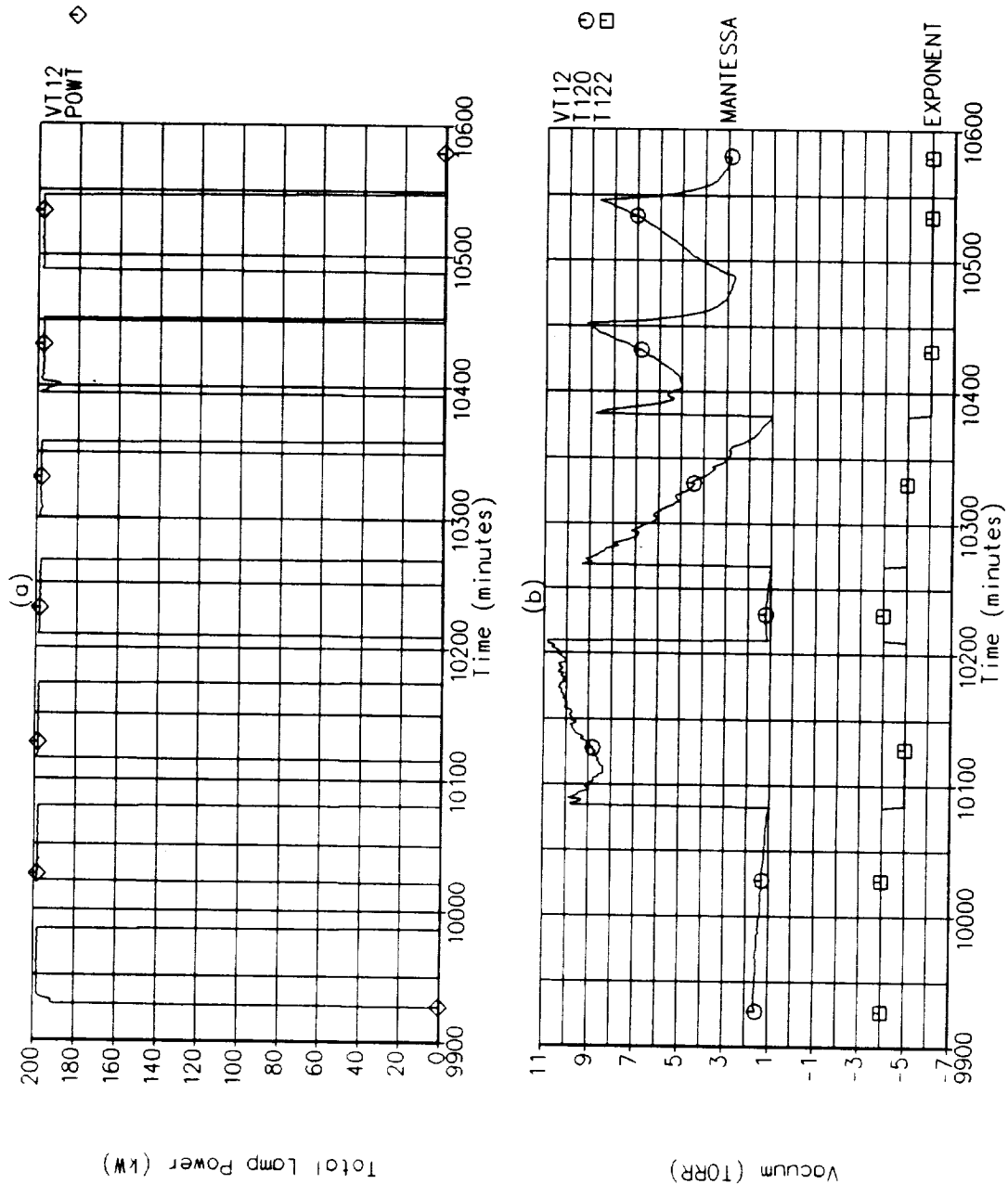


Figure 5-32: (a) Total Quartz Lamp Heater Power During VT.12; and (b) Chamber Vacuum Level During VT.12.

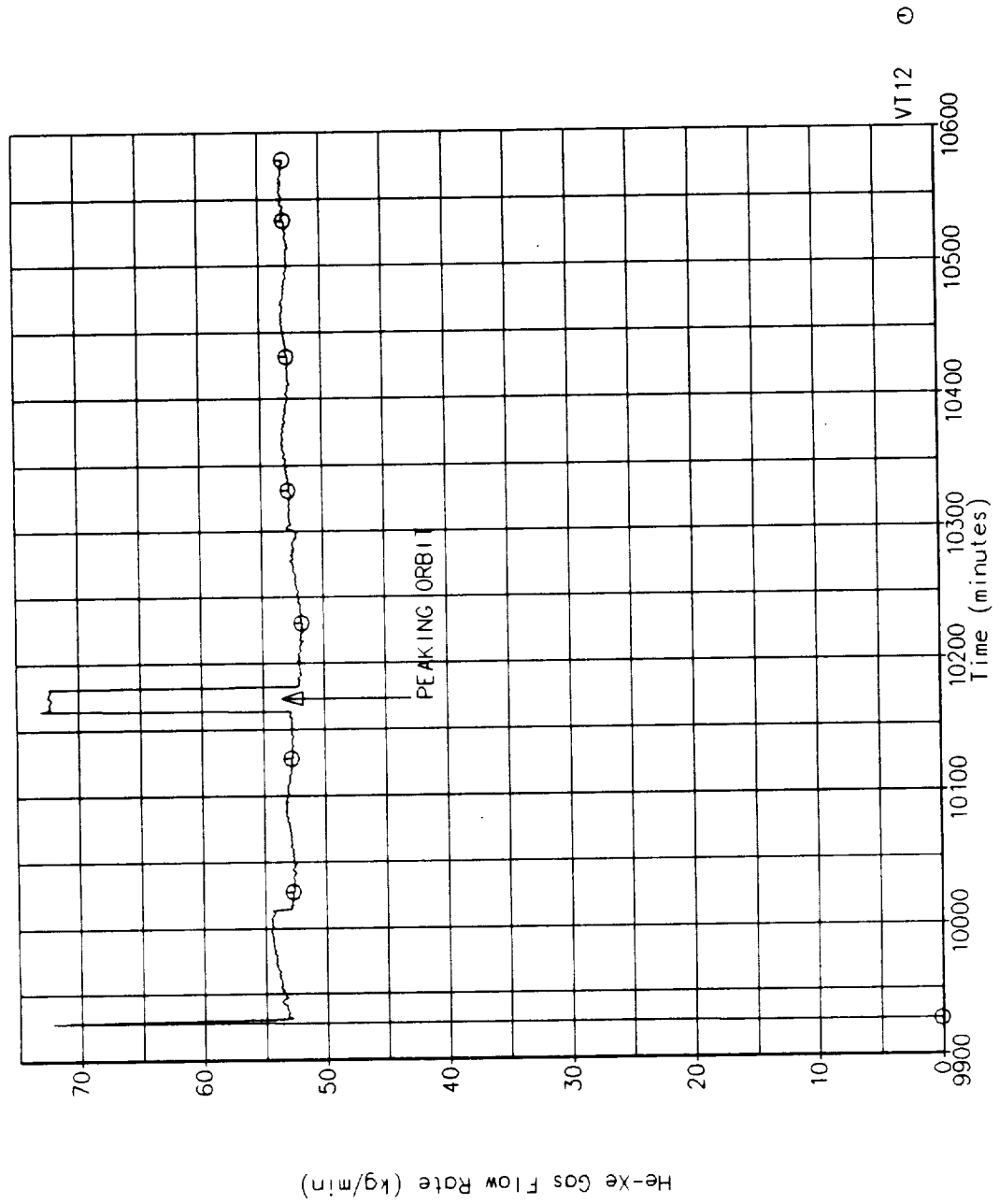


Figure 5-33: Helium-Xenon Gas Flow Rate During VT.12.

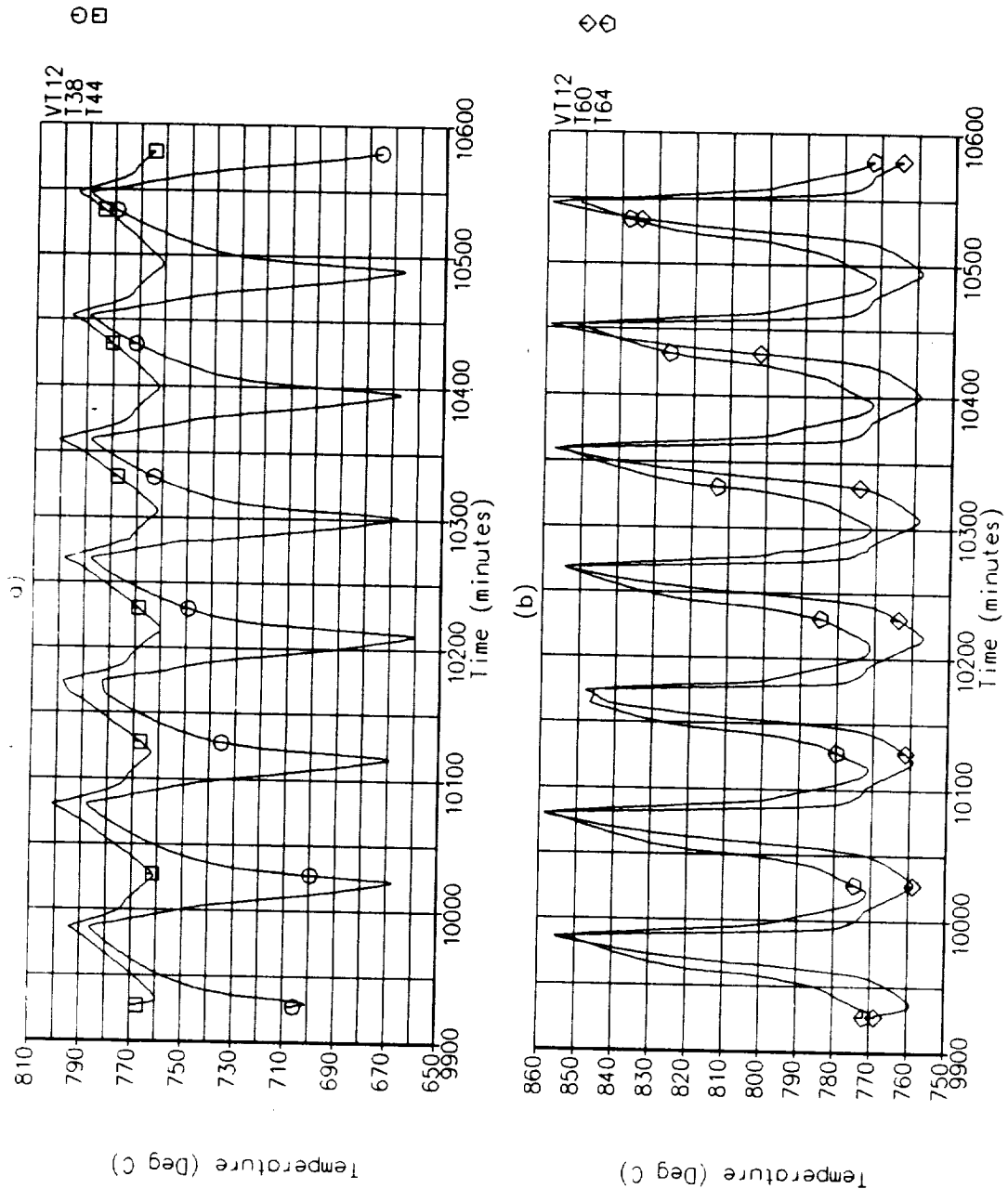


Figure 5-34: VT.12 Internal Salt Temperatures Closest to the Heat Exchanger Tube Located at the Inlet and Exit Ends of (a) the Flux-Facing Sides of Tube #12; and (b) the Top Sides of Tube #19.

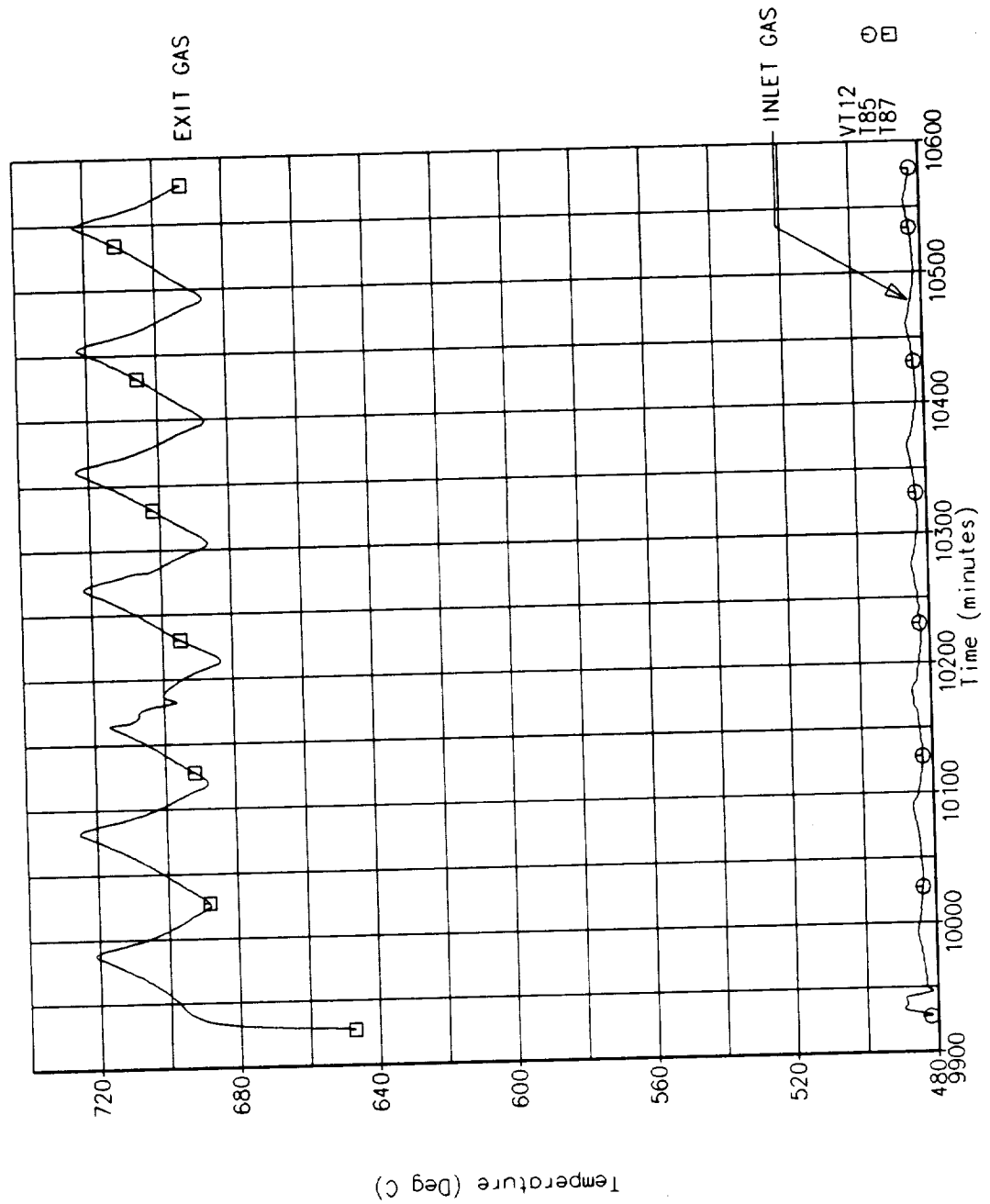


Figure 5-35: Inlet and Exiting Gas Temperatures During VT.12.

upon the SDHRT baseline orbit so that all performance differences can be attributed to the difference in the axial flux distribution. The gas inlet temperature and flow rate were held constant at their nominal values of 482°C and 53 kg/min.

Test mode SS.1 was initiated with the sunlit period of orbit #27 on 31 October. The flux-facing surface temperature located in the convolution valley at the inlet end of heat storage tube #4 is shown in Figure 5-36 with the significant SS.1 events and orbit numbers noted on the plot. Figure 5-37 (a) shows the total quartz lamp heater power and (b) the chamber vacuum level through the SS.1 test period.

Chamber vacuum levels continued to improve after the end of the last vacuum event, returning to the 10^{-6} torr level and cycled with the heater operation. The image through the borescope began to clear up as shown the Figures 5-38 through 5-40. Figure 5-38 shows the image during the sunlit period of orbit #27. The solid material deposited on the quartz lens began to flake off and about 1/6th of the cavity is visible. It is interesting to note the similarity in the lines of the contaminated regions shown in this figure and that shown previously in Figure 5-10. Figure 5-39 shows about 1/4th of the cavity image is visible 2 orbits later and almost the entire cavity view has returned to view in Figure 5-40 which was taken during the sunlit period of orbit #31. However, the image quality improvement was short lived and by the 34th orbit new material had deposited and almost completely blocked the view through the borescope as shown in Figure 5-41. The image quality continued to change through the remaining test simulation orbits but never improved much beyond that shown in Figure 5-38.

The conduct of test mode SS.1 was continued until steady-state temperatures were achieved. No unplanned events occurred during this period. Figure 5-42 shows the internal salt temperature closest to the heat exchanger tube (a) located at the flux-facing side of tube #12 at the inlet and exit end of the tube and (b) located on the top side of tube #19 at the inlet and exit ends of the tube. The inlet and exiting gas temperatures are shown in Figure 5-43. These data show stable temperatures had been achieved in the receiver.

5.11 Circumferential Flux Variation, SS.4

The Space Station Freedom off-axis concentrator will have a non-uniform flux distribution, both axial and circumferential (as will any real concentrator). Test mode SS.4 examines the SDHRT receiver performance using a quartz lamp power distribution with a large circumferential flux gradient. The distribution of electrical power for this and the other test modes are given in Section 6.3. Test mode SS.4 also used VT.3 baseline gas interface parameters to allow a comparison to be made with VT.3 and SS.1 data and quantify the effects of the non-uniform circumferential flux.

Test mode SS.4 was initiated with the sunlit period of orbit #35 on 1 November. The flux-facing surface temperature located in the convolution valley at the inlet end of heat storage tube #4 is shown in Figure 5-44 with the significant SS.4 events and orbit numbers noted on the plot. Figure 5-45 (a) shows the total quartz lamp heater power and (b) the chamber vacuum level through the SS.4 test period. Normal vacuum levels continued during test mode SS.4.

Test mode SS.4 was continued until stabilized temperatures were achieved and no significant unplanned events occurred during this period. Figure 5-46 shows the internal salt temperature closest to the heat exchanger tube (a) located at the flux-facing side of tube #12 at the inlet and exit end of the tube and (b) located on the top side of tube #19 at the inlet and exit ends of the tube. The inlet and exiting gas temperatures are shown in Figure 5-47. All of these data show stable temperatures had been achieved in the receiver.

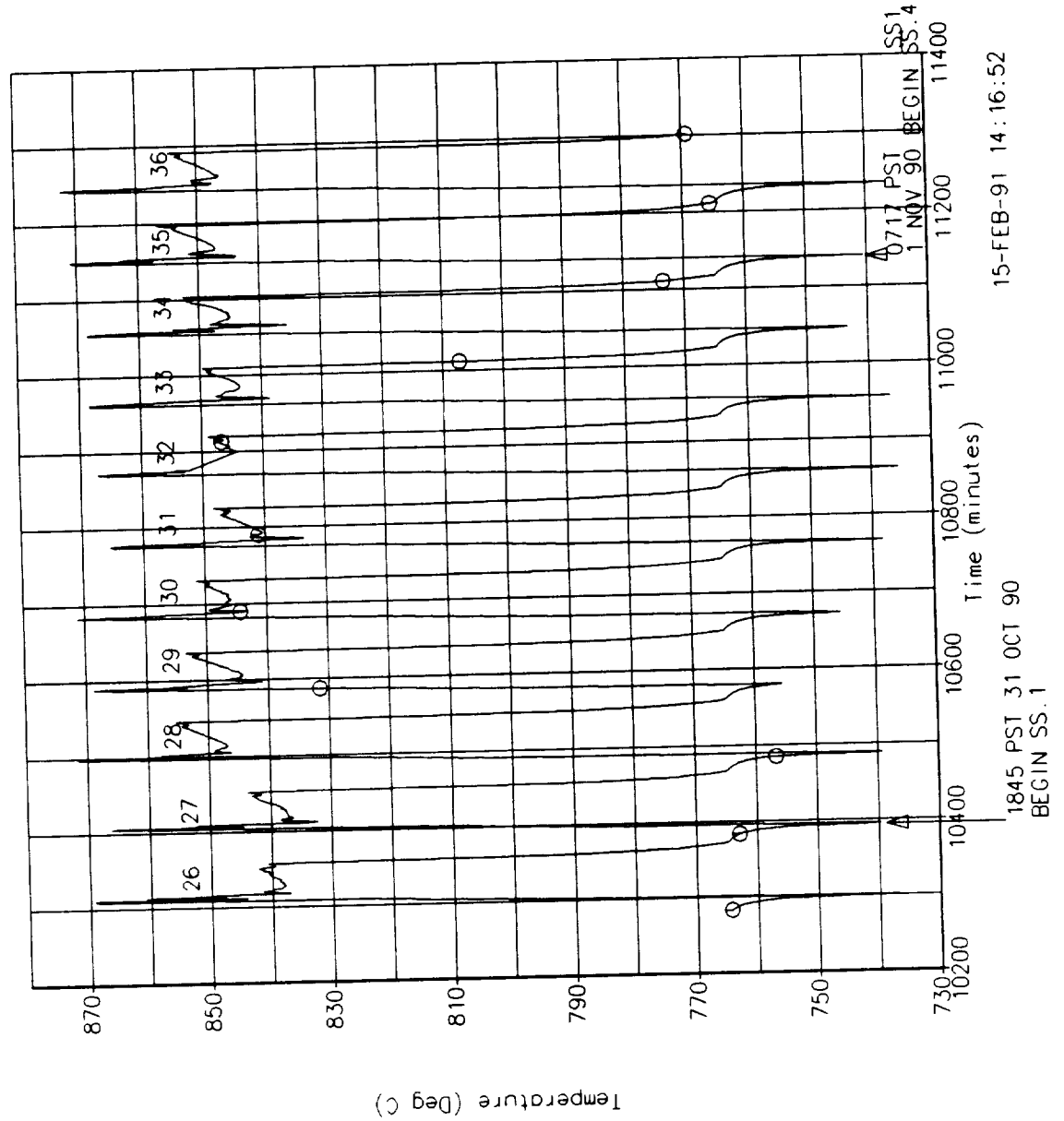


Figure 5-36: Flux-Facing Surface Temperature Located in the Convolution Valley at the Inlet End of Heat Storage Tube #4 During SS.1.

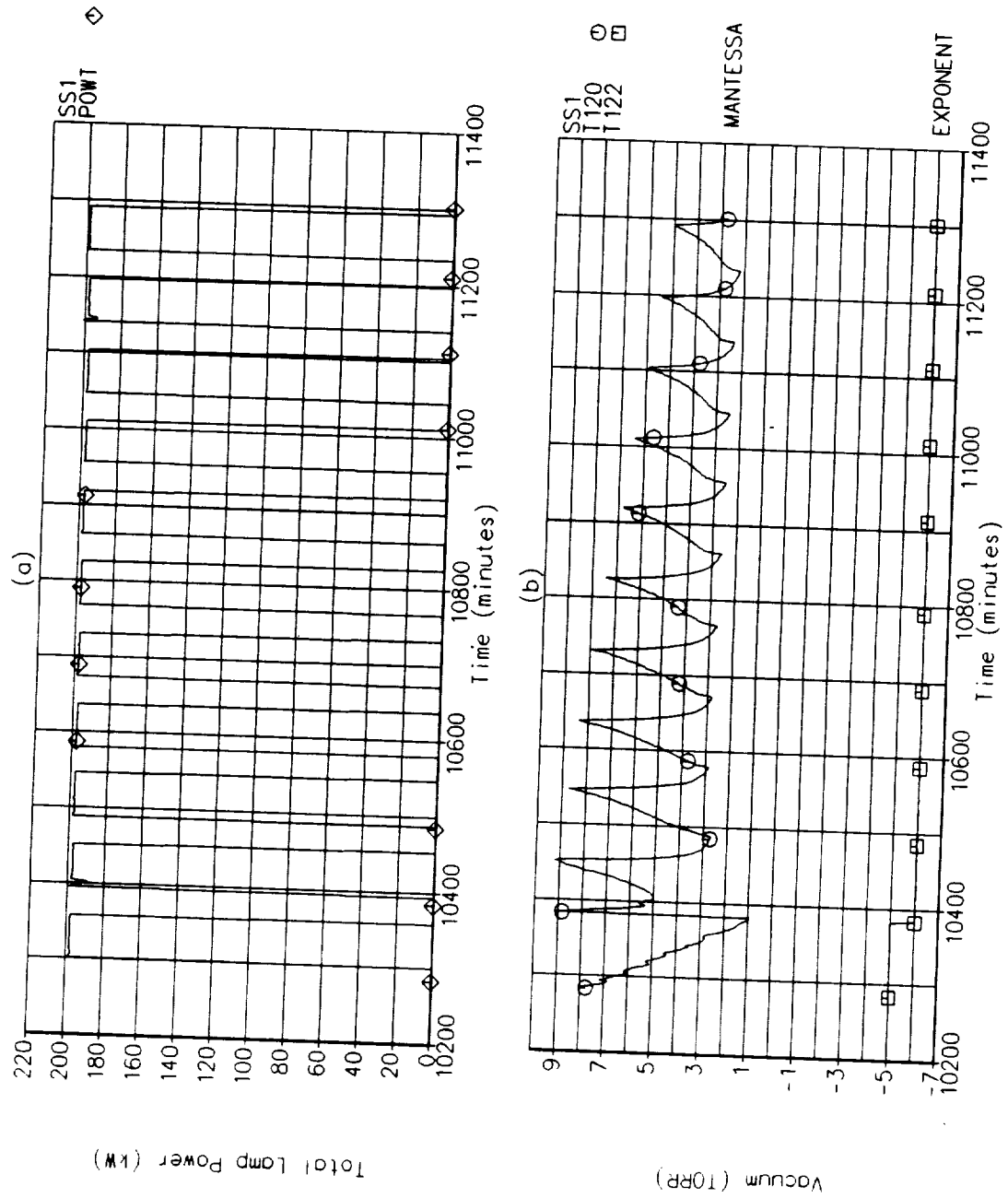


Figure 5-37: (a) Total Quartz Lamp Heater Power During SS.1; and (b) Chamber Vacuum Level During SS.1.



Figure 5-38: Beginning of Borescope Image Improvement As Solid Contamination Flakes Off Front Lens; Sunlit Period of Orbit #27.

ORIGINAL PAGE
BLACK AND WHITE PHOTOGRAPH

D180-32816-1



Figure 5-39: Continued Improvement in Borescope Image; Sunlit Period of Orbit #29.

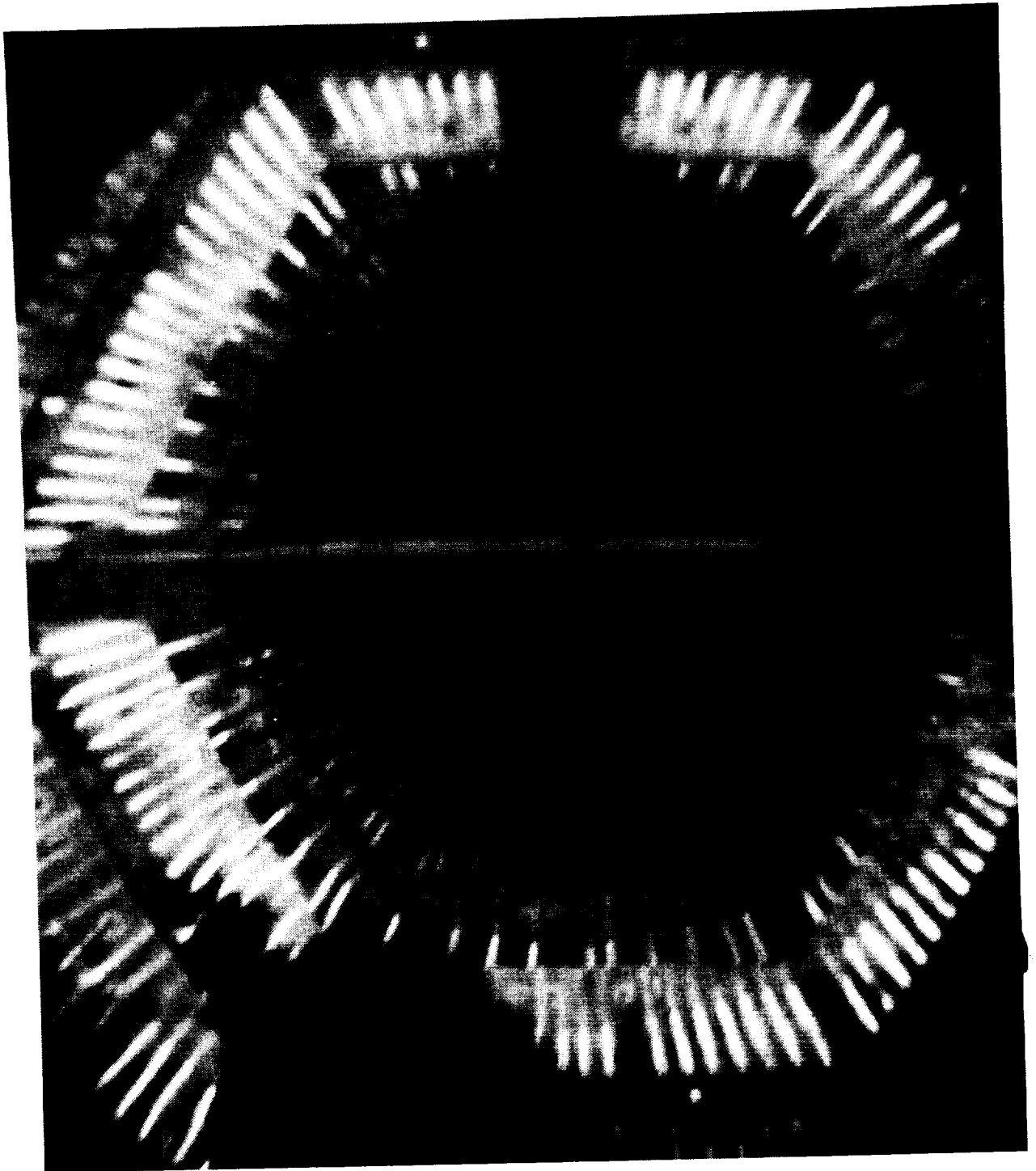


Figure 5-40: Return of Good Cavity Field of View Through the Borescope; Sunlit Period of Orbit #31.



Figure 5-41: Continued New Deposition of Solid Contamination of the Front Lens of Bore-scope; Orbit #34.

D180-32816-1

133

ORIGINAL PAGE
BLACK AND WHITE PHOTOGRAPH

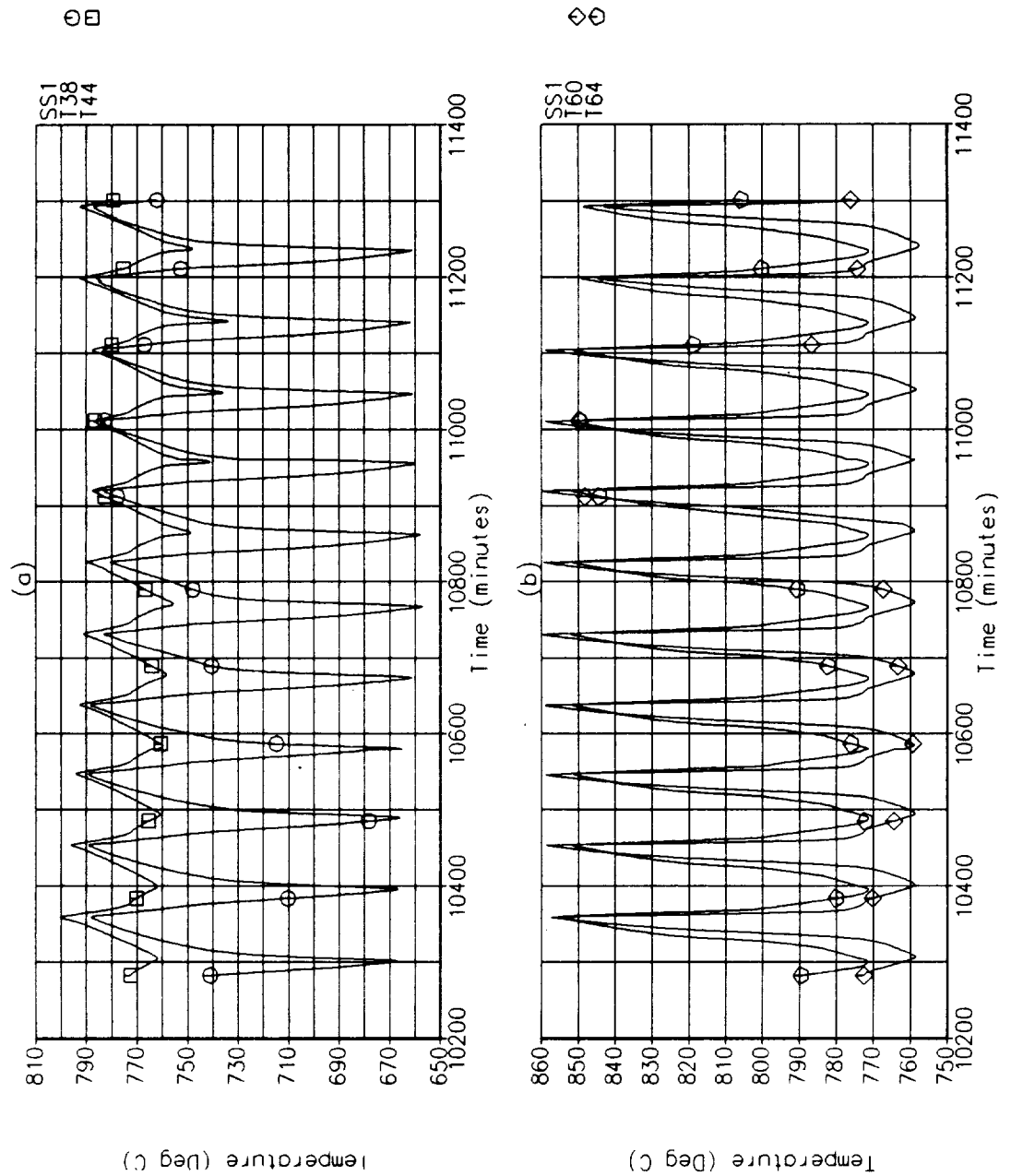


Figure 5-42: SS.1 Internal Salt Temperatures Closest to the Heat Exchanger Tube Located at the Inlet and Exit Ends of (a) the Flux-Facing Sides of Tube #12; and (b) the Top Sides of Tube #19.

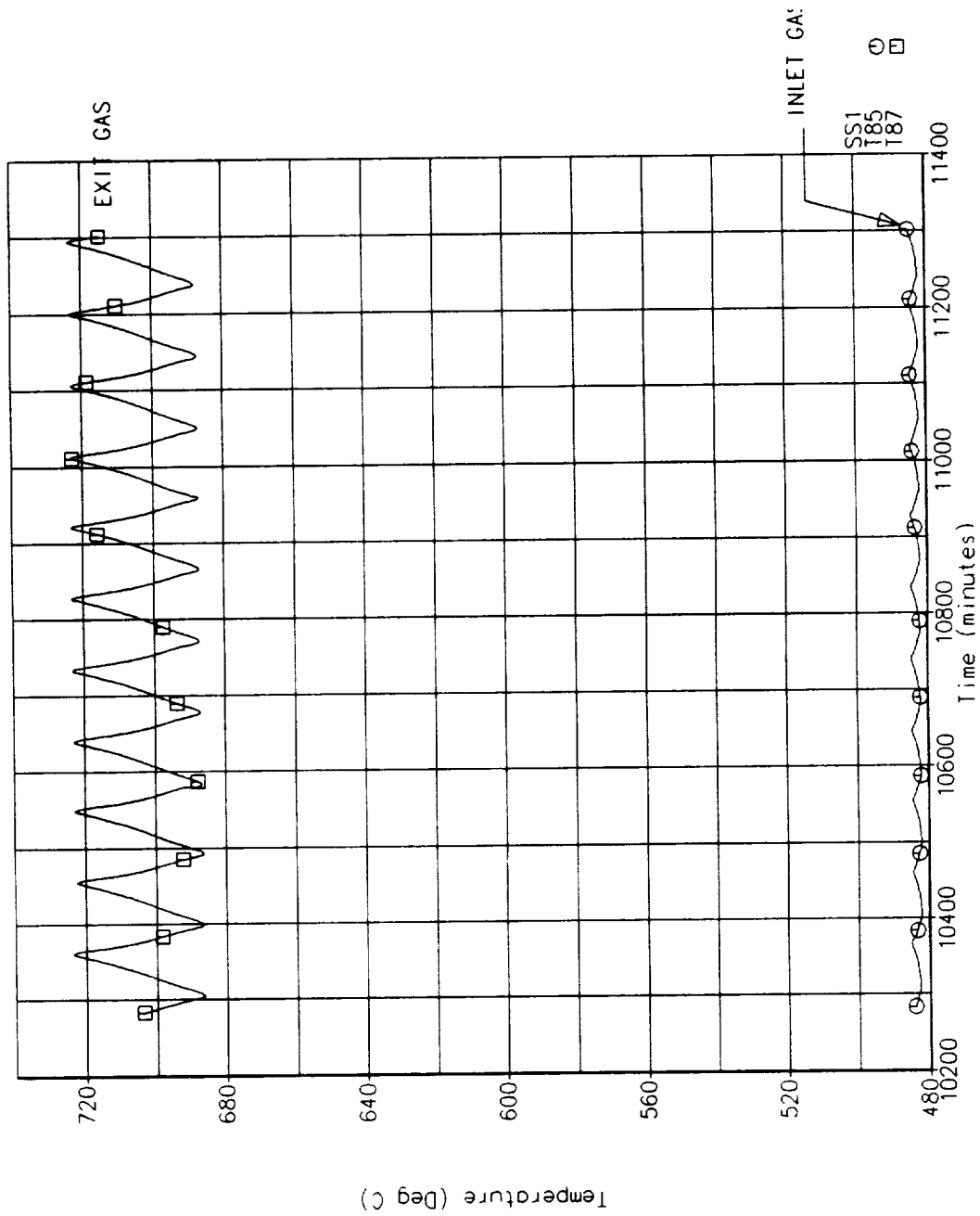


Figure 5-43: Inlet and Exiting Gas Temperatures During SS.1.

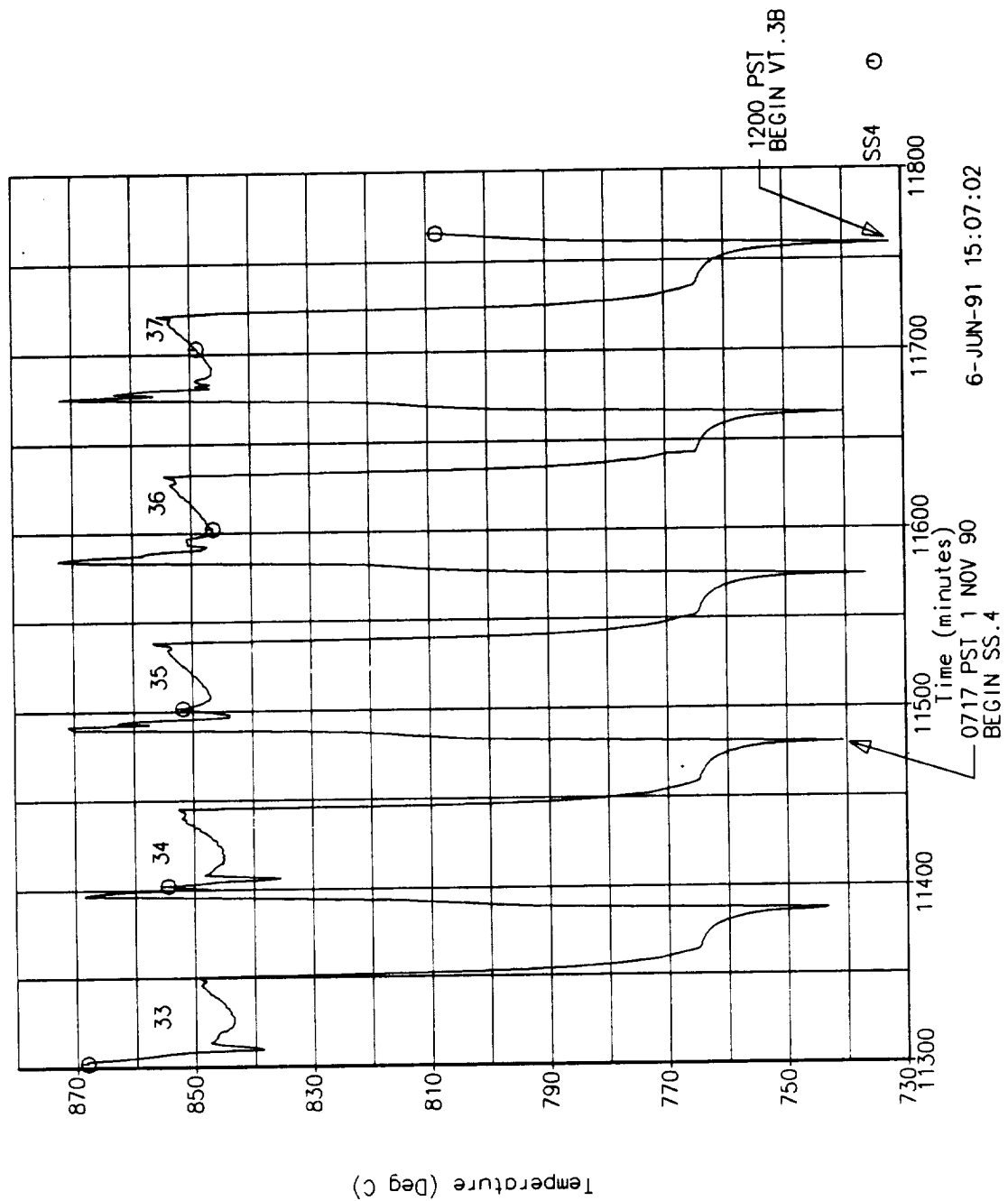


Figure 5-44: Flux-Facing Surface Temperature Located in the Convolution Valley at the Inlet End of Heat Storage Tube #4 During SS.4.

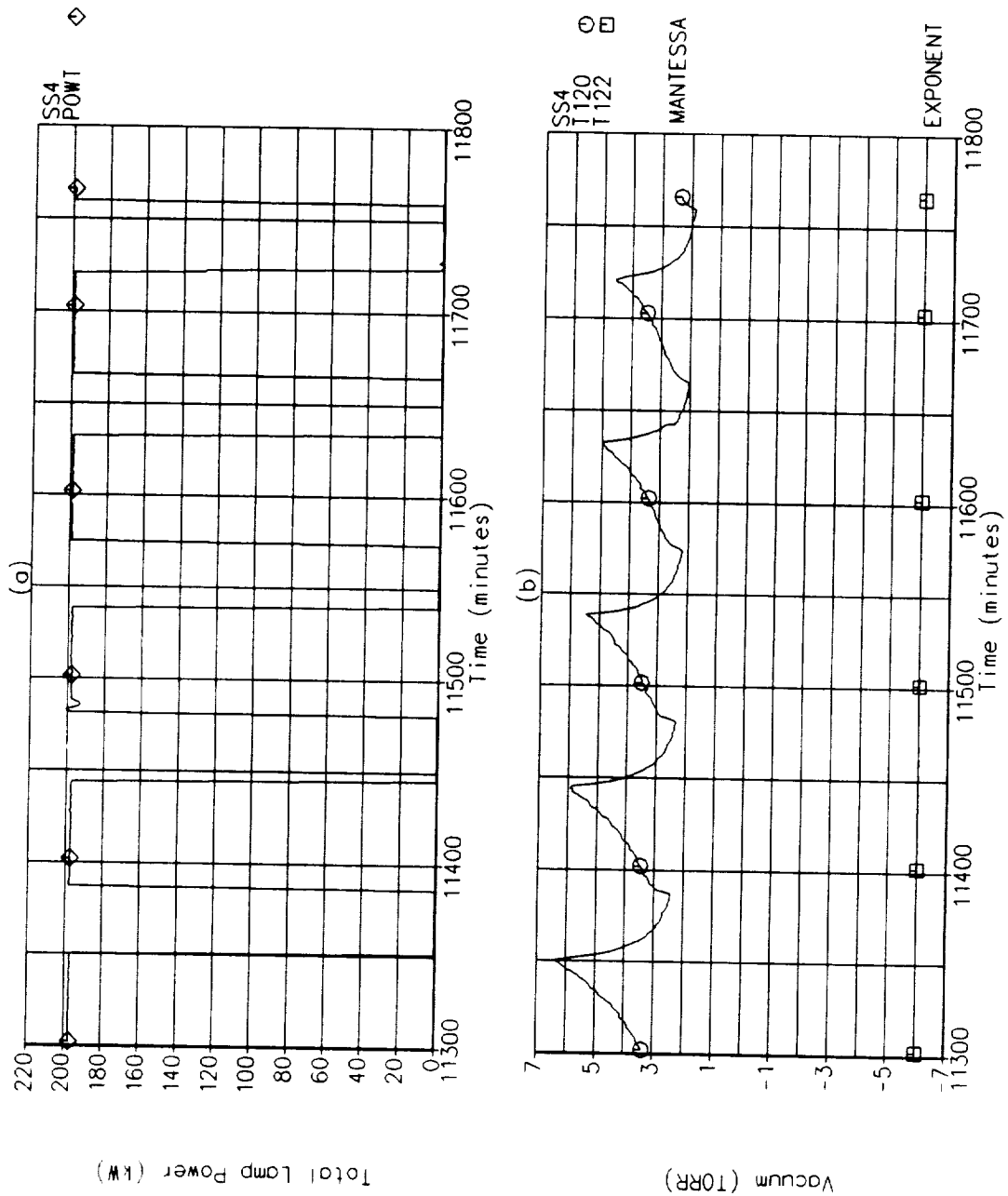


Figure 5-45: (a) Total Quartz Lamp Heater Power During SS.4; and (b) Chamber Vacuum Level During SS.4.

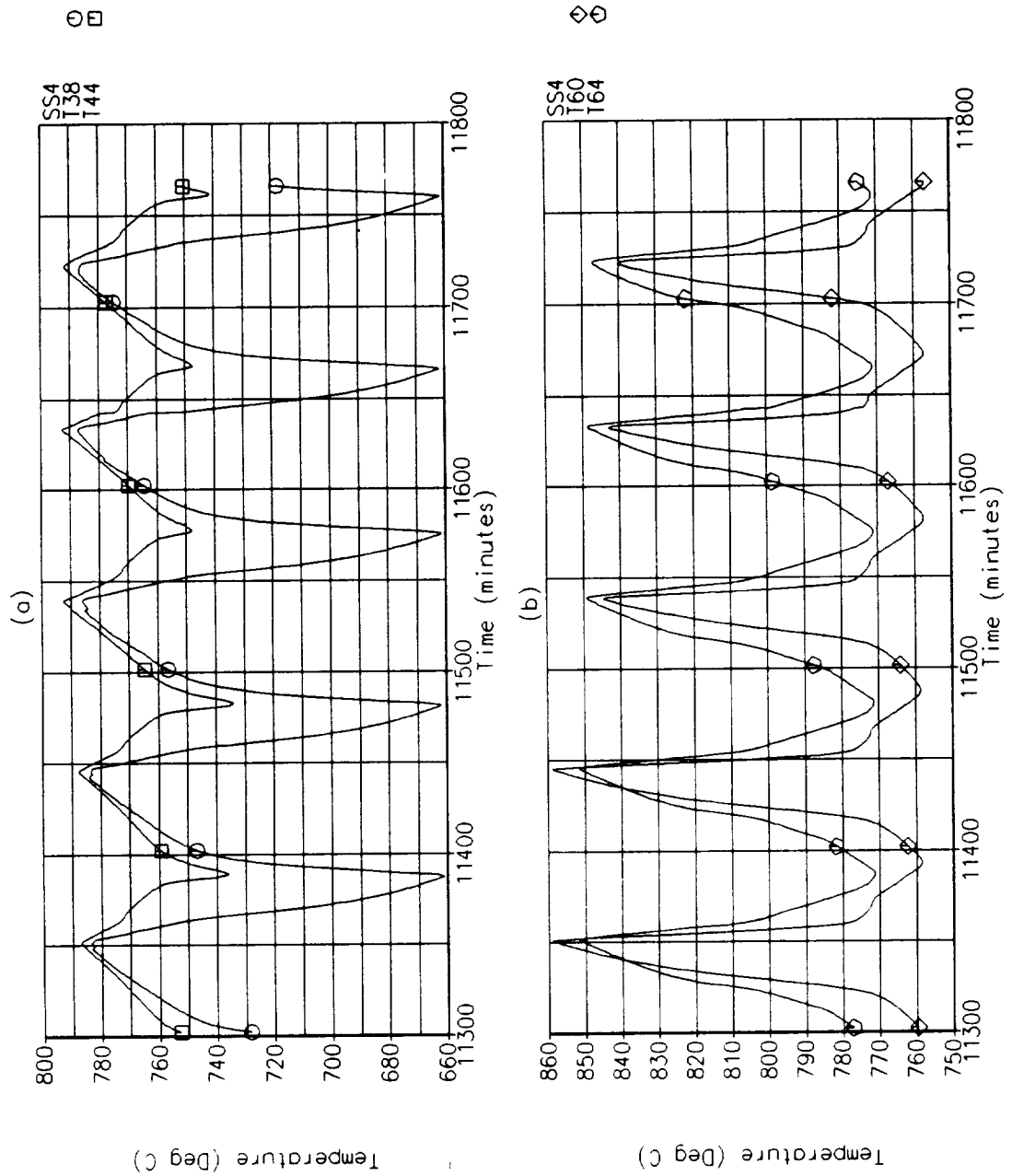


Figure 5-46: SS.4 Internal Salt Temperatures Closest to the Heat Exchanger Tube Located at the Inlet and Exit Ends of (a) the Flux-Facing Sides of Tube #12; and (b) the Top Sides of Tube #19.

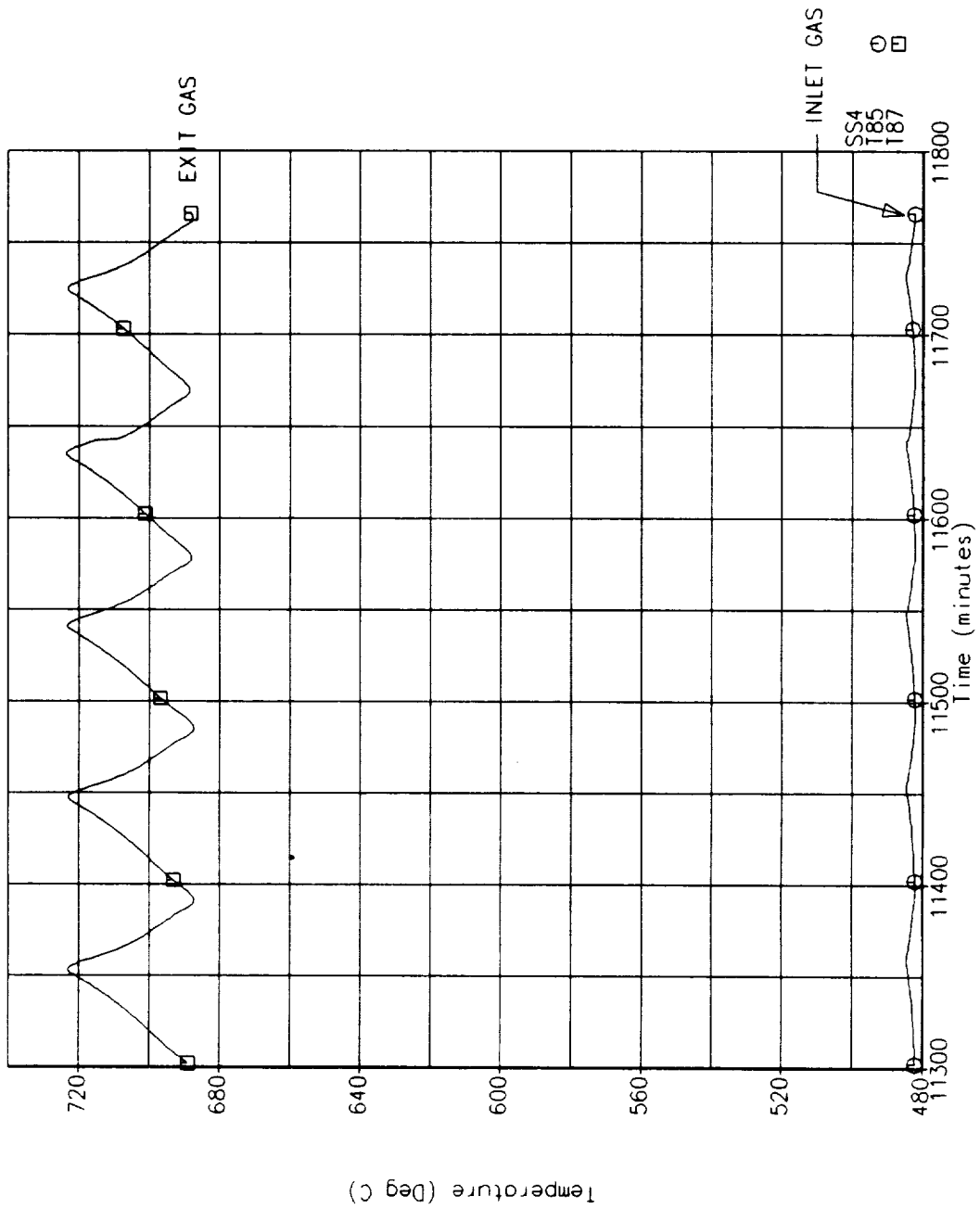


Figure 5-47: Inlet and Exiting Gas Temperatures During SS.4.

5.12 Modified Baseline Orbit, VT.3B

The baseline VT.3 orbital cycles conducted up to this point in the test matrix produced lower exiting gas temperatures than predicted by the thermal models. The difference appears to be related to higher losses through the receiver insulation (as measured during test modes VT.1 and VT.2). Therefore, a modified baseline test mode, called VT.3B, was conducted to characterize the receiver performance with additional heat input to the cavity to make up for the increased conductive losses.

Test mode VT.3B was begun with the sunlit period of orbit #38 on 1 November by increasing the total quartz lamp heater power by 7 kW to 205 kW. The percentage of the total power distributed to the 30 heater zones duplicated the normal baseline VT.3 power distribution. All other parameters were held constant at their VT.3 baseline values. The flux-facing surface temperature located in the convolution valley at the inlet end of heat storage tube #4 is shown in Figure 5-48 with the significant VT.3B events and orbit numbers noted on the plot. Figure 5-49 (a) shows the total quartz lamp heater power and (b) the chamber vacuum level through the VT.3B test period.

Normal vacuum levels continued through the VT.3B test mode and stabilized temperatures were achieved during orbit #43. No unplanned events occurred during this test mode except for a brief loss of zone 2B during orbit #38. Figure 5-50 shows the internal salt temperature closest to the heat exchanger tube (a) located at the flux-facing side of tube #12 at the inlet and exit end of the tube and (b) located on the top side of tube #19 at the inlet and exit ends of the tube. The inlet and exiting gas temperatures are shown in Figure 5-51. These data show stable temperatures had been achieved in the receiver. Figure 5-51 also shows that the control of the inlet gas temperature degraded to about $488^{\circ}\text{C} \pm 5^{\circ}\text{C}$ ($910^{\circ}\text{F} \pm 9^{\circ}\text{F}$). This was not seen by the test director during conduct of the test mode and, therefore, no change was made to correct the regenerator bypass valve setting.

5.13 Return to Baseline Orbit, VT.3A

A return to the baseline VT.3 equilibrium conditions was executed prior to the cool down to ambient for the cold soak start up test mode. This test mode, VT.3A, was conducted to see if any performance changes occurred during the testing period. It began with the sunlit period of orbit #44. Electrical power to the 30 quartz lamp heater zones was reduced back to the baseline distribution and all other parameters were held constant at their VT.3 values. The flux-facing surface temperature located in the convolution valley at the inlet end of heat storage tube #4 is shown in Figure 5-52 with the significant VT.3B events and orbit numbers noted on the plot. The cause of the rise in tube wall temperature level above that seen during test mode VT.3B (orbits 47-50) is not known but appears to be isolated to heat storage tube #4 as the trend is not duplicated in any of the other data. Figure 5-53 (a) shows the total quartz lamp heater power and (b) the chamber vacuum level through the VT.3B test period.

Normal vacuum levels continued through the VT.3A test mode and stabilized temperatures were achieved during orbit #50. No unplanned events occurred during this test mode. Figure 5-54 shows the internal salt temperature closest to the heat exchanger tube (a) located at the flux-facing side of tube #12 at the inlet and exit end of the tube and (b) located on the top side of tube #19 at the inlet and exit ends of the tube. The inlet and exiting gas temperatures are shown in Figure 5-55. These data show stable temperatures had been achieved in the receiver.

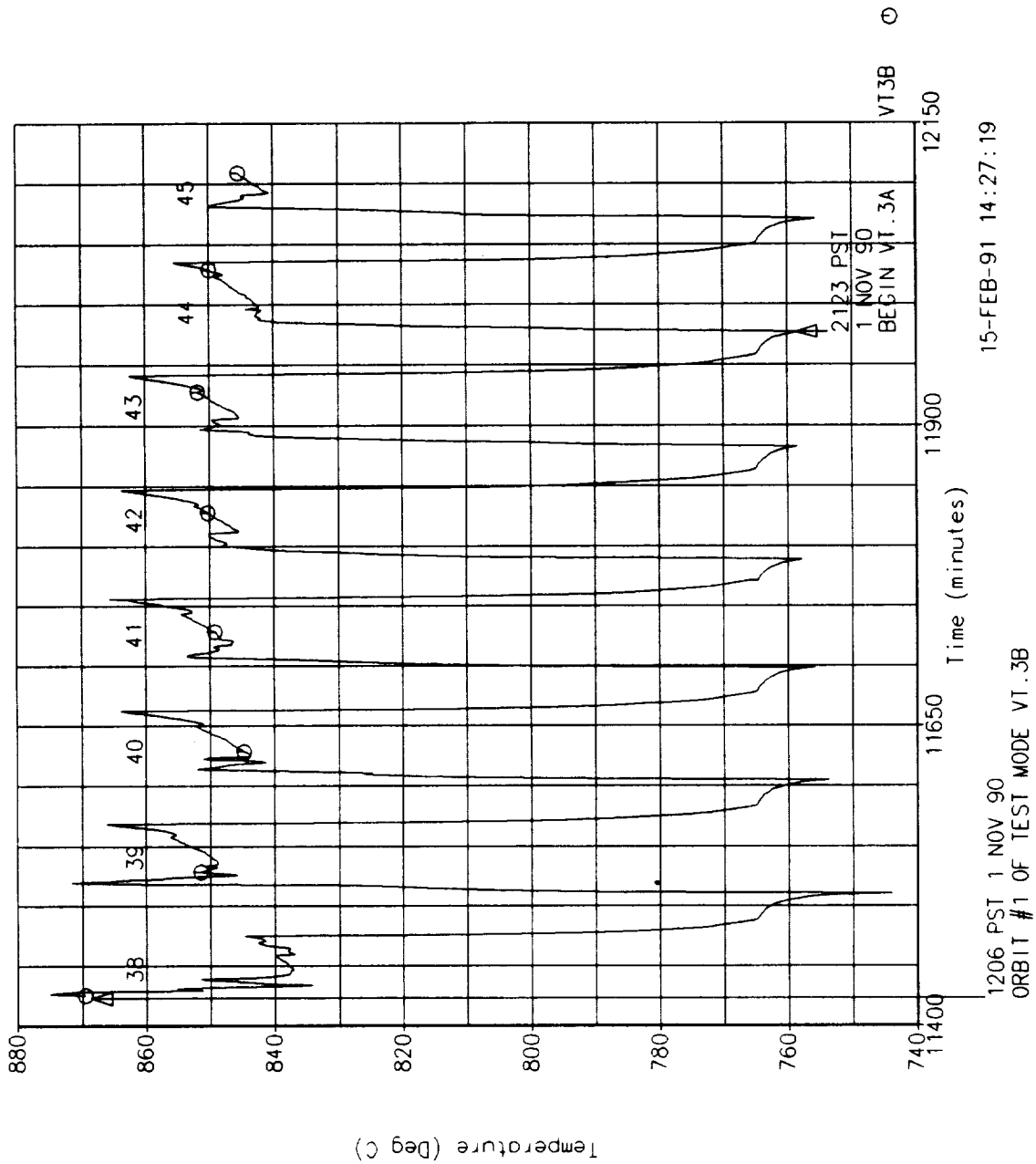


Figure 5-48: Flux-Facing Surface Temperature Located in the Convolution Valley at the Inlet End of Heat Storage Tube #4 During VT.3B.

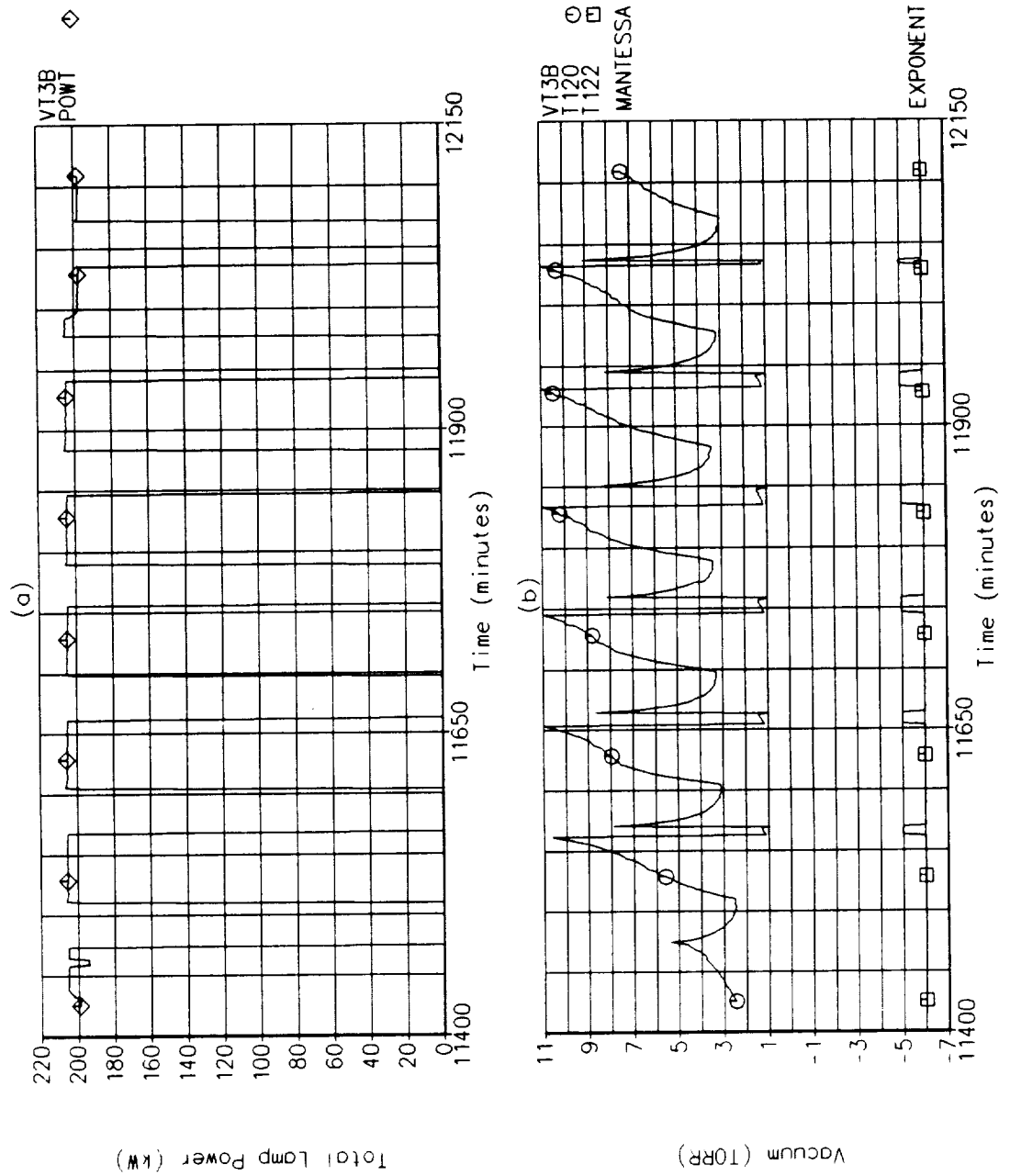


Figure 5-49: (a) Total Quartz Lamp Heater Power During VT.3B; and (b) Chamber Vacuum Level During VT.3B.

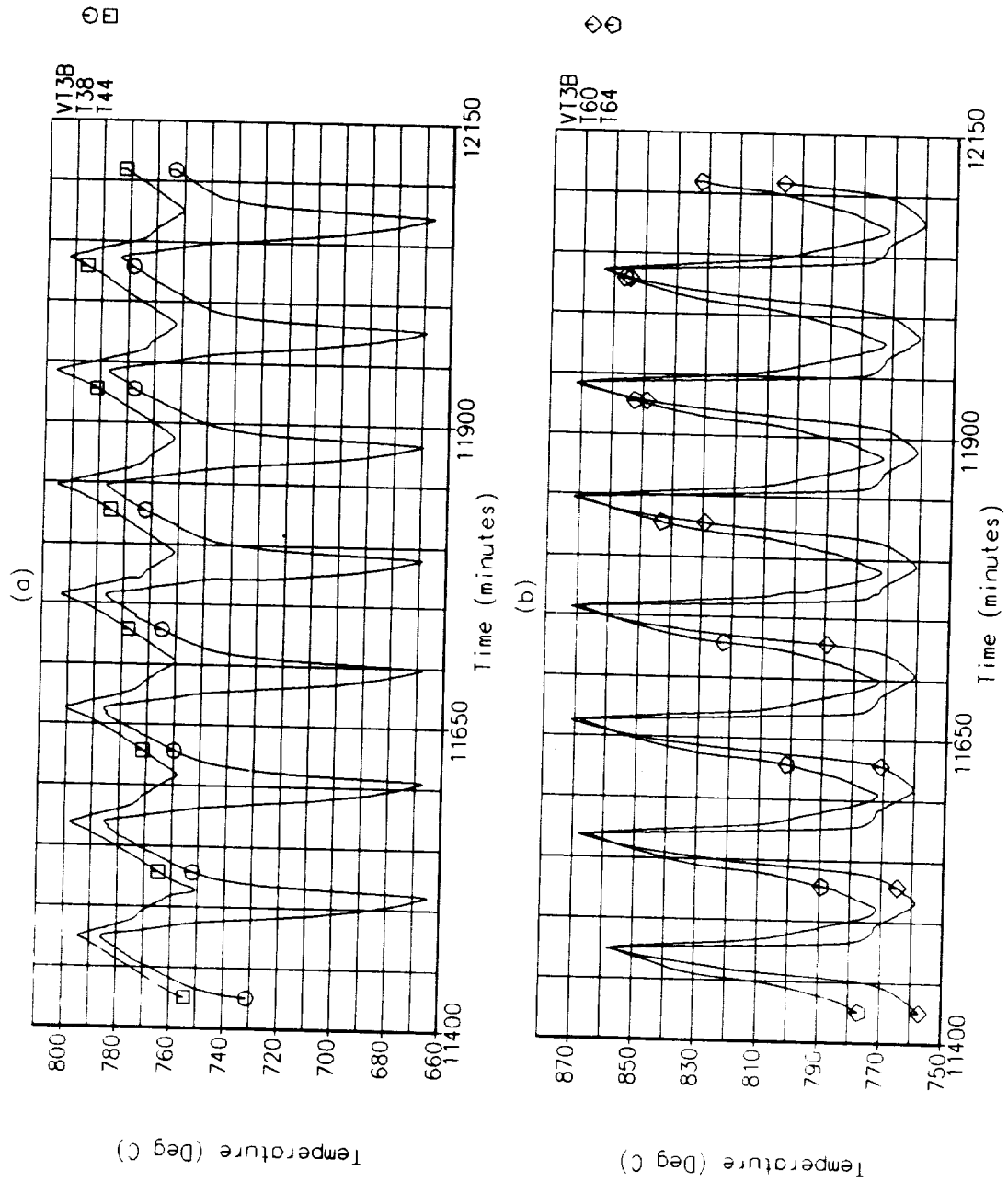


Figure 5-50: VT.3B Internal Salt Temperatures Closest to the Heat Exchanger Tube Located at the Inlet and Exit Ends of (a) the Flux-Facing Sides of Tube #12; and (b) the Top Sides of Tube #19.

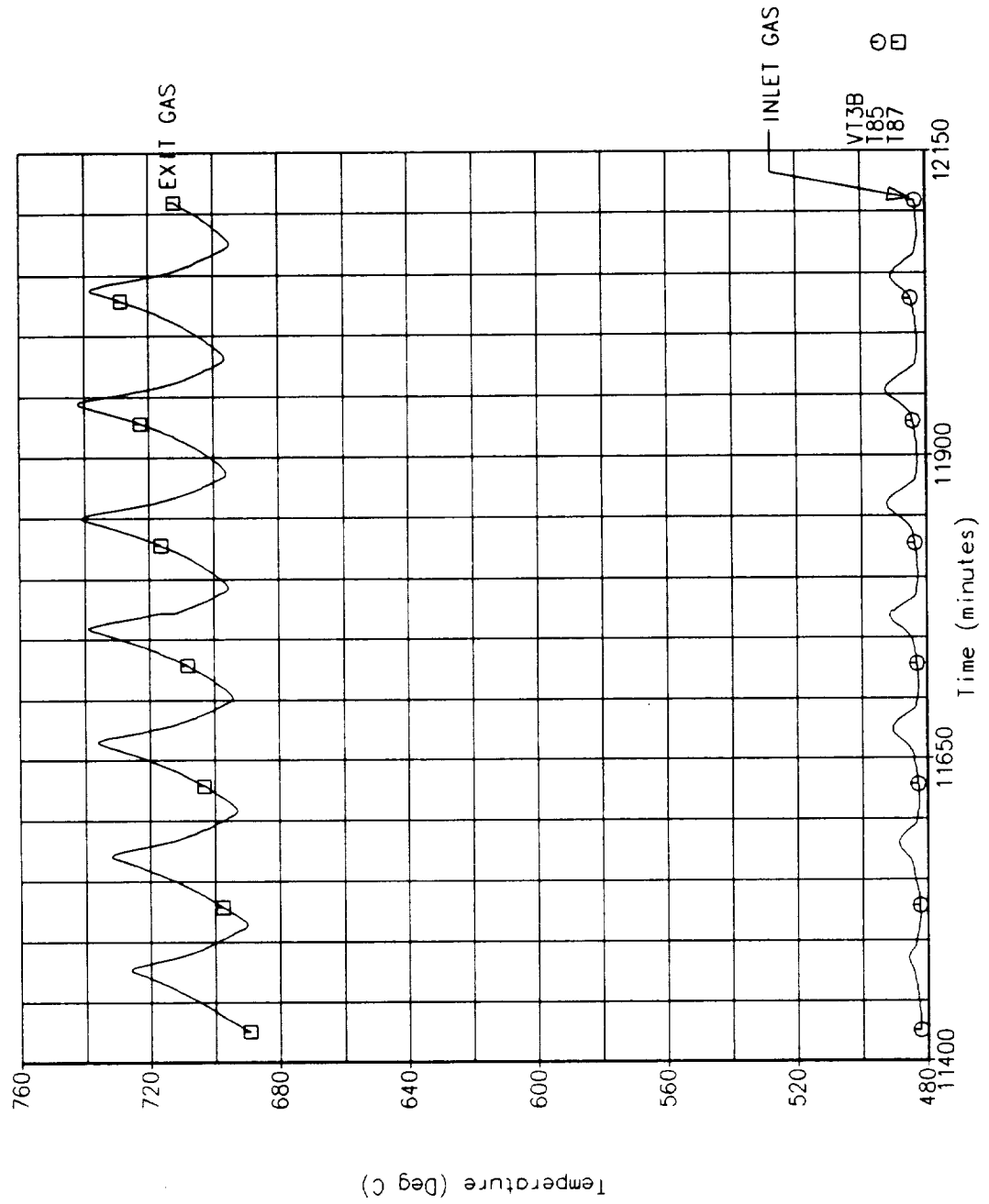


Figure 5-51: Inlet and Exiting Gas Temperatures During VT.3B.

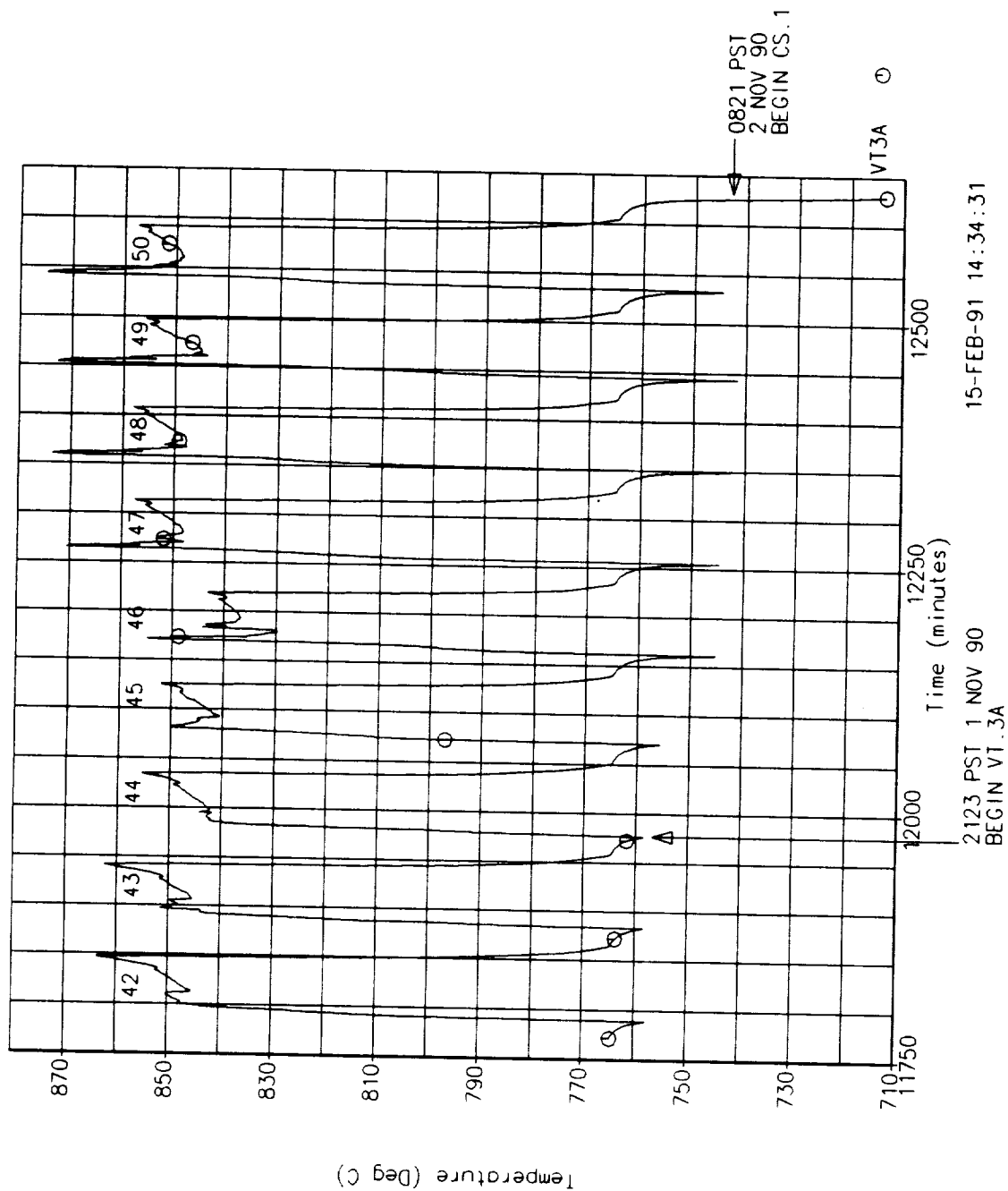


Figure 5-52: Flux-Facing Surface Temperature Located in the Convolution Valley at the Inlet End of Heat Storage Tube #4 During VT.3A.

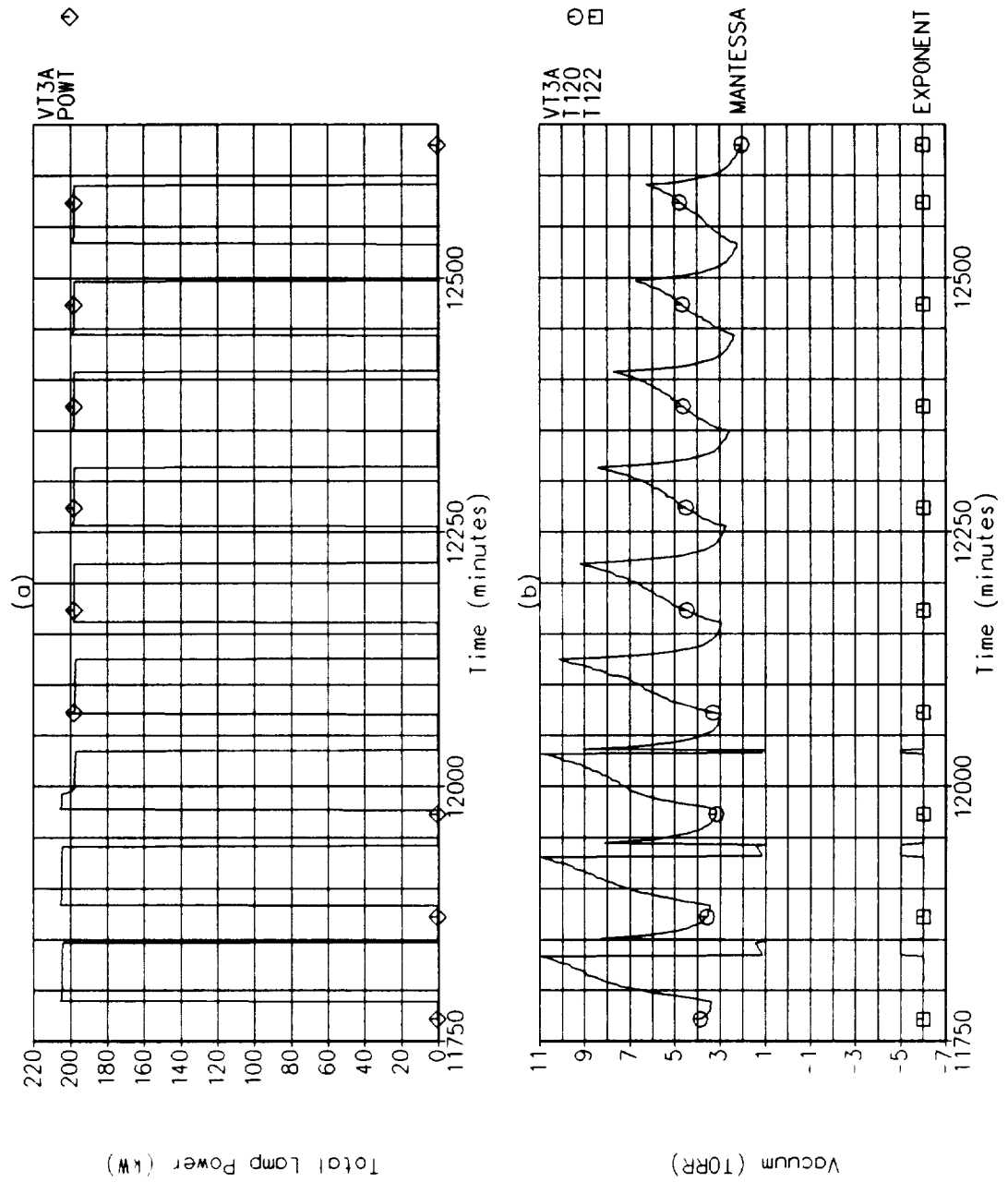


Figure 5-53: (a) Total Quartz Lamp Heater Power During VT.3A; and (b) Chamber Vacuum Level During VT.3A.

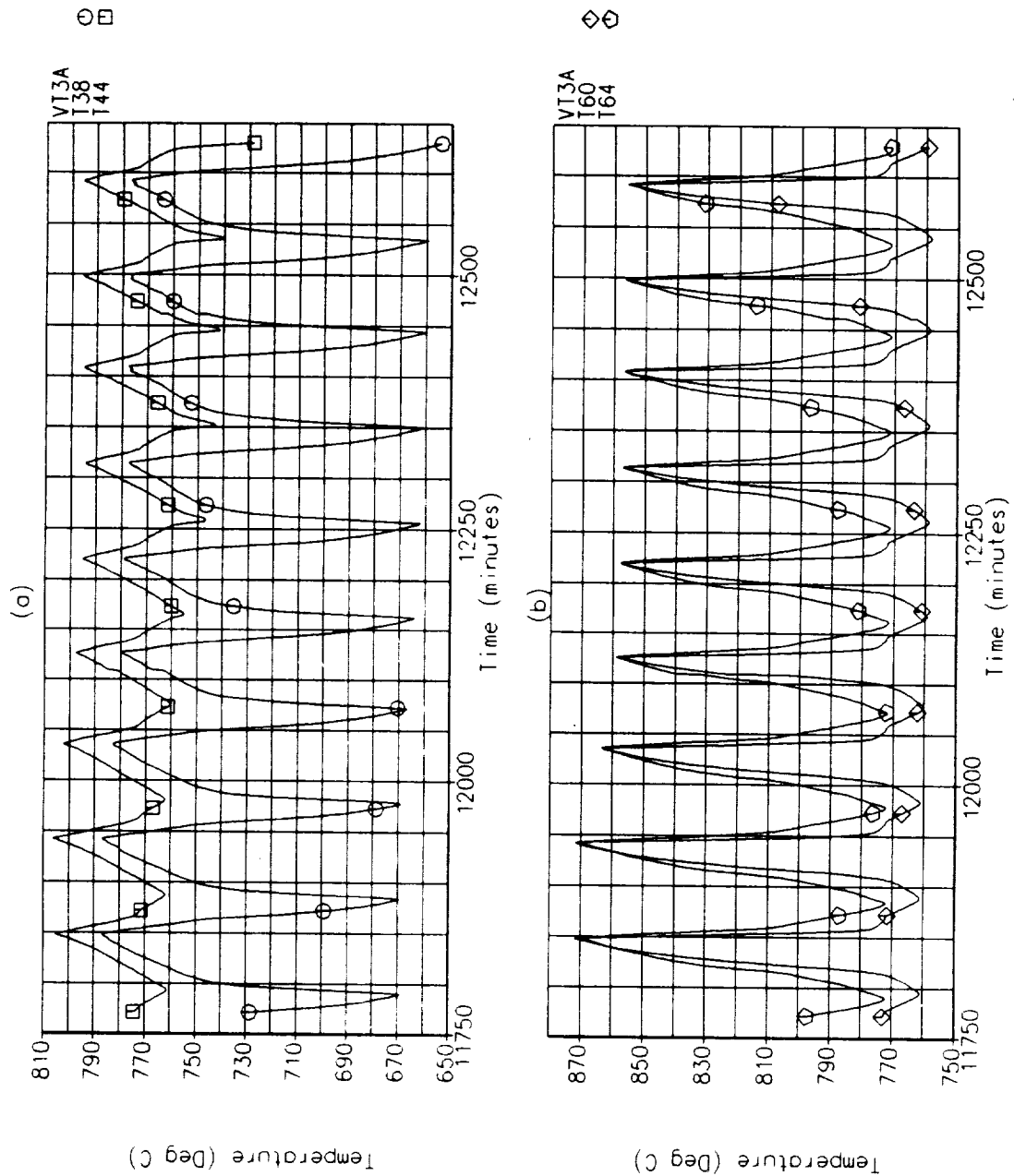


Figure 5-54: VT.3A Internal Salt Temperatures Closest to the Heat Exchanger Tube Located at the Inlet and Exit Ends of (a) the Flux-Facing Sides of Tube #12; and (b) the Top Sides of Tube #19.

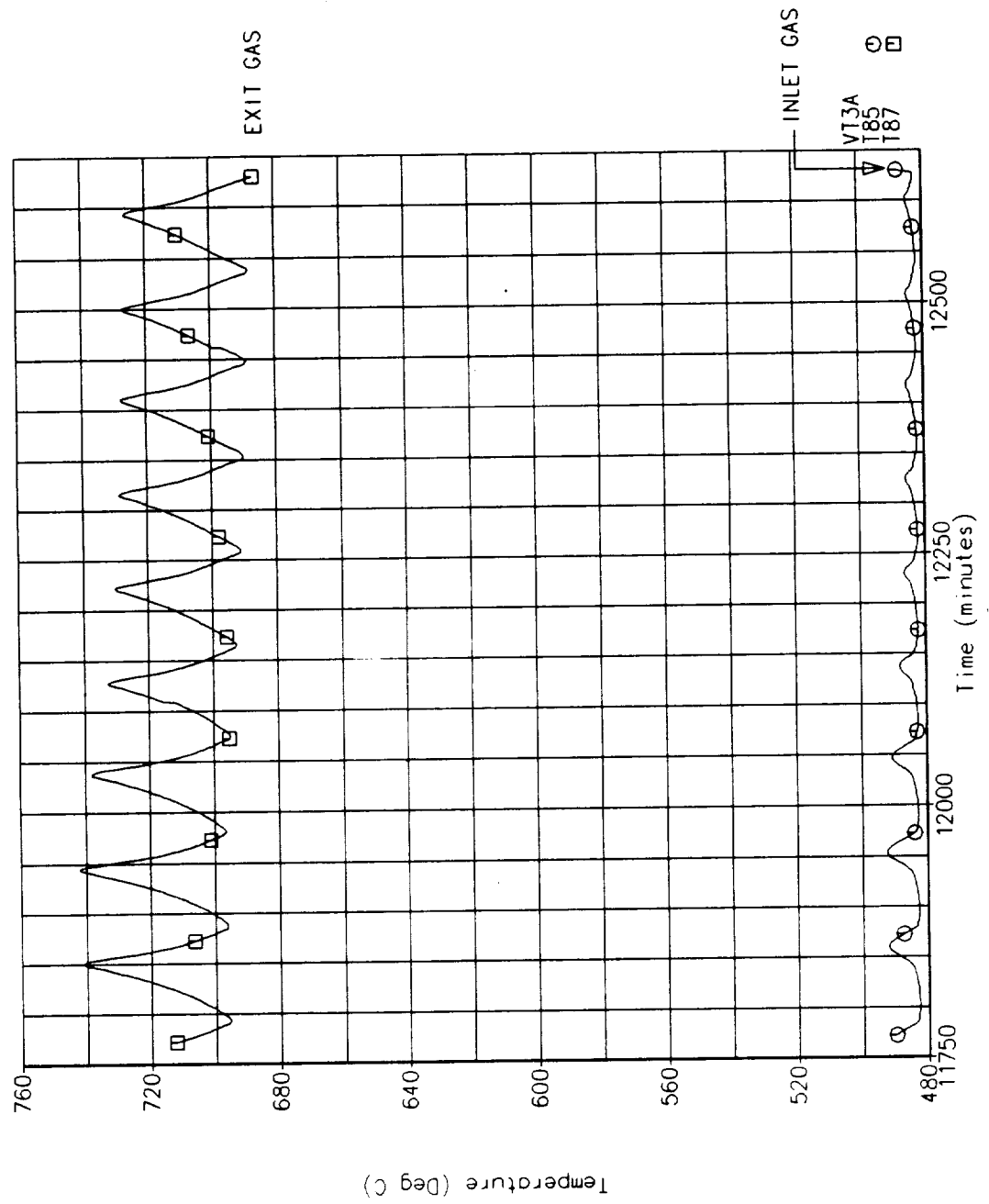


Figure 5-55: Inlet and Exiting Gas Temperatures During VT.3A.

5.14 Shutdown to Cold Soak, CS.1

Shut down to ambient was begun after the normal 36 minute eclipse period of orbit #50. The CBC engine simulator was kept running with a mass flow rate of 53 kg/min until the gas temperature exiting the receiver dropped below 538°C (1000°F). The blower bypass valve was then completely shut off forcing full flow through the receiver and the regenerator bypass valves were fully opened to obtain the coolest possible inlet gas temperature. A history of the gas flow rate is given in Figure 5-56. The sudden drop in gas flow rate to about 37 kg/min was a quick test to measure the minimum flow rate possible with the gas at cooler temperatures.

The flux-facing surface temperature located in the convolution valley at the inlet end of heat storage tube #4 is shown in Figure 5-57. Figure 5-58 (a) shows the exit gas temperature and (b) plots the difference in temperatures of the inlet and exit gas. The CBC was operated until the temperature difference dropped below 1°C.

Chamber vacuum dropped back into the 10^{-7} torr range as cavity temperatures lowered. Thus, very low vacuum was present for the cold soak start up test mode CS.3. No unplanned events occurred during cool down to ambient. Figure 5-59 shows the internal salt temperature closest to the heat exchanger tube (a) located at the flux-facing side of tube #12 at the inlet and exit end of the tube and (b) located on the top side of tube #19 at the inlet and exit ends of the tube.

An inspection of the receiver was desired to ascertain the condition of the cavity and heat storage tubes prior to conducting the cold soak start up test mode. However, a lack of remaining test conduct program funds did not allow this to occur. It was originally hoped that the optical borescope would provide some inspection capability but, as the cavity photographs presented previously have shown, little or none of the heat storage tubes can be seen because of heater blockage.

5.15 Cold Start Up Tests, CS.3

This test mode simulates a rapid start up from a near isothermal cold soak temperature. It was originally planned to cold soak the receiver cavity to -88°C (-126°F) but the limited test funds available when testing began required that the cold soak time line be substantially reduced (approximately 200 hours are required to cold soak to -88°C). The difference between start up at -88°C and +27°C (80°F) represents only a few minutes shorter time required to heat up to the desired conditions.

The test mode was initiated on 2 November with the receiver cavity at about 27°C and chamber vacuum at 7×10^{-7} torr. The 30 quartz lamp zones were powered up to their VT.3 power levels with no gas flow through the receiver. A 58 minute sun, 36 minute eclipse duty cycle was used for this test mode. The flux-facing surface temperature located in the convolution valley at the inlet end of heat storage tube #4 is shown in Figure 5-60. Significant events and orbit numbers are noted on the figure. The CBC blower was activated after 15 minutes into the 2nd sunlit period. The blower bypass valve was set to full open to reduce the gas flow rate to the minimum possible. Gas flow rate and the inlet static pressure to the receiver are shown in Figure 5-61 (a) and (b) respectively.

The first two orbital periods proceeded without any significant problems. However, after orbit #52, heater zones began to show signs of corona in the cavity. The ADRT test log given in Appendix A describes all of the events as they occurred during this period of test. Heater zone 2B experienced the most difficulties and continually shut itself off. Figure 5-62 (a) shows the total quartz lamp heater power and (b) the chamber vacuum level through the VT.3B test period.

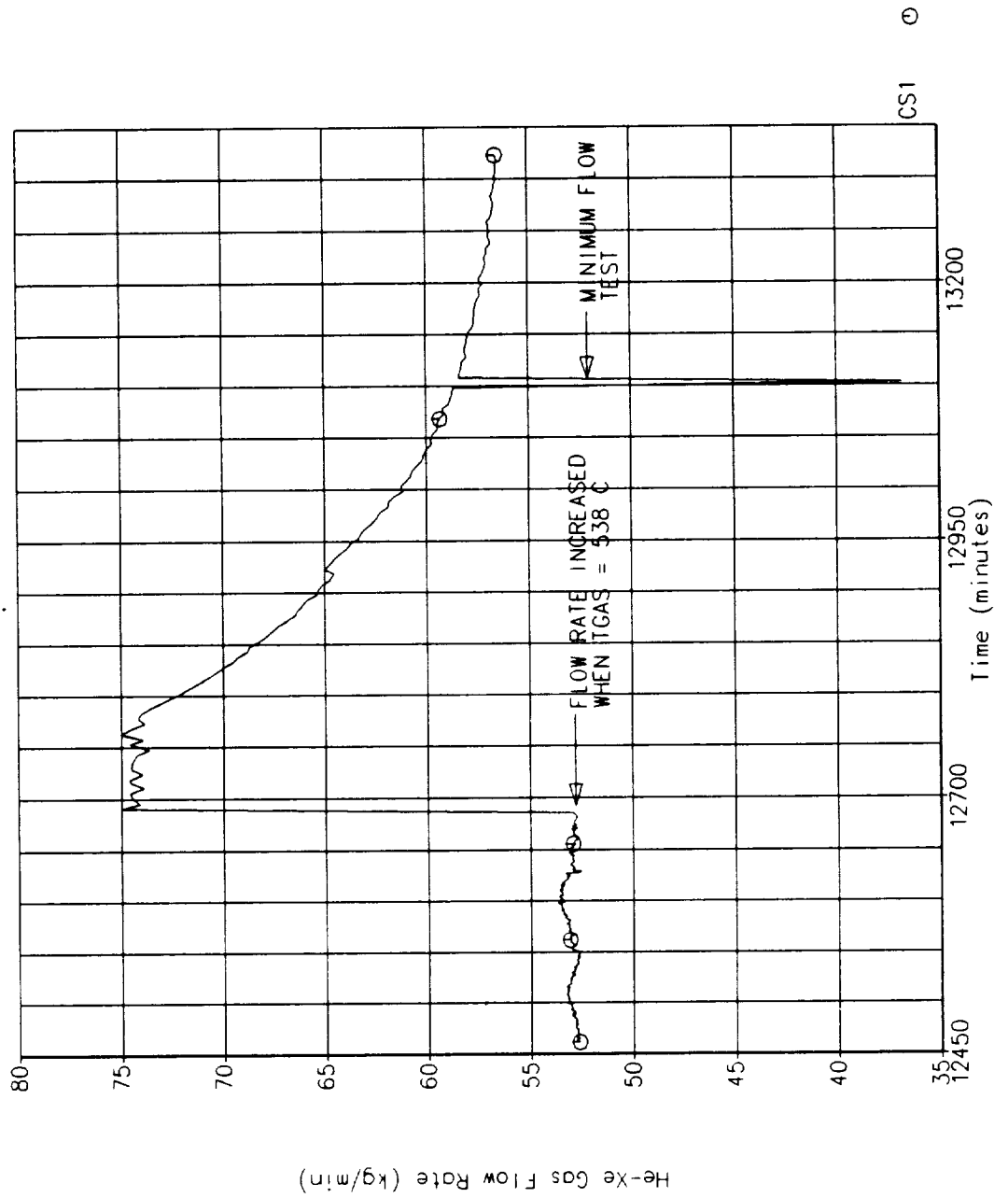


Figure 5-56: Helium-Xenon Gas Flow Rate During CS.1.

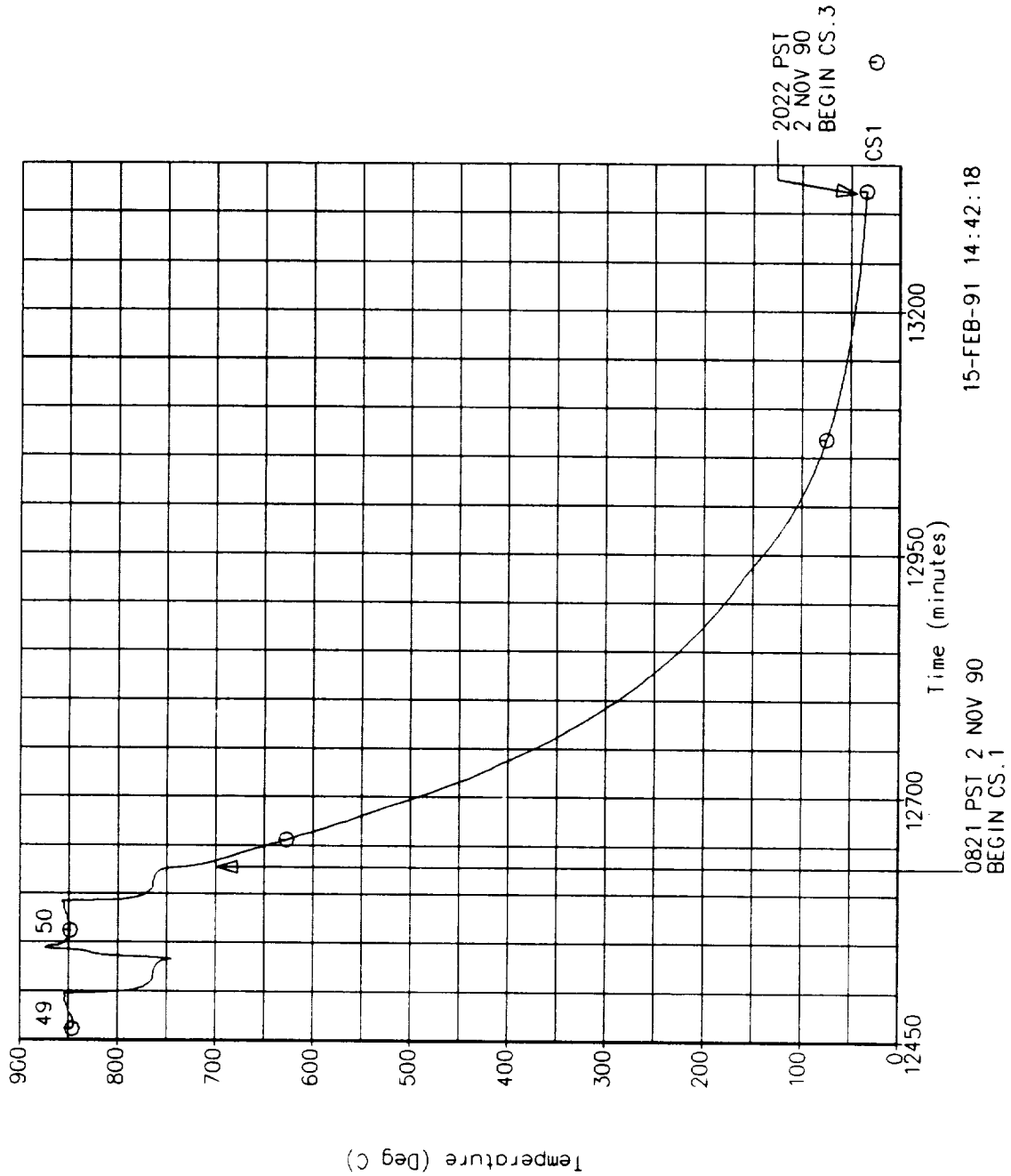


Figure 5-57: Flux-Facing Surface Temperature Located in the Convolution Valley at the Inlet End of Heat Storage Tube #4 During CS.1.

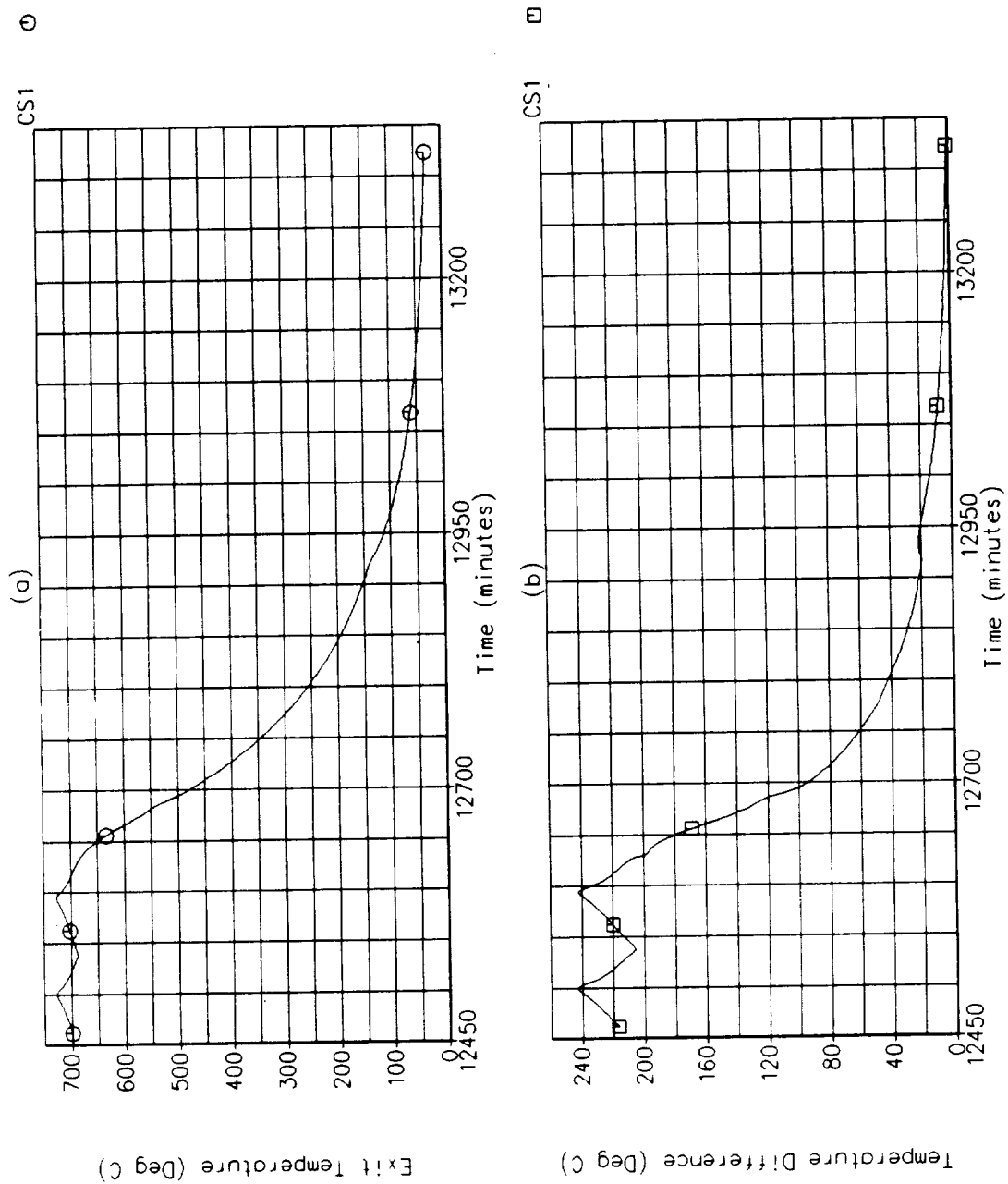


Figure 5-58: (a) Exiting Helium-Xenon Gas Temperature During CS.1; and (b) Temperature Difference of Gas Between Inlet and Exit During CS.1.

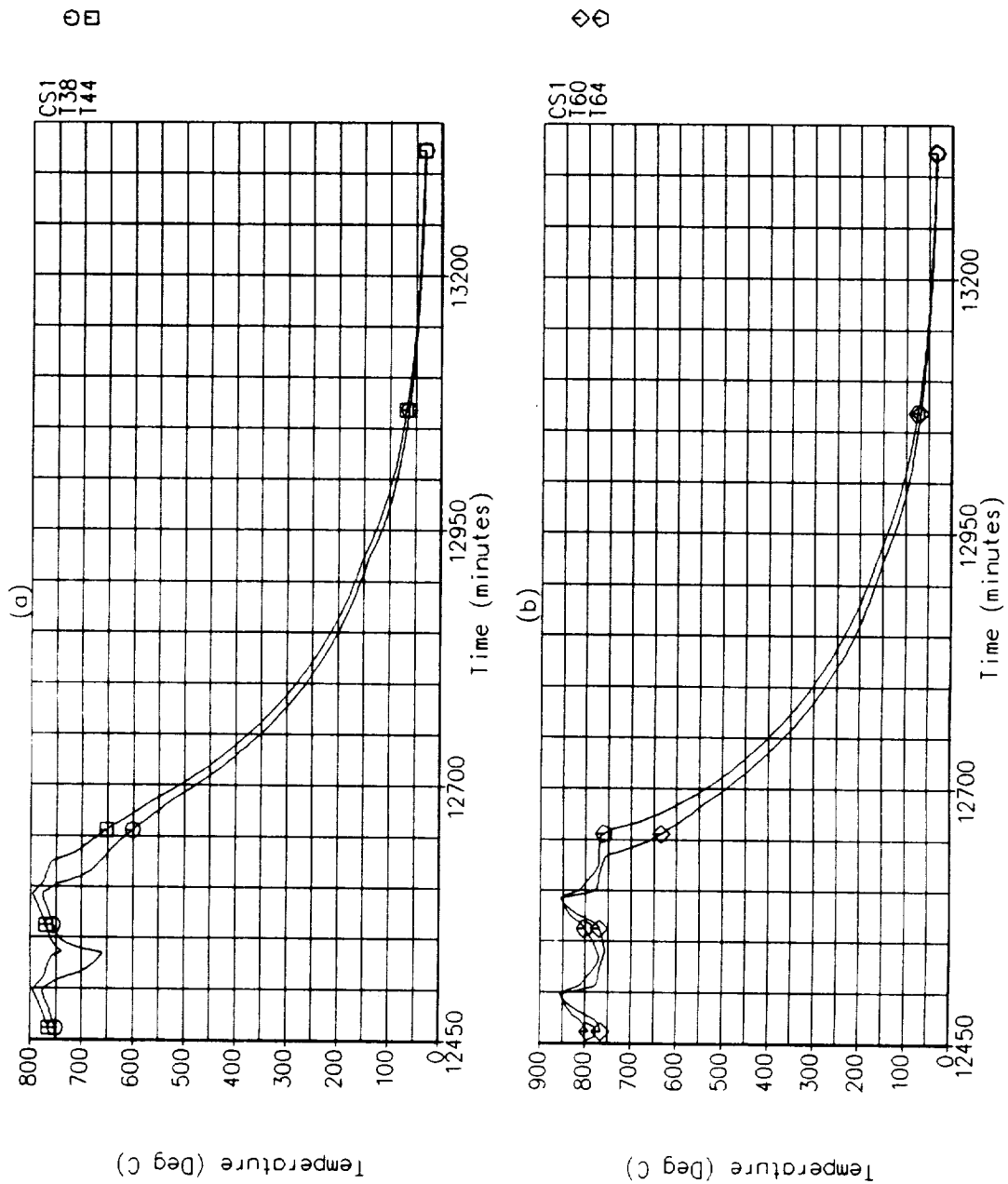


Figure 5-59: CS.1 Internal Salt Temperatures Closest to the Heat Exchanger Tube Located at the Inlet and Exit Ends of (a) the Flux-Facing Sides of Tube #12; and (b) the Top Sides of Tube #19.

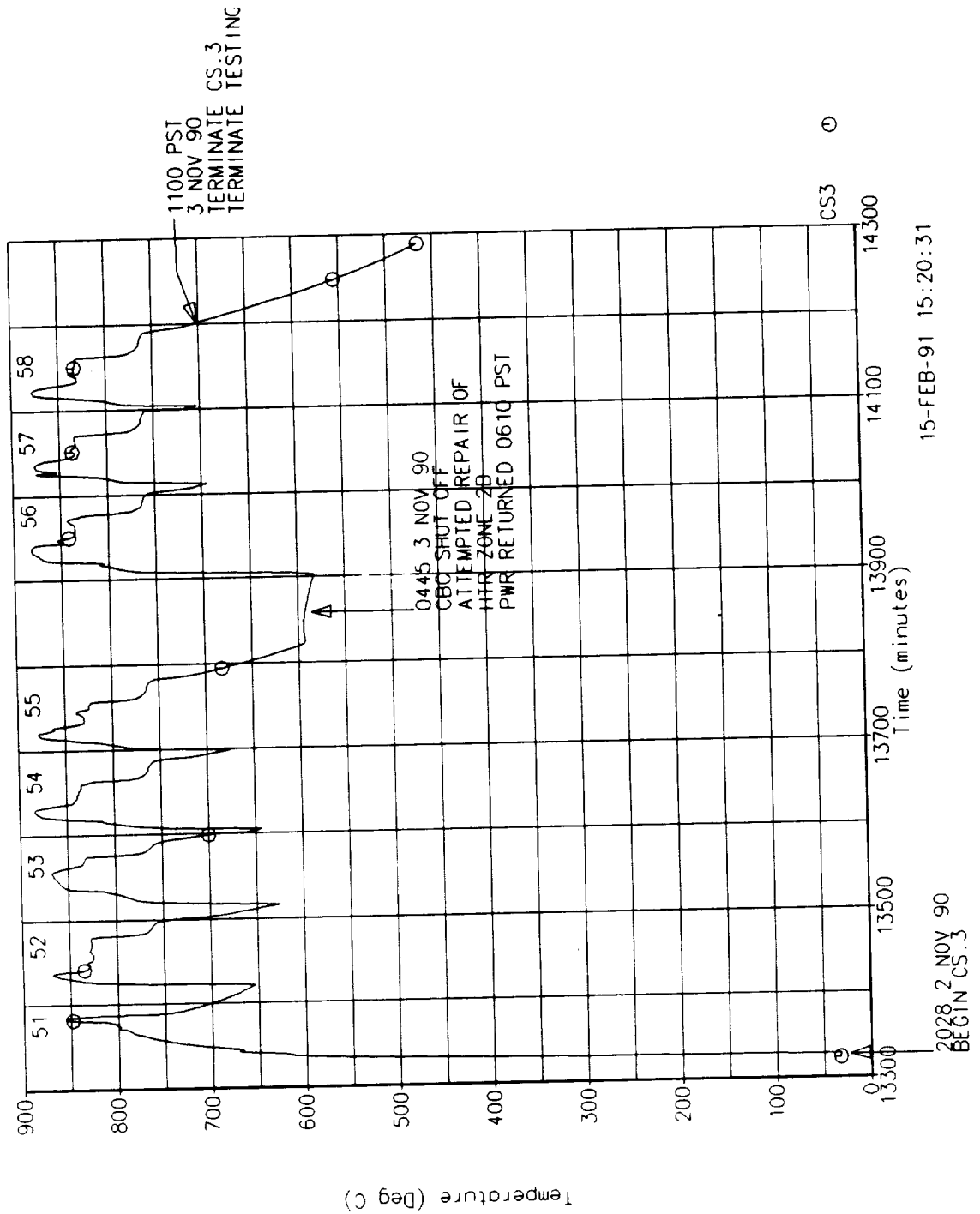


Figure 5-60: Flux-Facing Surface Temperature Located in the Convolution Valley at the Inlet End of Heat Storage Tube #4 During CS.3.

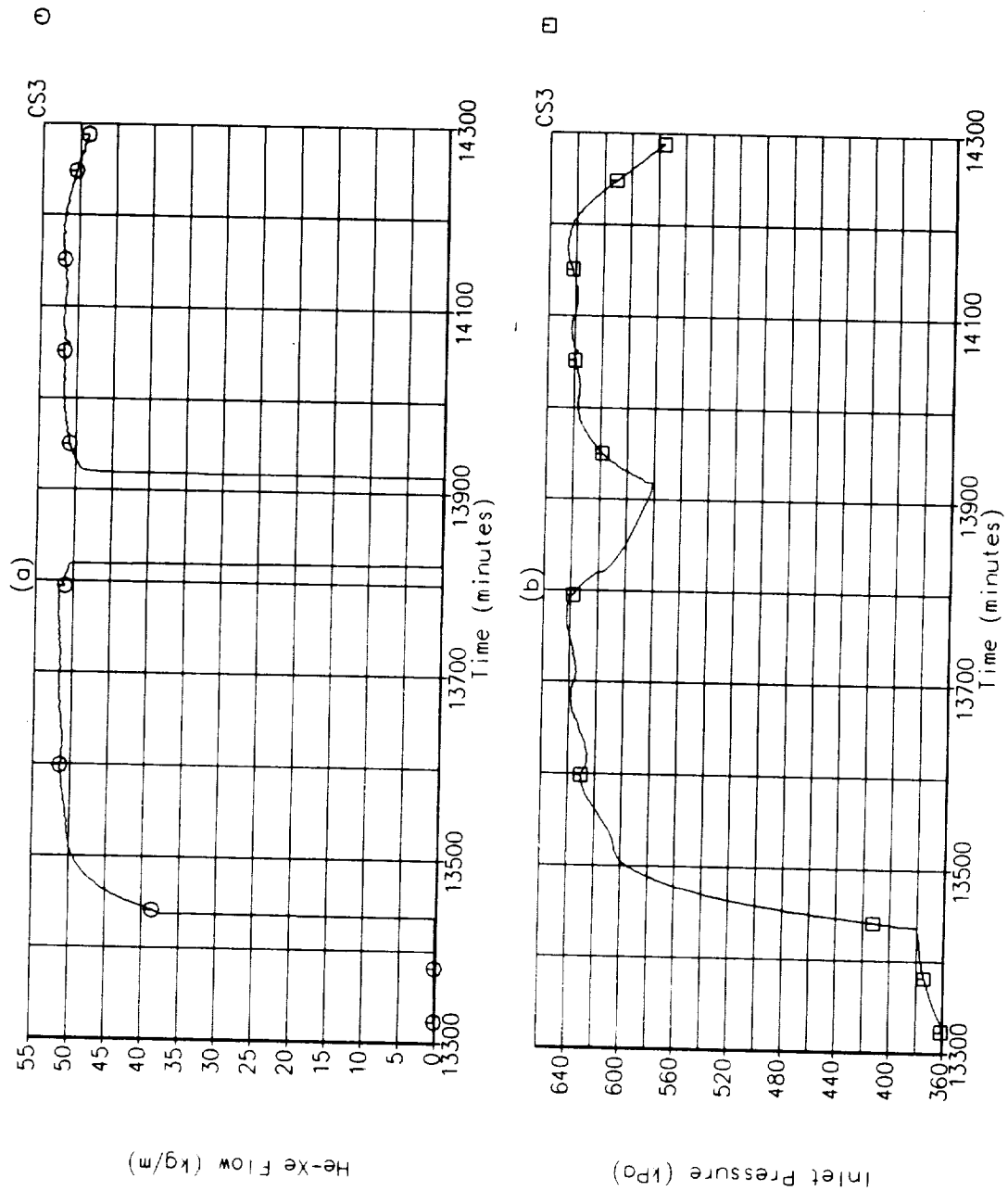


Figure 5-61: (a) Helium-Xenon Gas Flow Rate During CS.3; and (b) Static Pressure at the Receiver Inlet During CS.3.

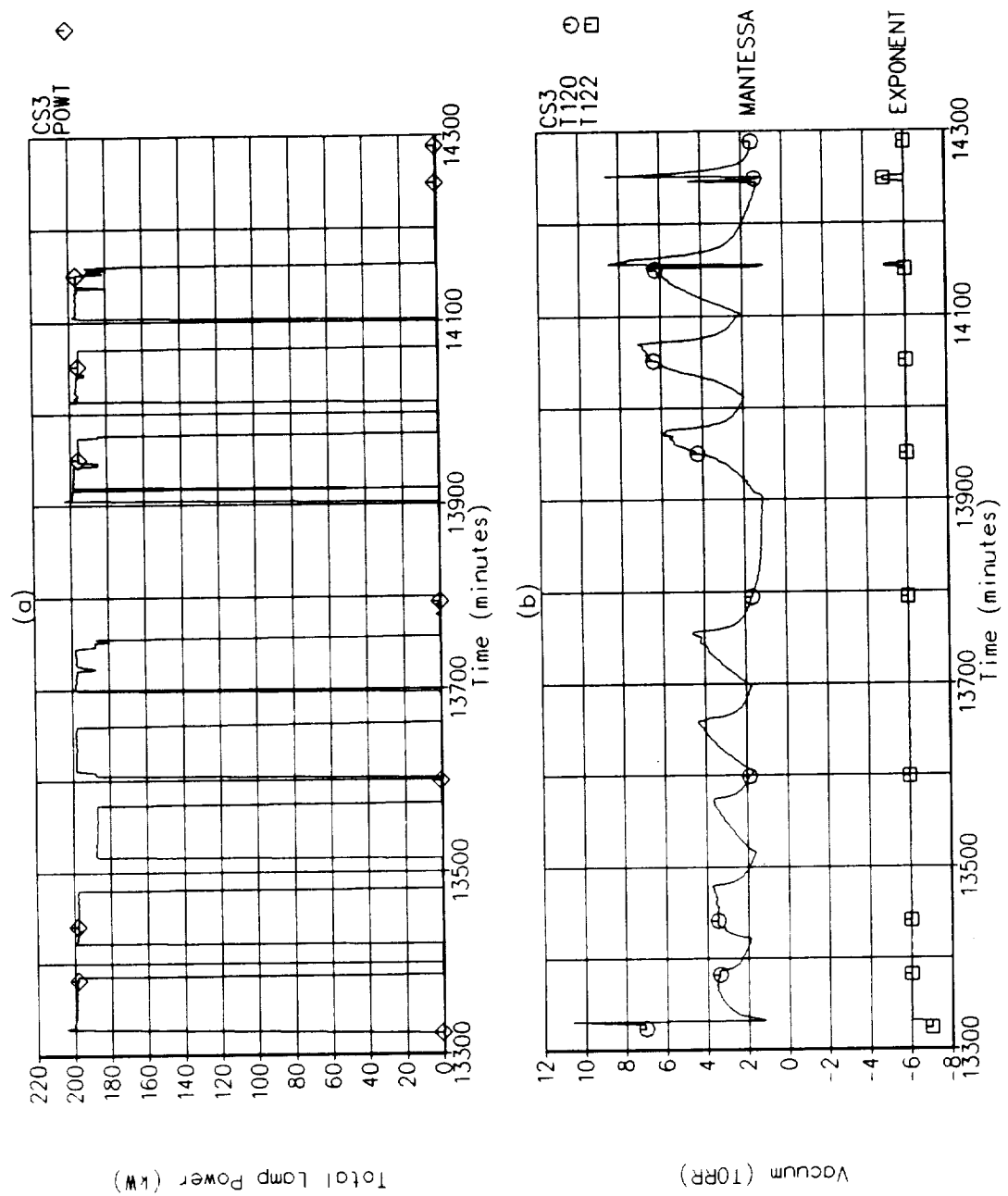


Figure 5-62: (a) Total Quartz Lamp Heater Power During CS.3; and (b) Chamber Vacuum Level During CS.3.

It is interesting to note that the vacuum chamber pressure did not show any significant degradation during this period, but because the transducer is located on the back wall of the chamber, the measured pressure does not reflect that in the cavity.

At first, the problem with zone 2B appeared to be caused by problems in the SCR controller circuit breaker. However, other zones began to shut down and show the "3-cycle" automatic start up attempts to repower. This was the first solid evidence of corona discharge occurring inside the receiver cavity. Finally, after orbit #58, the test conductor terminated the ADRT test conduct because electrical power to many of the heater zones could not be sustained.

Figure 5-63 shows the internal salt temperature closest to the heat exchanger tube (a) located at the flux-facing side of tube #12 at the inlet and exit end of the tube and (b) located on the top side of tube #19 at the inlet and exit ends of the tube. The inlet and exiting gas temperatures are shown in Figure 5-64. These data show that stable temperatures had not yet been achieved by orbit #58 but when compared to the VT.3A data, it can be seen that they were approaching temperatures close to those achieved at equilibrium.

5.16 Shutdown to Ambient and Test Termination

The shut down of the test conduct period was accomplished much like test mode CS.1. The CBC engine simulator was operated normally through a 36 minute eclipse and continued until a 538°C (1000°F) exiting gas temperature was achieved. The blower bypass valve was then completely shut off forcing full flow through the receiver and the regenerator bypass valves were fully opened to obtain the coolest possible inlet gas temperature. Operation of the CBC simulator was continued until the difference between the inlet and exiting gas temperatures dropped below 0.5°C (1°F). Power to the blower was then shut off and a GN₂ purge was used to begin heating up the shrouds and cold plate. After all temperatures rose above 0°C, the chamber vacuum system was slowly shut down and the chamber was back-filled with about 112 kPa (1.5 psig) of GN₂. The site was then left unattended until an inspection was made on 5 November 1991.

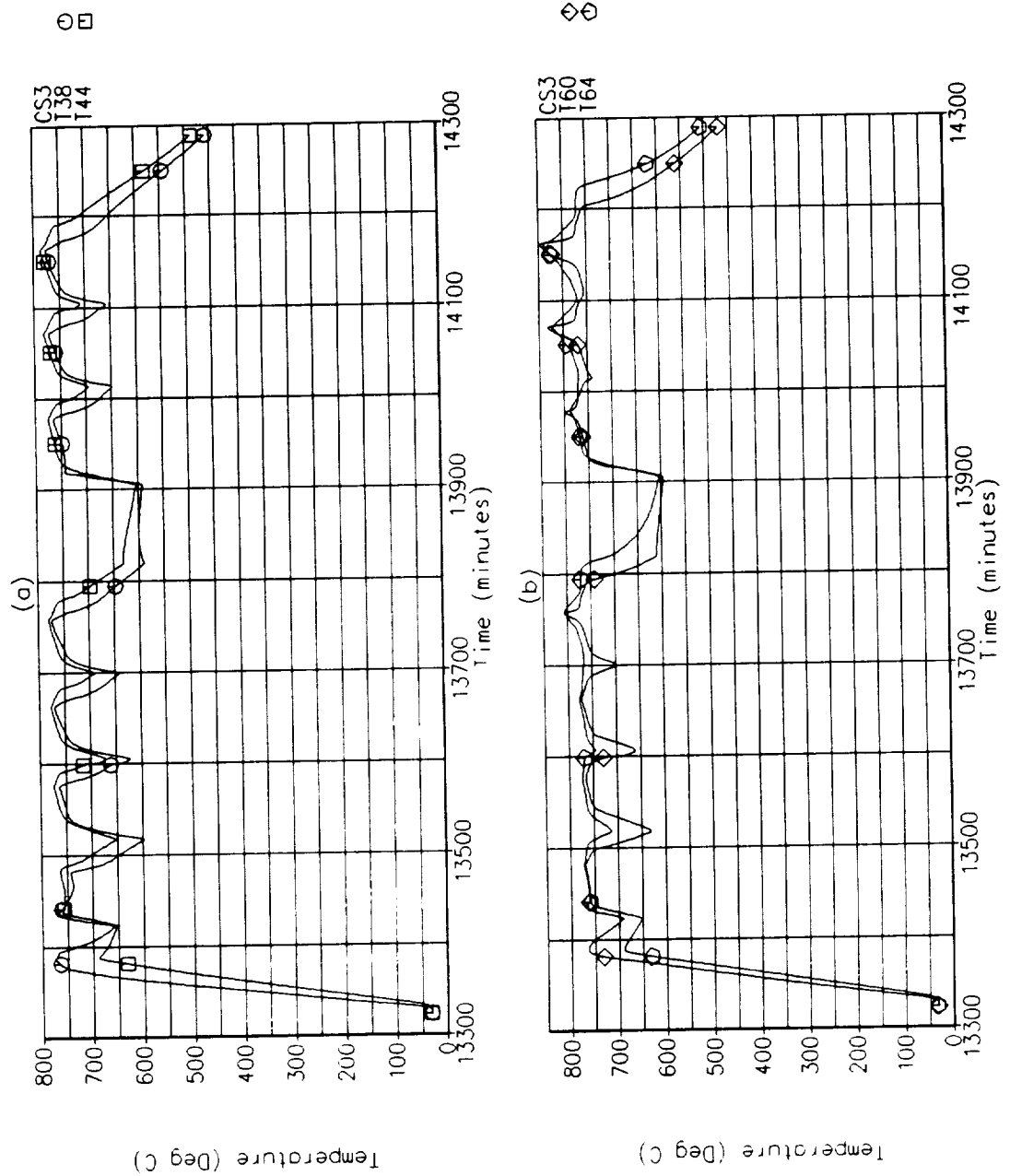


Figure 5-63: CS.3 Internal Salt Temperatures Closest to the Heat Exchanger Tube Located at the Inlet and Exit Ends of (a) the Flux-Facing Sides of Tube #12; and (b) the Top Sides of Tube #19.

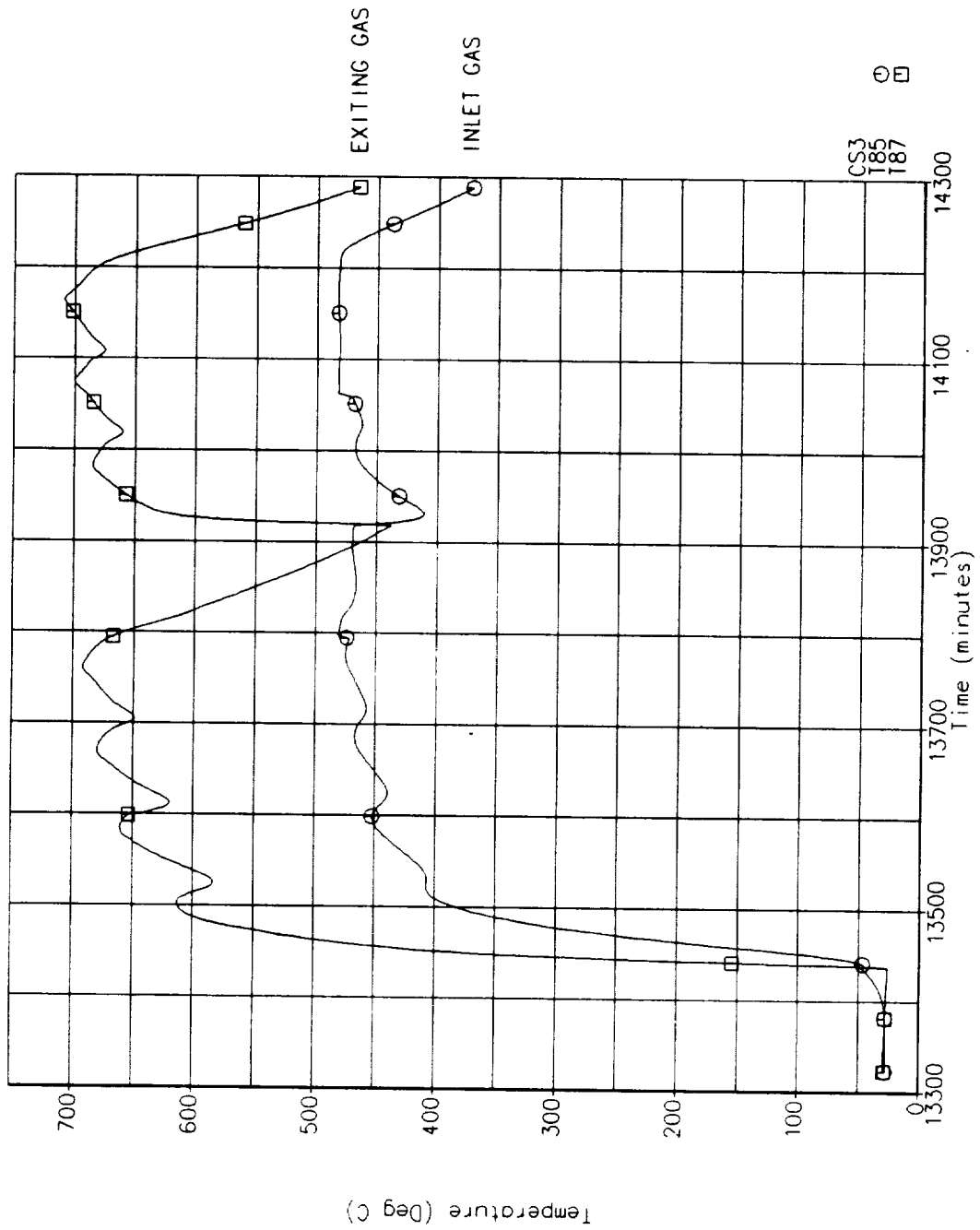


Figure 5-64: Inlet and Exiting Gas Temperatures During CS.3.

6.0 DISCUSSION OF RESULTS

This section provides a limited discussion and interpretation of the test data. Data summaries are provided to help compare and evaluate the receiver performance during the various test modes executed. The data shown in these summaries were obtained from the most stabilized orbit (or period) for each of the ADRT test modes. Figure 6-1 lists the orbits and/or periods used in all of the data summaries to follow. Data shown for more than a single orbit (or period) are provided to illustrate the changes in the receiver during transient periods of interest. For example, data shown for test mode VT.2 were taken during the most stabilized period between 6,651 minutes to 6,942 minutes while those listed under VT.2/M were recorded during the more transient heat up period between 5,971 minutes to 6,722 minutes. Data shown for test mode CS.3 include the initial heat up orbit (CS.3/1), the 2nd orbit with initiation of CBC gas flow (CS.3/2), and the 4th orbit after partial stabilization (CS.3/4).

6.1 Data Modifications

Discrepancies were noted with several of the internal salt temperatures on heat storage tube #12 during the test conduct. The wiring connecting the thermocouples with the computer were checked after the testing was completed and it was discovered that 4 of the 7 internal salt thermocouple leads were misnumbered. A complete check of all of the instrumentation showed no other thermocouples had mislabeled channels and the channel numbers for the 4 thermocouples have been corrected on the instrumentation list given previously in Figure 3-6.

It was also noticed during the test period that the reading displayed by the DACS for channel #129, helium-xenon gas flow rate, was slightly lower than that displayed by the flow computer mounted on the CBC simulator. The flow computer reads the signals from the vortex shedding flow meter, temperature transducer, and pressure gauge and computes mass flow rate. Flow rates were set for all of the test modes using this reading. The flow computer produces a 4-20 ma signal that was converted to 0-5 V for the DACS interface using a resistor bridge. The difference in readings indicates that the device was not properly calibrated. Therefore, manual readings were taken at the flow computer for later comparison with the DACS data. Figure 6-2 summarizes these readings and shows the differences in flow rate. A correction equation was developed by curve fitting the difference magnitude as a function of the reading on the DACS. The best-fit equation is a power function. The equation was applied to the DACS readings to obtain flow rates that match those displayed by the flow computer. The helium-xenon flow rate data shown in this report have been adjusted using the equation given in Figure 6-2 but the raw data remain unadjusted in the original ADRT data files.

6.2 Receiver Thermodynamic Performance

A summary of the thermodynamic performance by test mode is given in Figure 6-3. Values shown for the total quartz lamp power are averaged over the entire sunlit period. The ambient temperature, gas flow rates, static pressures, and values of pressure drop across the receiver are averaged over the entire orbital period including eclipse.

The integrated energy parameters shown in Figure 6-3 provide a method of calculating and comparing the overall cycle thermal efficiencies for the different test modes conducted. These terms and their methods of calculation are defined as follows:

$$\begin{aligned}\dot{Q}_{input} &= \text{total energy input during the orbital period} \\ &= \sum_{sun} P_{qt} \Delta t \text{ (kW-hrs)}\end{aligned}$$

where P_{qt} = total quartz lamp electrical power

Test Mode	Orbit # or Period	Avg Power	Avg Flow	Comments
VT.1		6.8	0	Period of stabilization
VT.2	6651-6942 mins	12.8	0	Most Stabilized period
VT.2/M	5971-6722 mins	20.4	0	Transient heat up period
VT.3	8	193.5	117	Most stabilized orbit
VT.5	12	193.2	162	Most stabilized orbit
VT.6	17	197.0	166	Most stabilized orbit
VT.8	20	223.5	168	Most stabilized orbit
VT.12/P	24	198.3	124	Peaking orbit
VT.12/R	25	198.1	115	Recovery orbit
VT.12/B	26	197.9	117	Stabilized orbit @ VT.3
SS.1	34	197.4	117	Most stabilized orbit
SS.4	37	196.3	117	Most stabilized orbit
VT.3B	43	204.9	117	Most stabilized orbit
VT.3A	50	198.0	117	Most stabilized orbit
CS.1	COOL	0	132	Entire period
CS.3/1	51	197.7	0	Initial orbit-no flow
CS.3/2	52	197.8	71	2nd orbit-begin CBC flow
CS.3/4	54	195.0	113	partial stabilization - prior to corona heater problems.

Figure 6-1: Stabilized Orbits or Periods Used to Compare Significant ADRT Test Data.

Date	Time PDT/PST	T °F	P psig	\dot{Q}_s SCFM	\dot{Q}_s ACFM	\dot{m}_{fm} lbm/min	\dot{m}_c lbm/min	$\Delta \dot{m}$ lbm/min
10-29-90	20:32	100.4	63.6	1437	290	151.0	144.5	6.5
10-30-90	20:18	-	-	-	-	153.9	147.8	6.1
	22:02	-	-	-	-	162.2	155.8	6.4
10-31-90	06:31	96.5	80.2	1580	265	166.0	159.0	7.0
	09:01	98.4	82.0	-	260	165.5	157.7	7.8
	09:17	97.2	81.4	1564	260	164.5	157.6	6.9
	17:11	-	-	-	-	117.0	111.9	5.1
11-1-90	15:13	-	-	-	-	117.0	111.7	5.3
11-2-90	07:07	-	-	-	-	117.0	112.1	4.9
	08:38	-	-	-	-	117.0	112.7	4.3
	09:23	-	-	-	-	165.1	158.6	6.5
	09:33	-	-	-	-	162.0	157.4	4.6
	15:08	77.6	42.4	1264	339	132.9	127.4	5.5
	16:13	76.6	40.7	1233	340	129.7	124.3	5.4
	20:12	74.9	38.0	1186	340	124.4	119.9	4.5
	22:20	-	-	-	-	83.7	80.9	2.8
	22:29	-	-	-	-	91.3	87.9	3.4
	22:51	68.8	63.0	966	190	101.5	98.3	3.2
11-3-90	00:02	76.2	74.6	1062	182	111.5	107.0	4.5

Note: English units were used during testing and data shown above were not converted to SI units for correction factor calculations:

\dot{m}_{fm} = flow measured at flow meter

\dot{m}_c = flow displayed at DACS

$\Delta \dot{m}$ = correction factor

Curvefit Equation for $\Delta \dot{m}$

$\Delta \dot{m} = A \dot{m}^B$ where $A = 1.8343 \times 10^{-2}$, $B = 1.1656$

Figure 6-2: Manual and DACS Helium-Xenon Flow Rate Measurements and Calculated Correction Factor.

Test Mode	Avg Power	Avg Flow	Avg P	Avg ΔP	Avg T_{-}	\dot{Q} Input	\dot{Q} Sun	\dot{Q} Ecl	\dot{Q} Loss	η
VT.1	6.8	0	0	-	9	-	-	-	-	-
VT.2	12.8	0	0	-	4	-	-	-	-	-
VT.2/M	20.4	0	0	-	8	-	-	-	-	-
VT.3	193.5	53	617	6.9	1	183.9	92.8	60.2	30.9	83.2
VT.5	193.2	73	596	12.4	12	181.6	95.0	62.8	23.7	87.0
VT.6	197.0	75	627	12.4	10	213.5	126.4	55.9	31.2	85.4
VT.8	223.5	76	638	12.4	10	242.1	136.7	60.9	44.5	81.6
VT.12/P	198.3	56	647	7.6	13	188.4	101.0	62.9	24.6	87.0
VT.12/R	198.1	52	647	6.2	10	188.2	93.2	54.3	40.7	78.4
VT.12/B	197.9	53	648	6.2	9	188.1	95.1	61.4	31.5	83.2
SS.1	197.4	53	651	6.2	7	187.0	95.1	62.7	29.2	84.4
SS.4	196.3	53	653	6.2	10	186.5	95.8	61.1	29.6	84.1
VT.3B	204.9	53	657	6.9	5	194.5	99.4	63.4	31.6	83.7
VT.3A	198.0	53	653	7.6	3	191.4	98.3	64.2	29.0	84.9
CS.1	0	60	491	7.6	6	0	-	215.3	-	-
CS.3/1	197.7	0	371	0	5	190.7	0	0	190.7	0
CS.3/2	197.8	32	477	4.8	5	189.5	70.9	56.9	61.8	67.4
CS.3/4	195.0	51	632	7.6	7	182.3	83.1	56.2	43.1	76.4

Notes: Power = Lamp power in kW
P = Inlet gas pressure in kPa
 \dot{Q} = Total integrated energy in kW-hrs

Flow = Gas flow rate in kg/min
 ΔP = Differential pressure in kPa
 T_{-} = Ambient temperature, °C

Figure 6-3: Summary of the AD Receiver Thermodynamic Performance by Test Mode.

Δt = time step between measurement points

$$\begin{aligned}\dot{Q}_{sun} &= \text{total energy removed by the gas during the sunlit period} \\ &= C_p \sum_{sun} (\dot{m} \Delta T \Delta t)\end{aligned}$$

where \dot{m} = gas mass flow rate

C_p = gas specific heat

ΔT = T87 - T85 (outlet-inlet) gas temperatures

$$\begin{aligned}\dot{Q}_{ecl} &= \text{total energy removed by the gas during the eclipse period} \\ &= C_p \sum_{ecl} (\dot{m} \Delta T \Delta t)\end{aligned}$$

$$\begin{aligned}\dot{Q}_{loss} &= \text{total energy not recovered by the working fluid gas} \\ &= \dot{Q}_{input} - \dot{Q}_{sun} - \dot{Q}_{ecl}\end{aligned}$$

$$\begin{aligned}\eta &= \text{total integrated receiver efficiency} \\ &= \left(1 - \left(\frac{\dot{Q}_{loss}}{\dot{Q}_{input}}\right)\right) * 100\end{aligned}$$

This definition of the receiver thermal efficiency is different from the first law efficiency calculated using the ratio of the maximum receiver loss over the power input from the concentrator and reflects the efficiency of energy recovered from the TES. However, if receiver temperatures have not stabilized, it is no longer accurate because the total energy stored and recovered over the unstabilized orbit, no longer balance. This is best illustrated by the data shown for test mode VT.12. Additional energy is delivered to the working fluid from energy stored in previous orbits and the calculated thermal efficiency shows improvement during the unstabilized peaking orbit (VT.12/P). The calculated efficiency then drops as additional energy is required to raise the temperatures back up to the pre-peaking conditions during the next orbit (VT.12/R). The calculated efficiency returns to a value of about 83% as cavity temperatures stabilize. Values shown for the most stabilized orbits using baseline or near baseline parameters show an integrated receiver thermal efficiency of about 84 percent and little variation is seen in the overall thermal efficiency of the receiver between stabilized receiver operating modes.

The average power delivered to the helium-xenon gas can be calculated by adding the integrated energy for the sunlit and eclipse periods and dividing by 1.57 hours. Orbits conducted at a total power level of 198 kW and using the baseline engine interfaces produced an average thermal output of about 100 kW. The modified baseline orbit produced an average power output of about 104 kW. These values bracket the 102 kWt required for the SDHRT heat receiver (reference 4).

6.3 Quartz Lamp Heater Power

A summary of the electrical power supplied to the 30° quartz lamp heater zones for selected orbits (or periods) is provided in Figure 6-4. The measured values are averaged over the entire sunlit period of the orbit. Measured heater powers by zone are summed axially (Ax Totals) and circumferentially (Cir Totals) and the axial and circumferential totals are added to both give the same total quartz lamp heater power. Also shown are the required axial zone

BOEING

Test Mode	Zone Powers	Zone 1	Zone 2	Zone 3	Zone 4	Zone 5	Cir Totals
VT.1	Zone A	0.241	0.251	0.210	0.192	0.218	1.112
(SS)	Zone B	0.255	0.252	0.208	0.205	0.203	1.123
	Zone C	0.242	0.243	0.198	0.201	0.203	1.087
	Zone D	0.247	0.247	0.208	0.201	0.196	1.099
	Zone E	0.246	0.260	0.200	0.203	0.204	1.113
	Zone F	0.257	0.367	0.190	0.210	0.201	1.225
	Ax Totals	1.488	1.620	1.214	1.212	1.226	6.760
	Required	1.020	1.020	0.612	0.612	0.612	3.876
VT.2	Zone A	0.641	0.646	0.562	0.565	0.563	2.977
(SS)	Zone B	0.666	0.658	0.562	0.563	0.563	3.012
	Zone C	0.647	0.670	0.546	0.552	0.544	2.959
	Zone D	0.650	0.654	0.546	0.554	0.548	2.952
	Zone E	0.643	0.668	0.541	0.548	0.547	2.947
	Zone F	0.661	0.764	0.565	0.541	0.543	3.074
	Ax Totals	3.909	4.060	3.322	3.322	3.308	17.921
	Required	2.640	2.640	1.584	1.584	1.584	10.032
VT.3	Zone A	10.607	10.669	4.829	3.411	2.738	32.254
(#8)	Zone B	10.619	10.638	4.797	3.417	2.828	32.299
	Zone C	10.643	10.610	4.825	3.476	2.789	32.343
	Zone D	10.344	10.362	4.761	3.431	2.825	31.723
	Zone E	10.655	10.705	4.824	3.510	2.879	32.573
	Zone F	10.668	10.729	4.791	3.436	2.730	32.354
	Ax Totals	63.538	63.714	28.827	20.681	16.789	193.549
	Required	66.000	64.200	29.880	20.880	16.920	197.880

Figure 6-4: Summary of the Quartz Lamp Zone Electrical Power Distributions by Test Mode.

BOEING

TEST MODE	Zone POWERS	Zone 1	Zone 2	Zone 3	Zone 4	Zone 5	Cir Totals
VT.5	Zone A	10.593	10.654	4.857	3.414	2.751	32.269
(#12)	Zone B	10.593	10.213	4.811	3.424	2.836	31.877
	Zone C	10.603	10.596	4.823	3.483	2.792	32.297
	Zone D	10.350	10.408	4.817	3.430	2.836	31.841
	Zone E	10.653	10.693	4.885	3.385	2.882	32.498
	Zone F	10.662	10.724	4.836	3.443	2.736	32.401
	Ax Totals	63.455	63.287	29.030	20.578	16.832	193.183
	Required	66.000	64.200	29.880	20.880	16.920	197.880
VT.6	Zone A	10.930	10.705	4.911	3.502	2.799	32.847
(#17)	Zone B	10.996	10.753	4.943	3.492	2.822	33.006
	Zone C	10.904	10.723	4.910	3.485	2.791	32.813
	Zone D	10.613	10.720	4.972	3.472	2.811	32.588
	Zone E	10.948	10.720	4.915	3.475	2.830	32.888
	Zone F	10.973	10.737	4.920	3.461	2.797	32.888
	Ax Totals	65.366	64.358	29.571	20.887	16.849	197.031
	Required	66.000	64.200	29.880	20.880	16.920	197.880
VT.8	Zone A	12.330	12.157	5.590	4.042	3.215	37.334
(#20)	Zone B	12.292	11.345	5.676	4.004	3.196	36.513
	Zone C	12.331	12.288	5.587	3.981	3.208	37.395
	Zone D	12.298	12.197	5.674	4.009	3.185	37.363
	Zone E	12.318	12.235	5.642	4.008	3.218	37.421
	Zone F	12.418	12.222	5.565	3.990	3.248	37.443
	Ax Totals	73.987	72.444	33.734	24.035	19.271	223.470
	Required	75.000	73.002	33.978	23.748	19.242	224.970

Figure 6-4 (con't): Summary of the Quartz Lamp Zone Electrical Power Distributions by Test Mode.

BOEING

TEST MODE	Zone POWERS	Zone 1	Zone 2	Zone 3	Zone 4	Zone 5	Cir Totals
VT.12B	Zone A	10.955	10.709	4.964	3.483	2.873	32.984
(#26)	Zone B	10.924	10.779	4.906	3.500	2.808	32.917
	Zone C	10.855	10.839	4.952	3.471	2.862	32.979
	Zone D	11.041	10.649	4.927	3.530	2.818	32.965
	Zone E	10.900	10.751	4.918	3.499	2.878	32.946
	Zone F	11.057	10.821	4.913	3.486	2.878	33.155
	Ax Totals	65.733	64.548	29.581	20.970	17.118	197.948
	Required	66.000	64.200	29.880	20.880	16.920	197.880
SS.1	Zone A	10.599	12.063	4.639	3.128	2.466	32.895
(#34)	Zone B	10.557	12.122	4.610	3.156	2.460	32.905
	Zone C	10.575	12.128	4.616	3.110	2.426	32.855
	Zone D	10.616	12.157	4.609	3.147	2.444	32.973
	Zone E	10.573	12.124	4.630	3.123	2.393	32.843
	Zone F	10.576	12.131	4.624	3.126	2.473	32.930
	Ax Totals	63.496	72.726	27.729	18.790	14.661	197.401
	Required	63.798	73.002	27.678	18.678	14.718	197.874
	Baseline	66.000	64.200	29.880	20.880	16.920	197.880
SS.4	Zone A Required	10.962 11.000	10.910 10.700	4.983 4.980	3.495 3.480	2.871 2.820	33.221 32.980
(#37)	Zone B Required	11.099 11.000	10.775 10.700	5.007 4.980	3.532 3.480	2.853 2.820	33.266 32.980
	Zone C Required	10.578 11.000	10.501 10.700	4.822 4.980	3.376 3.480	2.733 2.820	32.010 32.980
	Zone D Required	12.201 12.650	12.090 12.305	5.524 5.727	3.886 4.002	3.138 3.243	36.839 37.927
	Zone E Required	10.976 11.000	10.696 10.700	5.006 4.980	3.505 3.480	2.843 2.820	33.026 32.980
	Zone F Required	9.314 9.350	9.136 9.095	4.235 4.233	2.911 2.958	2.386 2.397	27.982 28.033
	Ax Totals Required	65.130 66.000	64.108 64.200	29.575 29.880	20.705 20.880	16.824 16.920	196.343 197.880

Figure 6-4 (con't): Summary of the Quartz Lamp Zone Electrical Power Distributions by Test Mode.

BOEING

TEST MODE	Zone POWERS	Zone 1	Zone 2	Zone 3	Zone 4	Zone 5	Cir Totals
VT.3B	Zone A	11.275	11.107	5.211	3.609	2.945	34.147
(#43)	Zone B	11.225	11.090	5.166	3.632	2.951	34.064
	Zone C	11.248	11.168	5.143	3.646	2.934	34.139
	Zone D	11.258	11.157	5.156	3.647	2.915	34.133
	Zone E	11.282	11.110	5.196	3.627	2.959	34.174
	Zone F	11.321	11.112	5.149	3.677	2.958	34.217
	Ax Totals	67.609	66.743	31.021	21.837	17.661	204.872
	Required	66.000	64.200	29.880	20.880	16.920	197.880
VT.3A	Zone A	10.964	10.680	4.986	3.490	2.855	32.975
(#50)	Zone B	11.010	10.710	4.982	3.479	2.836	33.017
	Zone C	11.000	10.760	4.952	3.468	2.827	33.007
	Zone D	10.986	10.712	5.002	3.497	2.828	33.025
	Zone E	11.006	10.770	4.988	3.478	2.841	33.083
	Zone F	10.986	10.709	4.932	3.439	2.846	32.912
	Ax Totals	65.952	64.340	29.843	20.850	17.033	198.019
	Required	66.000	64.200	29.880	20.880	16.920	197.880
CS.3	Zone A	10.868	10.721	5.000	3.544	2.882	33.015
(#52)	Zone B	10.830	10.746	5.006	3.511	2.866	32.959
	Zone C	10.789	10.780	4.982	3.496	2.857	32.904
	Zone D	10.837	10.742	5.024	3.524	2.865	32.992
	Zone E	10.838	10.797	5.024	3.503	2.857	33.019
	Zone F	10.859	10.767	4.970	3.470	2.874	32.940
	Ax Totals	65.022	64.553	30.005	21.047	17.200	197.827
	Required	66.000	64.200	29.880	20.880	16.920	197.880

Figure 6-4 (concluded): Summary of the Quartz Lamp Zone Electrical Power Distributions by Test Mode.

power settings and total heater powers required in the test procedures, reference 3. A zone-by-zone comparison of required and measured heater power supplied to all 30 zones is only provided for test mode SS.4, because it was the only test mode that used a nonuniform circumferential power distribution.

Test modes VT.1 and VT.2 both showed that the measured thermal losses are higher than those originally predicted by the thermal model. Test mode VT.1 was very close to stabilized at the required cavity temperature of 538°C (1000°F) at the power settings shown. Power settings shown for test mode VT.2 reflect the operational power at the most stabilized period of this test mode during the period 6,651 minutes to 6,942 minutes when cavity temperatures were approaching 810°C (1480°F).

With the exceptions described for the first 2 orbital cycle test modes, the electrical power supplied to the quartz lamp heater array was very close to that required in the test procedures, reference 3. The total quartz lamp power utilized during test modes VT.3 and VT.5 are about 4 kW lower than pretest requirements. The lower power settings were used early in the test at the direction of the test director because peak heat storage surface temperatures appeared to be too high (about 927°C). Evaluation of the test data during later test modes showed that surface temperature measurements, especially on the flux facing convolution peaks, had significant radiation error caused by a lack of surface contact of the thermocouple with the tubes and the high-flux environment facing the lamps. All other cavity temperatures were very close to or lower than pretest predictions. Therefore, it appeared safe to increase the total power up to the required 198kW for all the remaining test modes after VT.5.

6.4 Receiver Operating Temperatures and Gradients

Figure 6-5 lists the maximum and minimum heat storage tube surface temperatures, internal salt temperatures, and inlet and exit gas temperatures and Figure 6-6 lists the maximum and minimum cavity wall temperatures measured during the orbits listed in Figure 6-1. The measurement channels used to derive these data (and others) are plotted over the stabilized orbital periods given in Figure 6-1 in Appendix C.

The maximum heat storage tube surface temperatures in Figure 6-5 for tube #'s 12 and 19 show that the flux level, rather than the gas side, heat storage tube conditions (i.e., gas flow rate, inlet temperature, etc.), control the magnitude of the temperature peaks. In contrast are the internal salt temperatures which show significant changes in temperature range with variations in the tube side boundary conditions. All of the test modes that operated with a total heater power near the baseline value of 198 kW show peak surface temperatures on these 2 heat storage tubes of about 916°C (1680°F) regardless of the other receiver boundary conditions. Test modes VT.8 (224 kW) and VT.3B (205 kW) produced peak temperatures greater than 927°C (1700°F). The surface temperature data shown for heat storage tube #4 were derived from the measurements made in the convolution valleys and are lower in temperature than those measured on the peaks of the other 2 heat storage tubes. However, a similar nonresponsiveness to gas side conditions is seen suggesting that (1) the tube surface temperatures are strongly coupled to the heat flux rather than to the gas side heat transfer and (2) even these measurements have significant radiation error. Radiation error is suspected to be significant because the contact surface area between the thermocouple and the convolution surface is small and the surface area of the thermocouple not in contact with the tube has a direct view to the lamps.

Test Mode	TUBE #4			TUBE #12						TUBE #19						GAS			
	T _{max} surf	T _{min} surf		T _{max} surf	T _{min} surf	T _{max} salt	T _{min} salt	T _{max} salt	T _{min} salt	T _{max} surf	T _{min} surf	T _{max} salt	T _{min} salt	T _{max} inlet	T _{min} inlet	T _{max} exit	T _{min} exit		
VT.1	544	534	549	532	532	554	536	549	535	549	535	554	539	-	-	-	-		
VT.2	824	808	831	808	837	814	832	808	838	814	-	-	-	-	-	-	-		
VT.2/M	847	764	857	757	862	770	858	761	862	769	-	-	-	-	-	-	-		
VT.3	880	712	919	700	825	665	911	746	859	758	484	482	482	482	482	716	677		
VT.5	886	614	911	619	777	592	902	633	787	634	480	466	666	593	-	-	-		
VT.6	891	701	917	685	790	645	904	741	836	751	482	480	676	640	-	-	-		
VT.8	904	730	932	723	809	663	925	756	871	757	491	489	701	663	-	-	-		
VT.12/P	867	714	916	694	816	662	906	746	856	760	486	483	716	686	-	-	-		
VT.12/R	876	720	916	702	815	660	909	750	861	757	485	482	722	684	-	-	-		
VT.12/B	870	723	917	702	818	667	910	750	863	759	485	483	724	686	-	-	-		
SS.1	869	725	917	703	805	657	912	750	859	759	485	482	724	687	-	-	-		
SS.4	872	723	921	704	809	660	902	749	857	757	485	482	724	689	-	-	-		
VT.3B	871	751	927	721	825	669	925	755	877	761	493	483	742	696	-	-	-		
VT.3A	875	723	919	698	814	659	914	745	864	759	485	482	727	692	-	-	-		
CS.1	732	32	748	32	746	32	760	33	772	32	488	29	689	30	-	-	-		
CS.3/1	857	31	870	31	776	31	856	34	769	31	-	-	-	-	-	-	-		
CS.3/2	870	626	904	632	776	604	893	645	787	645	405	38	613	26	-	-	-		
CS.3/4	885	644	909	644	791	623	902	662	797	661	467	440	680	619	-	-	-		

Notes:
 All temperatures are in °C
 surf = Surface temperatures
 salt = Internal salt temperatures

Figure 6-5: Maximum and Minimum Gas and Heat Storage Tube Temperatures by Test Mode.

	CAVITY WALL TEMPERATURES						WALL CIRCUMFERENTIAL GRADIENTS					
Test Mode	T _{max} aper	T _{min} aper	T _{max} side	T _{min} side	T _{max} back	T _{min} back	ΔT aper	ΔT inlet	ΔT mid	ΔT exit	ΔT back	
VT.1	539	529	548	531	544	536	3	3	6	2	1	
VT.2	817	802	829	806	857	811	4	2	6	2	1	
VT.2/M	842	750	854	756	850	755	5	3	7	3	2	
VT.3	913	714	897	707	890	737	6	29	29	24	6	
VT.5	907	626	883	626	873	646	6	19	33	23	9	
VT.6	911	705	885	699	879	721	6	26	36	23	8	
VT.8	929	735	911	734	901	751	7	18	29	23	6	
VT.12/P	912	716	897	705	891	740	6	34	29	23	7	
VT.12/R	912	722	899	712	892	744	6	33	36	27	7	
VT.12/B	914	722	900	714	893	745	6	32	31	28	7	
SS.1	914	723	900	715	890	744	6	28	28	25	7	
SS.4	913	721	892	716	891	745	8	37	39	31	11	
VT.3B	926	734	916	734	910	751	9	19	30	23	6	
VT.3A	916	719	902	710	896	742	6	31	30	23	6	
CS.1	720	48	753	45	745	49	3	33	39	39	9	
CS.3/1	857	54	828	45	809	47	36	27	67	24	23	
CS.3/2	898	644	872	637	865	636	7	20	22	22	6	
CS.3/4	905	661	882	656	874	677	14	36	26	18	12	

Notes:

All temperatures in °C
aper = Aperture wall

Figure 6-6: Maximum and Minimum Cavity Insulation Temperatures and Temperature Gradients by Test Mode.

The thermocouples attached to the cavity insulation were covered with a piece of quartz cloth (see Figures 3-16 and 3-17) to block the direct view to the lamps. The temperatures of the cavity side walls should be hotter than the surface temperatures of the heat storage tubes because they are nearly adiabatic but the measured maximum temperatures shown in Figure 6-6 are often lower or nearly the same. This supports the theory of radiation error being associated with the tube surface temperature measurements. Another observation regarding the cavity side wall temperatures is that they are about 56°C (100°F) cooler than the pretest predictions (reference 2). This indicates higher conductive losses exist through the receiver insulation and structure which is consistent with the increased losses measured during the steady-state test mode VT.1.

A measurement was made using a sheathed thermocouple inserted approximately mid-length into the quartz lamp array box beam from the front end of the receiver. Therefore, no part of the thermocouple had any direct view to the lamp array and the measured temperature should be one of the hottest in the entire cavity. The temperatures measured at this location compare with those made on the cavity walls and were also lower than many of the measured peak surface temperatures on heat storage tube #'s 12 and 19.

The exiting gas temperatures shown in Figure 6-5 are all within the original SDHRT design requirement of 705°C±28°C (1300°F±50°F) except for test mode VT.5 and VT.6, neither of which simulates an actual design condition. The maximum and minimum gas temperatures measured during conduct of test mode VT.3B compare closely with pretest predictions for the baseline orbit, presumably because the increased heater power of 7 kW accounted for the higher heat loss through the insulation and structure. A comparison of the exit gas temperatures plotted through the stabilized orbits identified in Figure 6-1 is given in Figure 6-7.

Temperature gradients were also calculated from the test data and the maximum gradient values for the cavity side walls are shown in Figure 6-6. The cavity side wall gradients seem high at first glance but are being influenced by the locations of the measurements. At 60° and 270°, the location of the thermocouple is radially inward from the LN₂ cold shroud surface. However, at 180°, the thermocouple is located directly between the bottom cold shroud panels. The LN₂ cold shroud panels rest on the receiver support frame and, therefore, the regions between panels have very little geometric view to the cold shroud surfaces and will be appreciably warmer. Little change is seen in the magnitude of these gradients throughout the test matrix with the exception of during cold start up (which would be expected).

Axial and circumferential temperature gradients are shown for the heat storage tubes in Figure 6-8. The SDHRT heat receiver was designed to limit the maximum circumferential temperature gradients (except during a cold start up) to less than 83°C (150°F). It would appear that this design condition was successfully met except for several isolated cases. Highest temperature gradients were present in the highest flux region of the heat storage tubes.

The maximum temperature difference between the measurements made in the convolution valleys and peaks are shown for heat storage tube #4. Since both measurements suffer from radiation error, the difference in temperature between the measurements may be more accurate (error is subtracted out) and the 22°C-56°C (40°F-100°F) differences compare in magnitude with predictions made back in the design phase of the heat receiver (reference 4).

The temperature difference between the internal thermocouples measuring salt temperature are also presented in Figure 6-8 for heat storage tubes #12 and 19. One of the outer internal thermocouples at the inlet end on both of these heat storage tubes was lost during receiver fabrication operations. Therefore, the outside surface temperature was used to calculate the gradient on the flux facing inlet of tube #12 and the top inlet of tube #19. This explains the

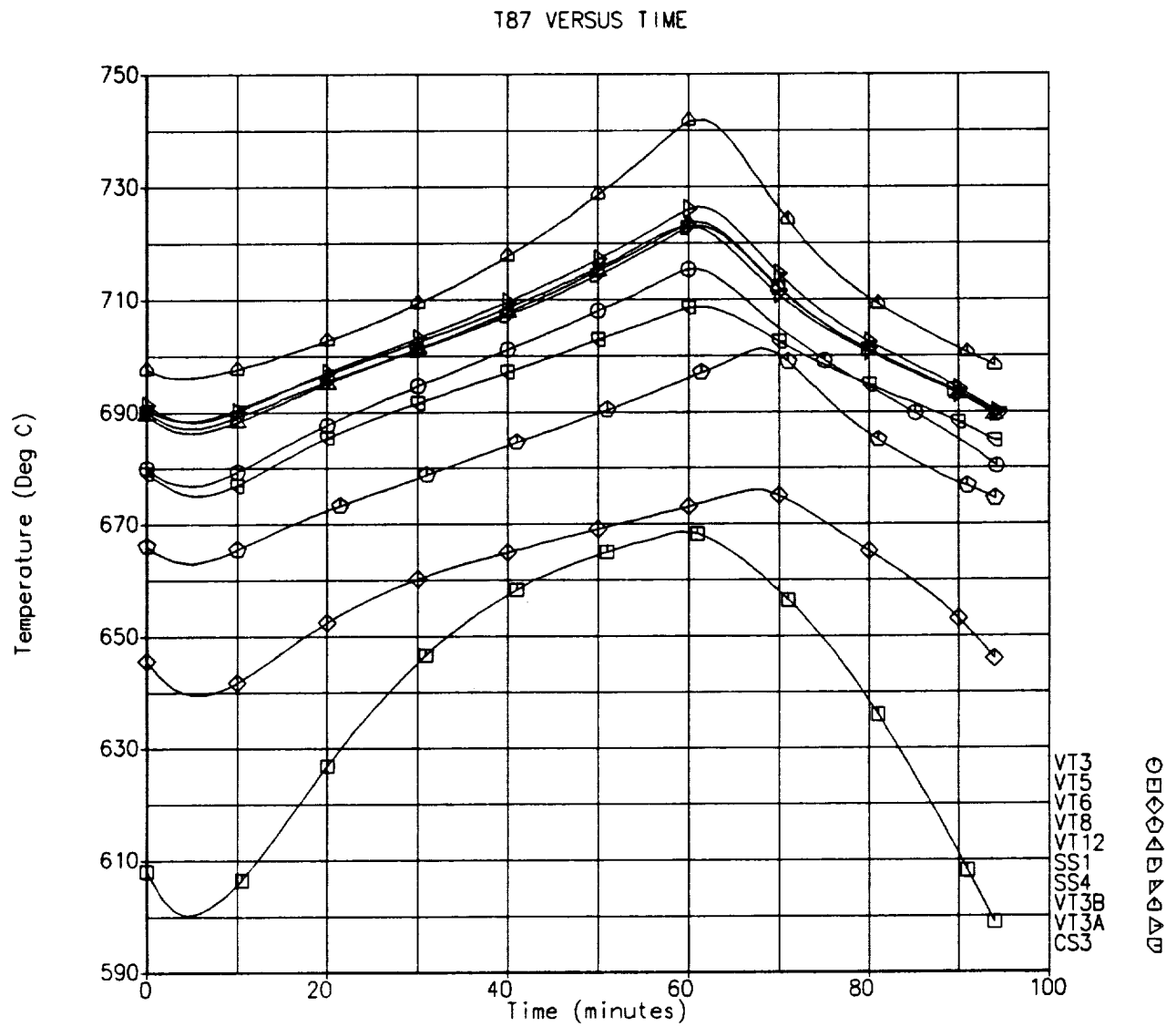


Figure 6-7: Comparison of Exiting Gas Temperatures Over the Most Stabilized Orbits of Testing

Test Mode	TUBE #4						TUBE #12						TUBE #19					
	ΔT	CIR	LOC	P/V	ΔT	AXL	LOC	ΔT	CIR	LOC	TES	LOC	ΔT	AXL	LOC	TES	LOC	ΔT
VT.1	3	I	I	3	0	7	I/M	3	3	I	6	I/F	8	I/T	6	I	I/T	8
	4	M	M	1	90	7	I/E	2	2	M	1	I/W	11	I/B	2	M	I/B	8
	2	E	E	0	180	3	M/E	3	3	E	1	E/F	4	E/T	1	E	E/T	2
VT.2	4	I	I	3	0	10	I/M	3	3	I	7	I/F	8	I/T	7	I	I/T	10
	4	M	M	1	90	11	I/E	2	2	M	1	I/W	12	I/B	3	M	I/B	12
	3	E	E	0	180	6	M/E	5	5	E	0	E/F	7	E/T	1	E	E/T	4
VT.2/M	7	I	I	5	0	16	I/M	7	7	I	16	I/F	17	I/T	10	I	I/T	18
	6	M	M	2	90	18	I/E	4	4	M	2	I/W	21	I/B	3	M	I/B	22
	5	E	E	2	180	8	M/E	7	7	E	1	E/F	8	E/T	1	E	E/T	7
VT.3	59	I	I	21	0	69	I/M	96	96	I	176	I/F	88	I/T	88	I	I/T	55
	61	M	M	22	90	69	I/E	70	70	M	18	I/W	93	I/B	19	M	I/B	62
	36	E	E	63	180	59	M/E	52	52	E	20	E/F	81	E/T	12	E	E/T	59
VT.5	52	I	I	24	0	71	I/M	111	111	I	211	I/F	104	I/T	147	I	I/T	75
	51	M	M	35	90	88	I/E	89	89	M	21	I/W	127	I/B	21	M	I/B	93
	30	E	E	52	180	66	M/E	60	60	E	16	E/F	111	E/T	9	E	E/T	88
VT.6	65	I	I	21	0	67	I/M	98	98	I	192	I/F	96	I/T	94	I	I/T	56
	51	M	M	27	90	87	I/E	87	87	M	22	I/W	109	I/B	20	M	I/B	73
	33	E	E	43	180	72	M/E	57	57	E	19	E/F	95	E/T	12	E	E/T	63
VT.8	77	I	I	28	0	68	I/M	105	105	I	198	I/F	97	I/T	101	I	I/T	58
	58	M	M	38	90	88	I/E	74	74	M	25	I/W	106	I/B	22	M	I/B	76
	52	E	E	40	180	77	M/E	50	50	E	12	E/F	92	E/T	14	E	E/T	68

Figure 6-8: Maximum Heat Storage Tube Temperature Gradients by Test Mode.

Test Mode	TUBE #4						TUBE #12						TUBE #19					
	ΔT CIR	LOC	P/V	ΔT LOC	ΔT AXL	LOC	ΔT CIR	LOC	TES	LOC	ΔT AXL	LOC	ΔT CIR	LOC	TES	LOC	ΔT AXL	LOC
VT.12/P	75 54 36	I M E	33 33 45 21	0 90 180 270	66 51 58	I/M I/E M/E	96 67 47	I M E	181 23 19 12	I/F I/W E/F E/W	92 91 80	I/M I/E M/E	53 50 40	I M E	87 19 12 14	I/T I/B E/T E/B	53 61 59	I/M I/E M/E
VT.12/R	81 57 37	I M E	34 35 56 21	0 90 180 270	61 61 61	I/M I/E M/E	99 72 44	I M E	184 20 18 11	I/F I/W E/F E/W	95 88 78	I/M I/E M/E	53 53 39	I M E	87 19 12 15	I/T I/B E/T E/B	54 59 58	I/M I/E M/E
VT.12/B	81 56 41	I M E	38 38 53 21	0 90 180 270	59 58 64	I/M I/E M/E	96 68 51	I M E	182 21 18 10	I/F I/W E/F E/W	92 89 80	I/M I/E M/E	53 49 41	I M E	86 19 12 14	I/T I/B E/T E/B	52 61 58	I/M I/E M/E
SS.1	81 62 34	I M E	31 39 46 21	0 90 180 270	66 58 65	I/M I/E M/E	76 61 38	I M E	178 16 17 6	I/F I/W E/F E/W	76 82 73	I/M I/E M/E	53 47 37	I M E	87 19 11 14	I/T I/B E/T E/B	51 64 66	I/M I/E M/E
SS.4	88 56 41	I M E	40 37 41 21	0 90 180 270	65 57 62	I/M I/E M/E	78 61 42	I M E	183 17 32 7	I/F I/W E/F E/W	79 82 73	I/M I/E M/E	52 46 37	I M E	82 19 12 15	I/T I/B E/T E/B	53 54 59	I/M I/E M/E
VT.3B	62 55 43	I M E	36 43 49 23	0 90 180 270	59 58 68	I/M I/E M/E	75 68 41	I M E	176 17 19 7	I/F I/W E/F E/W	79 74 69	I/M I/E M/E	52 52 37	I M E	89 19 11 15	I/T I/B E/T E/B	53 63 65	I/M I/E M/E
VT.3A	91 61 36	I M E	32 45 40 21	0 90 180 270	71 52 62	I/M I/E M/E	77 61 37	I M E	181 17 18 6	I/F I/W E/F E/W	77 72 68	I/M I/E M/E	52 56 36	I M E	89 19 12 15	I/T I/B E/T E/B	55 59 62	I/M I/E M/E

Figure 6-8 (con't): Maximum Heat Storage Tube Temperature Gradients by Test Mode.

Test Mode	TUBE #4						TUBE #12						TUBE #19					
	ΔT	CIR	LOC	P/V	LOC	ΔT	LOC	AXL	LOC	ΔT	CIR	LOC	TES	LOC	ΔT	AXL	LOC	ΔT
CS.1	13	17	17	7	0	59	I/M	8	I	44	I/F	I/M	11	I	16	61	I/T	I/M
				4	90	88	I/E	11	M	8	I/W	I/E	16	M	8	90	I/B	I/E
				6	180	53	M/E	16	E	6	E/F	M/E	2	E	2	61	E/T	M/E
				3	270					3	E/W						E/B	
CS.3/1	193	213	147	58	0	208	I/M	266	I	561	I/F	I/M	214	I	524	278	I/T	I/M
				62	90	300	I/E	243	M	21	I/W	I/E	221	M	23	349	I/B	I/E
				135	180	304	M/E	163	E	15	E/F	M/E	167	E	12	293	E/T	M/E
				77	270					11	E/W				14		E/B	
CS.3/2	76	79	52	26	0	104	I/M	76	I	163	I/F	I/M	69	I	98	89	I/T	I/M
				35	90	116	I/E	54	M	21	I/W	I/E	61	M	18	111	I/B	I/E
				56	180	94	M/E	49	E	15	E/F	M/E	55	E	12	82	E/T	M/E
				13	270					11	E/W				13		E/B	
CS.3/4	53	38	36	18	0	60	I/M	86	I	182	I/F	I/M	78	I	140	80	I/T	I/M
				23	90	82	I/E	54	M	19	I/W	I/E	63	M	20	84	I/B	I/E
				57	180	58	M/E	42	E	16	E/F	M/E	42	E	13	67	E/T	M/E
				16	270					6	E/W				16		E/B	

Notes:

All temperature gradients in °C

I = Inlet end

E = Exit end

W = Facing cavity wall

B = Bottom with respect to gravity

P/V = Peak to Valley

LOC = @ location

M = Middle

F = Facing flux from lamps

T = Top with respect to gravity

CIR = Circumferential gradient

AXL = Axial gradient

TES = Temperature difference between outer and inner internal salt thermocouples. The larger salt gradients shown at the inlet end of both tubes reflect the temperature difference between the tube wall and the inner salt thermocouple at these locations because the outer salt thermocouples were functionally lost prior to installation of these tubes inside the receiver cavity.

Figure 6-8 (concluded): Maximum Heat Storage Tube Temperature Gradients by Test Mode.

much larger gradients shown at these 2 locations. It is interesting to see that the magnitudes of the receiver temperature gradients does not appear to change dramatically between test modes except for the initial 2 orbits of the cold start up, CS.3. The magnitude of the temperature gradients measured during cold start up are large, but lower than expected.

6.5 Felt Metal Performance

The internal thermocouples on heat storage tube #19 were orientated perpendicular to the flux vector and just off the vertical plane to allow the felt metal performance to be examined (see Figure 3-9). In this orientation, the temperatures at the bottom of the heat storage tube should be nearly the same as those on top. Figure 6-9 (a) plots the internal salt temperatures at the inlet and (b) the exit end of heat storage tube #19 during the stabilized orbit of test mode VT.3B. The outer internal thermocouple at the inlet end was lost prior to test. The 2 inner thermocouples at the inlet end, T60 and T61, show identical behavior until the melt temperature is reached at which time the top temperature increases more rapidly and to an almost 44°C (80°F) higher temperature. The outer inlet end thermocouple on the bottom of the tube (T62) remains in thermal arrest throughout the eclipse and increases to a temperature about 11°C (20°F) higher than T61. These data suggest that unequal quantities of salt are present in the top and bottom halves of heat storage tube #19 at its inlet end. At the exit end of the tube, the thermal behavior of top and bottom thermocouples are also quite different even though the salt never freezes at this location. This is confusing data since it too suggests differences between the top and the bottom of the heat storage tube which is difficult to explain given that nearly all of the salt in this region should be molten.

Salt temperatures inside heat storage tube #12 are plotted for comparison in Figure 6-10. Here, the temperature trends shown at both ends of this heat storage tube are as expected. Temperatures on the top side of both ends of the tube are hotter than those on the bottom side because they face the heater and the shapes of the inner and outer thermocouples match at each end of the tube suggesting similar behavior of the salt inside the annulus.

6.6 Helium-Xenon Gas Composition

The mass spectrometer system set up for testing failed prior to conducting the first test mode. The cause of the failure could not be diagnosed during the test but was later found to be a blown resistor in the RF controller. Apparently, the vibration of the RF coil loosened in its mounting causing a short circuit that over-heated and failed the resistor. The failure prevented the real-time measurement of gas composition that was planned for during testing.

Gas samples were collected for analysis after testing was completed to determine if the gas composition changed during the test period. Two samples each were collected from the single helium-xenon gas bottle used to charge the CBC piping loop and from the CBC pressure piping loop. The samples were collected in 100 cc stainless steel sample cylinders after flushing them 3 times with the sample gas to exclude the water and air. The samples were then transported to a Boeing laboratory for composition analysis.

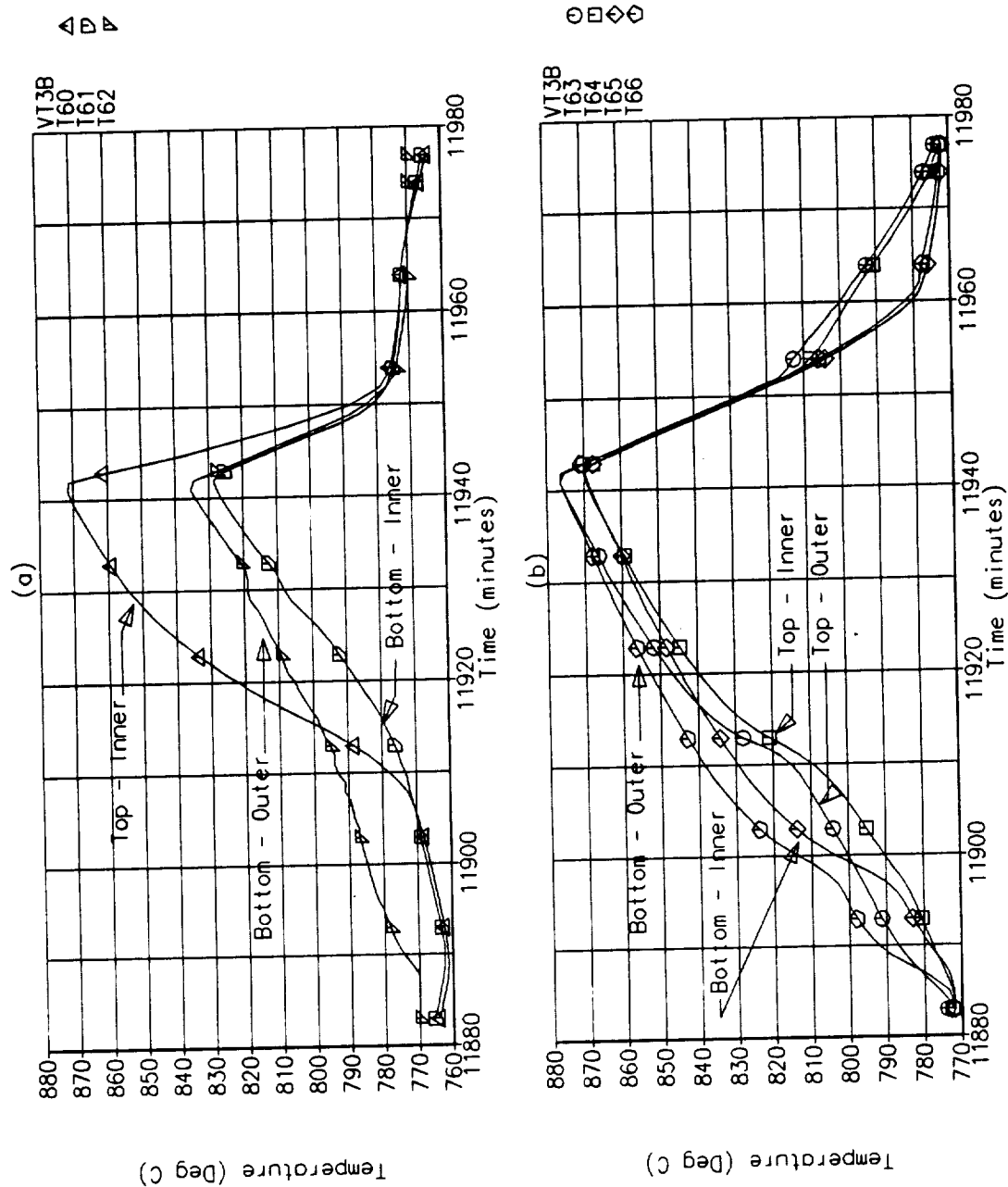


Figure 6-9: Internal Salt Temperatures of Heat Storage Tube #19 (a) At the Inlet End and (b) At the Exit End.

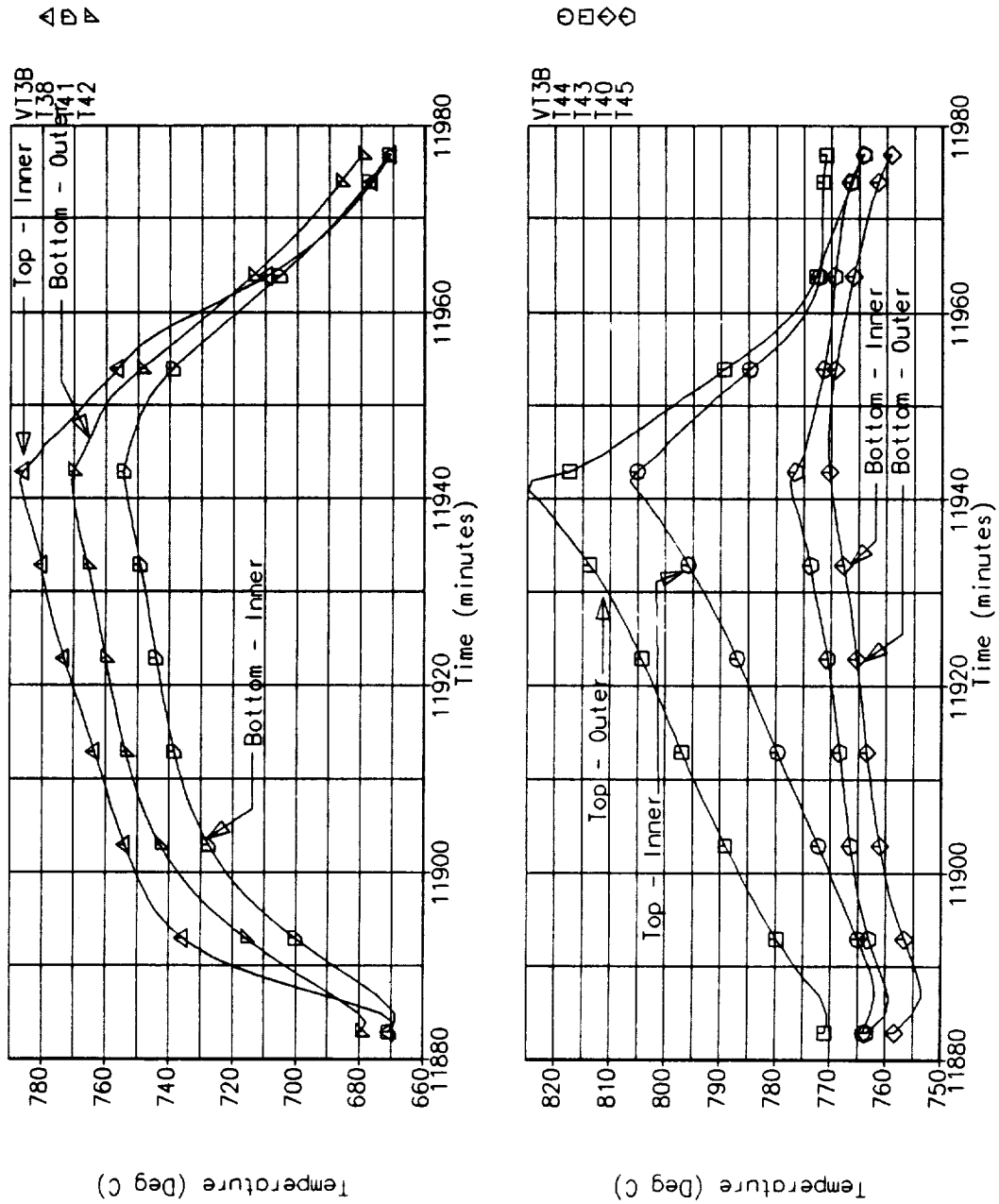


Figure 6-10: Internal Salt Temperatures of Heat Storage Tube #12 (a) At the Inlet End and (b) At the Exit End.

The mass spectrometer used in the post-test analysis of the gas samples was an Inficon QX-2000 mounted to a small turbomolecular-pumped vacuum chamber. Sample gas was introduced to this chamber using a Granville-Phillips variable leak valve. Tubing runs, valves, chamber walls, flanges, and the mass spectrometer housing all were heated to drive off absorbed water. However, some water and air from the sample cylinder and valve surfaces was detected.

Insufficient funding was available to quantify the gas compositions other than by a comparison of relative signal levels measured for helium and xenon (M/Z). The measured helium and xenon signal levels for the gas samples are shown in Figure 6-11. The measured compositions of the gas samples obtained from the loop bottle #2 and from both supply bottles compared closely, showing very little helium was lost during the test duration. Loop sample #1 was low in helium when compared with all of the other samples. This sample also showed a significant increase in the amount of water vapor and air present in the mixture. Therefore, it is believed that the lost helium leaked from the sample cylinder and does not provide an accurate measure of the CBC pressure piping loop gas composition. The results of the post-test gas analysis show evidence that very little helium was lost from the system.

Sample	Mass Spectral Amplitude, Amps	
	M/Z 4 (He)	M/Z 132 (Xe)
Bottle #1	6.1×10^{-11}	4.2×10^{-11}
Bottle #2	8.0×10^{-11}	4.2×10^{-11}
Loop #1	2.8×10^{-11}	3.4×10^{-11}
Loop #2	6.2×10^{-11}	4.1×10^{-11}

Figure 6-11: Post-Test Comparison of Compositions of Gas Samples Taken From the Supply Bottle and CBC Piping Loop.

6.7 Steady-State Heat Loss Adjustments

Figure 6-4 compared the quartz lamp electrical power distributions measured during test modes VT.1 and VT.2 with the pretest predicted power required to maintain 538°C (VT.1) and 788°C (VT.2). The measured heat losses were significantly higher than pretest predictions using the thermal model, SDTEST. Therefore, inaccuracies exist in either thermal property data or in the methods used to model the heat loss through the structure.

The SDHRT heat receiver uses Cerablanket insulation with a specified density of 29 kg/m³ (6 lbm/ft³). The insulation was supplied by Johns- Manville, located in Elkhart, IN. No thermal conductivity data were found in the literature for the Cerablanket insulation in a vacuum environment so these data were estimated using data developed for other similar types of insulation.

Reference 9 gives values of thermal conductivity for another Manville insulation, Q-fiber. These values were measured in both an air and vacuum environment at a number of temperature points. Figure 6-12 lists these data for insulation densities of 25 kg/m³ (5.1 lbm/ft³) and 36 kg/m³ (7.3 lbm/ft³). Values shown for a density of 29 kg/m³ were obtained by linear interpolation between the 25 kg/m³ and 36 kg/m³ density data. The interpolated data shown for 29

Q-Fiber Thermal Conductivity Data In Vacuum

°F	°R	k(5.1)	k(7.3)	k(6.0)
-200	260	0.0038	0.0022	0.0031
200	660	0.0043	0.0032	0.0039
400	860	0.0069	0.0043	0.0058
600	1060	0.0119	0.0071	0.0099
800	1260	0.0173	0.0117	0.0150
900	1360	0.0197	0.0140	0.0174
1000	1460	0.0233	0.0171	0.0208
1100	1560	0.0259	0.0199	0.0234
1200	1660	0.0300	0.0233	0.0273
1300	1760	0.0335	0.0264	0.0306
1400	1860	0.0378	0.0302	0.0347
1500	1960	0.0421	0.0335	0.0386
1600	2060	0.0475	0.0367	0.0431
1700	2160	0.0529	0.0413	0.0482
1800	2260	0.0583	0.0454	0.0530
2000	2460	0.0713	0.0540	0.0642

Values shown for 6.0 lb/ft³ extrapolated

$$k = ae^{bT} \quad \text{where } T \text{ is in Degrees Rankine}$$

Q-Fiber Insulation Curvefit Parameters

Density	a X 10⁻³	b X 10⁻³	r
5.1	2.3788	1.4605	0.973
6.0	1.9697	1.5064	0.976
7.3	1.4041	1.5952	0.975

Values shown for insulation densities are in units of lbm/ft³. Multiply density values by 16.0185 to convert to kg/m³.

Values shown for thermal conductivity are in units of Btu/hr/ft²/°F. Multiply values in table by 0.5778 to convert to w/m²/°K.

Figure 6-12: Thermal Conductivity of Manville Q-Fiber Insulation in Vacuum.

kg/m³ were curve-fitted as a function of temperature using an exponential function as shown in Figure 6-12. A factor was then developed to adjust the Q-fiber equation to represent the Cerablanket insulation.

Figure 6-13 shows reasonable correlation between values of thermal conductivity for the Q-fiber insulation in air obtained from the Boeing data in reference 9 and from Manville supplied data. The thermal conductivity values for the Q-fiber insulation were then compared with those for the Cerablanket insulation at the same density and at corresponding temperatures where data was available. On the average, the Cerablanket insulation had a thermal conductivity in air that was approximately 150% higher than the Q-fiber insulation at the same conditions. This factor was used to adjust the equation to obtain temperature dependant thermal conductivity for the Cerablanket insulation in the pretest thermal predictions.

Insufficient ADRT program budget existed to reevaluate the actual Cerablanket thermal conductivity in vacuum or review the detailed structural heat loss paths in the thermal model. Therefore, the thermal model was run using the VT.1 input conditions and the factor on the Q-fiber thermal conductivity equation was varied until a reasonable match in cavity temperatures was obtained. This match was achieved with a factor of 6.5. The factor was planned for use in the thermal mode to simulate the VT.3B test mode, but insufficient program resources remained after testing to complete this task.

Q-Fiber to Cerablanket Factor Adjustment (6.0 lb/ft³)

°F	Q-Fiber k in Air Boeing	Q-Fiber k in air Manville	Cerablanket k in air Manville	Factor
300	-	0.30	-	-
400	0.40	0.34	-	-
500	0.44	0.39	0.43	1.10
600	0.47	0.44	0.62	1.41
700	0.52	0.50	-	-
800	0.57	0.56	0.82	1.46
900	0.61	0.62	-	-
1000	0.67	0.68	1.00	1.47
1200	0.78	-	1.26	1.62
1500	1.01	-	1.61	1.59
2000	1.50	-	2.62	1.75
avg	-	-	-	1.49

Factor is defined as the ratio of Cerablanket to Q-Fiber thermal conductivities. The Q-Fiber thermal conductivity measured by Manville were used to calculate the factor except where these data were not available the Boeing data were used.

Values shown for insulation densities are in units of lbm/ft³. Multiply density values by 16.0185 to convert to kg/m³.

Values shown for thermal conductivity are in units of Btu-in/hr/ft²/°F. Multiply values by 6.9335 to convert to watts/m²/°K.

Figure 6-13: Comparison of Thermal Conductivities of Manville Q-Fiber and Cerablanket Insulations in Air.

7.0 POST-TEST HARDWARE INSPECTION

The vacuum chamber was opened for an initial inspection of the hardware on 5 November 1990, 2 days after termination of the test. A large quantity of solid materials was found on the face of the aperture plate as shown in Figure 7-1. A significant quantity of this material had fallen off the plate and collected below it on the chamber floor. Other solid contaminants were observed on the support cart members (especially near LN₂ lines), on the optical borescope, and on the vacuum chamber walls near the LN₂ lines. These contaminants were likely the materials that were liberated during the 3 long-term off-gassing events that occurred during the test conduct period. Figure 7-2 shows the materials that collected on the end of the borescope. Samples of all of the solid contaminants from the various areas of the chamber were carefully collected and delivered to NASA for possible future analyses. Current ADRT funding does not support this activity.

The quartz lamp array is shown in Figure 7-3 during its removal from the receiver cavity on 17 November 1990. Overall, the condition of the 30 quartz lamp array zones was excellent. The lamps were perfectly straight and their quartz envelopes were clear except for a slight amount of clouding near the lamp ends caused by high-temperature devitrification of the quartz. Lamps located in axial zones 4 and 5 showed no clouding at all because they were in the cooler region of the receiver cavity. Several of the lamps in zone 1C were damaged by leaking salt as visible in Figure 7-3. Salt can be seen on the quartz envelopes and the columbium bus rods. No other lamp zones suffered damage from leaking salt. An electrical check of all 30 lamp zones was performed after the heater was removed from the receiver cavity. Results are summarized in Figure 7-4. Most of the lamps that are shown as bad in Figure 7-4 actually began to light when power was applied but quickly burned out because their quartz envelopes were apparently cracked causing their elements to oxidize and break during the air testing. Probably almost all of the lamps were operational during the testing because the heated elements were in a non-oxidizing vacuum environment.

A detailed inspection of the receiver and vacuum chamber was performed on 20 November. A summary of the inspection observations is given in Figure 7-5. No post-test failure modes analyses were possible with the current ADRT program funding but some general statements can be made concerning the conditions of the receiver and heat storage tubes.

The post-test inspection of the receiver showed 10 of the 24 receiver heat storage tubes had ruptured and leaked small amounts of salt into the receiver cavity. Heat storage tube #3 had a very large crack and is pictured in Figure 7-6. The amounts of salt leakage from the heat storage tubes varied but was by no means large. The most significant ruptures all occurred at the inlet end of the corrugated TES containment tubes on the peak of the 1st convolution. All of the cracks seem to center on the low gravity side of the tube implying that the failure is attributable to gravity and is probably a result of localized expansion of salt that collects inside the bottom convolutions in this stiff region of the bellows.

It is believed that most or all of these convolution ruptures occurred during the cold soak start up test mode CS.3 for the following reasons:

- (1) No cooling gas flows through the heat exchanger tubes during the entire first orbit and during the first 15 minutes of the second sunlit period. Therefore, salt that normally remains solid at the very front end of the heat storage tube can rapidly melt.



Figure 7-1: Contamination Collected on Cold Plate Surface During Testing.



Figure 7-2: Contamination Collected on Borescope Lens During Testing.

ORIGINAL PAGE
BLACK AND WHITE PHOTOGRAPH

D180-32816-1

186

ORIGINAL PAGE
BLACK AND WHITE PHOTOGRAPH



Figure 7-3: Quartz Lamp Array During Removal From the Receiver Cavity.

Number of Non-Functioning Lamps per Zone

Zone	1	2	3	4	5
A	0	0	0	0	0
B	1	0	0	0	0
C	14	0	0	0	0
D	0	1	0	0	0
E	0	0	0	0	0
F	0	0	0	0	0

Figure 7-4: Results of the Electrical Testing of All 30 Lamp Zones After Its Removal From the Receiver Cavity.

Heat Receiver and Test Equipment Inspection Summary

- 1 When the vacuum chamber was opened for the first time after testing, a strong odor was detected. The odor was found to be associated with materials which off-gassed from unknown sources and collected on cold surfaces. The materials ranged in color, with probable differences not only due to source but also temperature history. For example, materials that collected on structure near LN₂ lines but away from the aperture, the color of the material was a light yellow-brown. The same odor was detected for a white-greyish ash-like material that had flaked off the cold plate probably during a temperature excursion when LN₂ flow was lost. A significant quantity of off-gassing materials collected on all of the LN₂ lines in the vacuum chamber and on surfaces in close proximity to these LN₂ lines. Samples of these materials were removed for future analyses.
- 2 A substantial quantity of materials collected on to the receiver aperture cold plate. Some of the materials had flaked off of the cold plate surface and had fallen to the chamber floor and onto the receiver support structure. Samples were collected from both the cold plate surface and from the chamber floor for future analyses.
- 3 A significant quantity of materials had collected on the end of the borescope. Samples of these materials were removed for future analyses.
- 4 Cavity side-wall and back-wall insulation appeared to be in good shape with structural rigidity. However, the quartz cloth material was quite brittle and flakes off the insulated surface when touched.
- 5 The exit-end half of all of the heat storage tubes appear to be in excellent condition with the exceptions noted in the inspection log for the tubes in positions 13 and 14 which leaked a slight amount of salt at the first convolution at exit end of tube.
- 6 Metallic components in the receiver which operated at a temperature of about 482°C (900°F) show a "blueing" (oxidation?) of their surfaces. This included the inlet end end-caps on the heat storage tubes, the inlet plenum, and sections of the inlet helium-xenon gas line.
- 7 The inlet HX tubes (i.e., the short section that can be viewed penetrating the front cavity insulation) are coated with what appears to be a thin salt film (first cold surface for salt vapors to solidify on).
- 8 The quartz lamp array was in excellent condition. An electrical check of all of the 30 lamp zones conducted in air during disassembly failed only 2 lamps (i.e., the quartz envelopes had opened up and the elements oxidized during operation in the air) except in zone 1C. Zone 1C was damaged by salt dripping onto the lamp quartz envelopes, breaking 2 of the lamps and apparently causing 12 more to open up (i.e., they failed during power up of this zone in air). However, it is likely that almost all of these lamps functioned during test operation because of the vacuum environment. Disassembly of the lamp array went very smoothly. No metallic parts diffusion bonded during the hot operation. The molybdenum rod holding the back end of the lamp array broke during disassembly operations and will have to be replaced.
- 9 The containment bellows on the heat storage tubes all appear to have bowed slightly at the middle in the direction of gravity by about 0.125-inches at the center.

Figure 7-5: Results of Post-Test Inspection of the Receiver Cavity and Vacuum Chamber.

- 10 All of the TES containment bellows that failed cracked at or very near the peak of the first convolution at the inlet end of the tube. The cracks are located at the bottom of the tube with respect to gravity. Fracture surfaces appeared to have a knife-edge geometry indicating material thinning took place.
- 11 Inlet end fill tubes showed no signs of distortion or salt leakage.

Tube Pos. #	Tube Ser. #	Results of Inspection
1	5	1 The TES containment tube has a significant kink located approximately 7-in from inlet end end-cap (1) that is approximately 11-in in length (2). The convolutions are bulged out towards the cavity centerline at an angle of approximately 210° off of the vertical axis (3). The first 5 convolution are compressed on the side of the bellows in-line with the direction of the kink. There is no evidence of salt leakage from the bellows.
		2 The exit end fill tube ruptured with a slight amount of salt leakage (4).
2	4	1 The TES containment tube appears normal with no visible abnormalities noted.
		2 The exit end fill tube is a short stub and shows no signs of bulging or rupture.
3	6	1 The TES containment bellows ruptured at the first convolution on the inlet end. The crack begins at about 150° and continues to about 360° around the circumference (5). Significant salt has leaked from the crack and the leaking salt appears to have dripped down onto some of the tubes (and probably zone 1C of the lamp array) located below it. The convolutions appear normal with no significant deformations.
		2 The exit end fill tube ruptured and shows a large amount of salt leakage.
4	12	1 The TES containment bellows ruptured at the first convolution on the inlet end. The crack begins at about 165° and continues to about 195° around the circumference. The convolutions appear normal with no significant deformations.
		2 The exit end fill tube ruptured and has a slight amount of salt leakage.
		3 All thermocouples are attached to the surface of the convoluted tube and appear unchanged in orientation and position.
5	30	1 Convolution #'s 2 and 3 (6) are deformed especially where they face the cavity centerline. The TES containment tube shows no evidence of salt leakage.
		2 The exit end fill tube shows slight bulging but shows no signs of salt leakage.

Figure 7-5 (con't): Results of Post-Test Inspection of the Receiver Cavity and Vacuum Chamber.

Results of Inspection			
Tube Pos. #	Tube Ser. #		
6	3	1	The TES containment bellows failed at the inlet end at the first convolution. The crack begins at about 170° and continues to about 190° around the circumference. Small amount of salt leakage. Convolution #10 is flattened facing the cavity centerline and is more normal on the side facing the cavity side wall.
		2	The exit end fill tube failed with a moderate amount of salt leakage.
7	11	1	Significant kink in the convoluted tube, approximately 12-in from inlet end cap and approximately 11-in in length. Convolutions are bulged out in the direction of gravity at approximately 180°.
		2	Convolution 27 (located approximately 7-in from the inlet end cap) is significantly deformed and flattened where it faces the cavity centerline but show no signs of salt leakage. No salt leakage at inlet end end-cap.
		3	Exit end fill tube failed with a slight amount of salt leakage.
8	32	1	The TES containment bellows failed at the inlet end at the first convolution. The crack begins at about 175° and continues to about 185° around the circumference. Slight amount of salt leakage from rupture crack. Convolution #2 is significantly deformed around the entire circumference.
		2	Exit end fill tube shows evidence of bulging but shows no signs of failure.
9	29	1	The TES containment bellows failed at the inlet end at the first convolution. The crack begins at about 100° and continues to about 280° around the circumference. There is a large amount of salt leakage relative to the other tubes and the salt has a bluish color and rougher texture which might indicate a longer exposure period. A significant amount of salt leaked from the tube and onto the cavity insulation below.
		2	Convolution #48, located approximately 12-in from inlet end cap, is significantly deformed but the tube has not ruptured or kinked in this region.
		3	Exit end fill tube failed with a moderate to large amount of salt leakage.
10	16	1	Convolution #'s 5 and 6 are significantly deformed and flattened but show no signs of salt leakage.
		2	Salt droppings from tube #9 cause an appearance of leakage at the inlet end end-cap but further inspection shows no leakage in this region.
		3	Exit end fill tube failed with a slight amount of salt leakage.
11	21	1	Convoluted tube appears normal. No abnormalities noted.

Figure 7-5 (con't): Results of Post-Test Inspection of the Receiver Cavity and Vacuum Chamber.

Tube Pos. #		Tube Ser. #	Results of Inspection
			2 Exit end fill tube shows slight bulging but has not ruptured.
12		19	1 Significant kink in the convoluted tube, approximately 18-in from inlet end cap and approximately 11-in in length. Convolutions are bulged towards the cavity side wall at approximately 210°. There is no salt leakage from the TES containment tube.
			2 Exit end fill tube shows slight bulging but has not ruptured.
			3 All thermocouples are still attached to the surface of the convoluted tube and appear unchanged in orientation and position.
			4 All internal thermocouples appear to be intact with no signs of salt leakage from the braze joints at the end-caps.
13		18	1 Convolution #'s 6 and 7 are significantly deformed but shows no signs of salt leakage.
			2 The TES containment bellows failed at the exit end at the first convolution. Exact crack location has not been determined but the region of salt leakage is confined to about an inch in length on the bottom (with respect to gravity), cavity wall facing side. Only a very small amount of salt leakage can be seen in this region. The convolutions in this region show no signs of distortion or change.
			3 Exit end fill tube failed with a slight amount of salt leakage.
14		22	1 Convoluted tube appears normal at inlet end and along its entire length. However, the TES containment bellows failed at the exit end at the first convolution. Exact crack location has not been determined but the region of salt leakage is confined to about an inch in length on the bottom (with respect to gravity), cavity wall facing side. Only a very small amount of salt leakage can be seen in this region. The convolutions in this region show no signs of distortion or change.
			2 Exit end fill tube failed with a moderate amount of salt leakage.
15		8	1 The TES containment bellows failed at the inlet end at the first convolution. The crack begins at about 100° and continues to about 280° around the circumference. The convolutions appear normal with no significant deformations. The salt that has collected at the crack has a blueish color and rougher texture which might indicate a longer exposure period. Some salt appears to have dripped onto the cavity insulation below.
			2 Exit end fill tube appears normal.

Figure 7-5 (con't): Results of Post-Test Inspection of the Receiver Cavity and Vacuum Chamber.

Results of Inspection		
Tube Pos. #	Tube Ser. #	
16	17	1 The TES containment bellows failed at the inlet end at the first convolution. The crack begins at about 175° and continues to about 190° around the circumference. Convolutions appear normal with no significant deformations.
		2 Exit end fill tube failed with a moderate amount of salt leakage.
17	31	1 The TES containment bellows appears normal but has salt collected on its inlet end from leakage from a neighboring tube.
		2 Significant kink in convoluted tube, approximately 7-in from inlet end cap and approximately 11-in in length. Convolutions are bulged out toward cavity wall at an angle of approximately 240°.
		3 Exit end fill tube failed with a slight amount of salt leakage.
18	1	1 The TES containment bellows failed at the inlet end at the first convolution. The crack begins at about 90° and continues to about 300° around the circumference. The first convolution is very distorted in the region of the crack. A relatively large amount of salt has leaked from the tube in comparison to most of the others and the salt has the same "bluish" tint and rough texture as that which leaked from the tube in position #9. A significant amount of salt has leaked onto the cavity wall below this tubes location.
		2 Exit end fill tube shows slight bulging but has not ruptured.
19	35	1 Convoluted tube appears normal. No abnormalities noted.
		2 Exit end fill tube appears normal.
		3 All thermocouples are still attached to the surface of the convoluted tube and appear unchanged in orientation and position.
		4 All internal thermocouples appear to be intact with no signs of salt leakage from the braze joints at the end-caps.
20	10	1 Convoluted tube appears normal. No abnormalities noted.
		2 Exit end fill tube shows slight bulging but has not ruptured.
21	23	1 Convolution #'s 5 and 6 as counted beginning from the inlet end cap show significant deformation but show no signs of leakage.
		2 Exit end fill tube appears normal.

Figure 7-5 (con't): Results of Post-Test Inspection of the Receiver Cavity and Vacuum Chamber.

Tube Pos. #	Tube Ser. #	Results of Inspection
22	34	1 Convolution #'s 4 and 5 show significant deformation but show no signs of leakage.
		2 Exit end fill tube failed with a large amount of salt leakage.
23	20	1 Convolved tube appears normal. No abnormalities noted.
		2 Exit end fill tube shows slight bulging but has not ruptured.
24	7	1 Convolved tube appears normal. No abnormalities noted.
		2 Exit end fill tube failed with a large amount of salt leakage.

Notes:

- (1) Kink locations are measured from the back (HX) facing side of the inlet end end-cap to center of the "bowed" region.
- (2) The length of the kink is measured from the ends of bowed region.
- (3) The angular direction the tube is bowed out is measured from 0° at the top (12 o'clock) position of vertical and rotates in the clockwise direction as viewed from the aperture end of the receiver cavity.
- (4) There is very little salt leakage from any of the fill tubes. Salt does not appear to have dripped off of any of the fill tubes. Leakage amounts ranged from slight (salt crystals just visible on the fill tube surface), to moderate (small amount of salt covering surface), and large (salt has balled up on the surface or is fairly thick on surface of the fill tube).
- (5) The angular measurement of the cracks in the TES containment convolutions are referenced from 0° at a vertical 12 o'clock position with respect to gravity and angles rotate in the clockwise direction as viewed from the aperture end of the receiver cavity.
- (6) Convolutions are identified by counting back from the first convolution at the inlet end end-cap.

Figure 7-5 (concluded): Results of Post-Test Inspection of the Receiver Cavity and Vacuum Chamber.



Figure 7-6: Crack At the Peak of the First Convolution at the Inlet End of Heat Storage Tube #3.

D180-32816-1

195

ORIGINAL PAGE
BLACK AND WHITE PHOTOGRAPH

(2) The melting phase front can propagate axially away from the end-cap because the end-cap acts as a heated thermal fin when no gas flow is present (it acts as a cooled thermal fin when gas is flowing and prevents salt at the very front end of the tube from melting).

(3) The gravity sides of the heat storage tubes in the lower region of the cavity face the cavity wall while at the top, the gravity sides face the heater. Failures occurred in both the top and bottom regions of the cavity. The only time that the salt on the bottom side of the heat storage tubes located in the lower cavity can melt at almost the same rate as that in heat storage tubes at the top of the receiver cavity is during the cold start up test mode.

(4) Temperature gradients are at least twice as large in magnitude during much of the cold soak start up period as than those during a normal orbit. Therefore, tube stresses are larger.

(5) Cavity corona was only confirmed during the cold soak start up test mode.

(6) Little or no change was seen in receiver temperatures or thermodynamic performance between VT.3 type of test conditions that were repeated at several different periods throughout the conduct of the test matrix.

The exact failure mode cannot be specified from existing knowledge of the tubes. A limited amount of thermal stress analysis was conducted on the TES containment bellows during its design. These analyses did not consider end effects, gravity induced salt collection in the bottom convolutions, or the different thermal gradients that occur in the heat storage tube during a cold start up. However, as bad as the convolution failures appear, it is believed that the problem could be corrected with further study and optimization of the salt containment tube, especially in the region next to the end cap. On the whole, the bellows were more than capable of accommodating the deflections encountered during receiver operation. The convolutions in most regions of the heat storage tube showed no signs of damage or significant loadings. However, 4 of the TES containment tubes had large kinks where the tube was void of felt metal disks, which probably occurred during the molten salt filling operations. The kink in heat storage tube #1 is shown in Figure 7-7. The buckling was confined to the bellows as later inspections by NASA showed the inner tube remained straight. The kinked regions were characterized by large convolution deformations, yet, none of these regions resulted in a rupture of the salt containment.

The felt-bellows buckling problem may have resulted from pretest damage to the felt metal during heat storage tube fabrication. The nickel felt metal disks used in the SDHRT heat storage tubes had compromised performance and quality for cost because it was considered good enough for the relatively short test life. However, highest felt metal temperatures occur during the operations to fill the heat storage tubes with molten salt as the tubes were heated to 927°C (1700°F). The 4 tubes that kinked had required 2 separate molten salt fill operations because they were not completely filled during the first attempt. Therefore, the felt in these tubes had experienced high temperature (871°C-927°C) longer than all but 2 of the other heat storage tubes in the receiver. The longer duration, high-temperature exposure likely caused the felt to sinter and compact in part of the heat storage tube, a phenomena that was demonstrated in early unsuccessful fill operations (reference 5). The bellows is free to kink or twist in regions void of the felt when the salt inside the annulus is molten.

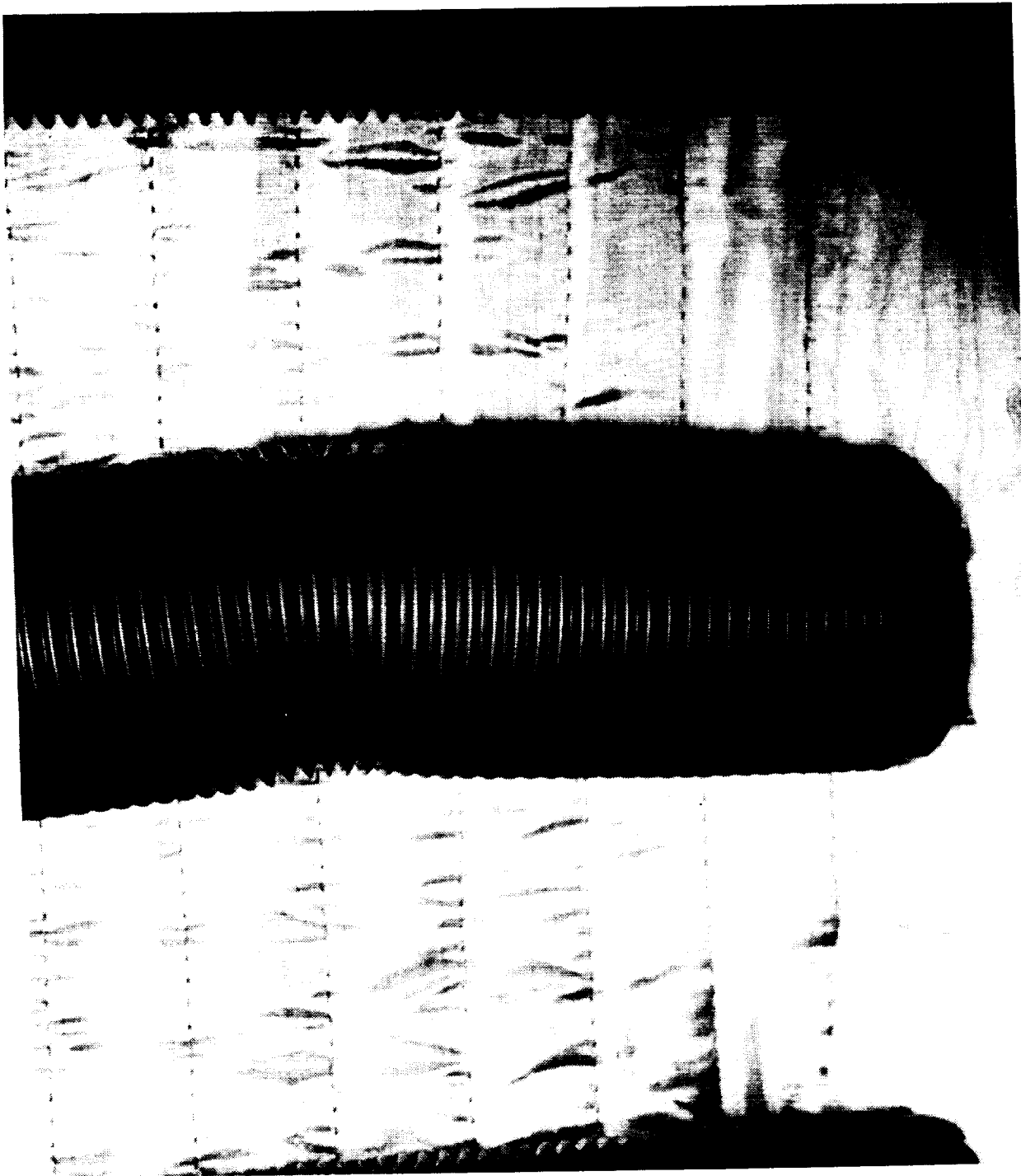


Figure 7-7: Buckled Felt Metal Kink Near the Inlet End of Heat Storage Tube #1.

BOEING

In addition to the ruptures of the TES containment bellows, 12 of the 24 exit end salt fill tubes cracked and leaked small amounts of salt. The cracks were caused by expansion of the salt inside the fill tubes during melt. This problem was probably worsened by the redesign of the closure weld which used weld wire instead of a solid plug as the filler material. The weld wire probably wicks molten salt up into the fill tube causing it to freeze with little or no shrinkage void. The subsequent remelt of the salt causes the fill tube to bulge and eventually failed. This problem is not considered very serious because it can be easily corrected with a simple redesign of the end closures. The fill tube could be made much shorter (short fill tubes showed no signs of damage) or could be eliminated altogether by electron-beam welding at the end-cap itself. This was considered early in the SDHRT program but was not pursued because the present configuration was successful during previous NASA heat storage tube testing (reference 10).

8.0 CONCLUSIONS AND RECOMMENDATIONS

The ADRT test program successfully demonstrated that a full-size SD heat receiver can be operated in vacuum to quantify performance. The AD heat receiver met all of its design requirements during operation of simulated Space Station Freedom operational modes. Its thermodynamic performance compares favorably with predictions although the measured receiver loss through the cavity insulation and/or structure is slightly higher than that predicted for the design. The accuracy of measured TES tube surface temperatures is difficult to ascertain but maximum receiver temperatures based upon measured insulation and structural temperatures are close to or lower than those predicted by the thermal model (reference 2).

Comparison of the test data for the most stabilized orbits of each of the ADRT test modes shows that receiver performance, maximum operating temperatures, and temperature gradients do not vary significantly. The receiver cavity radiation exchange appears to smooth off-design cavity flux distributions although further analysis is required to determine the incident flux profiles produced using the off-design quartz lamp power distributions.

The only required test interface not supplied by the test support hardware was the low-end receiver gas flow rates because the CBC engine simulator could not by-pass enough flow around the compressor. The pressure drop through the by-pass leg and through the regenerative heat exchanger and heat receiver balanced at a relatively high gas flow rate because the receiver pressure drop was lower than expected. This problem can easily be corrected by installing an orifice in the regenerator gas line to increase the pressure drop up to that assumed for sizing the by-pass valve. The quartz lamp heater operated very well, and appeared to suffer little or no degradation during the test conduct period.

The amount of program funding remaining after the conclusion of testing was sufficient to only cover the return of the test article and support hardware to NASA-LeRC and to prepare the final program documentation. The following additional tasks are recommended to NASA to best utilize and understand the available test data:

1. Selected test data should be correlated with the thermal math model. Insulation samples should be removed from the receiver and used to measure thermal conductivity in a vacuum environment. These data could then be compared with the values of thermal conductivity in use in the model and accurate adjustments made. Several improvements should be considered to more accurately model the structural heat loss path. The measured test data for the modified baseline orbit (VT.3B) shows more salt melt occurs at the inlet end of the heat storage tubes than that predicted by the thermal model. Therefore, the method used to predict an overall convective heat transfer coefficient should be modified to calculate localized (by control volume) values based upon the work presented in reference 11. Further analysis may also be necessary to ascertain the accuracy of the incident and absorbed flux at the inlet end of the heat storage tubes. These accuracy improvements would allow end-effects to be better characterized for failure modes analysis of the TES containment tubes. Finally, the following test modes should be correlated with the thermal model after the required modifications are made: VT.1, VT.2, VT.3A, VT.3B, SS.1, CS.1, and CS.3.
2. An analysis should be conducted to try and understand the mode(s) of failure of the TES containment bellows. Updated thermal model data would allow end effects to be characterized, especially during the cold start up test mode. A program developed during the SDHRT program to track the progression of the phase front through prototype test canisters could be modified for the receiver heat storage

tubes to give a graphic illustration of the potential problem areas near the end caps. The predicted temperatures and resulting temperature gradients would be used to perform additional stress analysis, especially near the ends of the tubes.

3. In addition to analytical studies, material inspections should be performed on the heat storage tubes themselves. Several new Inconel 617 bellows exist which could be sectioned to examine the characteristics of the first convolution. Material properties such as yield stress, rupture stress, and modulus of elasticity could be measured for the untested material. Several of the heat storage tubes should be removed from the heat receiver, weighed, balance tested to determine their center of gravity, and examined using computed tomography to determine the overall salt and felt metal distributions inside the TES annulus. The tubes could then be sectioned to physically examine the salt, felt metal, and bellows materials. Metallographic analysis of the failure region of the convolutions would aid in understanding the factors contributing to the failures. Material properties would be measured for the as-tested Inconel 617 and compared to the as-received material properties. Some of this work is currently being performed by NASA-LeRC.
4. Finally, the off-gassing samples taken from the heat receiver, support cart, aperture cold plate, and the vacuum chamber walls should be analyzed to try and determine the source of these off-gassing products. This information would be useful in understanding the off-gassing events that occurred during the testing and could be valuable in understanding what conditions contributed to these events. These samples have been forwarded to NASA-LeRC for possible future analysis.

The methods and hardware used to test the heat receiver were very successful but the following improvements should be made before any future receiver testing is conducted.

1. First, sufficient funds should be allocated to perform CT evaluation of all heat storage tubes prior to their installation into the receiver cavity. This nondestructive testing will show any pretest fabrication flaws that could contribute to a failure or performance problem.
2. The seal on the optical borescope needs to be improved and testing conducted to demonstrate its capability for operation inside the receiver cavity. Locating the end of the borescope outside the cavity like was done during the ADRT testing does not allow the heat storage tubes to be viewed because of the increased blockage by the heater support structure.
3. An orifice or a new blower bypass valve must be added to the CBC engine simulator to obtain the proper low-end flow range.
4. Another vacuum ion gauge should be installed inside the receiver cavity to permit measurement of cavity pressure.
5. An improved method of measuring TES tube surface temperatures needs to be developed and quantified to eliminate the significant radiation errors that are caused by the high-flux environment and lack of contact area between the thermocouple and tube surfaces.

The overall design of the AD receiver appears to be solid and the thermal performance should meet all of the Space Station SD power module requirements. The SDHRT program demonstrated that this receiver design can be fabricated at a reasonable cost, especially now that the problems associated with molten salt filling have been solved. Certainly, some of the key design aspects of this receiver should be considered in any receiver that is eventually built for space flight operation on the Space Station or other future space missions. However, a number of areas need to be addressed to extend the receiver design for space flight operation including:

1. Analysis to better understand the behavior and movement of the salt inside the TES tube annulus during operation of the receiver.
2. Analysis to quantify the impacts of contingency heating or cooling modes on the TES salt distributions.
3. Optimization of the metal matrix properties to promote good heat transfer, molten salt wicking characteristics, and structural strength.
4. Demonstration of long-term chemical compatibility and structural stability of the felt metal after repeated salt freeze-thaw cycling.
5. Redesign of the TES containment including bellows geometry, materials of construction, salt fill tube sealing methods, and methods of installing the metal matrix material.
6. Possible resizing of the flow control spud to improve the heat transfer characteristics of the heat storage tube.
7. Development of lower weight, higher performance, high-temperature cavity thermal insulations.
8. A new method of sealing the salt annulus must be qualified.

Other significant study areas were described in the SDHRT Final Report (reference 5) and are summarized here for completeness:

1. The development of a low-cost and reliable aperture protection system.
2. The potential for contamination of the concentrator and/or the space craft from the off-gassing of receiver materials.
3. Damage potential from micrometeoroid and space debris.
4. The survivability and thermal performance of candidate cavity insulations in the solar wavelength.
5. Required make-up rates of helium because of diffusion and/or leaks from the pressure piping system and component seals.

The analyses that were performed in these areas show that these topics are important to quantify before a operational SD module can become a reality. However, it must be emphasized that no SD module "show stoppers" were found during the conduct of either the SDHRT or ADRT programs and all of these areas can be adequately addressed by proper design.

REFERENCES

1. Boeing Document D180-31880-1, "Advanced Development Receiver in Thermal/Vacuum Environment Work Plan", dated 4 December 1989.
2. Boeing Document D180-32359-1, "Advanced Development Receiver Thermal Vacuum Tests With Cold Wall - Test Plan Document", dated 10 July 1990.
3. Boeing Document D180-32566-1, "Advanced Development Receiver Thermal Vacuum Tests With Cold Wall - Detailed Test Procedures", dated 24 October 1990.
4. Boeing Document D180-29711-1, "Solar Dynamic Heat Receiver Technology, Design Analysis Report", dated September 1988.
5. NASA CR 187040, "Solar Dynamic Heat Receiver Technology - Final Report", Sedgwick, L.M., NASA Lewis Research Center, January 1991.
6. LeRC-SS-001, Electrical Power System (EPS) Requirements Document, NASA Lewis Research Center, 3 February 1987.
7. LeRC-SS-003, Solar Dynamic Power Module System Part 1 Control End Item Specification, NASA Lewis Research Center, 3 February 1987.
8. Jeffries, K.S., "Concentration of Off-Axis Radiation by Solar Concentrators for Space Power", IECEC Proceedings, 1989.
9. Boeing Material Standards
10. NASA TN D-6665, "Measured Performance of a 1089 K (1500°F) Heat Storage Device for Sun-Shade Orbital Missions", Namkoong, D., NASA Lewis Research Center, February 1972.
11. Taylor, M.F., Bauer, K.E., And McEligot, D.M., "Internal Forced Convection to Low-Prandtl-Number Gas Mixtures", International Journal of Heat Mass Transfer, Vol. 31, No. 1, pp. 13-25, 1988.

Appendix A
Test Summaries

BOEING

Test Set Up Log

BOEING

DATE	EVENT
03-21-90	CBC engine simulator delivered to Tulalip Test Site, Area 5.
06-28-90	SDHRT heat receiver delivered to Tulalip Test Site, Area 5.
07-09-90	SDHRT heat receiver tilted from vertical to horizontal orientation and installed in the receiver support structure.
07-13-90	Gas piping and vacuum chamber feed-through components installed between the CBC engine simulator and vacuum chamber. Jumper installed inside vacuum chamber to allow checkout of the CBC.
08-10-90	CBC engine simulator argon checkout 1.
08-10-90	LN ₂ cold shrouds and cold plate delivered to Tulalip Test Site, Area 5.
08-15-90	LN ₂ cold shrouds installed on heat receiver.
09-14-90	Area 5 vacuum chamber demonstrated pump down to a vacuum level of 1.2×10^{-6} torr.
09-19-90	Quartz lamp array assembled and installed inside heat receiver.
09-21-90	Jumper removed from gas lines inside vacuum chamber and helium-xenon gas piping installed between the vacuum chamber gas feed-throughs and the inlet and outlet plenums on the heat receiver.
10-03-90	CBC engine simulator argon checkout 2.
10-09-90	Test Readiness Review meeting conducted. Borescope installed and vacuum chamber closed and ready for test.

BOEING

Summary of Test Conduct Log

ADRT Test Conduct Summary

DATE	TIME	TEST MODE	EVENT
10-09-90	15:45 PDT	VT.1	Begin initial pumping on vacuum chamber.
10-10-90	12:00	VT.1	<u>Unplanned Event 1</u> - Discovered electrical dielectric leak from electrical feed-throughs on chamber to ground. Also discovered leak through the optical borescope. Terminated test mode VT.1 to correct problems.
10-12-90	18:30	VT.1	All problems corrected and vacuum chamber closed to resume testing. Begin pumping on vacuum chamber.
10-15-90	14:30	VT.1	<u>Unplanned Event 2</u> - Chamber vacuum at 1.6×10^{-6} torr. Ready to establish LN_2 flow through the cold plate and initiate quartz lamp heater operation. However, LN_2 flow through the feed-through flange damaged the o-ring seal and chamber vacuum was lost. Test mode VT.1 terminated at 18:00 to correct problems flange and borescope seal problems.
10-22-90	21:30	VT.1	LN_2 chamber feed-through flange rebuilt with copper gasket seal. Fittings on the LN_2 lines inside the vacuum chamber replaced by welded connections. Chamber closed and vacuum pumping resumed.
10-23-90	05:30	VT.1	Initiated flow of LN_2 through cold plate and shrouds for final checkout of LN_2 system. Chamber vacuum at 3×10^{-5} torr. A system level helium leak check after shut down of the shrouds and cold plate showed no leaks in the LN_2 or chamber hardware.
10-24-90	12:46	VT.1	LN_2 flow established through the cold plate; chamber vacuum at 6×10^{-6} torr.
10-24-90	14:56	VT.1	Begin power up of quartz lamp heater zones to VT.1 power levels; chamber vacuum at 6×10^{-7} torr.
10-25-90	17:55	VT.1	Performed a cold plate purge operation. Peak cold plate temperature reached 200°F and chamber vacuum reached 4×10^{-4} torr.
10-26-90	01:20	VT.1	Restored LN_2 flow through the cold plate. Power restored to quartz lamp zones; chamber pressure at 2×10^{-6} torr.

DATE	TIME	TEST MODE	EVENT
10-27-90	06:50	VT.1	Receiver cavity temperatures stabilized at about 1000°F and test mode VT.1 declared complete. Total electrical lamp power was approximately 6,700 watts and chamber vacuum at 5.4×10^{-6} torr.
10-27-90	08:47	VT.2	LN ₂ flow established through the cold shrouds.
10-27-90	08:58	VT.2	Power increased to quartz lamp heater zones to ramp cavity temperature to 1600°F.
10-27-90	20:50	VT.2	Began melting salt in the heat storage tubes. Total lamp power level set at about 25.8 kW.
10-28-90	02:00 PDT	VT.2	Local time change to PST. Clocks set back 1 hour.
10-28-90	01:15 PST	VT.2	Thermal arrest completed in about 5.4 hours close to the predicted time of about 5.8 hours assuming total receiver loss of 13 kW and heater power of 25.8 kW. Note the time change to PST.
10-28-90	13:26	VT.2	<u>Unplanned Event 3</u> - Partial electrical power loss to the test site caused by power surge (source unknown). Electrical power lost to the quartz lamp heaters, LN ₂ subcooler, DACS, and RGA.
10-28-90	15:00	VT.2	Electrical power returned to site. Loss of power caused a noticeable loss of clarity through the optical borescope, loss of T/C's on cold plate, and loss of RGA operation.
10-29-90	03:40	VT.2	<u>Unplanned Event 4</u> - Vacuum level degrading in chamber from 3.9×10^{-6} torr to 2.2×10^{-4} torr. Cause believed to be material out-gassing. Continue VT.2 test mode.
10-29-90	08:40	VT.2	<u>Unplanned Event 4 (con't)</u> - Vacuum level continues to deteriorate. Vacuum level rose to approximately 5×10^{-3} torr. Power removed from all heater zones during pressure surge. Helium leak check failed to show any leaks in chamber.
10-29-90	09:55	VT.2	<u>Unplanned Event 4 (con't)</u> - Vacuum level continues to deteriorate. Vacuum level rose to 2×10^{-2} torr. Tubes discharged below the melt temperature by operating the CBC engine simulator using argon gas.

DATE	TIME	TEST MODE	EVENT
10-29-90	10:45	VT.2	<u>Unplanned Event 4 (con't)</u> - CBC engine simulator off. Lamps powered at low power to prevent cavity temperatures from dropping too low. Total lamp power set at about 10 kW.
10-29-90	16:37	VT.2	Vacuum has recovered to 1×10^{-6} torr. Will proceed with test mode VT.3 orbital baseline cycling to preserve test matrix hours. Terminate test mode VT.2 and will use a power of 18 kW to hold receiver temperatures at about 1480°F.
10-29-90	17:25	VT.3	Charged CBC with 35 psig He-Xe gas. Initiated CBC operation.
10-29-90	17:26	VT.3	Begin power adjustments to quartz lamp heater zones to VT.3 baseline power levels. Begin the sunlit period of orbit #1. Full power to lamp zones obtained at about 17:45.
10-29-90	17:58	VT.3	<u>Unplanned Event 5</u> - Power lost to zones E and F. Power lost to CBC engine simulator, LN ₂ subcooler, and DACS. Power loss caused by an overload on 1 of the three primary site load circuits. Power returned at 18:00. LN ₂ flow through sub-cooler reestablished without problems because of fast turn-around.
10-29-90	18:15	VT.3	<u>Unplanned Event 5 (con't)</u> - Begin eclipse of orbit #1 8 minutes early to allow switching of CBC and DACS power to another circuit.
10-29-90	18:40	VT.3	<u>Unplanned Event 5 (con't)</u> - Power switched off to the CBC and DACS near the end of eclipse to switch distribution to another circuit. Additional time required to replace bad breaker on power distribution cart.
10-29-90	19:09	VT.3	Electrical problems corrected. Begin sunlit period of orbit #2.
10-29-90	19:20	VT.3	<u>Unplanned Event 6</u> - Power lost momentarily to DACS because of unseated connector in power cart. Some data lost from file. Problem corrected within minutes and loss of power did not shut down the CBC or quartz lamp operation.
10-29-90	20:05	VT.3	<u>Unplanned Event 7</u> - Power to lamp zones E and F lost. Circuit breaker problems in power cart for these zones. Sensitive to temperature. Problem corrected during the eclipse period for orbit #2 by increasing the air flow to the power transformers from ventilation fan.
10-29-90	20:43	VT.3	Begin sunlit period of orbit #3.
10-29-90	22:15	VT.3	Added 10 psig He-Xe to CBC loop to increase static pressure.

DATE	TIME	TEST MODE	EVENT
10-29-90	22:17	VT.3	Begin sunlit period of orbit #4.
10-29-90	23:20	VT.3	Added an additional 5 psig He-Xe to CBC loop to increase static pressure.
10-29-90	23:52	VT.3	Begin sunlit period of orbit #5.
10-30-90	01:25	VT.3	Begin sunlit period of orbit #6.
10-30-90	02:59	VT.3	Begin sunlit period of orbit #7.
10-30-90	04:33	VT.3	Begin sunlit period of orbit #8. Temperatures appear to be reasonably stable. Terminate test mode VT.3 at the completion of eclipse of orbit #8.
10-30-90	06:07	VT.5	Begin sunlit period of orbit #9. Begin test mode VT.5. Adjust mass flow rate to 165 lbm/min.
10-30-90	07:35	VT.5	<u>Unplanned Event 8</u> - Vacuum level beginning to degrade. Chamber vacuum at 8×10^{-5} torr and increasing. This event appears to have begun at about 06:16 PST.
10-30-90	07:41	VT.5	Begin sunlit period of orbit #10.
10-30-90	09:15	VT.5	Begin sunlit period of orbit #11. Vacuum continues to fluctuate and increasing to about 2×10^{-4} torr.
10-30-90	10:49	VT.5	Begin sunlit period of orbit #12. Cavity temperatures stabilizing so terminate test mode VT.5 at the end of the eclipse of orbit #12.
10-30-90	12:07	VT.5	Added about 4 psig He-Xe to the CBC loop to increase the static pressure.
10-30-90	12:23	VT.5	<u>Unplanned Event 8 (con't)</u> - End of the eclipse period of orbit #12. The vacuum level continues to degrade. Chamber vacuum is at 4×10^{-4} torr. Terminate orbital cycling. Shut off CBC engine simulator and power to quartz lamps. Set quartz lamp power controller to manual mode.
10-30-90	12:48	VT.5	<u>Unplanned Event 8 (con't)</u> - After power removed and temperatures dropping in receiver, vacuum rose to 9×10^{-4} torr and continues to fluctuate widely.
10-30-90	13:51	VT.5	<u>Unplanned Event 8 (con't)</u> - Set heater zones to low power settings to keep tube temperatures stabilized near 1200°F.

DATE	TIME	TEST MODE	EVENT
10-30-90	15:40	VT.5	<u>Unplanned Event 8 (con't)</u> - Vacuum continues to fluctuate. Vacuum has increased to 1×10^{-3} torr. Heater power shut off to stabilize vacuum.
10-30-90	16:04	VT.5	<u>Unplanned Event 8 (con't)</u> - Power returned to lamps at low power level to maintain cavity temperatures around 1200°F. Vacuum has improved to 2×10^{-4} torr.
10-30-90	18:12	VT.6	Lamp power shut off to set panel controllers to VT3 power settings.
10-30-90	18:20	VT.6	<u>Unplanned Event 9</u> - Vacuum chamber pressure has stabilized at about 2×10^{-4} torr. Resume testing to preserve test hours and keep careful eye on chamber vacuum. Begin test mode VT.6 with the sunlit period of orbit #13. CBC blower will not start and attempts to activate blows the circuit breaker. Shut down power to DACS to swap blower and trailer power connections so that the CBC blower will be on a 70 amp breaker.
10-30-90	20:00	VT.6	Electrical problems fixed. Begin test mode VT.6 with the sunlit period of orbit #13.
10-30-90	21:35	VT.6	Begin sunlit period of orbit #14.
10-30-90	23:09	VT.6	Begin sunlit period of orbit #15.
10-31-90	00:43	VT.6	Begin sunlit period of orbit #16.
10-31-90	02:17	VT.6	Begin sunlit period of orbit #17. Temperatures stabilizing so last full orbit of test mode VT.6.
10-31-90	03:51	VT.8	Begin test mode VT.8 with the sunlit period of orbit #18.
10-31-90	05:25	VT.8	<u>Unplanned Event 10</u> - No power at command for sunlit period of orbit #19. Blown fuses in racks. CBC shut off at 05:35 to preserve tube temperatures and fuses replaced in racks.
10-31-90	05:52	VT.8	CBC restarted. Begin sunlit period of orbit #19.
10-31-90	06:27	VT.8	<u>Unplanned Event 11</u> - Power lost to heater zones E & F. Temperature problem with supply transformer. Cooling air adjusted and full power restored at 06:29.
10-31-90	06:32	VT.8	<u>Unplanned Event 12</u> - Zone 2B lost but left unnoticed until beginning of orbit 20. Reset at 07:35 PST.

DATE	TIME	TEST MODE	EVENT
10-31-90	06:58	VT.8	<u>Unplanned Event 13</u> - Manual shut down of power to lamps. Operator error. Power resumed to lamps for several more minutes to complete sunlit period of orbit 19.
10-31-90	07:31	VT.8	Begin sunlit period of orbit #20.
10-31-90	07:35	VT.8	<u>Unplanned Event 12 (con't)</u> - Reset zone 2B.
10-31-90	09:05	VT.8	Begin sunlit period of orbit #21.
10-31-90	10:42	VT.8	<u>Unplanned Event 14</u> - Power lost at beginning of sunlit period of orbit #22. CBC shut off to preserve cavity temperatures. Test director terminates test mode VT.8 even though temperatures not quite stabilized because of possible corona events and risk of operating the lamp array at highest power level with relatively high vacuum level (1.4×10^{-5} torr).
10-31-90	10:57	VT.12	CBC restarted and begin sunlit period of orbit #22 at VT.3 baseline power levels, orbital time-lines, and CBC interface parameters.
10-31-90	12:29	VT.12	Begin sunlit period of orbit #23.
10-31-90	14:03	VT.12	Begin sunlit period of orbit #24. Noted as time, $t=0$ for the simulation of peaking orbits.
10-31-90	14:51	VT.12	CBC flow rate set to 161 lbm/min.
10-31-90	15:09	VT.12	<u>Unplanned Event 15</u> - an attempt to set the gas flow rate down to 102 lbm/min is unsuccessful. The CBC flow rate can only be adjusted to obtain 115 lbm/min at full blower by-pass. Peaking orbital simulation test mode aborted and receiver allowed to stabilize at current (near VT.3 baseline) conditions.
10-31-90	15:37	VT.12	Begin sunlit period of orbit #25.
10-31-90	15:40	VT.12	Noticeable improvement in chamber vacuum level to the 10^{-5} torr range.
10-31-90	17:11	VT.12	Begin sunlit period of orbit #26. Adjust gas flow rate to 117 lbm/min. Last full orbit of the VT.12 test mode (return to VT.3 conditions).
10-31-90	17:16	VT.12	Continued improvement in chamber vacuum back to the 10^{-6} torr range.
10-31-90	18:45	SS.1	Begin test mode SS.1 with the sunlit period of orbit #27.

DATE	TIME	TEST MODE	EVENT
10-31-90	19:18	SS.1	Borescope image beginning to clear up.
10-31-90	20:19	SS.1	Begin sunlit period of orbit #28.
10-31-90	21:54	SS.1	Begin sunlit period of orbit #29.
10-31-90	23:28	SS.1	Begin sunlit period of orbit #30.
11-01-90	01:01	SS.1	Begin sunlit period of orbit #31.
11-01-90	02:35	SS.1	Begin sunlit period of orbit #32.
11-01-90	04:09	SS.1	Begin sunlit period of orbit #33.
11-01-90	05:43	SS.1	Begin sunlit period of orbit #34. Temperatures have stabilized. Terminate test mode SS.1 at the end of the eclipse period of orbit #34.
11-01-90	07:17	SS.4	Begin test mode SS.4 with the sunlit period of orbit #35.
11-01-90	08:51	SS.4	Begin sunlit period of orbit #36.
11-01-90	10:25	SS.4	Begin sunlit period of orbit #37. Temperatures reasonably steady and test director terminates test mode SS.4 at the end of the eclipse period of orbit #37 to preserve the test matrix.
11-01-90	11:21	SS.4	<u>Unplanned Event 16</u> - Power to all of zone "C" lost. Blown fuses in racks occurred at the end of the sunlit period. Repaired during the eclipse period of orbit #37.
11-01-90	11:59	VT.3B	Begin a revised VT.3 test mode adding an additional 7000 watts to the cavity to makeup for additional losses through the insulation. Test mode VT.3B begun with the sunlit period of orbit #38.
11-01-90	12:42	VT.3B	<u>Unplanned Event 17</u> - Power lost to zone 2B. Breaker temperature problem. Power restored to zone 2B at 12:47.
11-01-90	13:33	VT.3B	Begin sunlit period of orbit #39.
11-01-90	15:07	VT.3B	Begin sunlit period of orbit #40.
11-01-90	16:41	VT.3B	Begin sunlit period of orbit #41.
11-01-90	18:15	VT.3B	Begin sunlit period of orbit #42.

DATE	TIME	TEST MODE	EVENT
11-01-90	19:49	VT.3B	Begin sunlit period of orbit #43. Temperatures stabilized and test mode VT.3B terminated at the end of eclipse of orbit #43.
11-01-90	21:23	VT.3A	Begin a rerun of test mode VT.3 with the sunlit period of orbit #44.
11-01-90	22:57	VT.3A	Begin sunlit period of orbit #45.
11-02-90	00:31	VT.3A	Begin sunlit period of orbit #46.
11-02-90	02:05	VT.3A	Begin sunlit period of orbit #47.
11-02-90	03:39	VT.3A	Begin sunlit period of orbit #48.
11-02-90	05:13	VT.3A	Begin sunlit period of orbit #49.
11-02-90	06:47	VT.3A	Begin sunlit period of orbit #50. Temperatures stabilized and will terminate test mode VT.3A at the end of the eclipse period of orbit #50.
11-02-90	07:45	VT.3A	Begin eclipse period of orbit #50. At the end of the 36 minute eclipse period, continue cooling with no lamp power for CS.1 cool down test mode.
11-02-90	08:21	CS.1	End of eclipse period for orbit #50. Temperature control feed-back control valve set to manual position at last auto-set position. Begin CS.1 test mode.
11-02-90	09:19	CS.1	Exit gas temperature now 1000°F. Flow increased to 165 lbm/min.
11-02-90	10:55	CS.1	Flow by-pass valve fully closed. All available flow now going through the receiver. Flow rate is 164 lbm/min and drops with decreasing temperature.
11-02-90	12:42	CS.1	Flow by-pass valve is fully opened to check CBC low flow rate capability (measures approximately 90 lbm/min). Set back to fully closed position.
11-02-90	13:14	CS.1	Regenerator manual by-pass valve set to fully open to provide cooler gas to the receiver.
11-02-90	20:12	CS.1	Flow by-pass valve is fully opened to check CBC low flow rate capability (measures approximately 79 lbm/min). Set back to fully closed position.
11-02-90	20:22	CS.1	CBC shut off. End of test mode CS.1. Cavity temperatures approximately 125°F. Ready to begin cold soak start up test mode even though not at 60°F to minimize the test conduct hour over-run.

DATE	TIME	TEST MODE	EVENT
11-02-90	20:28	CS.3	Begin cold start-up of receiver. Full power restored to lamp zones with no CBC gas flow. Begin sunlit period of orbit #51.
11-02-90	22:02	CS.3	Begin sunlit period of orbit #52.
11-02-90	22:17	CS.3	Begin operation of CBC engine simulator 15 minutes into 2nd sunlit period. Helium-xenon gas flow rate set to minimum attainable of 83.7 lbm/min (at these conditions).
11-02-90	23:36	CS.3	Begin sunlit period of orbit #53.
11-02-90	23:36	CS.3	Unplanned Event 18 - Zone 2B off and was not detected for the entire heat up of cycle #53. Zone 2B reset at 01:15 PST as described below.
11-03-90	01:11	CS.3	Begin sunlit period of orbit #54.
11-03-90	01:15	CS.3	Unplanned Event 18 (con't) - Discovered heater zone 2B had no power. Reset at rack breaker.
11-03-90	02:07	CS.3	Unplanned Event 19 - Heater zones E and F lost. Transformer breaker tripped. Not restored before beginning of eclipse at 02:09. Reset transformer breaker.
11-03-90	02:45	CS.3	Begin sunlit period of orbit #55.
11-03-90	03:09	CS.3	Unplanned Event 20 - Heater zone 2B lost again. Difficult to reset at rack.
11-03-90	03:33	CS.3	Unplanned Event 21 - Heater zone 2B lost again. Tried to switch to spare circuit on rack with no success as voltage control card missing.
11-03-90	03:40	CS.3	Unplanned Event 21 (con't) - Switched heater zone 2B back to original circuit and tried to repower. Lost zone 2B again 2 minutes later and other zones (4B and 5B) showed evidence of cycling due to corona discharge in cavity. All zones reset prior to beginning eclipse at 03:43.
11-03-90	04:05	CS.3	Unplanned Event 22 - Transformer carts shut off to cool during eclipse period of orbit #55. Lost rack for zone C at attempted repower for sunlit period due at 04:19.
11-03-90	04:45	CS.3	Unplanned Event 22 (con't) - CBC shut off to preserve cavity temperatures during repair of zone C rack. Difficulty in locating blown fuse. Required extended shut down until arrival of electrician at test site (approximately 114 minutes after end of eclipse of orbit #55).

DATE	TIME	TEST MODE	EVENT
11-03-90	06:10	CS.3	Unplanned Event 22 (con't) - Lamps turned on manually for checkout and preheat of cavity. The CBC engine simulator was not operated during this period. Total duration of operation was about 11 minutes.
11-03-90	06:22	CS.3	Unplanned Event 22 (con't) - Lamp power removed and cycle controller set to automatic.
11-03-90	06:24	CS.3	CBC gas flow reestablished and lamp power restored at full VT.3 power levels. Begin sunlit period of orbit #56.
11-03-90	06:45	CS.3	Unplanned Event 23 - Lamp zone 5B cycling off and on. Zone 5B off for remainder of orbit #56. Not detected until 07:11.
11-03-90	07:11	CS.3	Unplanned Event 23 (con't) - Attempted repower of zone 5B; will not stay on and cycles to restart. Probable corona discharge occurring in cavity.
11-03-90	07:21	CS.3	Unplanned Event 24 - Lost zone 2B; difficult to reset at breaker. Begin eclipse period of orbit #56 at 07:22.
11-03-90	07:59	CS.3	Begin sunlit period of orbit #57.
11-03-90	08:00	CS.3	Unplanned Event 25 - Continue to lose zone 5B even at reduced power settings. Cycles indicating probable corona discharge.
11-03-90	08:30	CS.3	Unplanned Event 25 (con't) - Swapped zones 4B and 5B at SCR rack. Zone 5B continues to cycle shut down on new circuit confirming problem is with heater and not the SCR.
11-03-90	08:57	CS.3	Unplanned Event 25 (con't) - Power leads for lamp zones 4B and 5B swapped back to original channels on SCR rack during eclipse of orbit #57.
11-03-90	09:31	CS.3	Begin sunlit period of orbit #58.
11-03-90	09:33	CS.3	Unplanned Event 26 - Zone 5A power high at power up. No apparent cause noted. Reset to proper value.
11-03-90	09:36	CS.3	Unplanned Event 27 - Zones 4B and 5B cycling to trip off.
11-03-90	10:03	CS.3	Unplanned Event 27 (con't) - Zone 5B tripping off and drifting in power draw. Zone 1C tripped off. Reset at rack breaker.

DATE	TIME	TEST MODE	EVENT
11-03-90	10:23	CS.3	<u>Unplanned Event 27 (con't)</u> - Zone 5B off again. Zone 2C off.
11-03-90	10:27	CS.3	<u>Unplanned Event 28</u> - Zones 2C and 3C tripped. Vacuum level dropping into the 10 ⁻³ torr range (previously in low 10 ⁻⁶ torr range).
11-03-90	10:29	CS.3	<u>Unplanned Event 28 (con't)</u> - Zones 1C, 2C, 3C, and 5B tripped. Begin the eclipse of orbit #58.
11-03-90	11:00	CS.1	Test director terminates test mode CS.3 and the remaining test mode CS.6 because of corona problems inside cavity. Suspect salt leakage from tube because chamber vacuum appears to be reasonably good (but increasing). Continue to cool in a CS.1 type cool down test mode.
11-03-90	11:23	CS.1	Regenerator auto by-pass valve set to manual and flow rate held at 117 lbm/min.
11-03-90	12:52	CS.1	Flow by-pass valve fully closed (max flow through receiver) and regenerator by-pass fully opened (minimum gas inlet temperature).
11-03-90	23:34	CS.1	LN ₂ flow shut off to cold shrouds and cold plate. Inlet and exit gas temperatures within 1°F. End of CS.1. Begin final shut down operations.
11-04-90	00:10	-	GN ₂ purge established through shrouds and cold plate.
11-04-90	09:27	-	Shut chamber valve V25 and shut off diffusion pump.
11-04-90	09:40	-	CBC gas flow terminated.
11-04-90	10:34	-	Chamber back-filled with 1.5 psig GN ₂ . Temperatures of cold shrouds and cold plate greater than 32°F.
11-05-90	13:00	-	DACS operation discontinued. CBC loop pressure conditions (11:30 PST) were as follows: P _s = 34.5 psig, T _s = 46.0°F, P _r = 15.3 psi, P _t = 34.5 psig, T _t = 53.0°F.

BOEING

Equipment Disassembly Log

BOEING

DATE	EVENT
11-05-90	Vacuum chamber door opened for preliminary receiver inspection. Optical borescope removed from chamber. Cold plate removed from chamber. Off-gasing samples removed from chamber, support cart, cold plate, and borescope. Helium-xenon gas samples taken from the CBC loop in special containers.
11-15-90	Connected a nearly empty, 1.55 ft ³ argon bottle to CBC loop. Bleed off argon gas remaining in bottle out connecting line until nearly at 1 atmosphere pressure. Open up valve and flowed helium-xenon gas into bottle until equilibrium established. CBC loop pressure conditions after gas transfer to bottle (14:45 PST) were as follows: $P_s = 32.8$ psig, $T_s = 46.8^\circ\text{F}$, $P_a = 14.9$ psi.
11-16-90	Inlet and exit gas lines severed inside of vacuum chamber. CBC loop pressure conditions before cutting lines (13:30 PST) were as follows: $P_s = 32.9$ psig, $T_s = 53.6^\circ\text{F}$, $P_a = 14.7$ psi, $P_r = 33.0$ psig, $T_r = 55.0^\circ\text{F}$.
11-17-90	Quartz lamp array removed from receiver and disassembled. Axial zones assemblies placed inside of crates but not packaged for shipping to allow inspection by NASA personnel.
11-20-90	Inspection of receiver cavity and lamp zone assemblies by Mr. Kerry McLallin of NASA-LeRC and Mr. Chuck Kudija of Rocketdyne. Photographs taken on heat storage tubes.
12-07-90	CBC Piping runs removed and attached to CBC pallet. CBC loop back filled with argon gas. CBC pallet ready for shipping.
12-12-90	Final receiver inspection. Prepare misc lamp hardware for shipment to NASA-LeRC.
1-28-91	Disassembly of test hardware complete and ready to ship.
1-31-91	Hardware shipped to NASA-LeRC in Cleveland, OH.

BOEING

Summary of Vacuum Events

BOEING

DATE	TIME	TEST MODE	VACUUM (torr)	DESCRIPTION
10-24-90	12:50 PDT	VT.1	6.3×10^{-6}	Begin cold plate operation.
10-24-90	14:56	VT.1	7.3×10^{-7}	Begin increasing lamp power for VT.1
10-25-90	17:55	VT.1	6.8×10^{-6}	Shut off LN ₂ subcooler. Begin cold plate purge operation.
10-25-90	18:51	VT.1	4.2×10^{-4}	Maximum chamber vacuum during cold plate purge operation.
10-26-90	01:20	VT.1	2.0×10^{-6}	Restart LN ₂ subcooler operation.
10-26-90	01:30	VT.1	2.0×10^{-4}	Maximum chamber vacuum during LN ₂ subcooler start up.
10-27-90	06:50	VT.2	5.5×10^{-6}	End of test mode VT.1. Begin to initiate LN ₂ flow through cold shrouds.
10-27-90	08:47	VT.2	3.5×10^{-6}	Flow established through cold shrouds. Begin to increase heater power to ramp to 1600°F.
10-28-90	00:32	VT.2	1.1×10^{-6}	Begin off-gasing period 1.
10-28-90	05:20 PST	VT.2	1.5×10^{-4}	Maximum chamber vacuum during off-gasing period 1.
10-28-90	07:11	VT.2	1.0×10^{-4}	End of off-gasing period 1.
10-28-90	08:00	VT.2	1.2×10^{-5}	Vacuum has stabilized.
10-28-90	13:26	VT.2	1.3×10^{-5}	Partial loss of site power. Vacuum system remained functional but loss of LN ₂ flow because subcooler power lost.
10-28-90	13:50	VT.2	2.4×10^{-3}	Maximum chamber vacuum during loss of power event except for a brief spike excursion to the 10^{-2} range at about 16:00 PST.
10-28-90	18:50	VT.2	3.7×10^{-6}	Vacuum beginning to stabilize after return to normal operation.
10-29-90	03:15	VT.2	4.0×10^{-6}	Begin off-gasing period 2.
10-29-90	03:36	VT.2	3.7×10^{-4}	Vacuum level has increased 2 orders of magnitude in 21 minutes. Dropping cavity temperatures has no effect on vacuum level. Vacuum continues to degrade.

BOEING

DATE	TIME	TEST MODE	VACUUM (torr)	DESCRIPTION
10-29-90	08:50	VT.2	10^{-2}	Vacuum degrades to the point that the chamber ion gauge cuts out. Remains in the 10^{-2} range for about 143 minutes.
10-29-90	10:32	VT.2	1.8×10^{-3}	End of off-gasing period 2. Vacuum rapidly improving.
10-29-90	11:55	VT.2	2.1×10^{-6}	Vacuum level has decreased 2 orders of magnitude in 83 minutes.
10-29-90	17:26	VT.3	1.1×10^{-6}	Begin orbital cycling with VT.3 power levels.
10-30-90	06:07	VT.5	4.0×10^{-6}	Very good vacuum performance throughout VT.3. Vacuum varies between about 4 and 9×10^{-6} with orbital cycling.
10-30-90	06:16	VT.5	5.3×10^{-6}	Begin off-gasing period #3. Orbital cycling no longer effects chamber vacuum level.
10-30-90	12:23	VT.5	3.5×10^{-4}	Orbital cycling discontinued. CBC flow terminated and low level heating in cavity does not cause vacuum to improve. Vacuum level continues to fluctuate in the 10^{-4} range with occasional transient into the 10^{-3} range.
10-30-90	16:37	VT.5	2.5×10^{-4}	Vacuum beginning to stabilize at this new degraded level.
10-30-90	20:00	VT.6	2.3×10^{-4}	Begin orbital cycling with VT.6. Cycles have no effect on vacuum level confirming off-gasing is not originating inside the receiver cavity.
10-31-90	13:48	VT.12	1.0×10^{-4}	End of off-gasing period #3. Vacuum improving rapidly and beginning to be effected again by orbital cycling.
11-02-90	07:45	VT.3A	2.3×10^{-6}	Very good vacuum throughout orbital simulations 24-50. Chamber vacuum follows cavity temperatures and very repeatable after quasi-steady conditions have been achieved.
11-02-90	20:28	CS.3	7.1×10^{-7}	Good vacuum for cold soak start up simulation.

BOEING

DATE	TIME	TEST MODE	VACUUM (torr)	DESCRIPTION
11-03-90	06:24	CS.3	1.2×10^{-6}	Despite corona problems inside the receiver cavity, chamber vacuum has been well behaved. However, chamber vacuum levels shows a more rapid increase during orbits 56, 57, and 58 than the rate of increase in the previous 3 orbits. Chamber vacuum remains in the 10^{-6} range with only 2 brief transients to the 10^{-5} range at the ends of the sunlit periods of orbits 57 and 58.
11-03-90	11:00	CS.3	1.5×10^{-6}	End of orbital simulation testing.
11-03-90	23:23	-	6.8×10^{-7}	LN ₂ subcooler operation terminated. LN ₂ lines purged with GN ₂ .

BOEING

Borescope Picture Log

BOEING

Roll #	Pix #	Date	Time	Test Mode	Comments
1	-	-	-	VT.1/2	Approximately 5 pictures taken that did not expose. Too dark inside cavity.
1	1	10-27-90	14:18	VT.2	Image is faint and needs processing corrections (PC). Image appears to be blurred by contamination on the front quartz lens.
1	2-3	10-27-90	18:00	VT.2	Images are brighter and have improved in quality but are still blurred by contamination on the front lens. (PC)
1	4-5	10-27-90	18:45	VT.2	Images have cleared.
1	6-7	10-27-90	20:20	VT.2	Very clear images of the receiver cavity and improved field of view adjustment by camera positioning.
1	8	10-28-90	07:55	VT.2	Image is clear but faint. (PC)
1	9	10-28-90	10:09	VT.2	Image is brighter and clear. (PC)
1	10-11	10-28-90	13:30	VT.2	Pictures taken immediately after losing site power. Image is clear but faint. (PC)
1	12	10-28-90	15:10	VT.2	Picture taken after power returned to lamps. Image quality has been severely degraded by the collection of contamination on the front lens caused by the loss of LN ₂ flow to the cold plate and shrouds during loss of site power.
1	13	unk	unk	unk	Image is very faint (PC). Cannot determine image quality and there is no record of when this photograph was taken. Probably shot immediately before increasing power to VT.3 levels as sequenced in pictures 14-23.
1	14-23	10-29-90	17:26	VT.3	Initial power up sequence of heater zones to VT.3 power levels. Images are bright but are blurred presumably from contamination that already collected on the lens.

BOEING

Roll #	Pix #	Date	Time	Test Mode	Comments
1	24-28	10-29-90	17:35	VT.3	Full power shots of the cavity during the sunlit period of orbit #1. Images are bright but blurred.
1	29-30	10-29-90	17:48	VT.3	Near the end of the sunlit period of orbit #1 during the loss of power to lamp zones E and F.
1	31	10-29-90	17:53	VT.3	Re-power of lamp zones E and F at the end of the sunlit period of orbit #1.
2	-	10-29-90	17:58	VT.3	Film roll #1 out. Begin film roll #2.
2	1-5	10-29-90	18:05	VT.3	Near the end of the sunlit period of orbit #1.
2	6-8	10-29-90	18:16	VT.3	Beginning of the eclipse period of orbit #1.
2	9-11	10-29-90	18:20	VT.3	Beginning of the eclipse period of orbit #1 while altering the camera aperture settings to brighten images.
2	12-14	10-29-90	19:15	VT.3	Sunlit period of orbit #2. Distortion of the lamp images remains. Caused by contamination on the front lens.
2	15	10-29-90	20:05	VT.3	Loss of heater zones E & F near the end of the sunlit period of orbit #2 but exact time not recorded.
2	16-25	10-29-90	20:07	VT.3	The eclipse period of orbit #2. Aperture settings varied during sequence shootings. Note that the contamination pattern on the bore-scope lens can be seen in pix #'s 23 and 24.
2	26	10-29-90	unk	VT.3	Sunlit period of orbit #3.
2	27-28	10-29-90	21:41	VT.3	Eclipse period of orbit #3.
3	-	10-29-90	21:45	VT.3	Film roll #2 out. Begin film roll #3.
3	1-2	10-29-90	22:17	VT.3	Sunlit period of orbit #4. No change in image quality.

BOEING

Roll #	Pix #	Date	Time	Test Mode	Comments
3	3-19	10-29-90	23:15	VT.3	Eclipse period of orbit #4.
3	20-35	10-29-90	23:52	VT.3	Power up sequence for the sunlit period of orbit #5. Some variations in camera aperture settings during sequence shootings.
4	-	10-30-90	00:15	VT.3	Film roll #3 out. Begin film roll #4.
4	1	10-30-90	00:50	VT.3	End of sunlit period of orbit #5.
4	2-10	10-30-90	00:50	VT.3	Eclipse period of orbit #5.
4	11-12	10-30-90	06:18	VT.5	Sunlit period of orbit #9.
4	13-15	10-30-90	unk	VT.5	Sunlit period(s) of orbit #'s 10-12. Time and/or notes not recorded in test log.
-	-	10-30-90	13:00	VT.5	Small heating pad mounted to the camera side lens assembly. Inspection showed possible ice crystals on back lens could be responsible for blurring of images seen through borescope. Heater left on overnight.
4	16-18	10-30-90	20:00	VT.6	Turning on lamps for the beginning of the sunlit period of orbit #13 after vacuum event #7. Image quality seems to have improved after vacuum event.
4	19-22	10-30-90	21:06	VT.6	Eclipse period of orbit #13.
4	23	unk	unk	VT.6	Sunlit period of orbit #14-16? Time and/or notes for these pictures not recorded in the test log.
4	24-28	unk	unk	VT.6	Eclipse period of orbit #14-16? Time and/or notes for these pictures not recorded in the test log.
4	29	10-31-90	03:15	VT.6	End of sunlit period of orbit #17.
4	30-35	10-31-90	03:23	VT.6	Eclipse period of orbit #17. Note the contamination pattern on the front lens can be seen in image #35 and has not changed from that seen in roll 2, pix 24.

BOEING

Roll #	Pix #	Date	Time	Test Mode	Comments
4	-	10-31-90	03:23	VT.6	Film roll #4 out. Last roll of 400 ASA film. Decided to wait until morning to obtain more film from the photo laboratory.
-	-	10-31-90	9:00	VT.8 VT.12	Heater pad removed from the end of the borescope because no change in image quality had been detected from its use. However, within 1 hour after its removal, the lens was completely coated with solid, opaque, contaminates blocking all view of the cavity. The heater pad was reinstalled back onto the end of the borescope but the image did not improve until much later in the test (see below). Unfortunately, no pictures were taken during this period because film was not reloaded as described above.
5	-	10-31-90	19:18	SS.1	Borescope beginning to clear up. Decided to load 100 ASA film into camera and boost 1 f-stop to 200 ASA.
5	1-17	10-31-90	19:20	SS.1	Sunlit period of orbit #27. Solid materials on the front of the bore-scope beginning to flake off. Can now view about 1/6 th of the borescope cross-sectional area. Note that the lines that show in the solid material on the front lens have a pattern very similar to that seen for the off-gasing, transparent materials collected previously (see roll 2, pix #24 and roll 4, pix #35).
5	18-19	10-31-90	20:19	SS.1	Sunlit period of orbit #28. Can now view about 1/5 th of the bore-scope cross-sectional area.
5	20-21	10-31-90	22:05	SS.1	Sunlit period of orbit #29. Can now view about 1/4 th of the bore-scope cross-sectional area.

BOEING

Roll #	Pix #	Date	Time	Test Mode	Comments
5	22-23	11-1-90	00:23	SS.1	Sunlit period of orbit #30. Can now view about 1/2 of the bore-scope cross-sectional area but clarity is poor.
5	24-26	11-1-90	01:45	SS.1	Sunlit period of orbit #31. Can now view almost all of the bore-scope cross-sectional area and clarity has improved but is still rather poor. Note however, that some of the blurring of lamp lines has improved in areas that used to be poor (zone 2E for example).
5	27	11-1-90	04:10	SS.1	Sunlit period of orbit #33. The borescope image quality is beginning to degrade but most of the image cross-section is visible.
5	28	11-1-90	04:28	SS.1	Sunlit period of orbit #33. The borescope image quality is rapidly deteriorating. Material is again depositing on the quartz lens and very little of the cavity is visible.
5	29-30	11-1-90	05:43	SS.1	Sunlit period of orbit #34. The image quality and field of view is continuing to degrade and change with time with materials flaking off the front lens and other materials being deposited.
5	31	11-1-90	10:26	SS.4	Sunlit period of orbit #37. Continual change in the image quality and field of view.
5	32	11-1-90	unk	unk	Sunlit period of orbit #38-42?. Continual change in the image quality and field of view.
5	33	11-1-90	19:49	VT3B	Sunlit period of orbit #43. Continual change in the image quality and field of view.
5	34	11-1-90	20:29	CS.3	Sunlit period of orbit #51. Beginning of cold start-up. Image quality and field of view are poor.

BOEING

Roll #	Pix #	Date	Time	Test Mode	Comments
6	-	11-1-90	unk	CS.3	Sunlit periods of 1 or more orbits taken during the cold start-up simulation. In all, 3 rolls of film were shot during this operation but only 1 of the rolls turned out. No notations were made in the test log to identify the time frames of the rolls shot.
6	1-38	11-1-90	unk	CS.3	Sunlit period of orbit #53?. Image quality and field of view are poor and little change through sequence of pictures. No times noted in test log to identify when these pictures were taken except that they were during the cold start-up CS.3. Best estimates are for the orbit shown.

Summary of LN₂ Consumption During Testing

BOEING

Date	Time	Test Mode	LN ₂ Rate (GPH)	Comments
10/25/90	08:57	VT.1	228	Cold plate operation only.
10/25/90	10:45	VT.1	244	
10/25/90	13:00	VT.1	187	
10/25/90	14:00	VT.1	282	
10/25/90	16:00	VT.1	207	
10/25/90	17:55	VT.1	-	Performed a cold plate purge operation - LN ₂ inventory too low to continue sub-cooler operation.
10/26/90	01:20	VT.1	-	Restore LN ₂ flow through cold plate with subcooler operation.
10/26/90	06:15	VT.1	146	
10/26/90	08:05	VT.1	401	
10/26/90	12:10	VT.1	256	
10/26/90	13:15	VT.1	212	
10/26/90	16:00	VT.1	222	
10/27/90	07:10	VT.1	230	
10/27/90	08:20	VT.2	-	Established LN ₂ flow through cold shrouds.
10/27/90	08:50	VT.2	334	Cold plate and cold shroud operation.
10/27/90	10:00	VT.2	337	
10/27/90	11:00	VT.2	212	
10/27/90	11:50	VT.2	233	
10/27/90	13:45	VT.2	215	
10/27/90	14:45	VT.2	289	
10/27/90	16:00	VT.2	214	
10/27/90	16:30	VT.2	420	
10/27/90	17:00	VT.2	138	
10/27/90	18:00	VT.2	356	
10/27/90	22:00	VT.2	333	
10/27/90	23:00	VT.2	336	
10/27/90	24:00	VT.2	297	

BOEING

Date	Time	Test Mode	LN ₂ Rate (GPH)	Comments
10/28/90	01:00	VT.2	311	
10/28/90	03:00	VT.2	273	
10/28/90	04:00	VT.2	416	
10/28/90	05:45	VT.2	242	
10/28/90	07:00	VT.2	399	
10/28/90	08:35	VT.2	316	
10/28/90	10:25	VT.2	311	
10/28/90	12:15	VT.2	305	
10/28/90	13:30	VT.2		Lost power to LN ₂ subcooler. LN ₂ flow lost to cold shrouds and cold plate. Established LN ₂ flow through cold plate only by direct feed of LN ₂ from tank.
10/28/90	14:30	VT.2	202	
10/28/90	15:00	VT.2	-	Power returned to LN ₂ subcooler.
10/28/90	17:00	VT.2	276	
10/28/90	19:00	VT.2	384	
10/28/90	20:00	VT.2	285	
10/28/90	21:00	VT.2	357	
10/28/90	22:00	VT.2	281	
10/28/90	23:30	VT.2	336	
10/29/90	01:15	VT.2	283	
10/29/90	03:00	VT.2	316	
10/29/90	04:00	VT.2	335	
10/29/90	06:05	VT.2	308	
10/29/90	07:25	VT.2	359	
10/29/90	12:00	VT.2	374	
10/29/90	13:00	VT.2	65	
10/29/90	15:00	VT.2	305	
10/29/90	17:00	VT.2	245	

BOEING

Date	Time	Test Mode	LN ₂ Rate (GPH)	Comments
10/29/90	17:58	VT.3	-	Electrical power lost to subcooler. LN ₂ flow reestablished within 2 minutes without problem.
10/29/90	19:00	VT.3	318	
10/29/90	21:00	VT.3	286	
10/30/90	05:00	VT.3	347	
10/30/90	08:00	VT.5	333	
10/30/90	12:00	VT.5	299	
10/30/90	14:00	VT.5	337	
10/30/90	16:00	VT.5	297	
10/30/90	23:00	VT.6	350	
10/31/90	02:00	VT.6	357	
10/31/90	05:00	VT.8	321	
10/31/90	17:00	VT.12	353	
11/1/90	-	-	-	No LN ₂ readings taken.
11/2/90	11:30	CS.1	190	
11/2/90	13:00	CS.1	237	
11/2/90	15:00	CS.1	245	
11/2/90	16:00	CS.1	275	
11/2/90	18:00	CS.1	236	
11/3/90	08:15	CS.3	281	
11/3/90	09:17	CS.3	359	
11/3/90	10:17	CS.3	338	
11/3/90	11:23	CS.1	363	
11/3/90	14:00	cool	238	
11/3/90	23:34	cool	-	LN ₂ flow to cold plate and cold shrouds terminated. LN ₂ subcooler shut off.



Appendix B
ADRT Data File Description

File Name	Begin Date	Begin Time	End Date	End Time	Ending Test Mode	Ending Cycle #	COMMENTS
VT11	10-23-90	00:06	10-23-90	08:00	C/O	-	Operational check out of LN ₂ system.
VT12	10-23-90	08:00	10-23-90	20:38	VT1	-	Heat up of shrouds and cold plate after LN ₂ C/O. Vacuum pumping.
VT13	10-23-90	20:38	10-24-90	12:12	VT1	-	Vacuum pumping. No lamp power.
VT14	10-24-90	12:12	10-25-90	00:52	VT1	-	Begin operation of the cold plate. Begin low level heating of cavity.
VT15	10-25-90	00:52	10-25-90	12:52	VT1	-	Low power heat up continued.
VT16	10-25-90	12:52	10-26-90	01:54	VT1	-	Cold plate purge operation.
VT17	10-26-90	01:54	10-26-90	15:56	VT1	-	Heat up to and stabilized at 1000°F.
VT21	10-26-90	15:56	10-27-90	15:17	VT2	-	Continue 1000°F + begin VT2 heat up. Begin shroud operation.
VT22	10-27-90	15:17	10-28-90	11:02	VT2	-	Loss of site power. Approximately 4.5 hours of data lost. Data retrieved from backup file.
VT23	10-28-90	15:00	10-29-90	03:38	VT2	-	VT2 continue
VT24	10-29-90	03:38	10-29-90	16:37	VT2	-	Vacuum event on temp shut down.
VT31	10-29-90	16:37	10-29-90	17:43	VT3	1	Electrical power loss. Approximately 21 minutes of data lost. Data retrieved from backup file.
VT32	10-29-90	18:04	10-29-90	18:39	VT3	1	DACS shut off to swap breakers. Approximately 14 minutes of data lost. Data retrieved from backup file.

File Name	Begin Date	Begin Time	End Date	End Time	Ending Test Mode	Ending Cycle #	COMMENTS
VT33	10-29-90	18:53	10-29-90	19:42	VT3	2	
VT34	10-29-90	19:42	10-30-90	01:13	VT3	5	
VT35	10-30-90	01:13	10-30-90	06:08	VT3	9	Begin vacuum event.
VT51	10-30-90	06:08	10-30-90	12:25	VT5	12	End of VT5. Shut off heaters because of vacuum.
VT52	10-30-90	12:25	10-30-90	17:55	VT5	12	Low heat vacuum stabilization.
VT53	10-30-90	17:55	10-30-90	18:51	VT5	12	Low heat vacuum stabilization.
VT54	10-30-90	19:00	10-30-90	19:52	VT5	12	Low heat vacuum stabilization. DACS shut off for 9 minutes to repair breakers.
VT61	10-30-90	19:52	10-31-90	02:00	VT6	16	
VT62	10-31-90	02:00	10-31-90	05:26	VT6	18	
VT81	10-31-90	05:26	10-31-90	10:55	VT8	21	
VT121	10-31-90	10:55	10-31-90	16:50	VT12	25	
SS11	10-31-90	16:50	10-31-90	21:50	SS1	28	
SS12	10-31-90	21:50	11-01-90	04:15	SS1	33	
SS13	11-01-90	04:15	11-01-90	10:00	SS4	36	
SS41	11-01-90	10:00	11-01-90	12:06	SS4	38	
VT3B1	11-01-90	12:06	11-01-90	17:55	VT3B	41	
VT3B2	11-01-90	17:55	11-01-90	23:38	VT3A	45	
VT3A1	11-01-90	23:38	11-02-90	05:32	VT3A	49	
CS11	11-02-90	05:32	11-02-90	20:11	CS1	50	

File Name	Begin Date	Begin Time	End Date	End Time	Ending Test Mode	Ending Cycle #	COMMENTS
CS31	11-02-90	20:11	11-03-90	01:02	CS3	53	
CS32	11-03-90	01:02	11-03-90	09:25	CS3	57	Problems.
CS33	11-03-90	09:25	11-03-90	12:38	CS3	58	Problems continued. Terminate testing.
COOL	11-03-90	12:38	11-05-90	11:15	CS1	58	Cool down from about 900°F. End of DACS operation.

Appendix C

**Selected Plots Comparing
Data Over Stabilized Orbits**

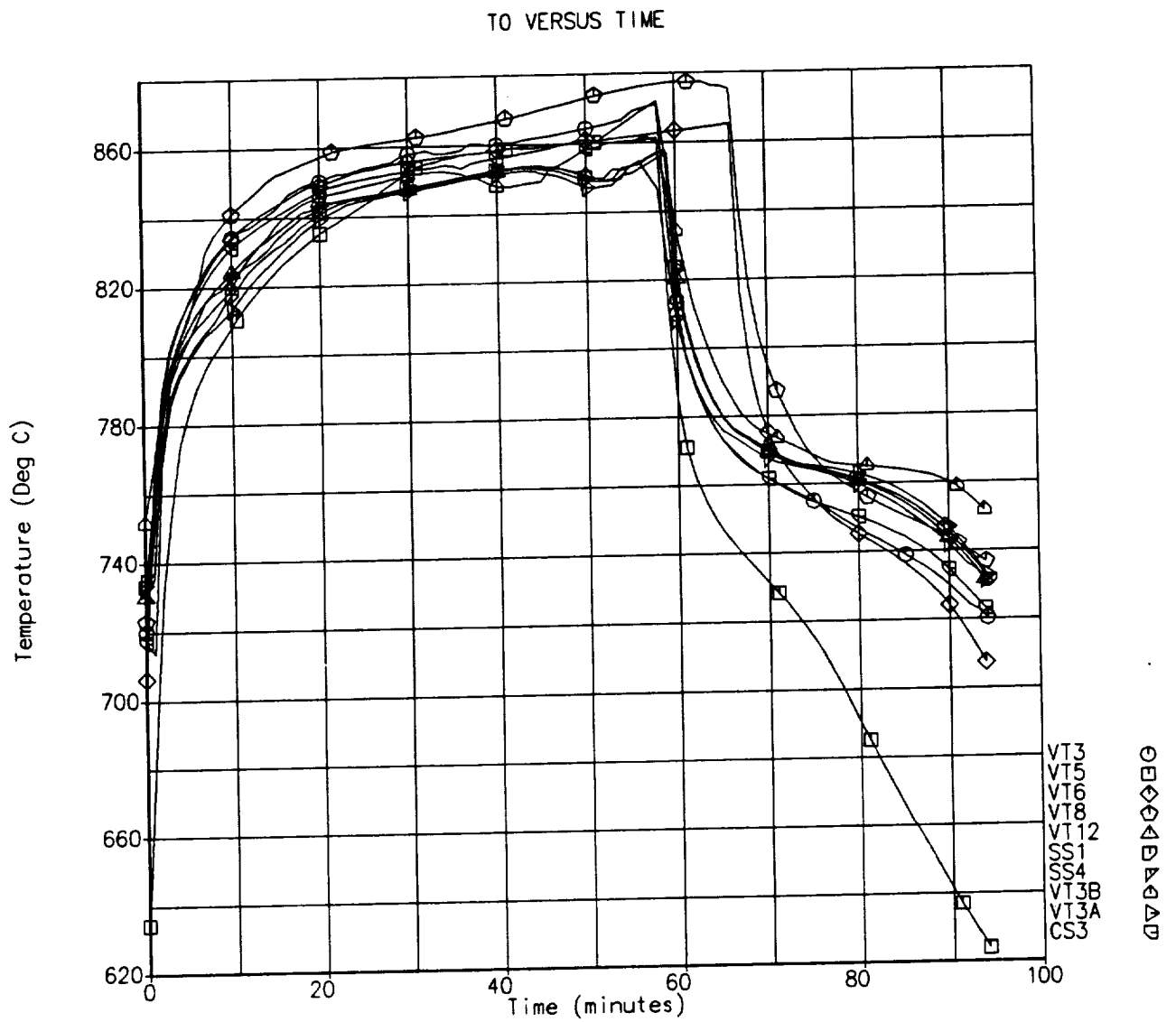


Figure C-1: Tube 4, Inlet End, Convolution Peak @ 0°

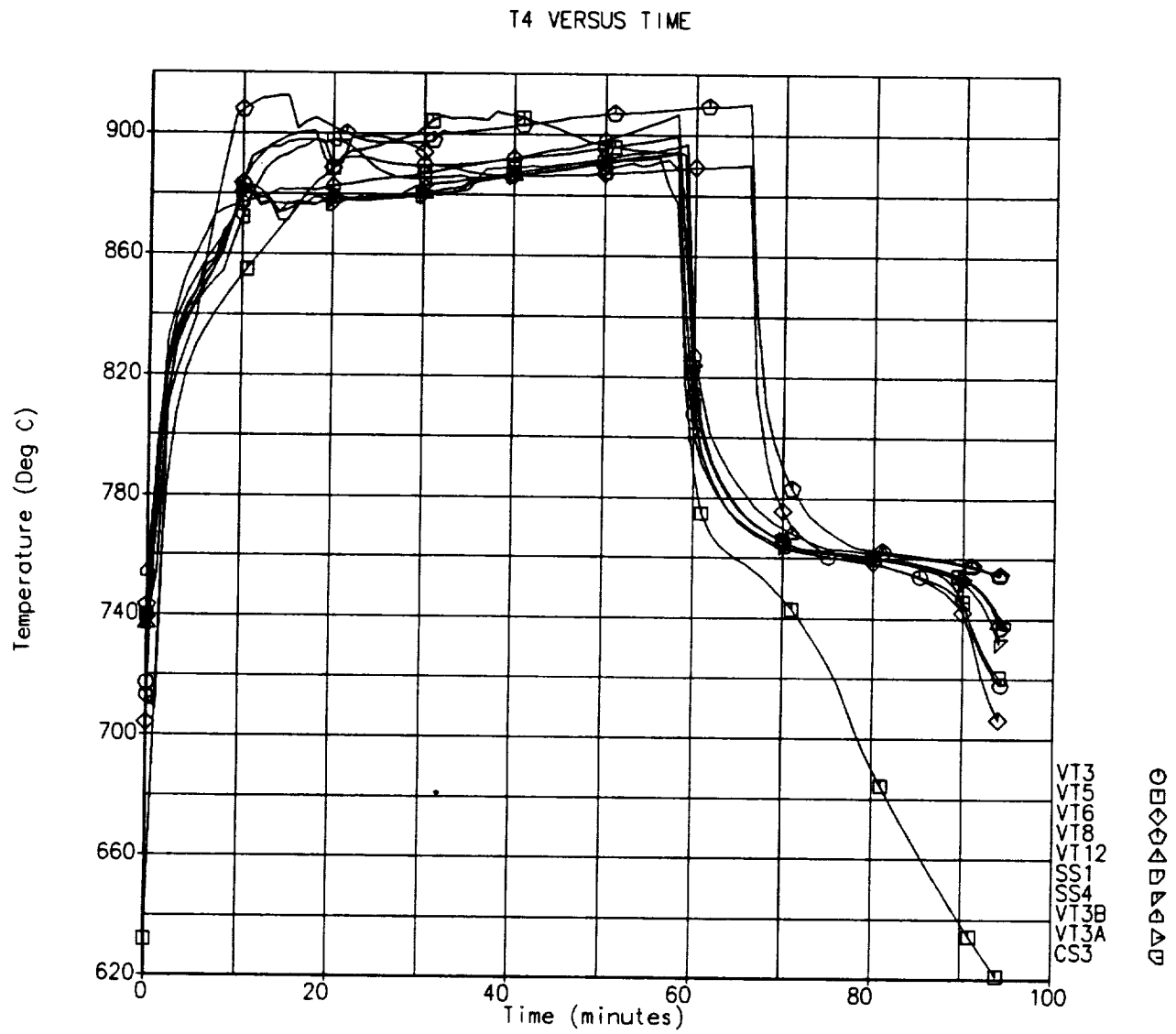


Figure C-2: Tube 4, Inlet End, Convolution Peak @ 180°

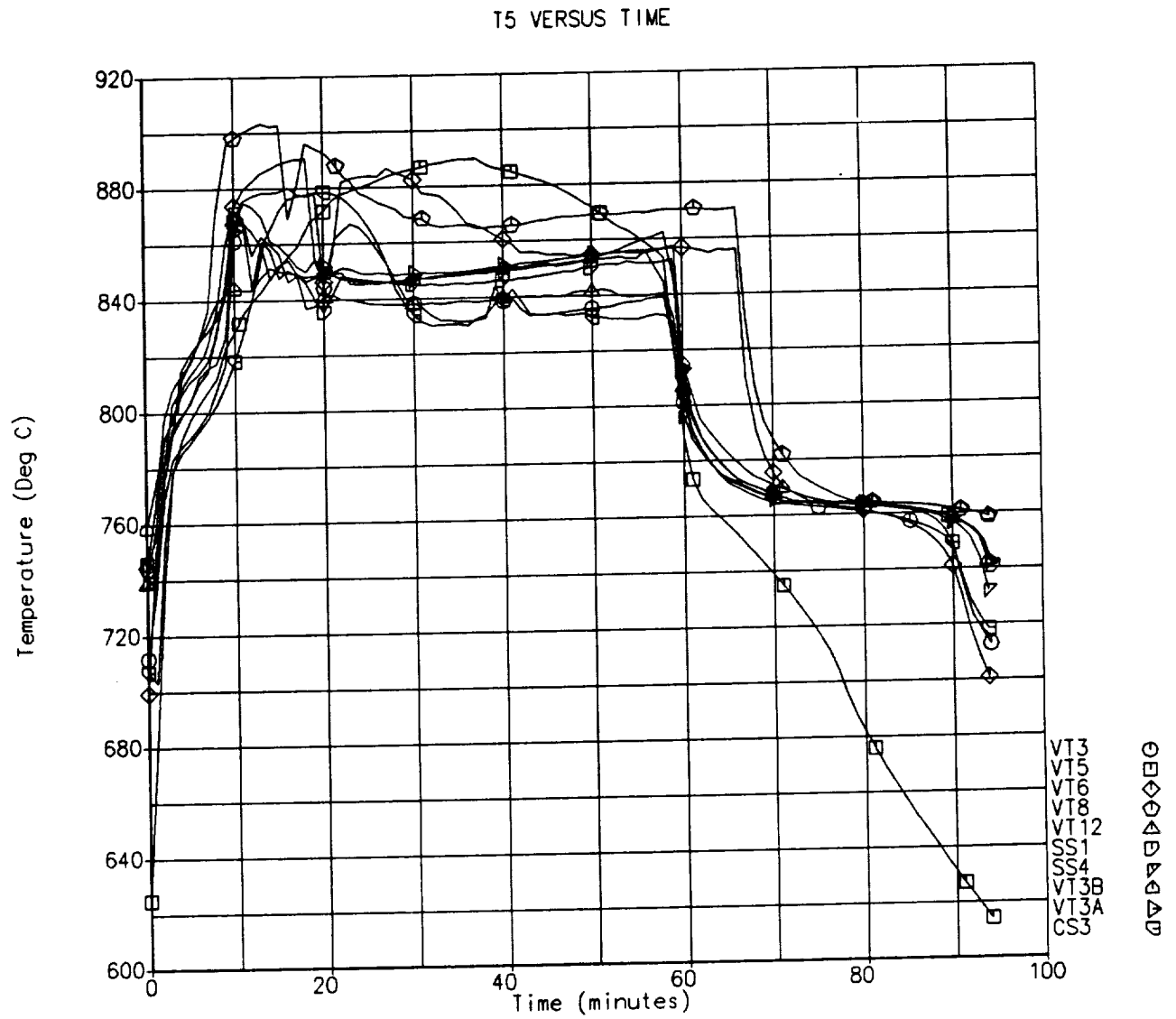


Figure C-3: Tube 4, Inlet End, Convolution Valley @ 180°

T8 VERSUS TIME

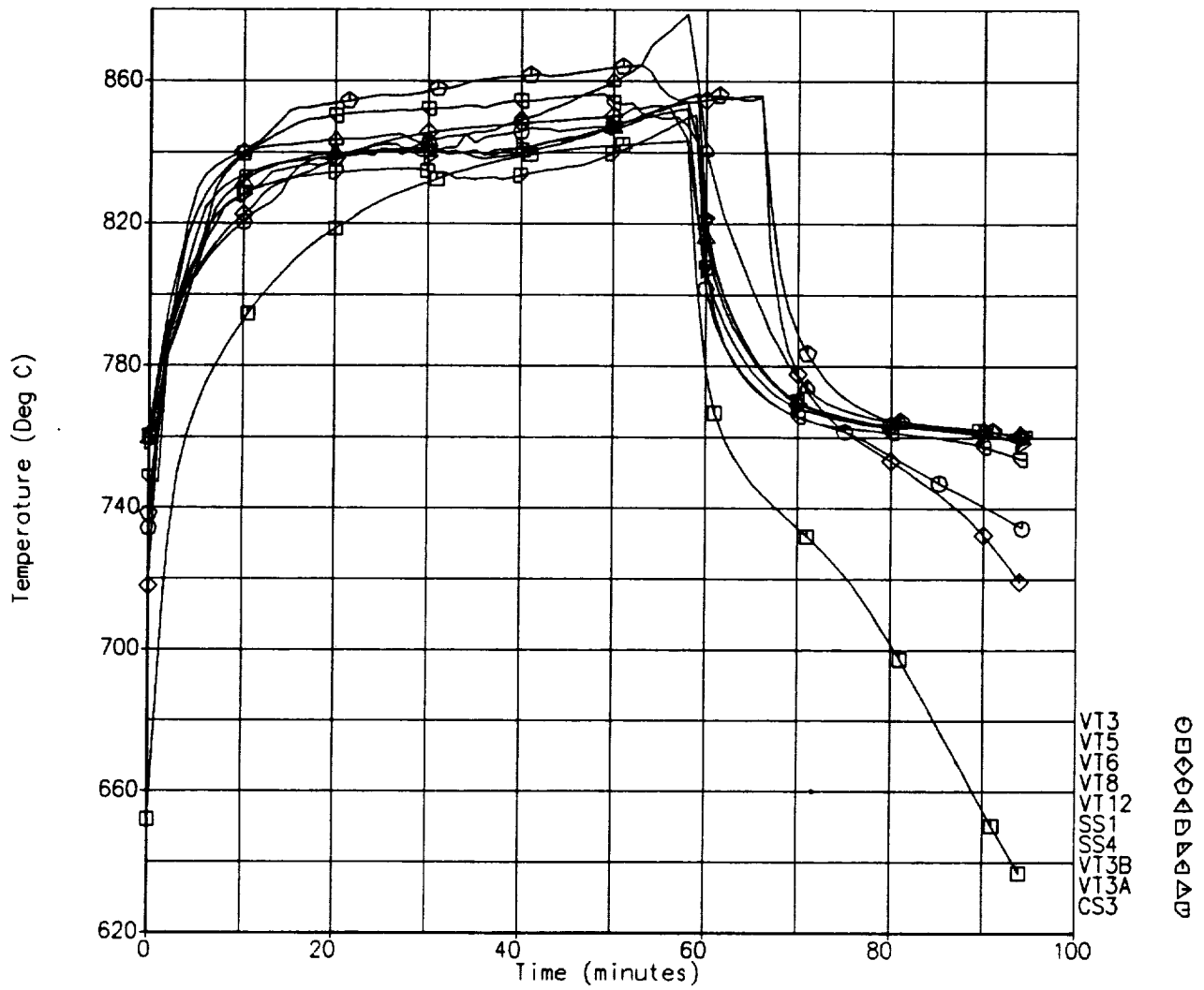


Figure C-4: Tube 4, Middle, Convolution Peak @ 0°

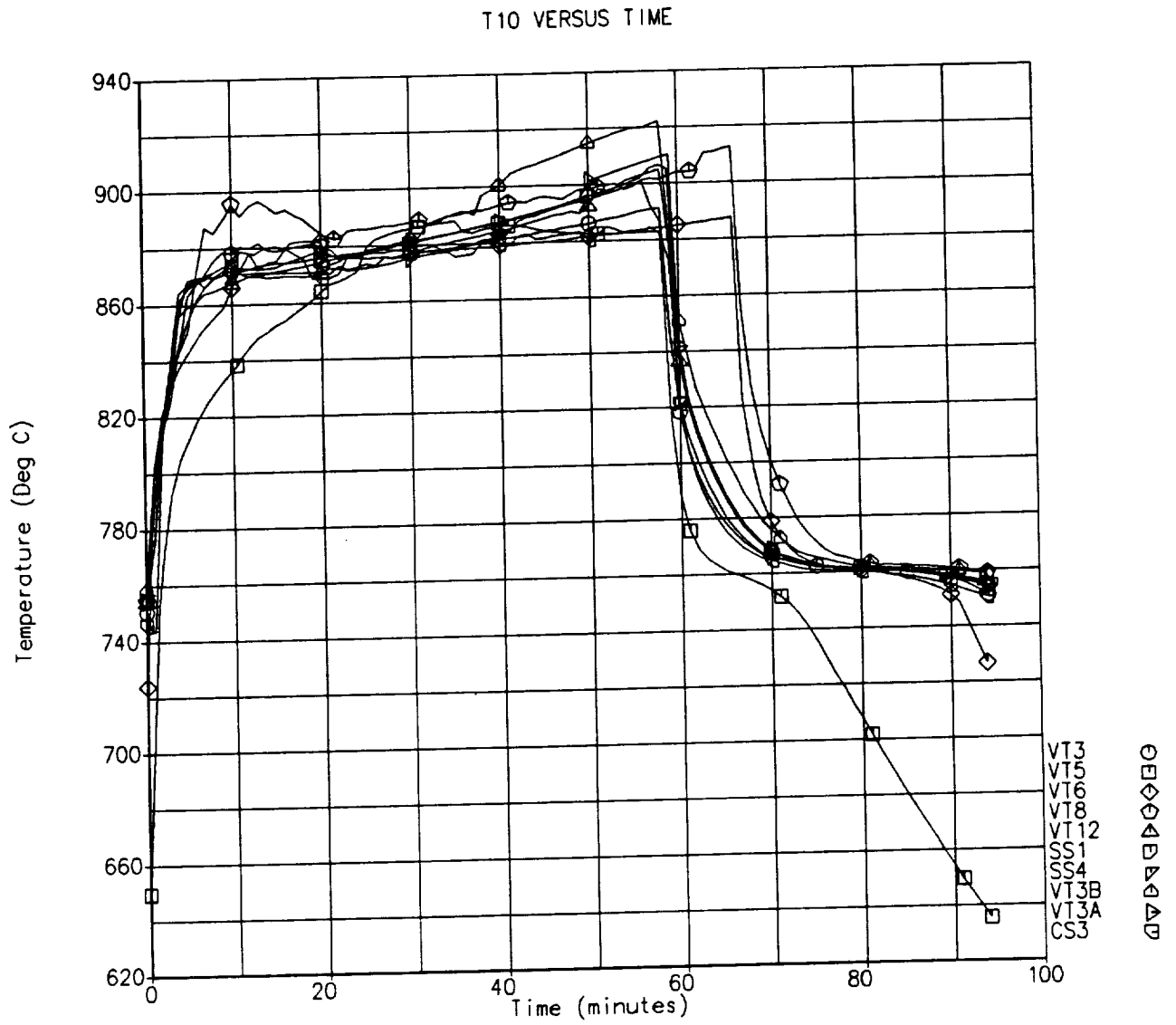


Figure C-5: Tube 4, Middle, Convolution Peak @ 180°

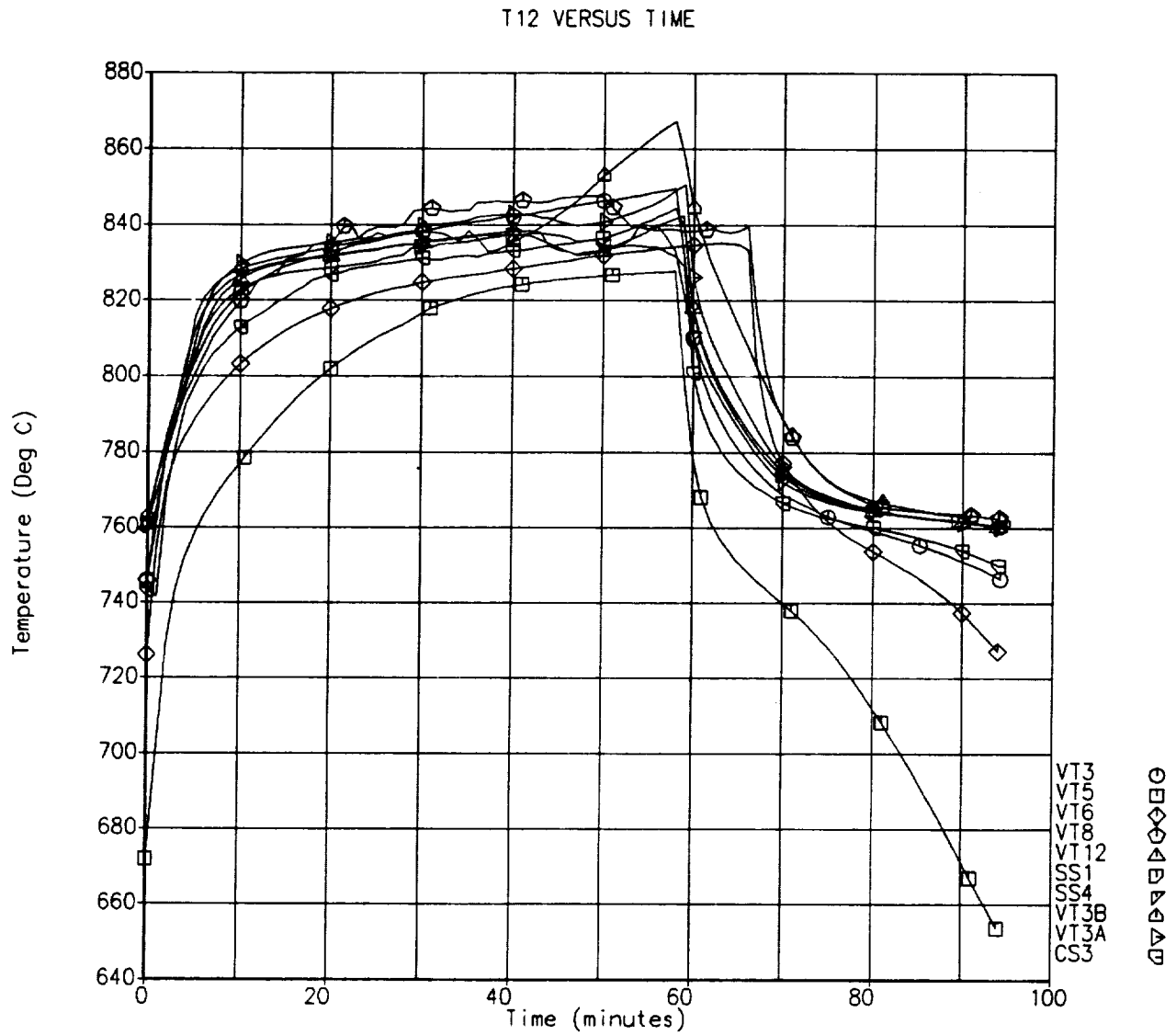


Figure C-6: Tube 4, Exit End, Convolution Peak @ 0°

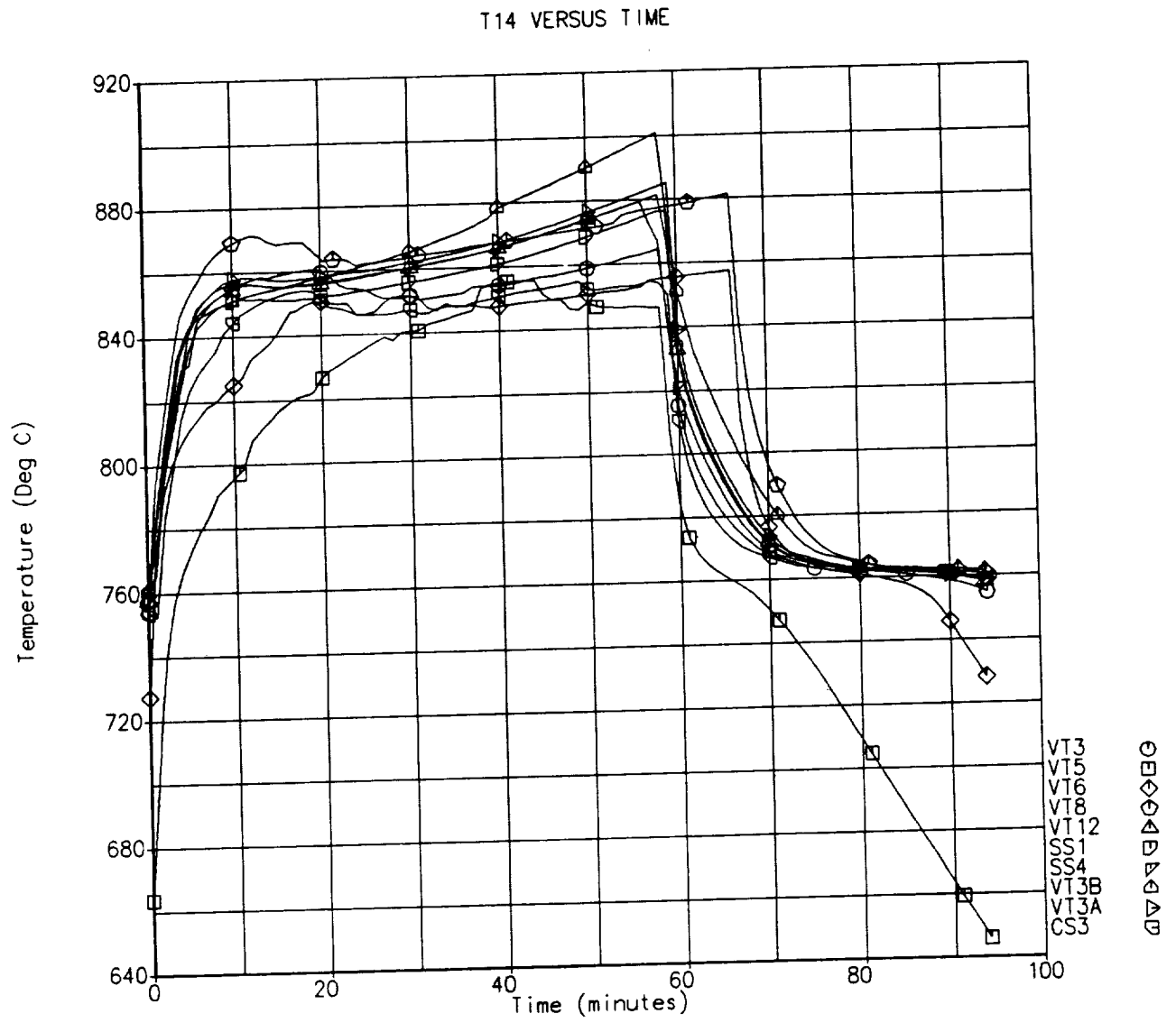


Figure C-7: Tube 4, Exit End, Convolution Peak @ 180°

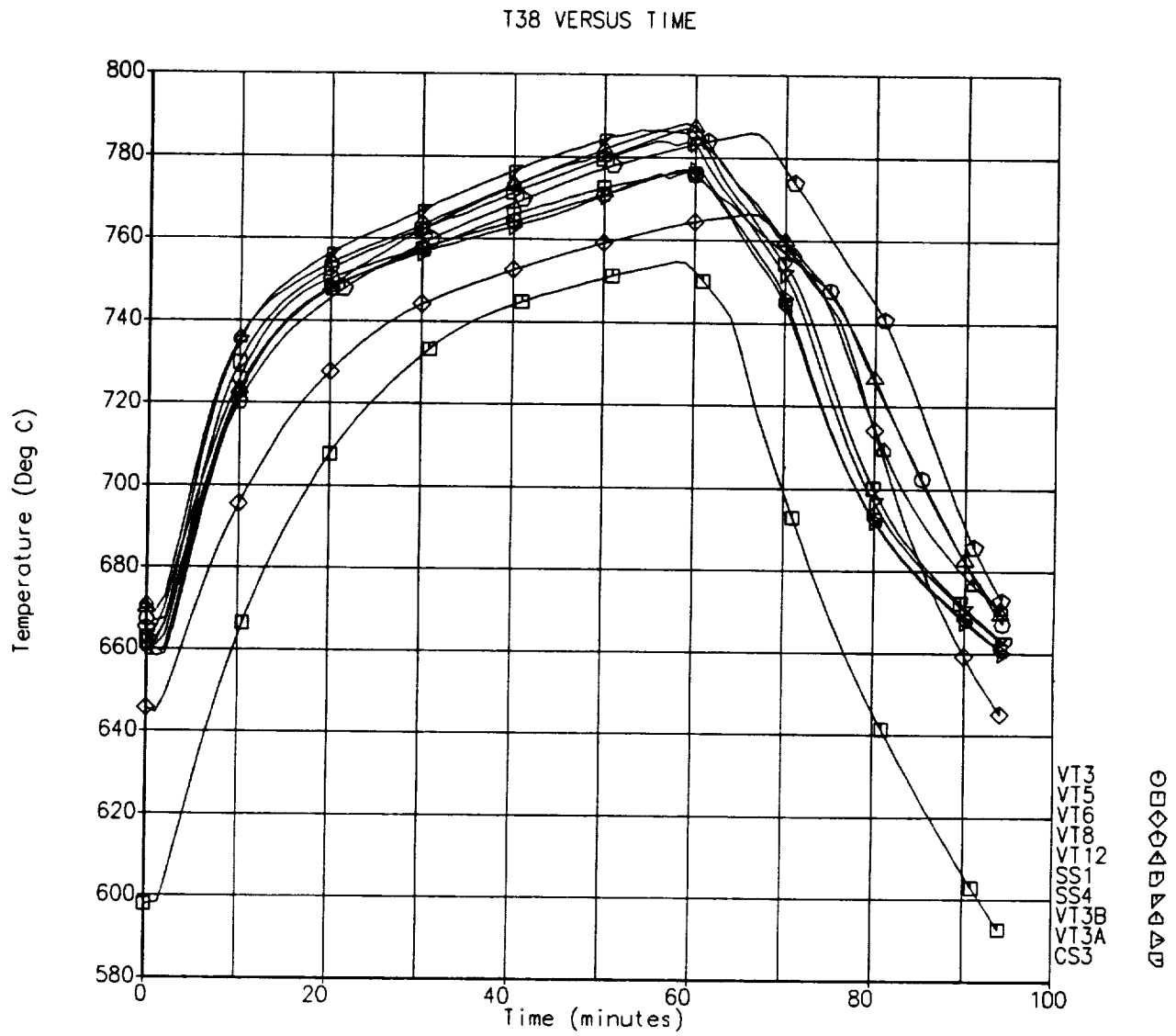


Figure C-8: Tube 12, Inlet End, Inner TES @ 90°

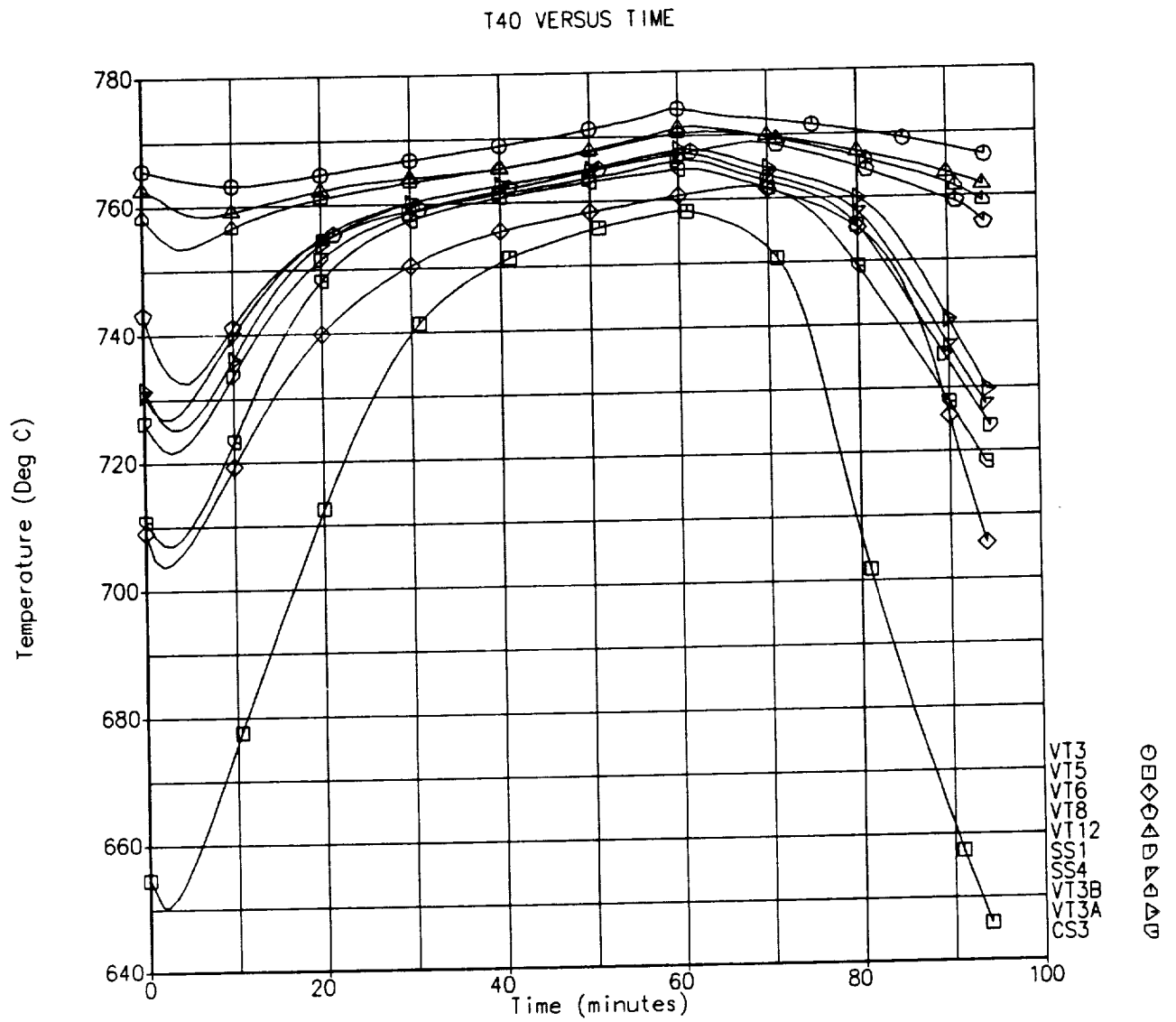


Figure C-9: Tube 12, Exit End, Inner TES @ 270°

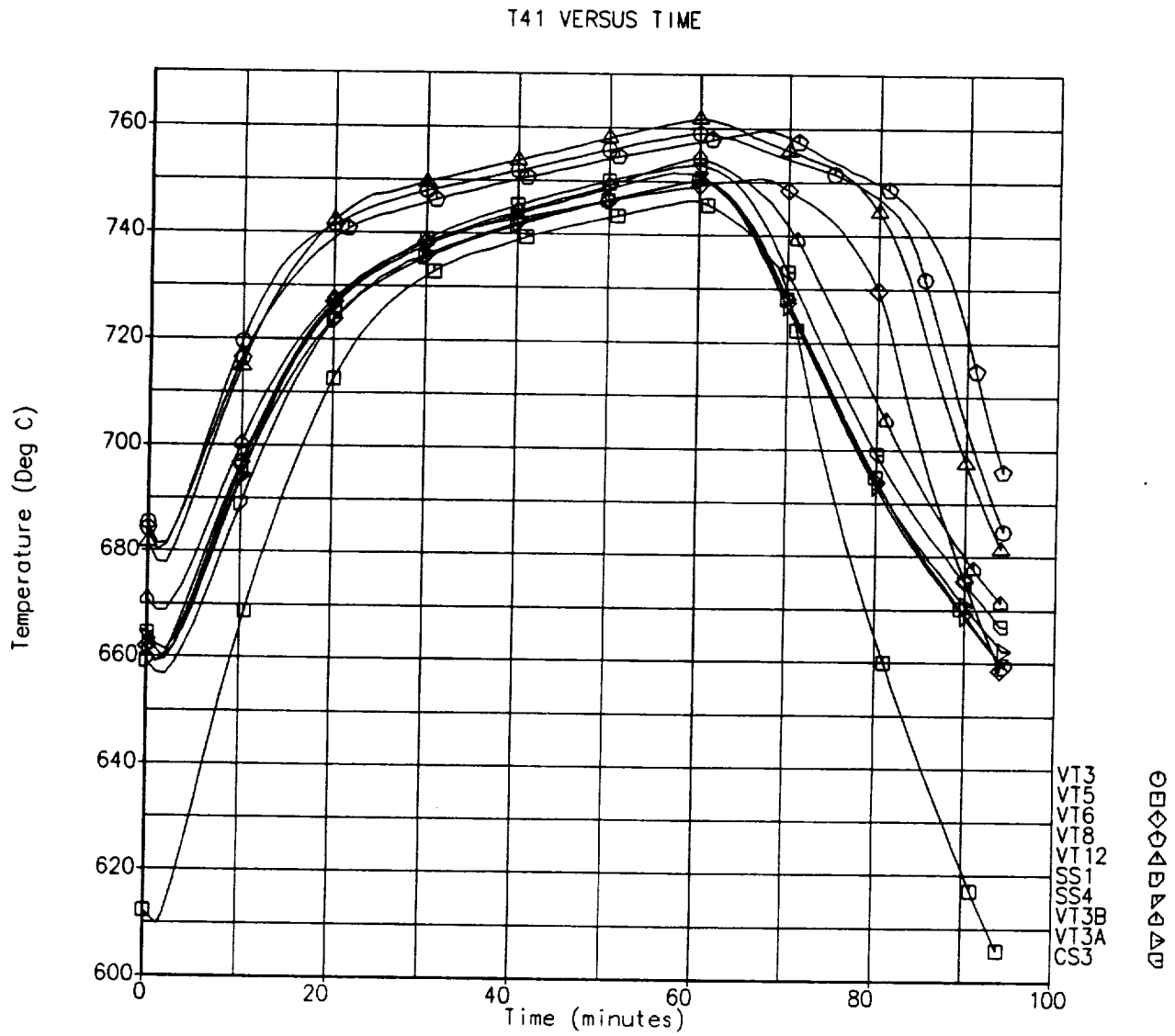


Figure C-10: Tube 12, Inlet End, Inner TES @ 270°

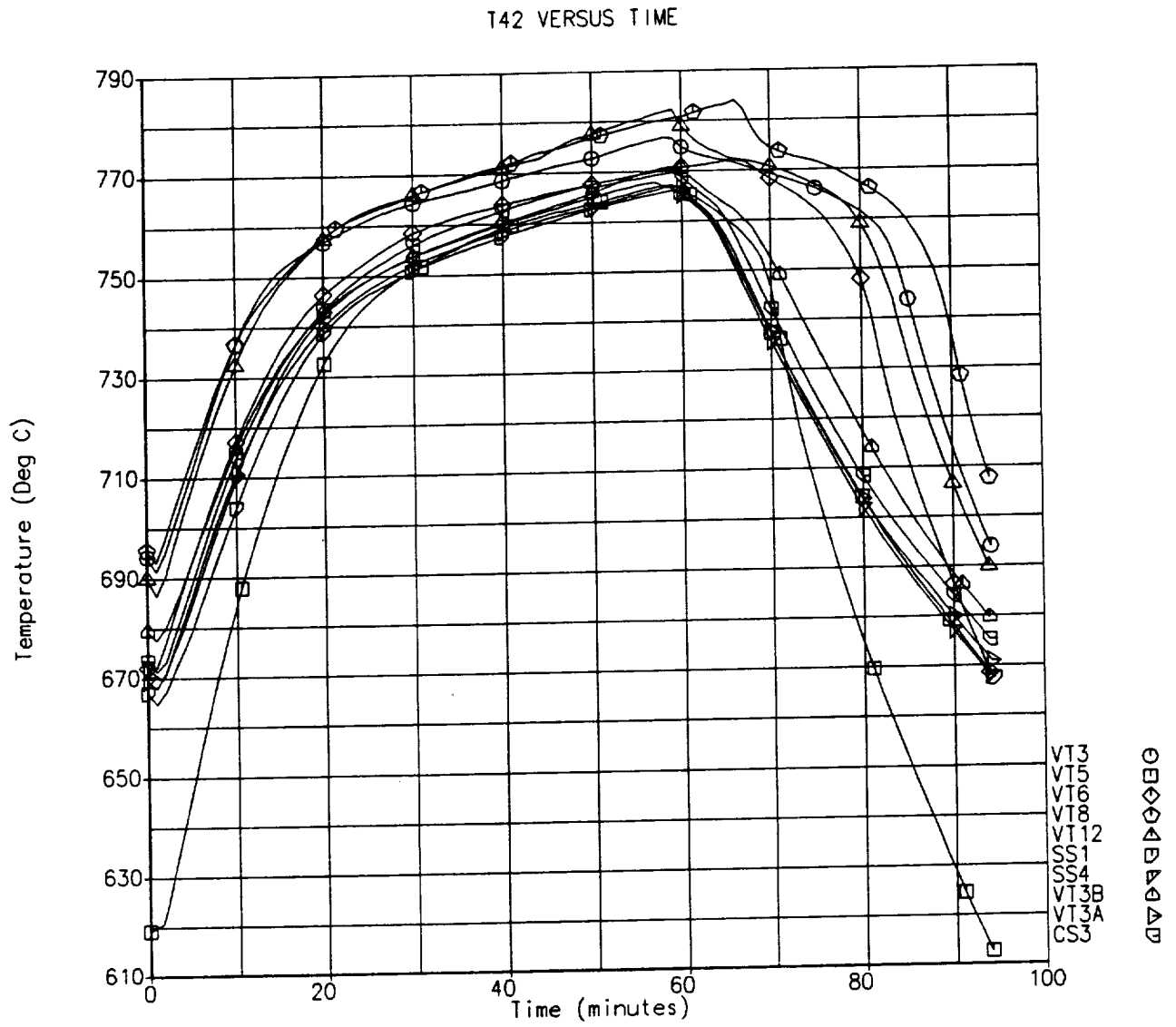


Figure C-11: Tube 12, Inlet End, Outer TES @ 270°

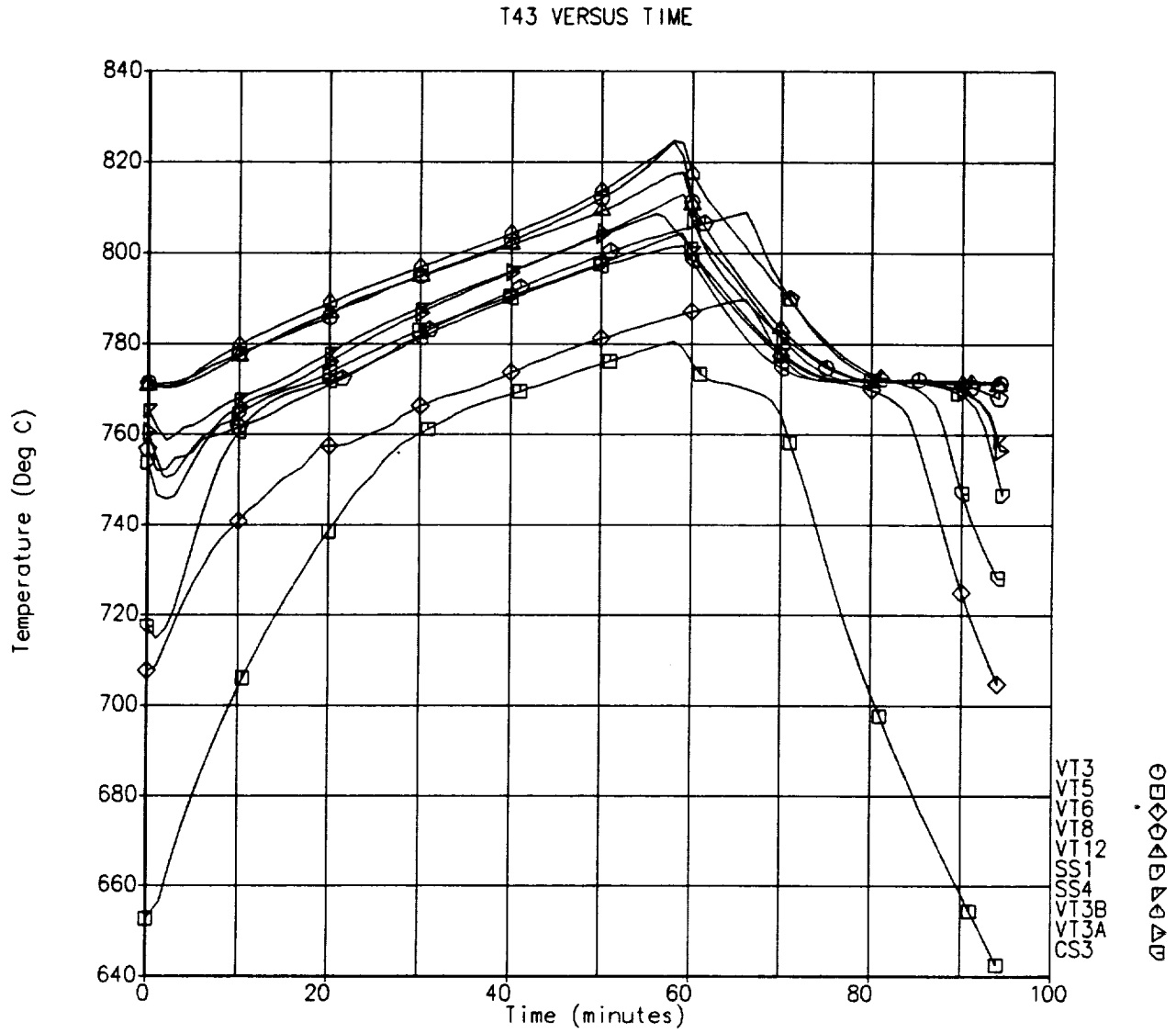


Figure C-12: Tube 12, Exit End, Outer TES @ 90°

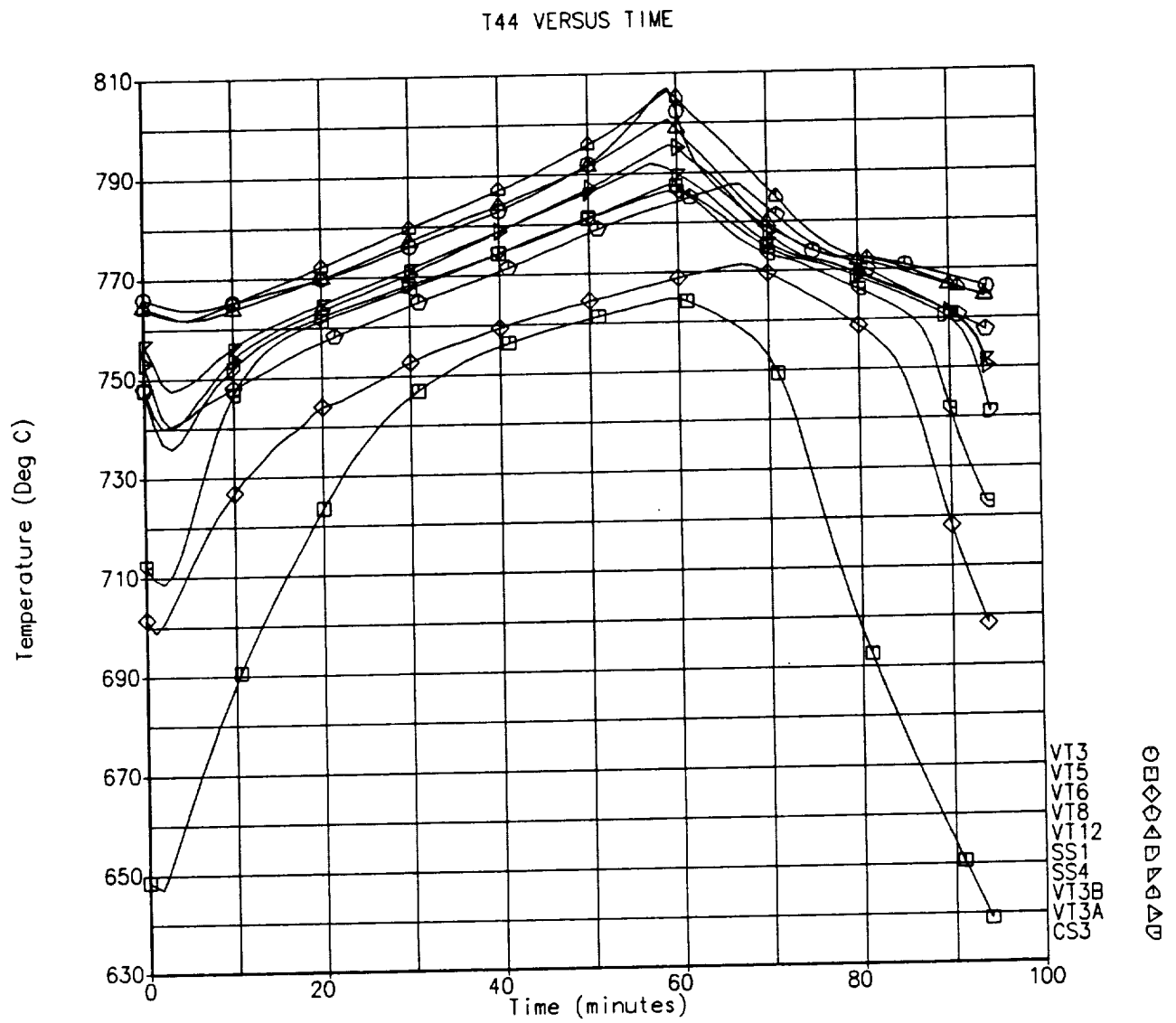


Figure C-13: Tube 12, Exit End, Inner TES @ 90°

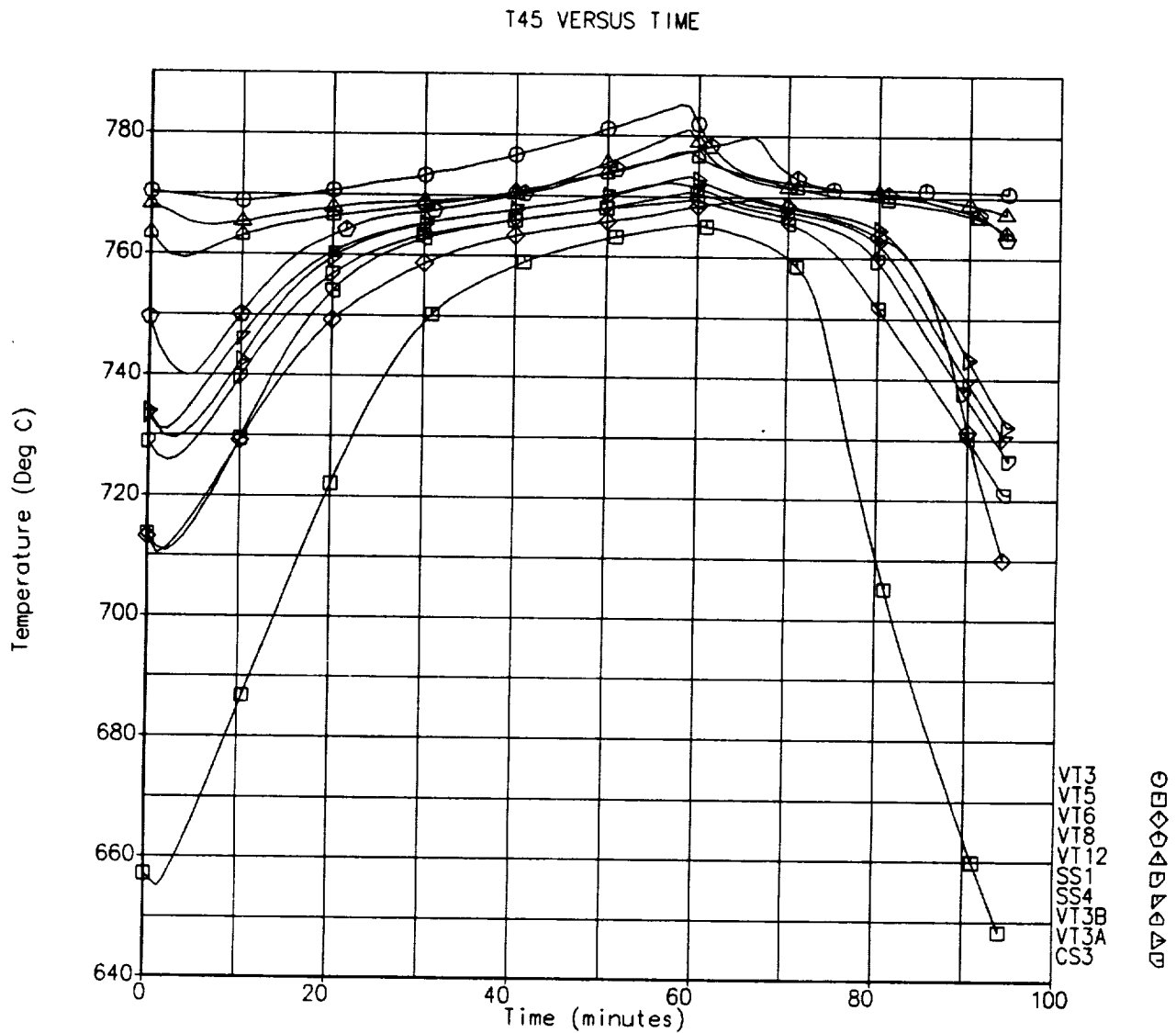


Figure C-14: Tube 12, Exit End, Outer TES @ 270°

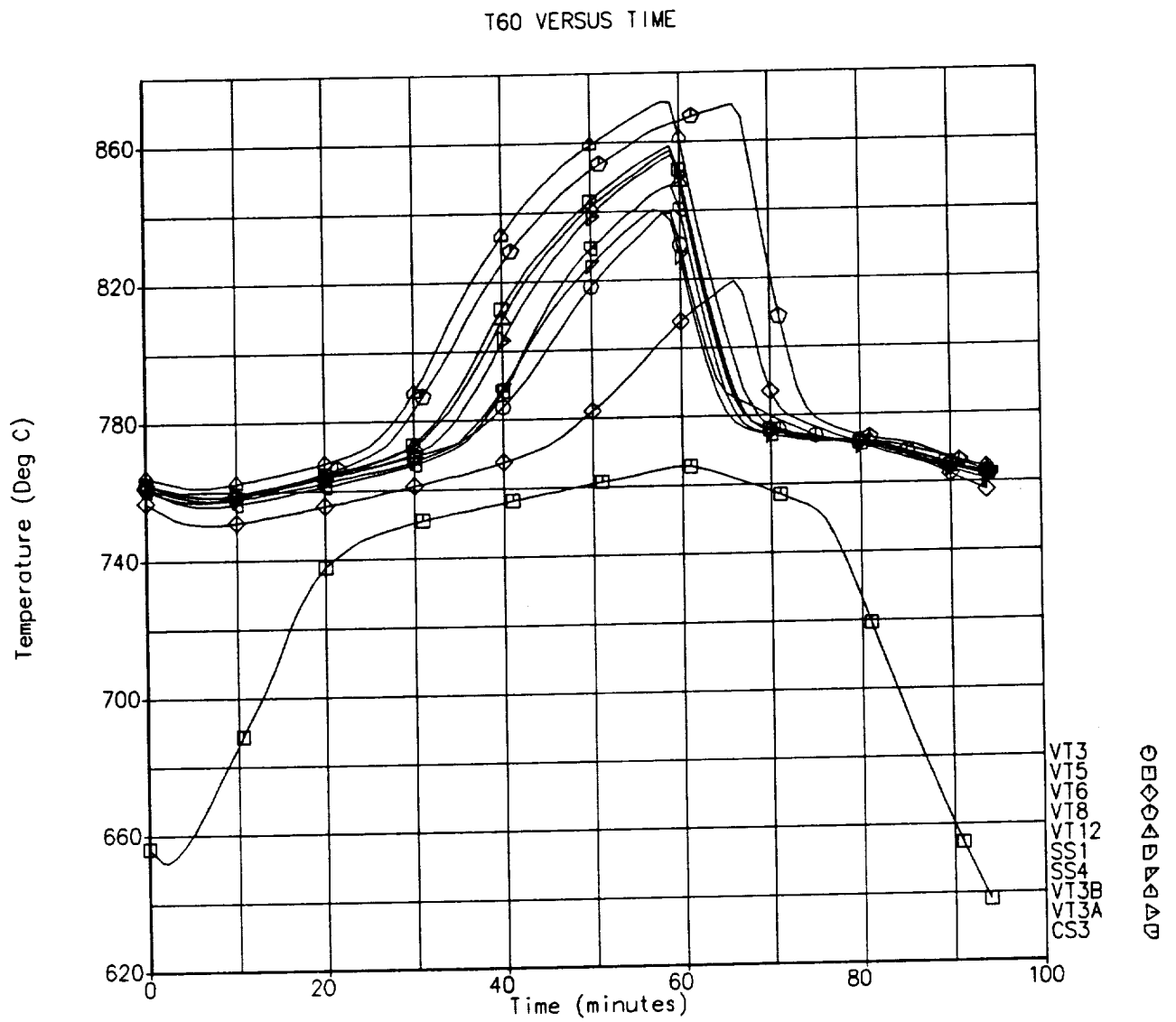


Figure C-15: Tube 19, Inlet End, Inner TES @ 90°

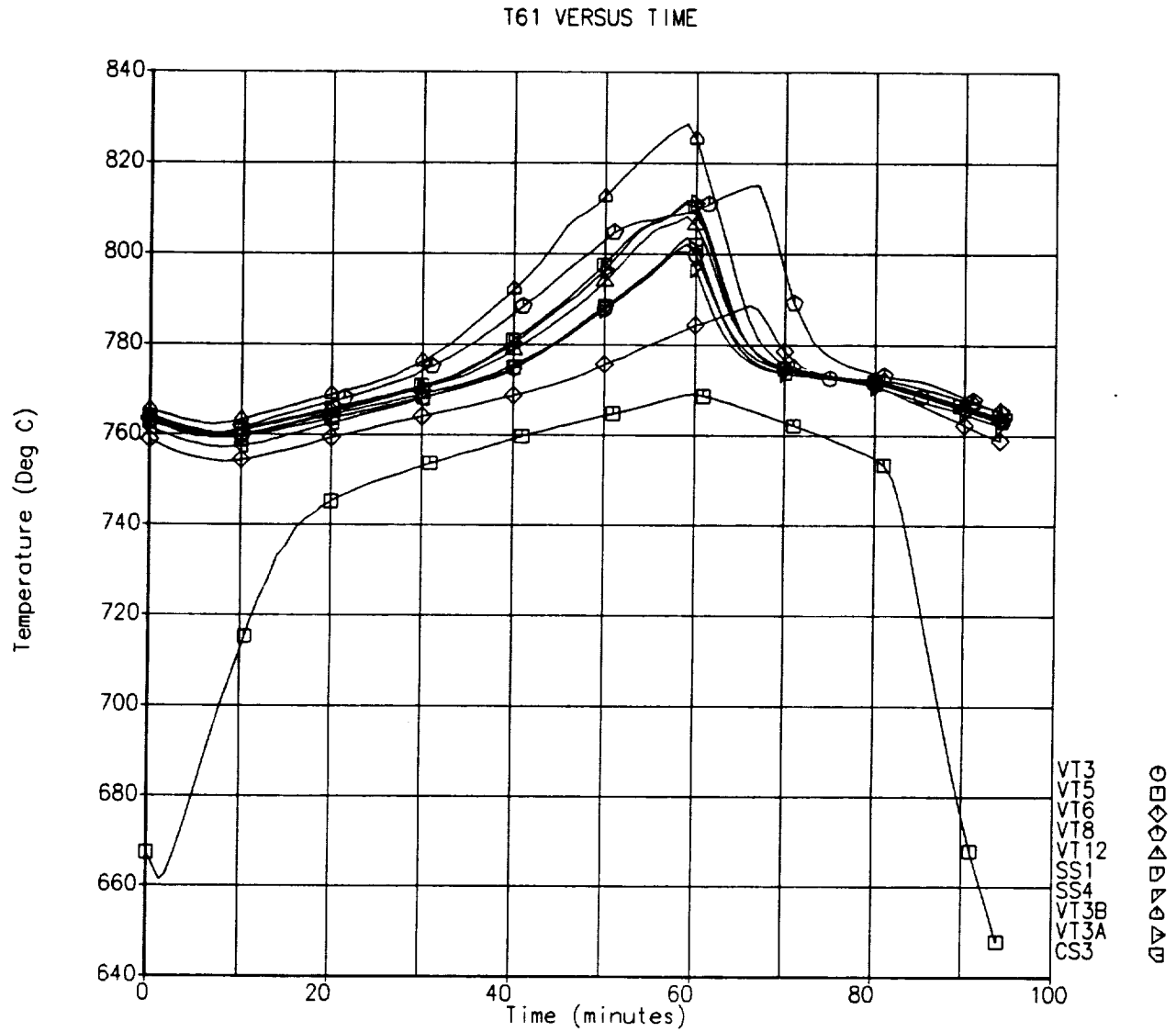


Figure C-16: Tube 19, Inlet End, Inner TES @ 270°

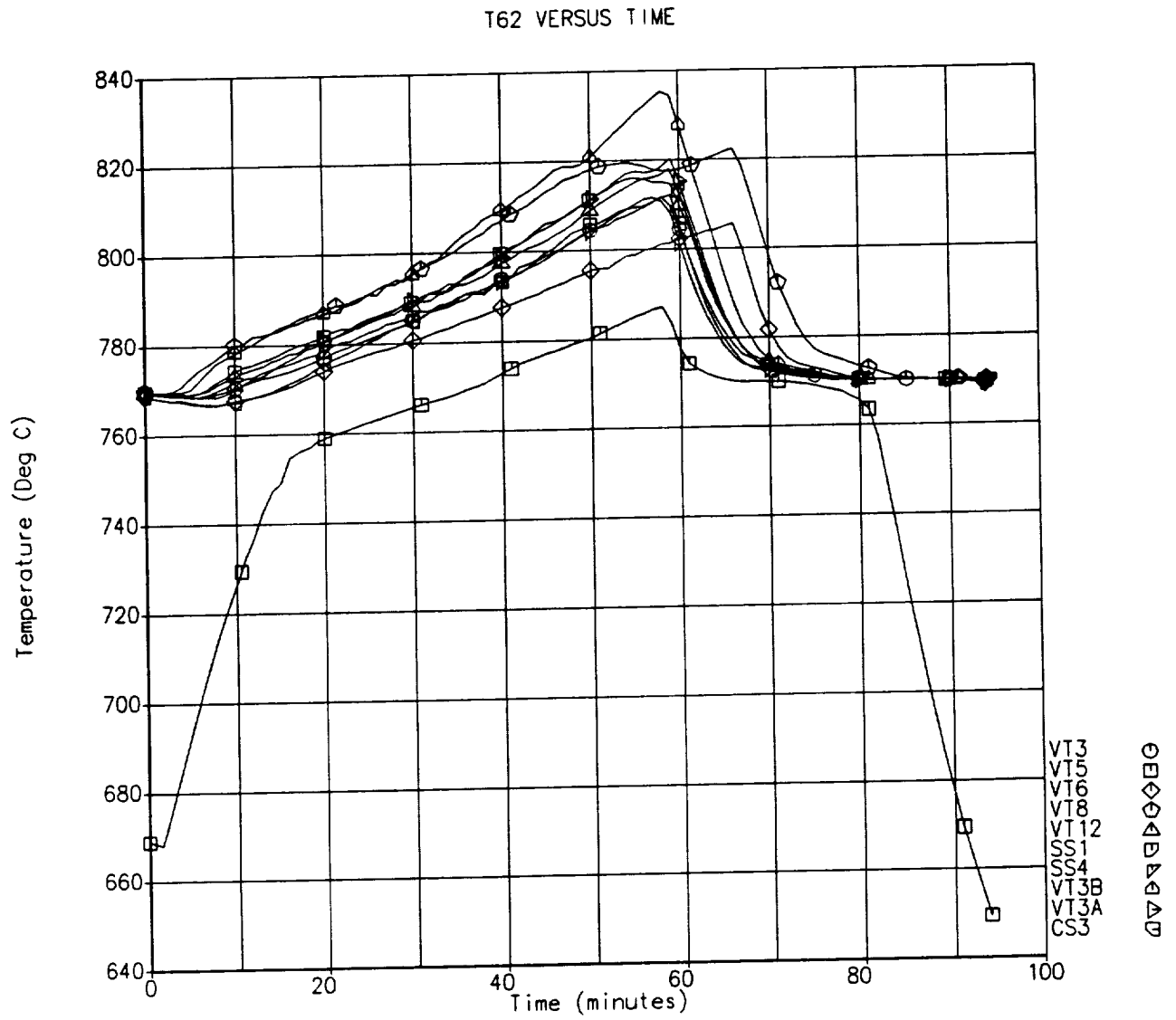


Figure C-17: Tube 19, Inlet End, Outer TES @ 270°

T63 VERSUS TIME

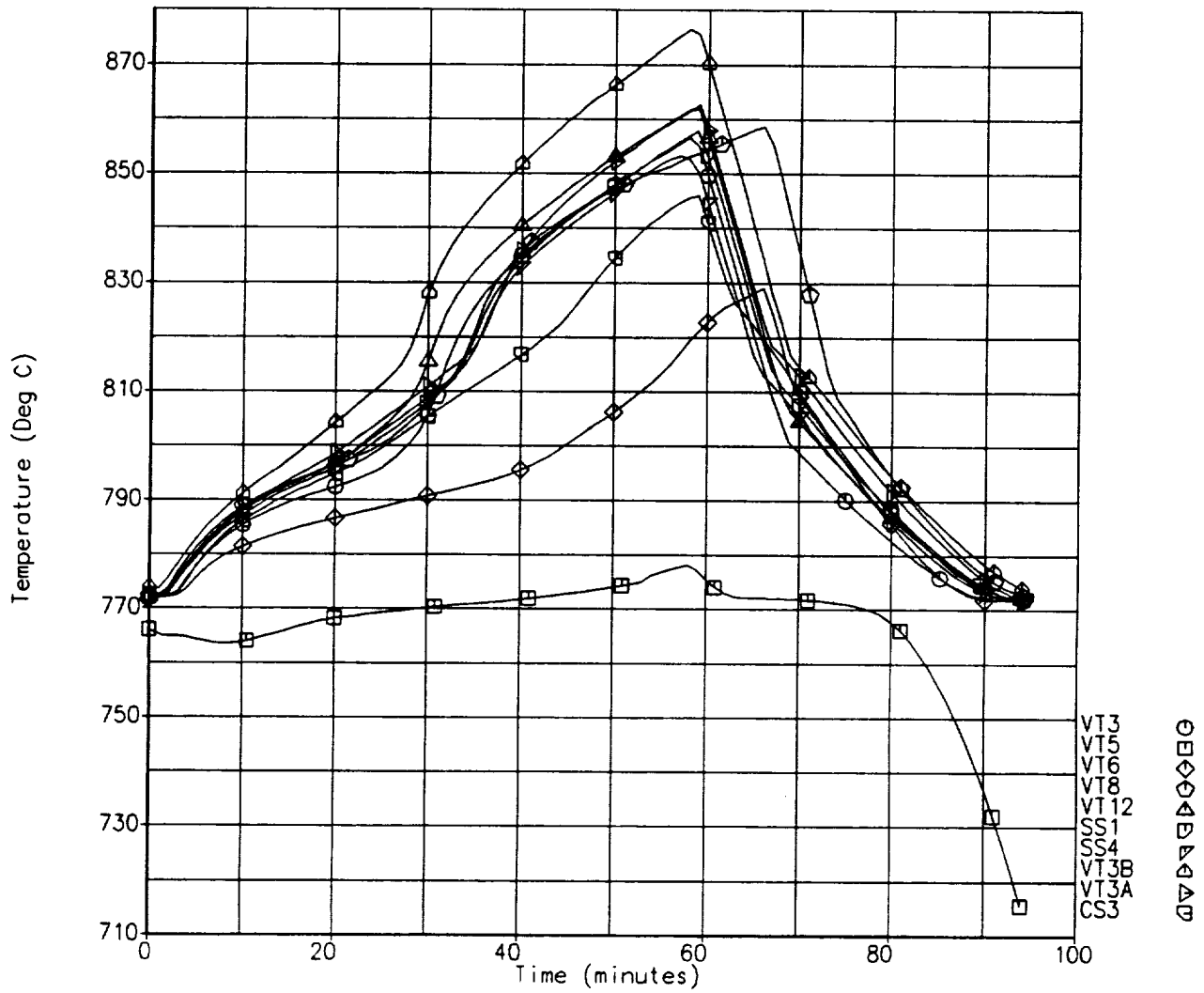


Figure C-18: Tube 19, Exit End, Outer TES @ 90°

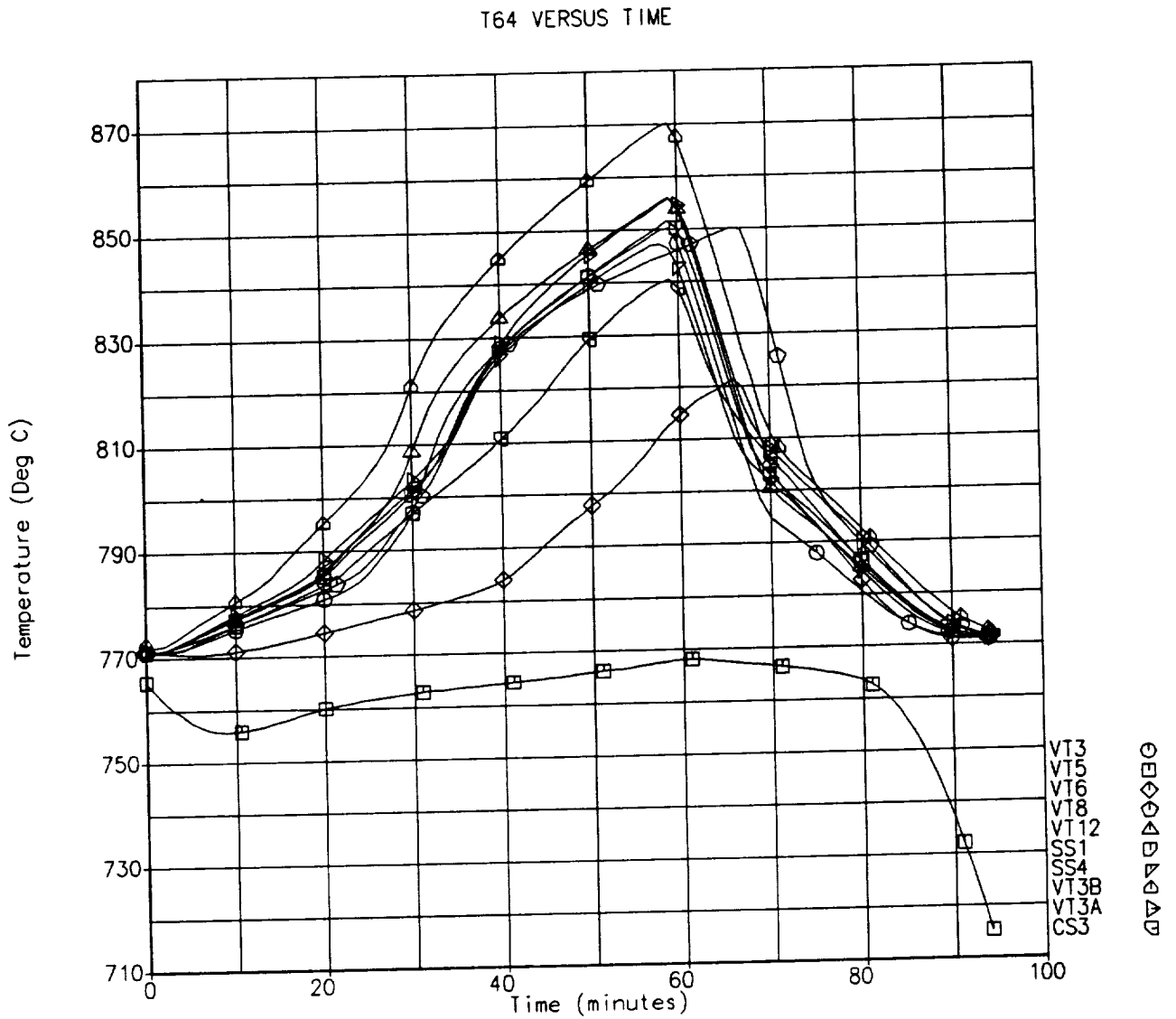


Figure C-19: Tube 19, Exit End, Inner TES @ 90°

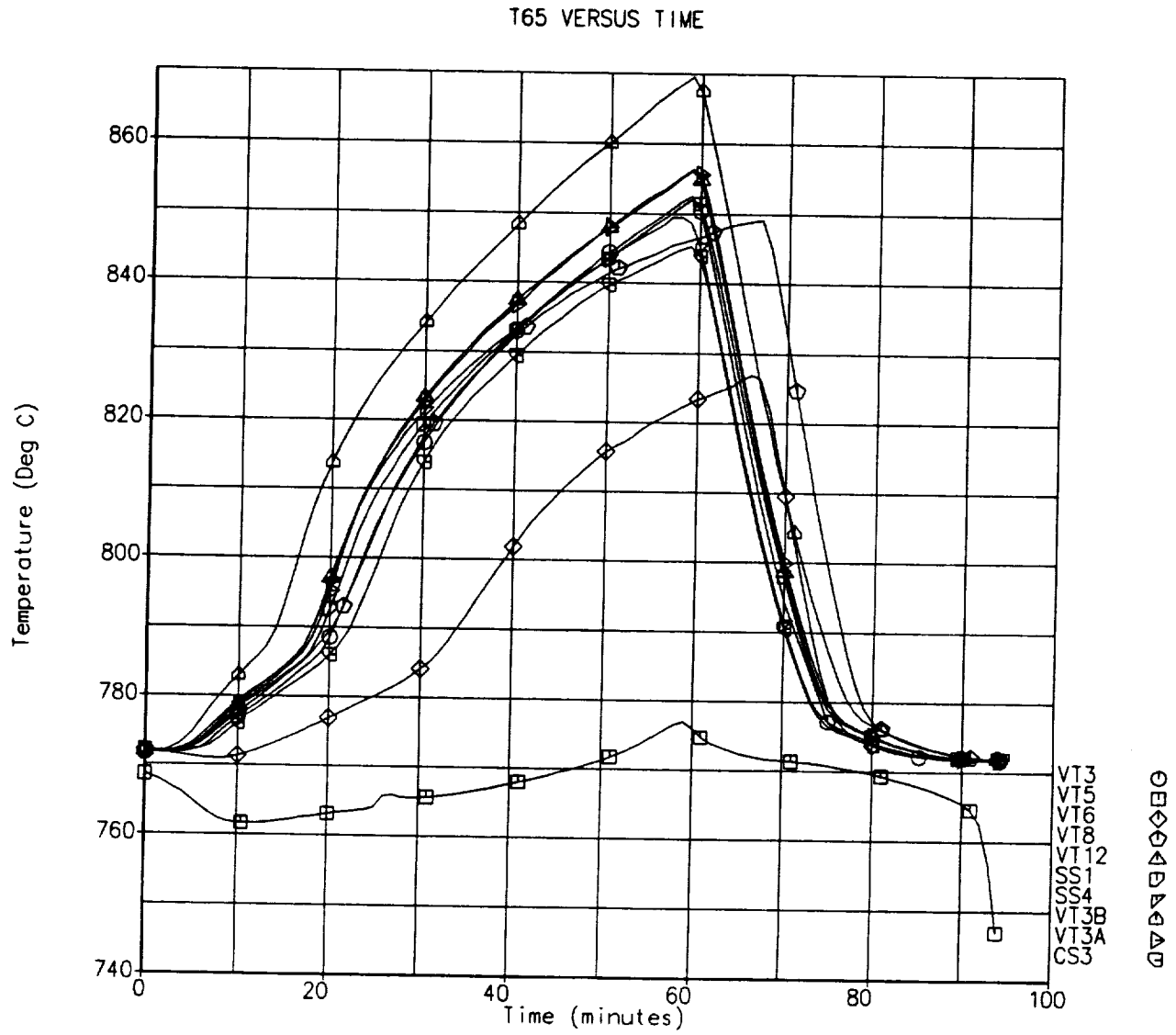


Figure C-20: Tube 19, Exit End, Inner TES @ 270°

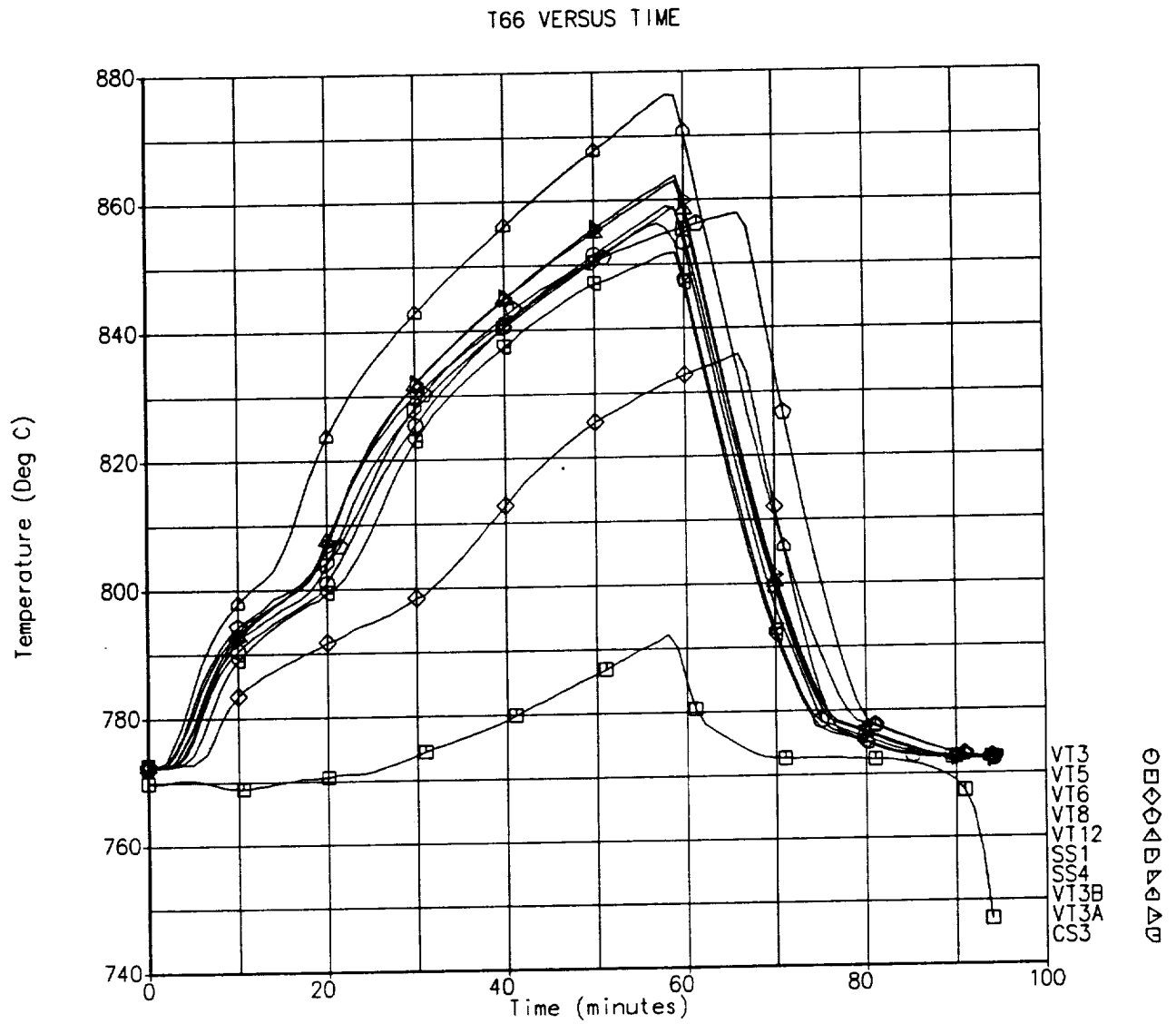


Figure C-21: Tube 19, Exit End, Outer TES @ 270°

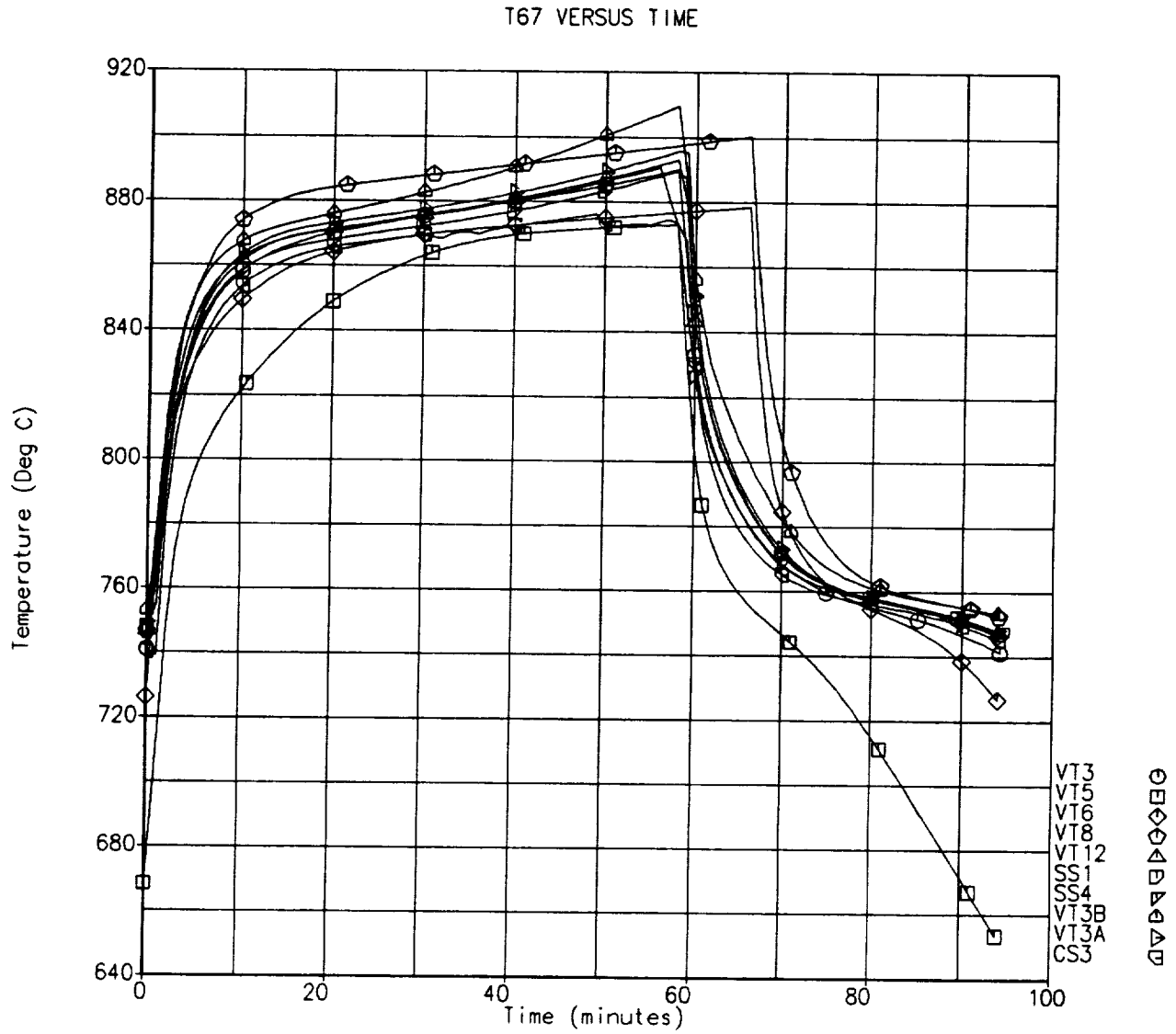


Figure C-22: Cavity, Back Wall, @ 60°

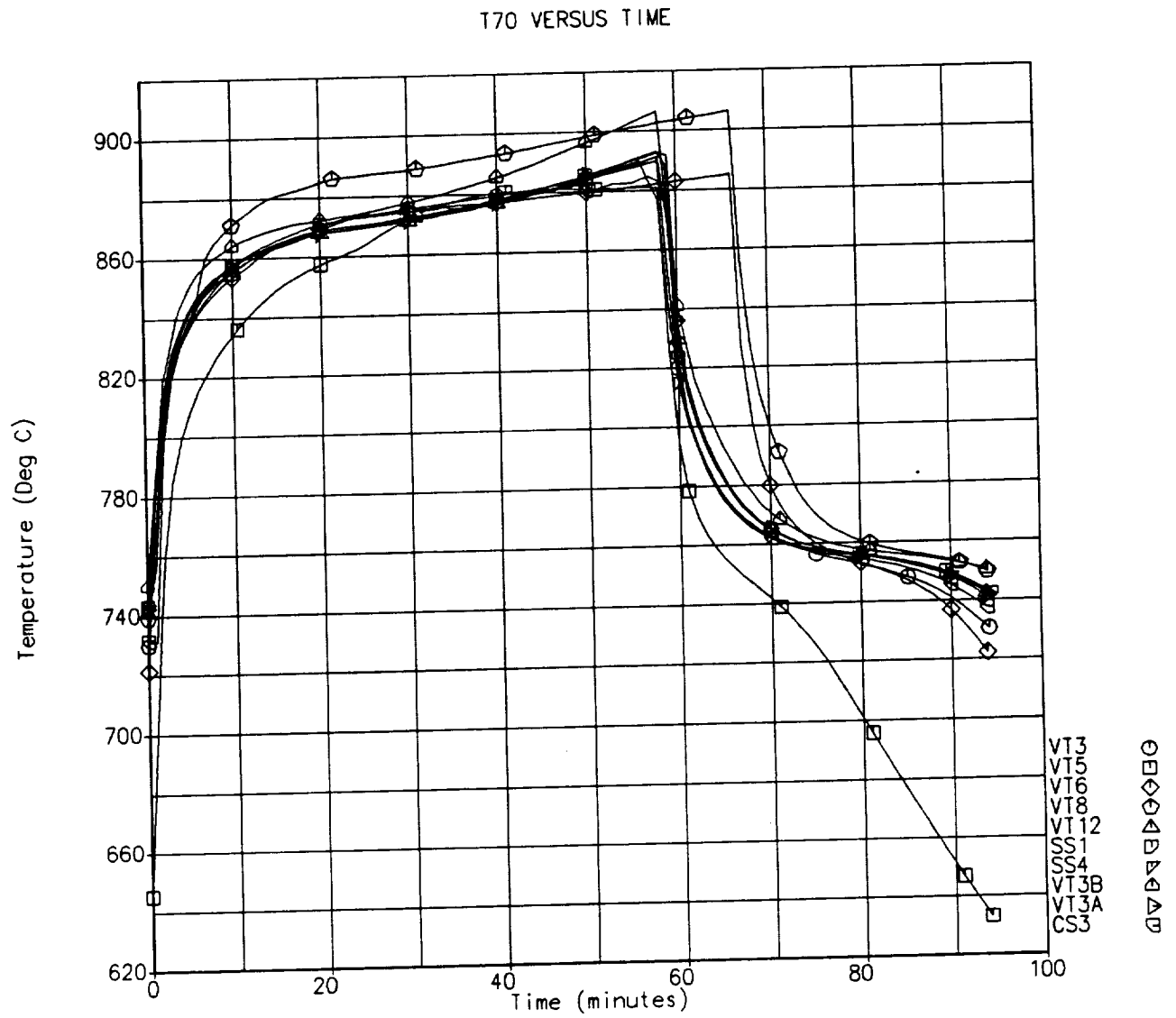


Figure C-23: Cavity, Front Side Wall, @ 60°

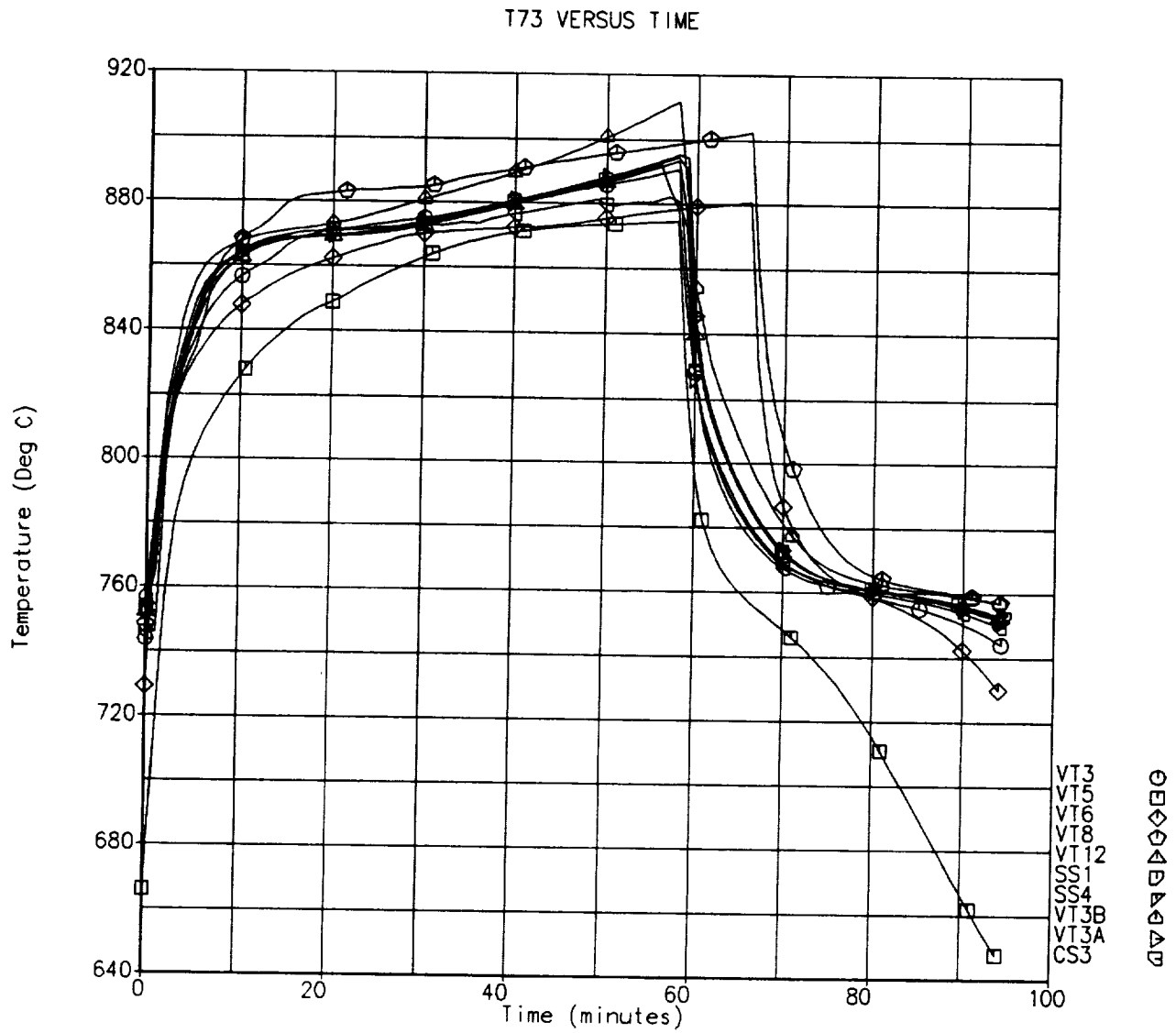


Figure C-24: Cavity, Mid Side Wall, @ 60°

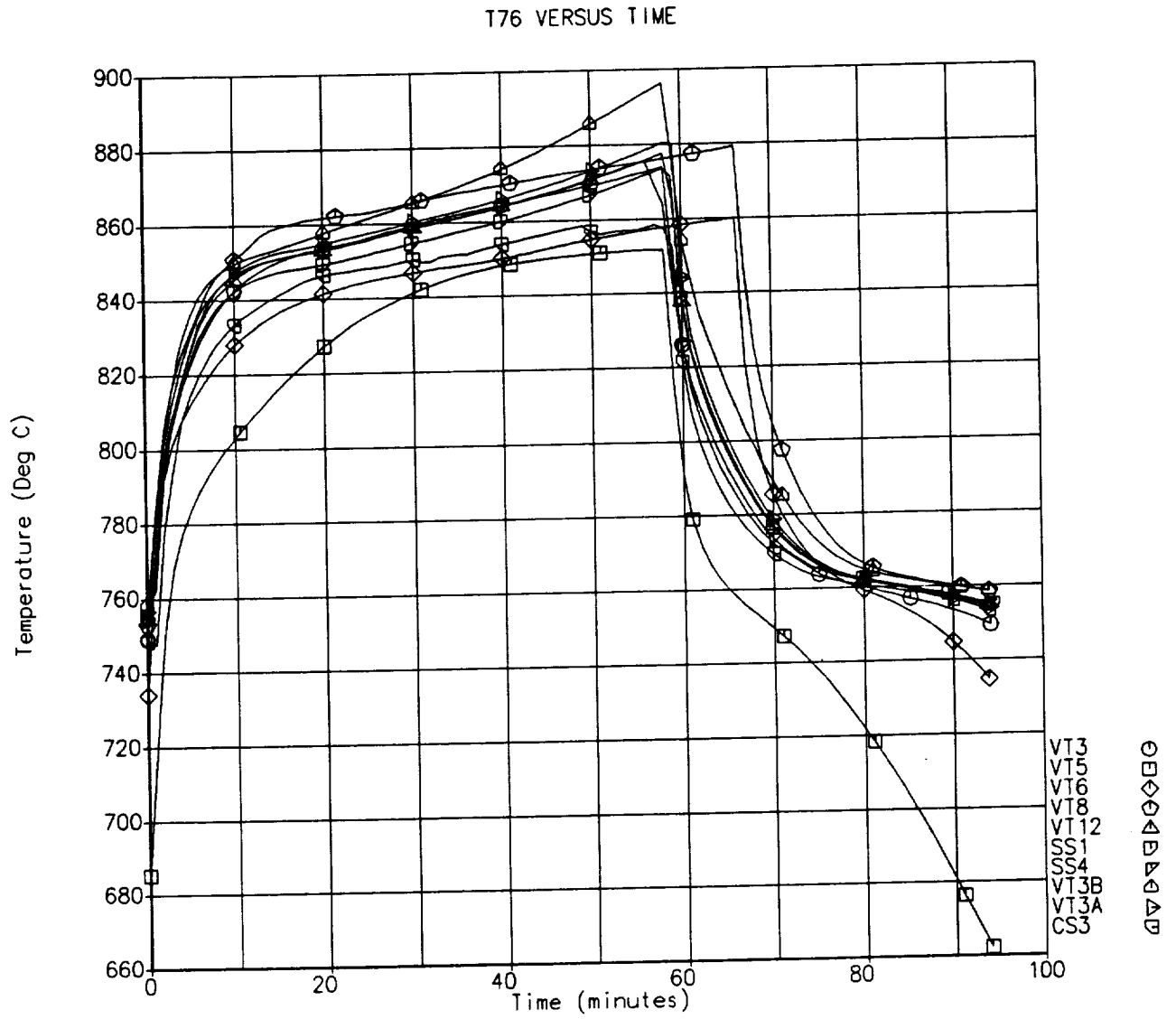


Figure C-25: Cavity, Rear Side Wall, @ 60°

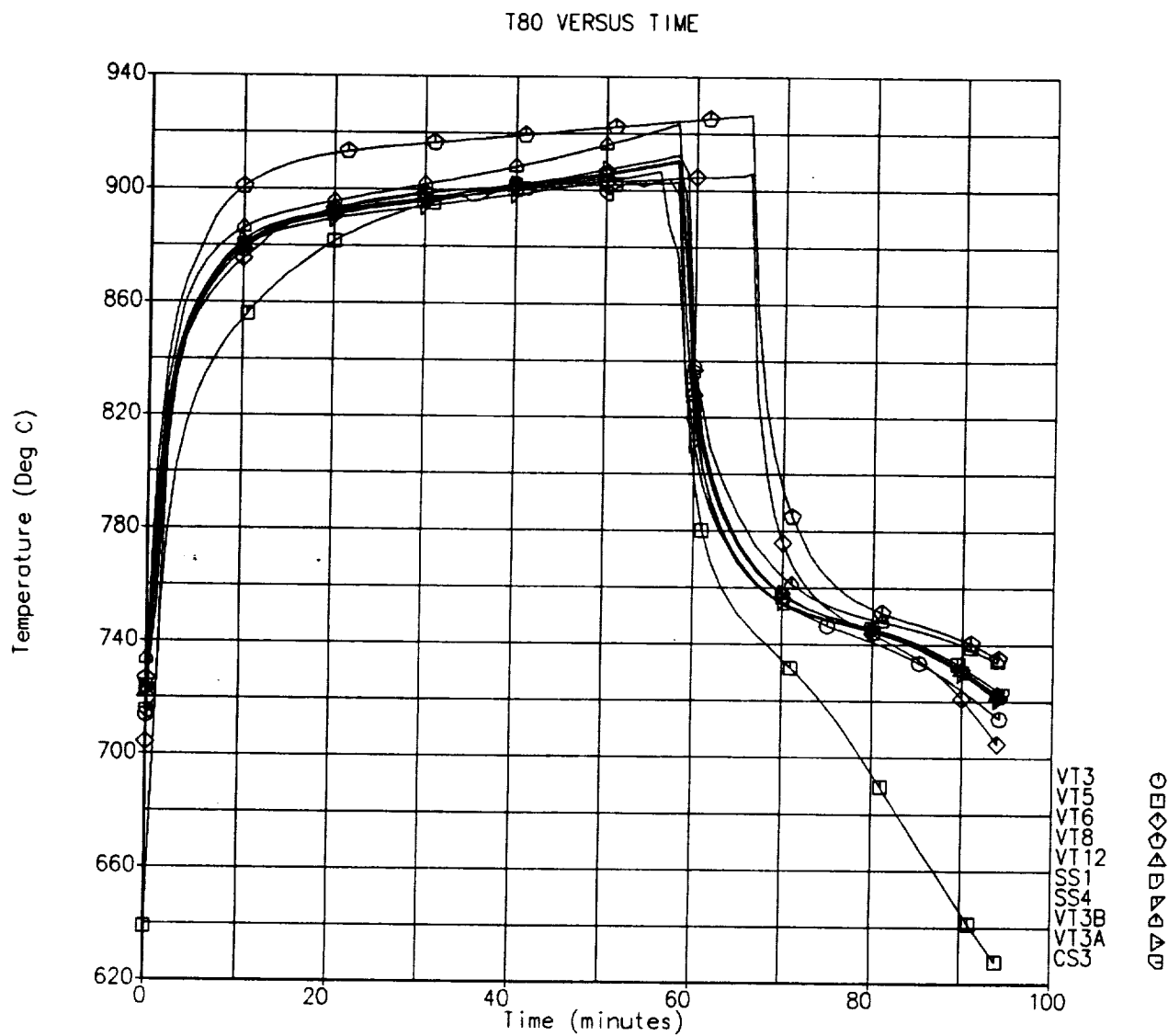


Figure C-26: Cavity, Inner Aperture, @ 60°

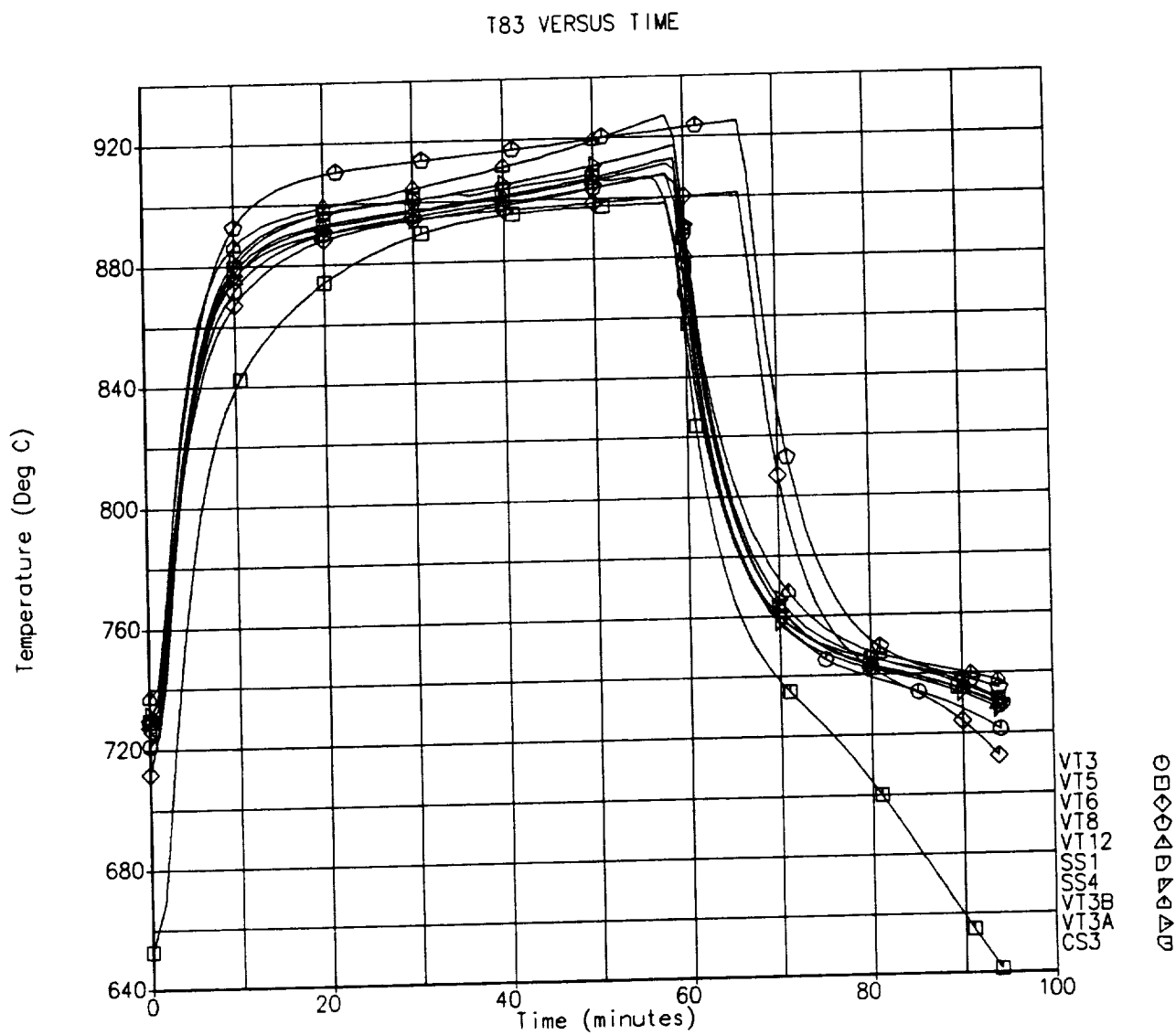


Figure C-27: Lamp Array, Zone 2 Box Beam

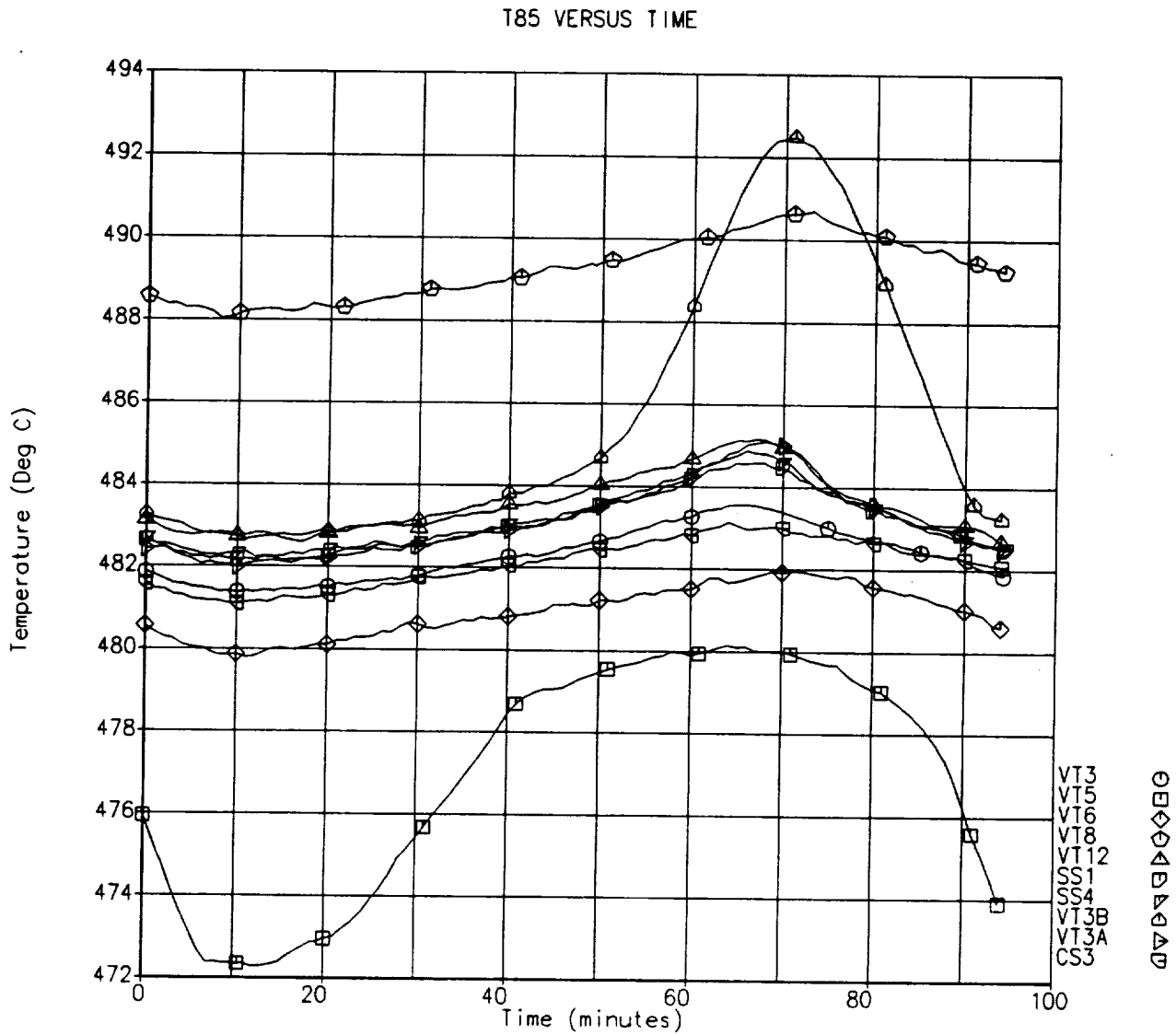


Figure C-28: Inlet Gas Temperature

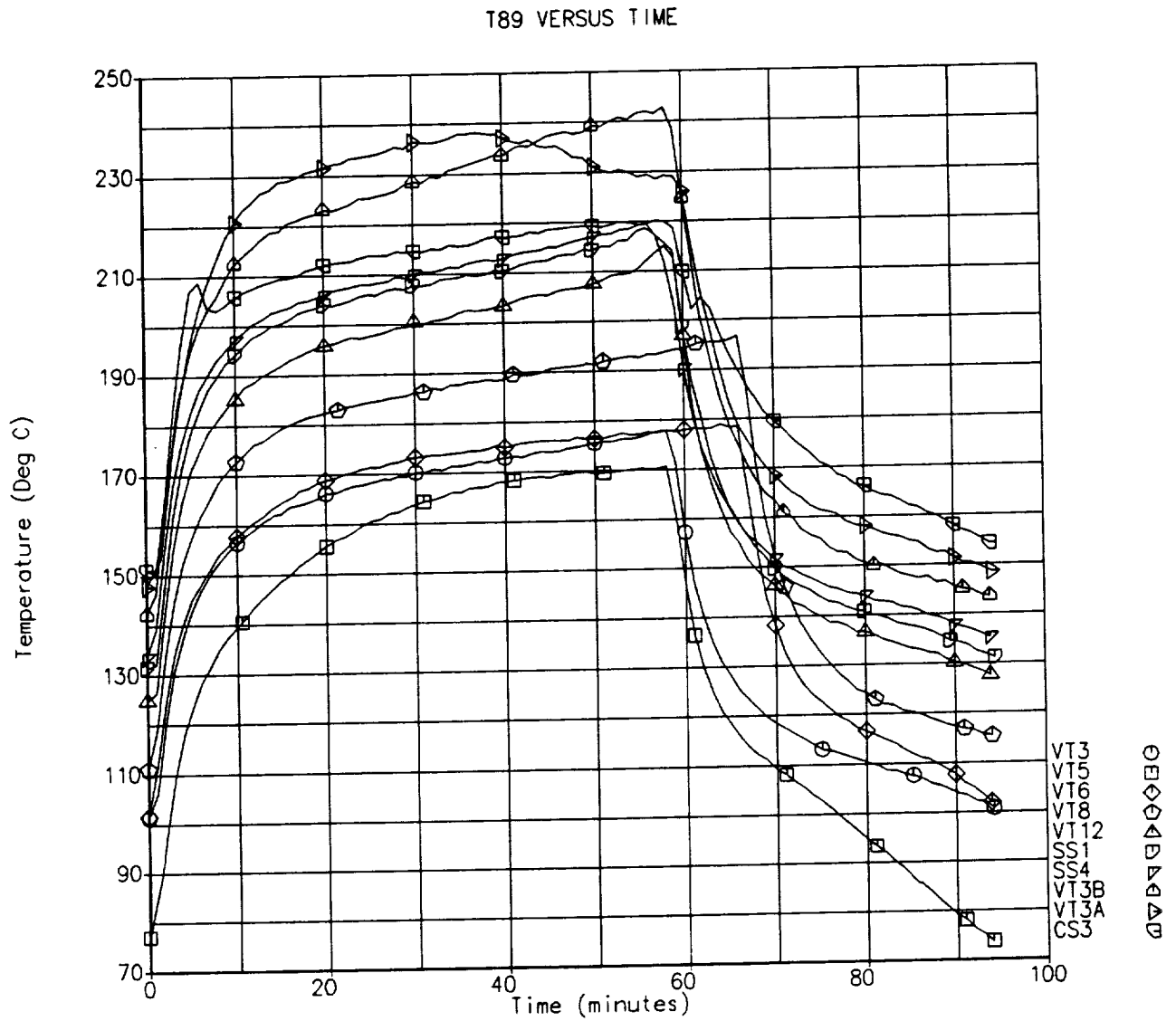


Figure C-29: Tip of Borescope

Figure C-30: Exterior, Front Side Wall, @ 60°

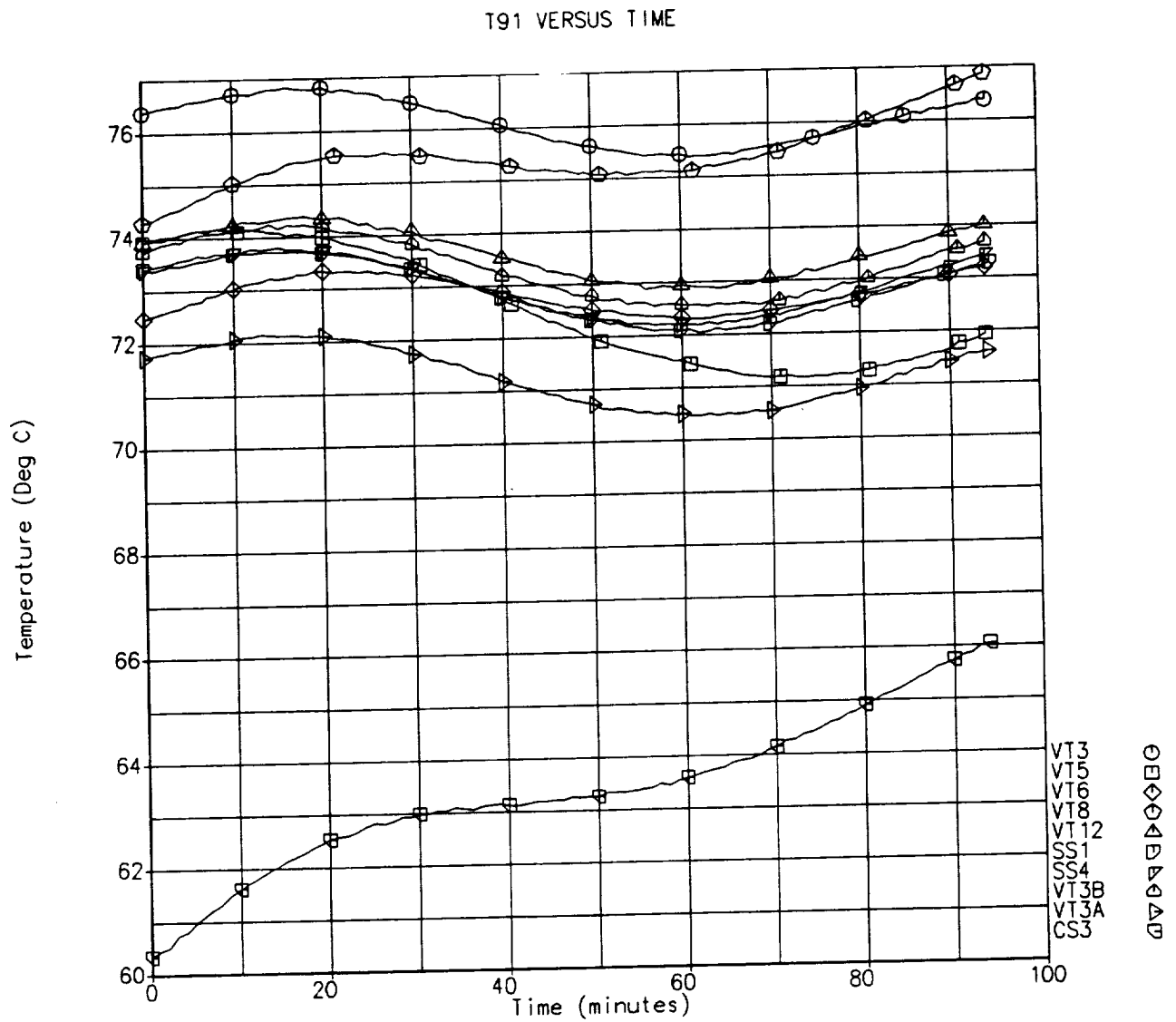


Figure C-31: Exterior, Front Side Wall, @ 180°

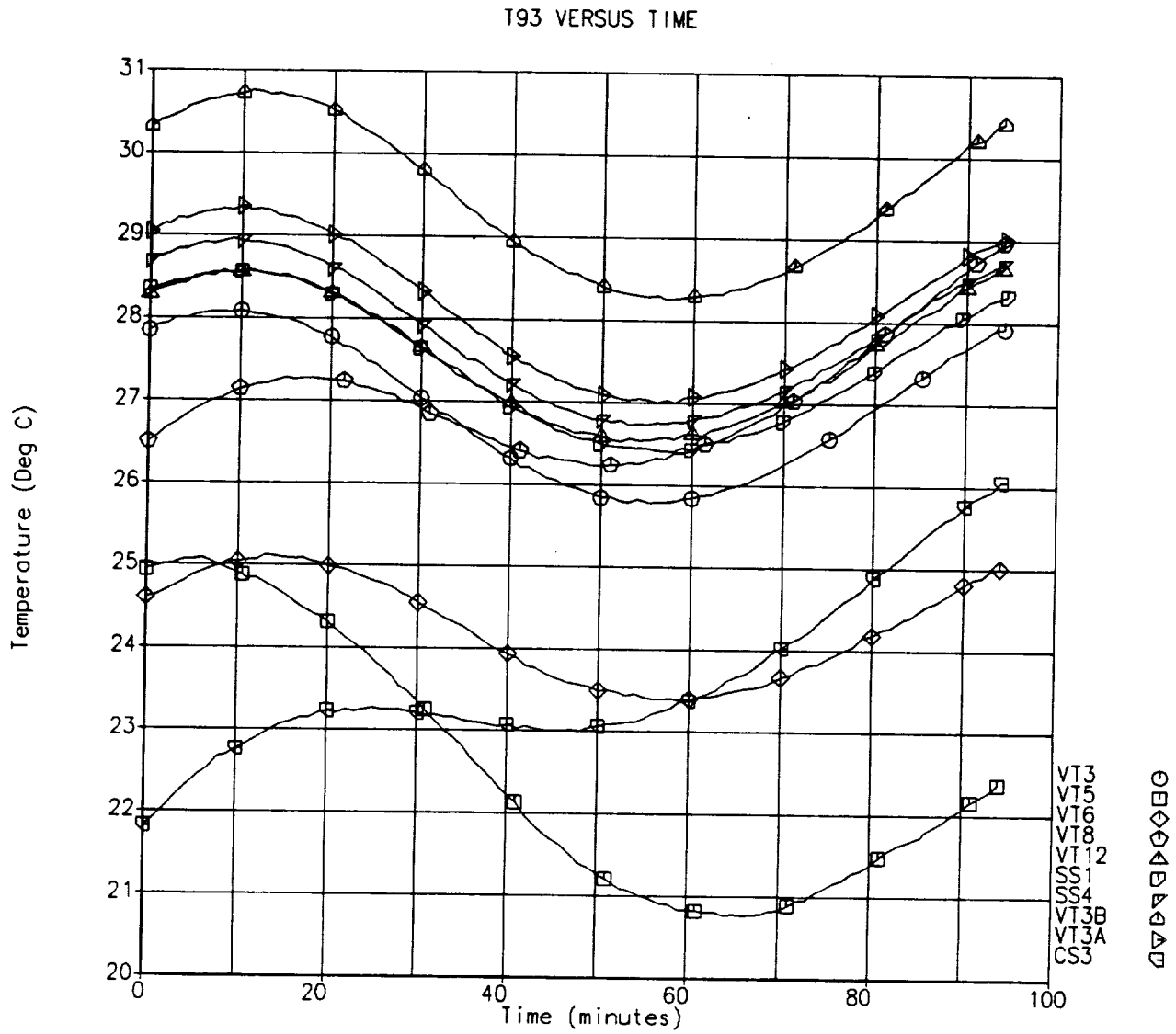


Figure C-32: Exterior, Rear Side Wall, @ 60°

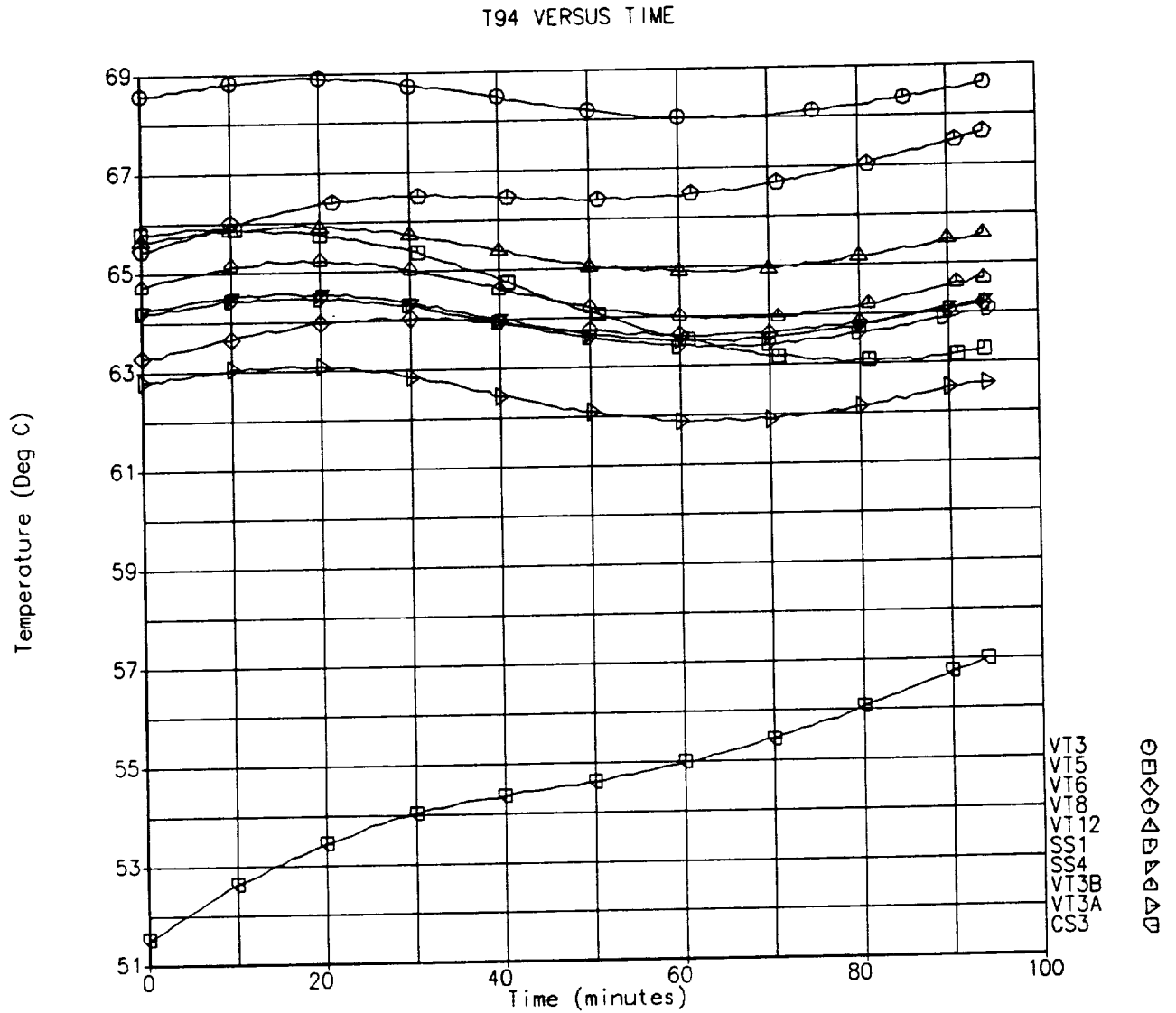


Figure C-33: Exterior, Rear Side Wall, @ 180°

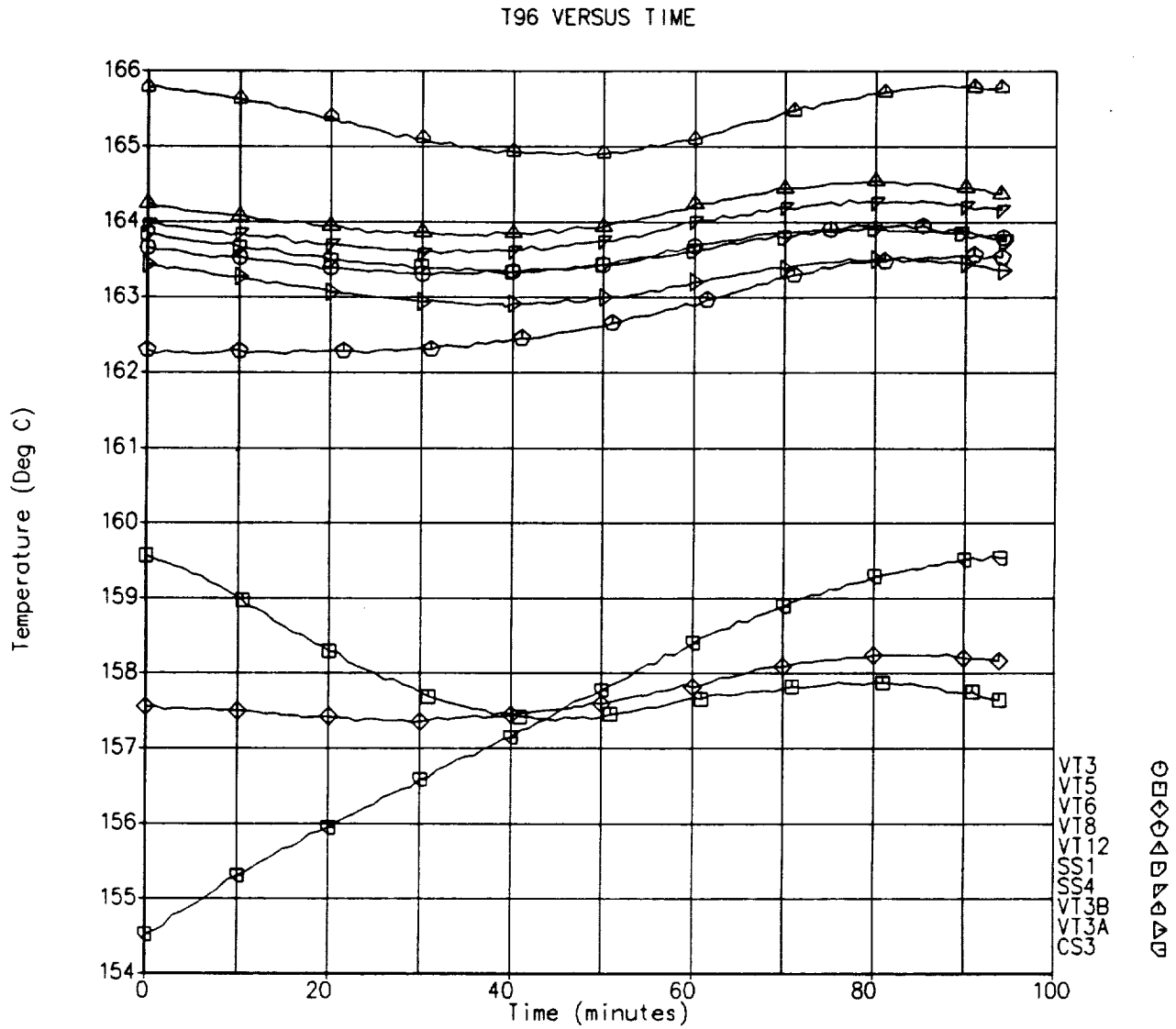


Figure C-34: Exterior, Aft Wall, @ 60°

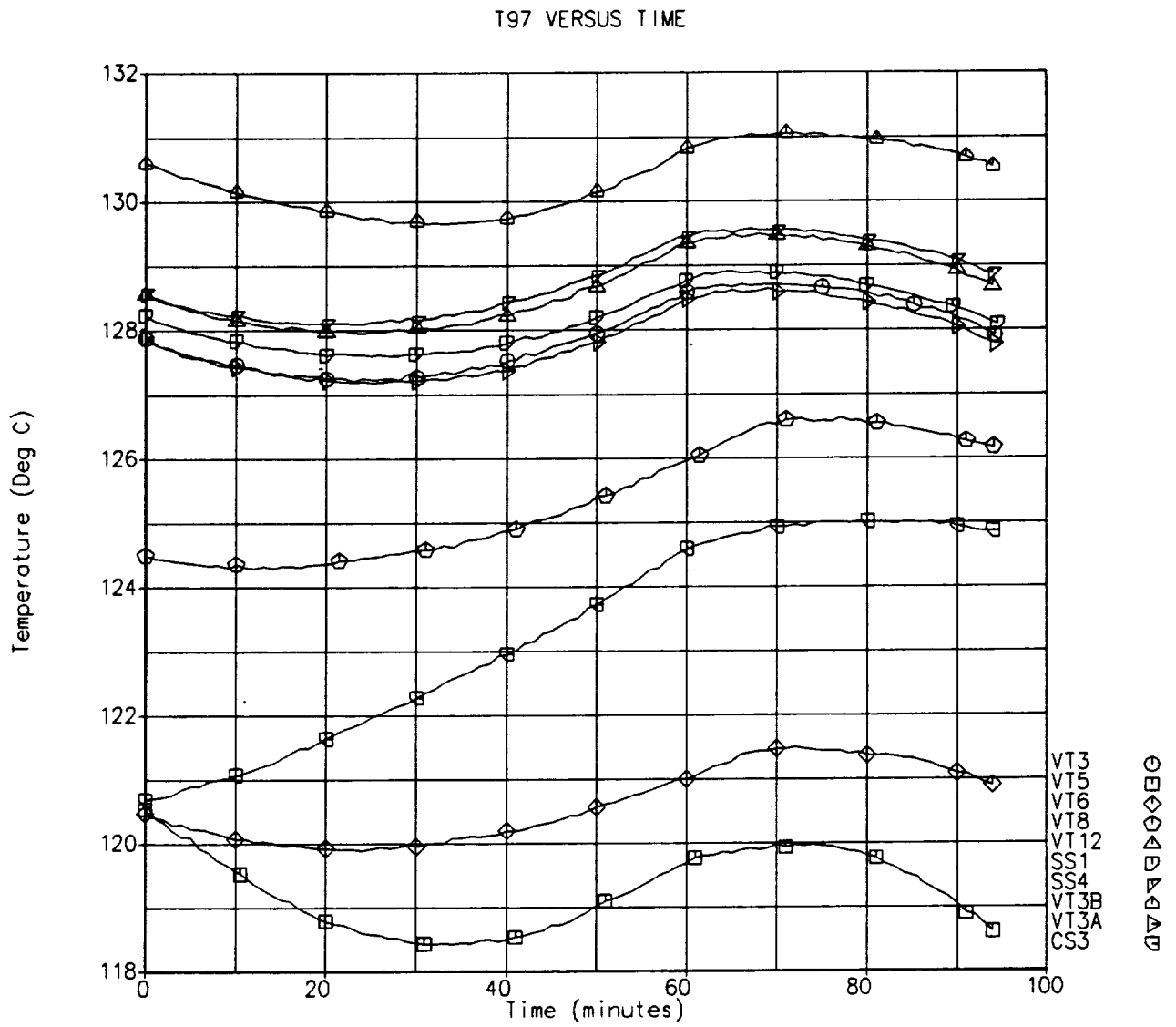


Figure C-35: Exterior, Aft Wall, @ 180°

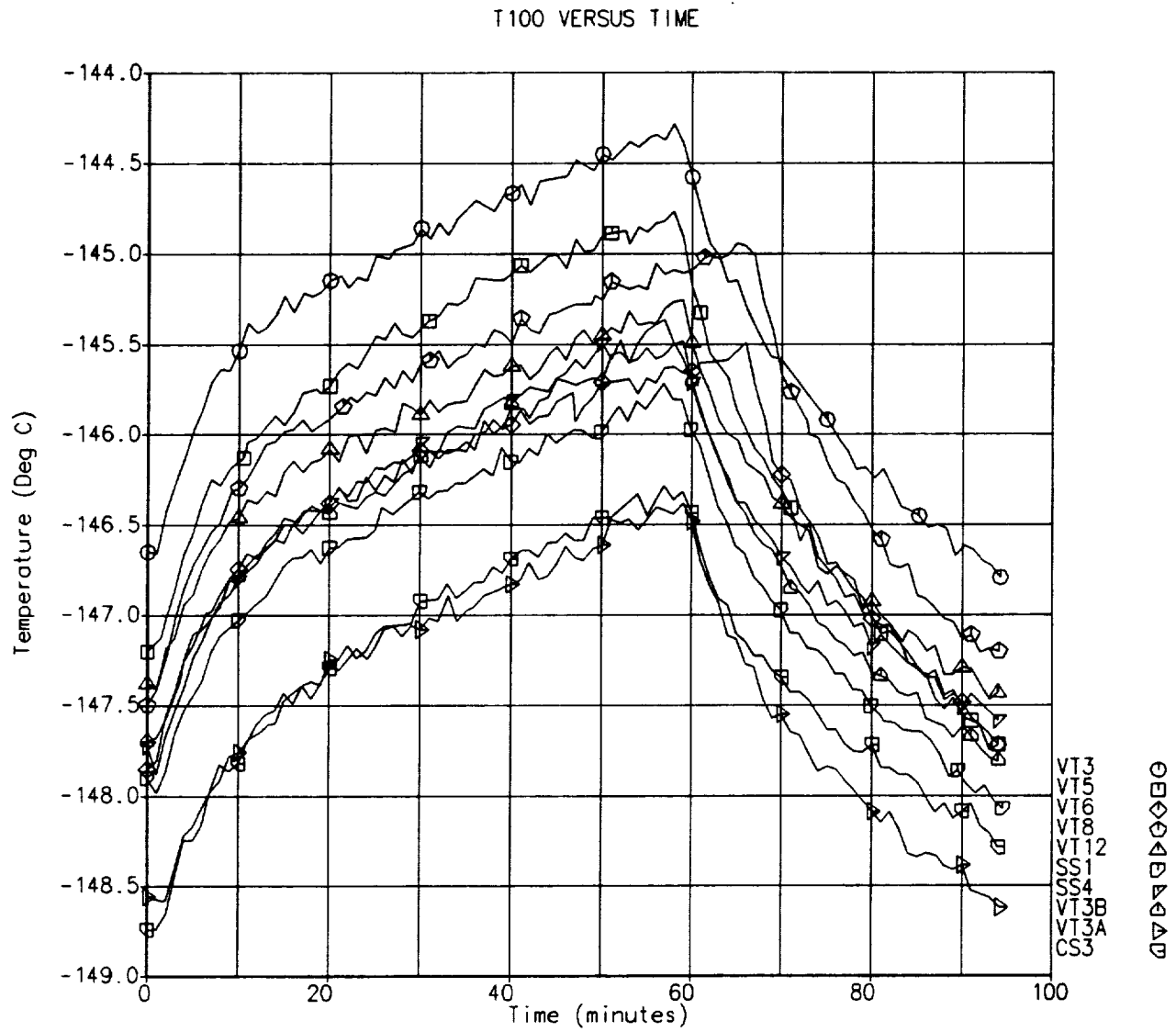


Figure C-36: LN₂ Line Exiting Cold Plate

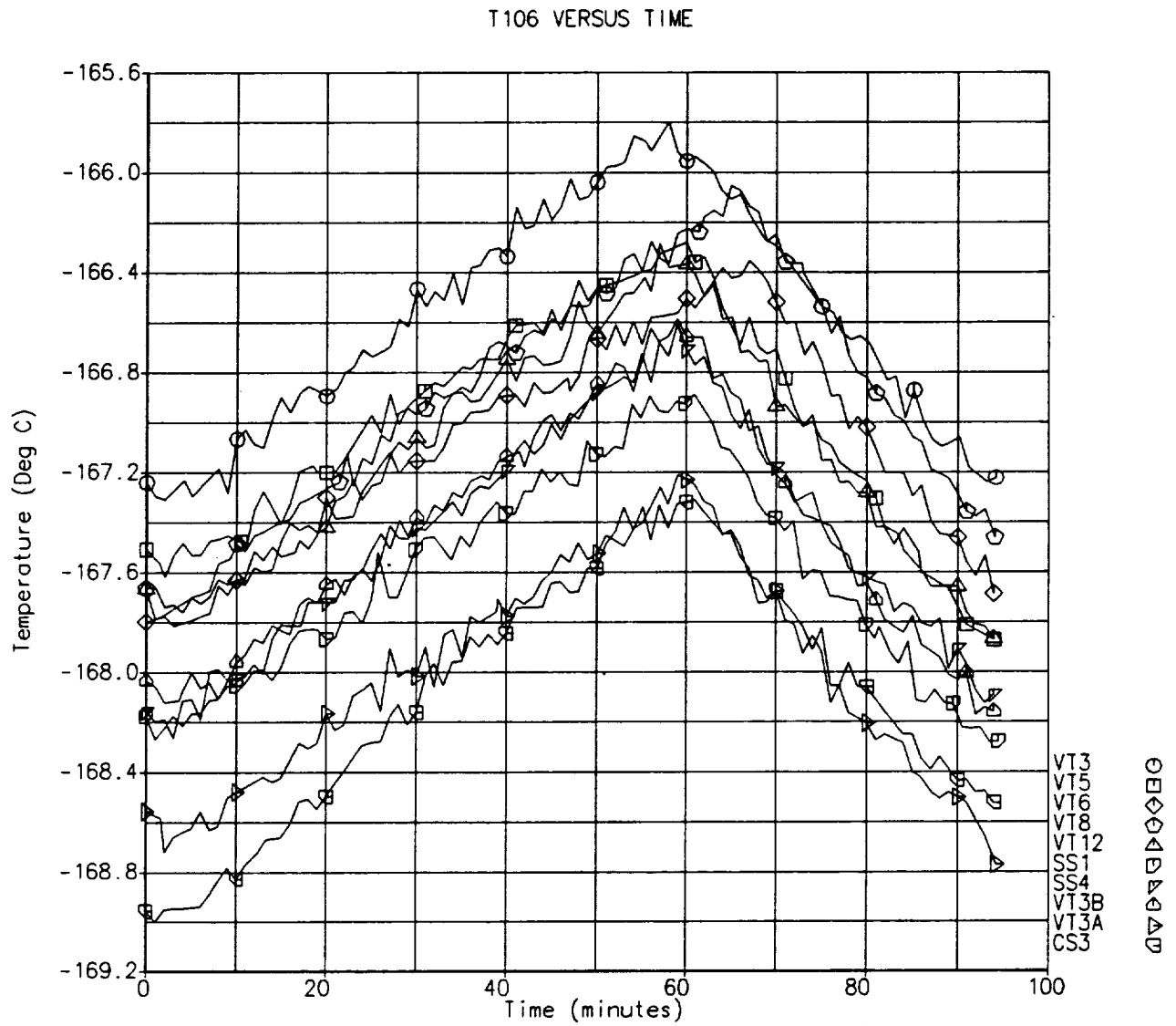


Figure C-37: Cold Shroud Panel, Upper Center

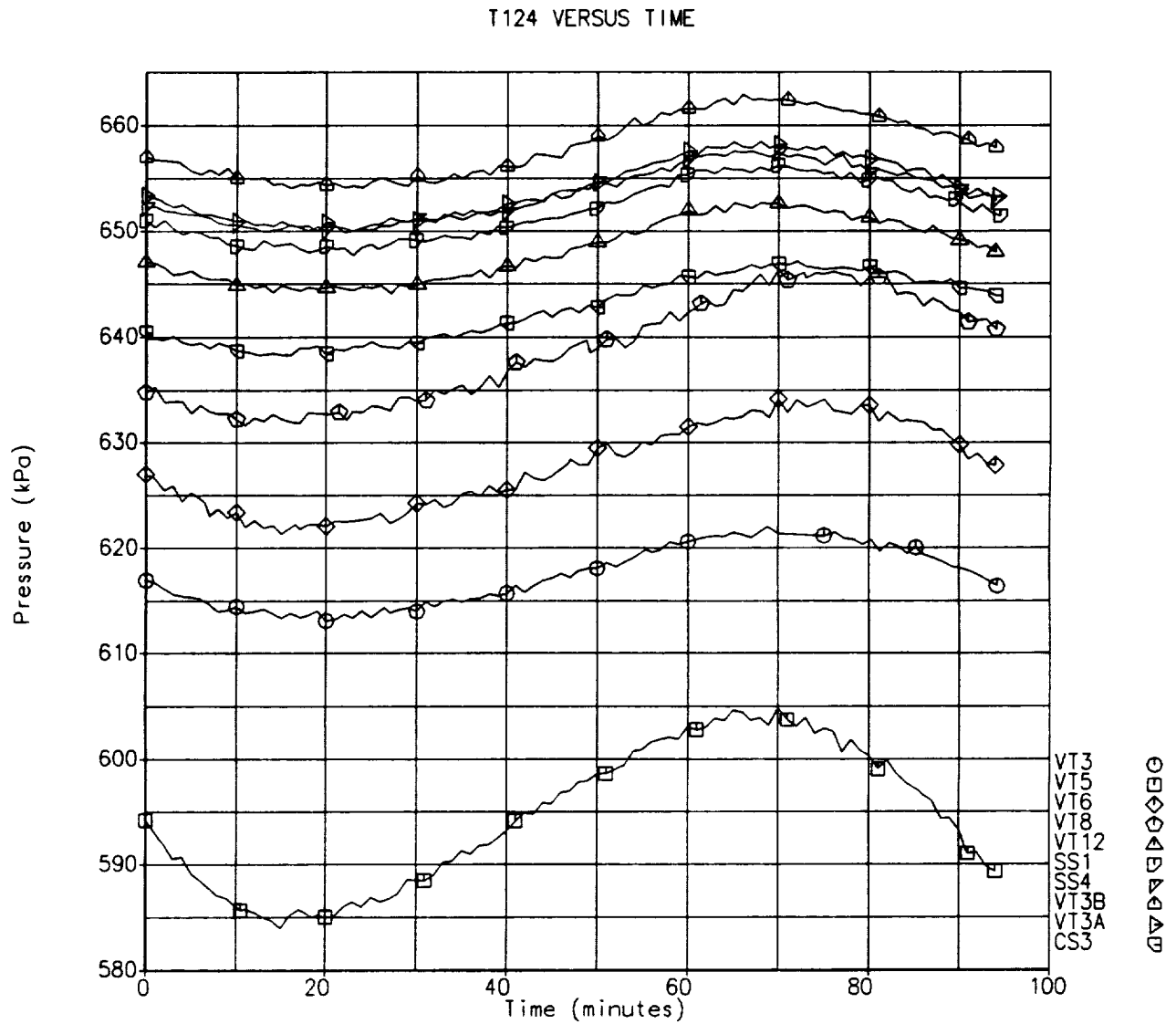


Figure C-38: Static Pressure, Receiver Inlet

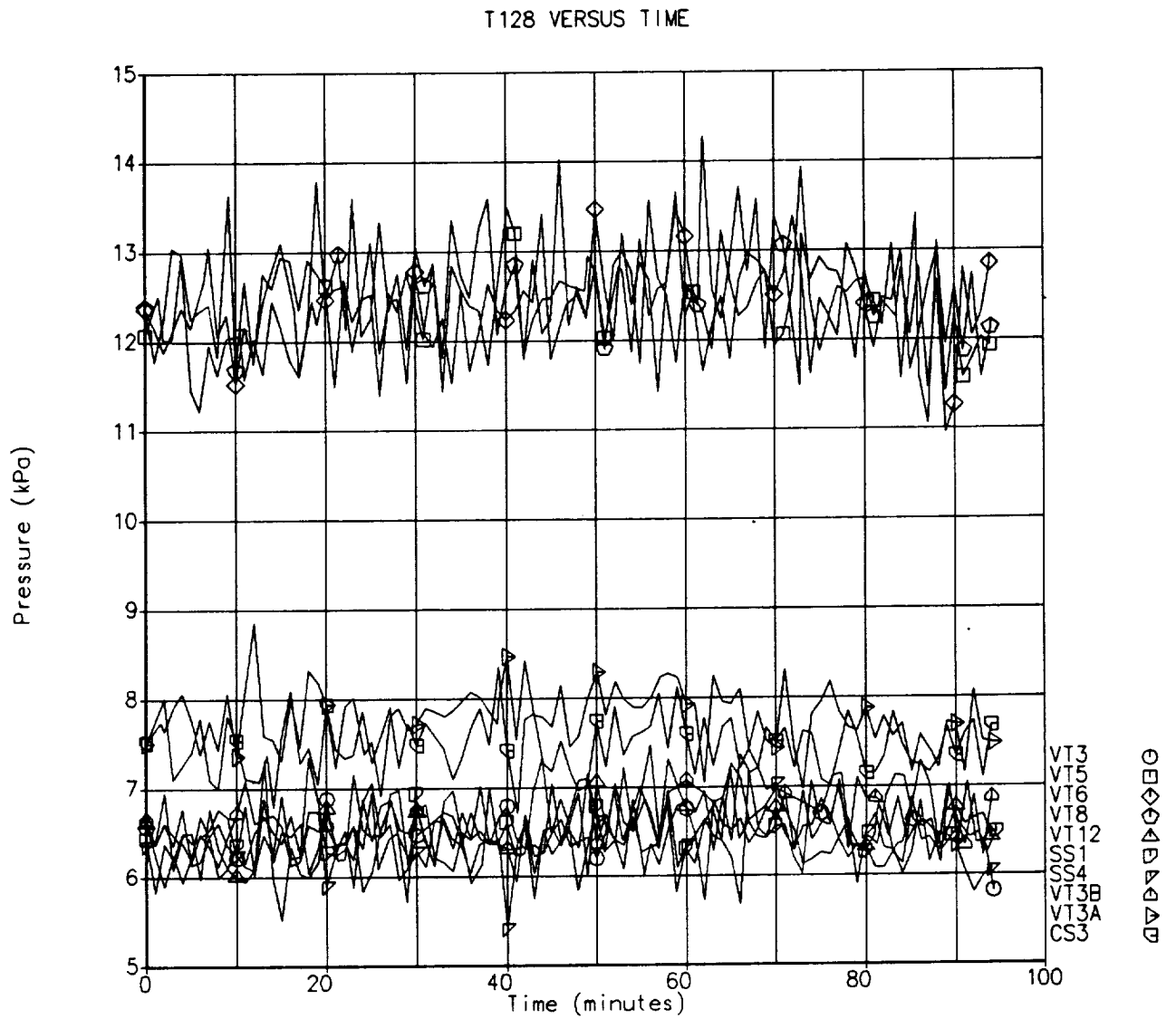


Figure C-39: Inlet to Exit Differential Pressure

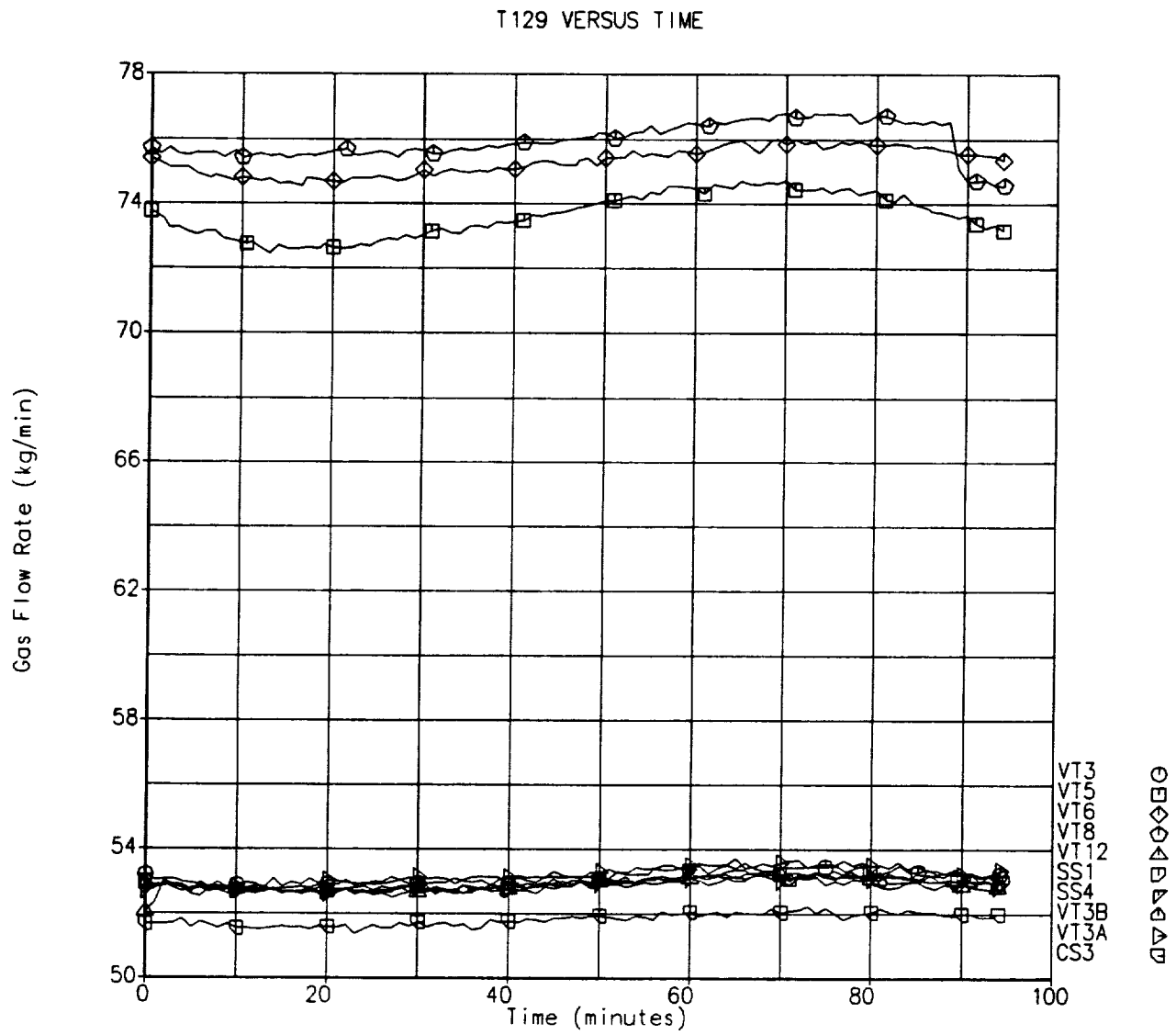


Figure C-40: Helium-Xenon Gas Flow Rate

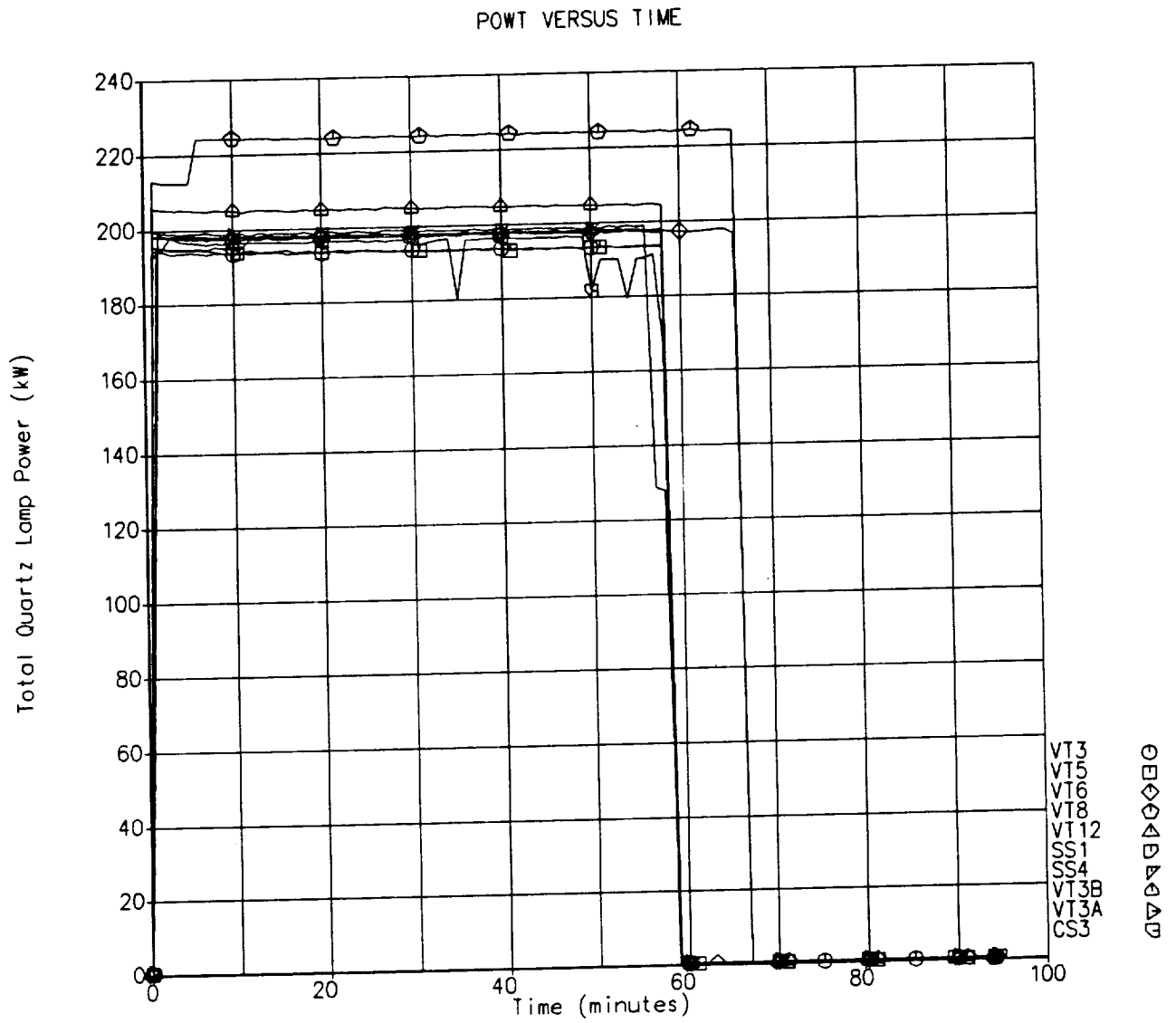


Figure C-41: Total Quartz Lamp Power

